



MONASH University

**Advances in Droplet Microfluidics for On-chip
Reactions and Study of Cell Biology**

by

Mohammad Reza Raveshi

Master of Science in Mechanical Engineering

A thesis submitted for the degree of *Doctor of Philosophy* at
Monash University 2020

Department of Mechanical and Aerospace Engineering
Faculty of Engineering
Monash University

September 2020

© Copyright
by
Mohammad Reza Raveshi
2020

Advances in Droplet Microfluidics for On-chip Reactions and Study of Cell Biology

Copyright notice

Notice 1

© Mohammad Reza Raveshi (2020).

Under the Copyright Act 1968, this thesis must be used only under the normal conditions of scholarly fair dealing. In particular no results or conclusions should be extracted from it, nor should it be copied or closely paraphrased in whole or in part without written consent of the author. Proper written acknowledgement should be made for any assistance obtained from this thesis.

Notice 2

© Mohammad Reza Raveshi (2020).

I certify that I have made all reasonable efforts to secure copyright permissions for third-party content included in this thesis and have not knowingly added copyright content to my work without the owner's permission.

Abstract

This thesis is focused on droplet microfluidics and droplet manipulation techniques to enhance high throughput screening and on-chip reactions. The most impactful contributions of this thesis are inventing a selective droplet splitting technique using a single layer microfluidic valve (Chapter 3), demonstrating an integrated droplet generation, splitting, and merging technique for producing products of different concentrations (Chapter 4), and resolving the interaction mechanisms of sperm with soft curved interfaces using droplet microfluidics (Chapter 5).

A novel, on demand and compact high throughput screening platform is introduced in Chapter 3 by using a single layer valve to selectively split droplets. In this chapter, the transition behaviour of the system is characterised for a range of oil and water inlets and valve actuation pressures, showing that the valve can be actuated such that the next droplet to pass the bypass loop will be split, but subsequent droplets will not be. Control over the pressure of two inlets and one valve simultaneously gives users the capability to dictate the range of droplets that can be produced in the valve-induced selective splitting platform. When the splitting technique is combined with the selective generation and merging systems, it can be used as a high throughput system for combinatorial library purposes as is shown in Chapter 4.

The platform introduced in Chapter 4 uses pneumatic single layer valves to integrate generating, splitting, and merging in a single microfluidic device for the first time. These single layer valves are used to control the generation of droplets and the location of splitting. The generated droplets act as vessels that transport different samples around the chip, these vessels can then be subdivided at splitting locations, just as pipettes can be used to dispense a fraction of its total volume. The split droplets enter a merging channel in which daughter droplets of different types and sizes can be reacted together. As a result, a matrix of products with different concentrations from an array of ingredients is produced. This work advances research into a major application of droplet microfluidics, that of high throughput screening, in which libraries of reagents are mixed together in different permutations. A second major application is in single cell investigations, which is the topic of Chapter 5.

Single cell analysis techniques isolate individual cells in droplets, allowing their contents to be analysed, for example, post lysis. In Chapter 5, instead of examining a cells lysate, the

behaviour of live, swimming cells are studied. Single sperm cells are isolated in droplets ranging from 30 μm to 140 μm in radius, and the resulting sperm swimming characteristics are examined. It is revealed for the first time that curvatures activate a dynamic response mechanism in sperm to switch from a progressive surface-aligned motility mode at low curvatures to an aggressive surface-attacking mode at high curvatures. In the attacking mode, the sperm head is consistently aligned at 70° with respect to the interface and swim $\sim 35\%$ slower, spending 1.66-fold longer time at the interface than progressive mode. The results reveal that the increasing geometrical complexity of the female fallopian tube alters sperm motion to guide the locomotion at lower curvatures, but to increase and prolong surface contact at higher curvatures, enabling sperm capacitation and fertilization closer to the site of fertilization.

List of Publications

Articles in Peer-reviewed Journals

1. **Mohammad Reza Raveshi**, Sagar N Agnihotri, Muhsincan Sesen, Rajneesh Bhardwaj, Adrian Neild, “Selective droplet splitting using single layer microfluidic valves”, *Sensors and Actuators B: Chemical*, Vol. 292, pp. 233-240, 2019.
2. **Mohammad Reza Raveshi**, Sagar N Agnihotri, Rajneesh Bhardwaj, Adrian Neild, “Controlled Droplet Manipulation and Interaction using Single Layer Microvalves” – Under Review in *Sensors and Actuators B: Chemical*.
3. **Mohammad Reza Raveshi**, Melati Abdul Halim, Sagar N Agnihotri, Moira K. O’Byrne, Adrian Neild, Reza Nosrati, “Curvature in the Reproductive Tract Alters Sperm-Surface Interaction” – Awaiting Revision in *Nature Communications*.
4. Sagar N Agnihotri, **Mohammad Reza Raveshi**, Rajneesh Bhardwaj, Adrian Neild, “Microfluidic Valves for Selective On-chip Droplet Splitting at Multiple Sites”, *Langmuir*, Vol. 36, no. 5, pp. 1138-1146, 2020.
5. Sagar N Agnihotri, **Mohammad Reza Raveshi**, Rajneesh Bhardwaj, Adrian Neild, “Droplet breakup at the entrance to a bypass channel in a microfluidic system”, *Physical Review Applied*, Vol. 11, no. 3, 034020, 2019.

Conference Proceedings

6. **Mohammad Reza Raveshi**, Melati Abdul Halim, Adrian Neild, Reza Nosrati, “The Role of Interface Curvature on Sperm Behaviour”, *23rd International Conference on Miniaturized Systems for Chemistry and Life Sciences*, October 27-31, 2019, Basel, Switzerland, pp. 1538-1539.
7. **Mohammad Reza Raveshi**, Sagar N Agnihotri, Muhsincan Sesen, Rajneesh Bhardwaj, Adrian Neild, “Selective Partitioning of Microdroplets Using Horizontal Microvalves”, *23rd International Conference on Miniaturized Systems for Chemistry and Life Sciences*, October 27-31, 2019, Basel, Switzerland, pp. 957-958.
8. Melati Abdul Halim, **Mohammad Reza Raveshi**, Adrian Neild, Reza Nosrati, “Droplet-based sperm motility analysis”, *10th Australia and New Zealand Nano and Microfluidics Meeting*, July 1-3, 2019, Wollongong, Australia.

9. Melati Abdul Halim, **Mohammad Reza Raveshi**, Adrian Neild, Reza Nosrati, “Sperm motility at curved interfaces”, *1st MedTech: Into the Future Symposium*, October 2, 2019, Monash University, Melbourne, Australia.
10. Sagar N Agnihotri, **Mohammad Reza Raveshi**, Rajneesh Bhardwaj, Adrian Neild, “Droplet Breakup in a Bypass Channel of a Microfluidic System”, *7th International and 45th National Conference on Fluid Mechanics and Fluid Power*, December 10-12, 2018, IIT Bombay, Mumbai, India.
11. Sagar N Agnihotri, Rajneesh Bhardwaj, Adrian Neild, **Mohammad Reza Raveshi**, “Interaction of a Droplet with T-junction of a Microfluidic Bypass Channel”, *71st Annual Meeting of the APS Division of Fluid Dynamics, Bulletin of the American Physical Society*, November 18-20, 2018, Atlanta, Georgia, USA, Paper No.: F07.00002.
12. Sagar N Agnihotri, **Mohammad Reza Raveshi**, Rajneesh Bhardwaj, Adrian Neild, “Towards High Throughput Screening for Drug Discovery in Multi Splitting and Merging System Using Microvalves”, *24th International Conference on Miniaturized Systems for Chemistry and Life Sciences*, October 4-9, online.

Thesis Declaration

I hereby declare that this thesis contains no material which has been accepted for the award of any other degree or diploma at any university or equivalent institution and that, to the best of my knowledge and belief, this thesis contains no material previously published or written by another person, except where due reference is made in the text of the thesis.

Signature:

Print Name: Mohammad Reza Raveshi

Date: 22 September 2020

I hereby certify that the above declaration correctly reflects the nature and extent of the student's and co-authors' contributions to this work.

Main Supervisor Signature:

Print Name: Prof. Adrian Neild

Date: 22 September 2020

Acknowledgments

I would like to express my deepest appreciation and sincerest gratitude to my main supervisor Professor Adrian Neild, for his invaluable guidance, patience, motivation and immense knowledge. I had the good fortune to work with him. He always encouraged me to do my best and helped to minimise the difficulties. He is an exceptional role model for both my academic and personal life, many thanks again Adrian. Special thank you to my co-supervisor Dr. Reza Nosrati for his encouragement, creativity, project management and insightful guidance. My PhD research always benefited from his constructive and invaluable scientific guidance. I consider myself very lucky to have him as my supervisor, thanks for everything Reza. I would like to thank Dr. Rajneesh Bhardwaj at the Indian Institute of Technology Bombay for his time and effort to evaluate my work and for providing me with thoughtful and valuable feedback.

I would like to also thank my dear friend, Dr. Muhsincan Sesen, who is an expert in droplet microfluidics. He helped me a lot during the first year of my PhD to learn about microdroplets. A huge thank you to my colleague and close friend in the Laboratory of Microsystems (LMS), Mr. Sagar Narhari Agnihotri for his help, patience, support and friendship along the way and for his significant contributions on the projects we worked closely. A big thank you to my colleague and close friend Ms. Melati Abdul Halim in the Applied Microfluidics and Bioengineering Laboratory (AMB Lab) for always finding the time to help me. Her knowledge and expertise in handling biological samples helped me a lot during the last year of my PhD. Also, thank you to my friend Ms. Junyang Gai in the LMS for sharing her expertise in surface acoustic waves. I extend my thanks to all past and present members of LMS and AMB Labs. It was an amazing experience and honour to work with a group of friendly, motivated, and knowledgeable scholars.

Last but not the least, I would like to thank my family for their love and support. My deepest gratitude and appreciation go to my wonderful and lovely parents for their unconditional and endless support, encouragement, and love. Their continuous support has made it possible for me to get where I am today, thank you. A special thank you to my amazing brother for his supportive words and encouragements in all years of my life. I am extremely lucky to have him in my life.

Contents

Abstract	iv
List of Publications	vi
Thesis Declaration	viii
Acknowledgments	ix
List of Tables	xiii
List of Figures	xiv
Chapter 1 - Introduction	1
1.1. Motivation.....	2
1.2. Thesis Overview	3
Chapter 2 - Literature Review and Research Aims	6
2.1. Preface for Chapter 2	7
2.2. Droplet Microfluidics.....	7
2.3. Generation of Microdroplets	8
2.3.1. Passive Droplets Generation	10
2.3.2. Active Droplets Generation	12
2.4. Fission of Microdroplets	13
2.4.1. Passive Droplets Fission	14
2.4.2. Active and Combined Droplets Fission	18
2.5. Fusion of Microdroplets.....	21
2.5.1. Passive Droplets Fusion	22
2.5.2. Active Droplets Fusion	23
2.6. Microvalves.....	23
2.6.1. Multi-Layer Pneumatic Valves	25
2.6.2. Single-Layer Pneumatic Valves.....	26
2.7. Droplet Microfluidics for On-chip Reactions and High Throughput Screening.....	29
2.8. Droplet Microfluidics for Single Cell Biology Study	31
2.9. Conclusion and Research Aims	33
Chapter 3 - Selective Droplet Splitting Using Single Layer Microfluidic Valves	35
3.1. Preface for Chapter 3	36
3.2. Introduction.....	37
3.3. Working Principle.....	40
3.3. Results and discussion	44
3.4. Conclusions.....	51
3.5. Methodology	51
3.5.1. Microfabrication	51
3.5.2. Experimental Set-up.....	52
3.5.3. Image Processing	52
3.5.4. Numerical Methods.....	52

3.6. Supplementary Information	53
3.6.1. Supplementary Figures	53
3.6.2. Valve Characterization.....	56
Chapter 4 - Controlled Droplet Manipulation and Interaction using Single Layer Microvalves	58
4.1. Preface for Chapter 4	59
4.2. Introduction.....	60
4.3. Methods and Materials.....	62
4.4. Results and Discussion	63
4.4.1. Droplet Generation.....	64
4.4.2. Droplet Splitting.....	66
4.4.3. Selective Droplet Splitting Using Valves at Four Junctions	69
4.4.4. Droplet Merging.....	70
4.5. Conclusions.....	73
4.6. Supplementary Information	73
4.6.1. Channel Flow Rate Examination	73
4.6.2. Characterisation of Single-Layer Microvalves	75
Chapter 5 - Curvature in the Reproductive Tract Alters Sperm-surface Interactions	77
5.1. Preface for Chapter 5	78
5.2. Introduction.....	79
5.3. Results.....	82
5.3.1. Sperm Motility Modes at Physiologically Relevant Curvatures.....	82
5.3.2. Kinematics of Sperm Motility at Curvatures	85
5.4. Discussion.....	86
5.5. Methods.....	91
5.5.1. Sperm Sample Preparation.....	91
5.5.2. Device Fabrication	92
5.5.3. Experimental Procedure.....	92
5.5.4. Microscopy	92
5.5.5. Image Analysis.....	93
5.6. Supplementary Information	93
5.6.1. Supplementary Figures	93
5.6.2. Supplementary Table	95
5.6.3. Theoretical Model for the Angle of Attack.....	95
Chapter 6 - Conclusions and Future Work	97
6.1. Thesis Contributions	98
6.1.1. Droplet Manipulation Techniques for High Throughput Reactions	98
6.1.2. Understanding Sperm Behaviour at Soft Curved Interfaces using Microdroplets.....	99
6.2. Future Work	100
Bibliography	105

Appendix I - Droplet breakup at the Entrance to a Bypass Channel in a Microfluidic System	132
AI.1. Preface for Appendix I.....	133
AI.2. Introduction.....	133
AI.3. Methodology.....	136
AI.3.1. Experimental Methods.....	136
AI.3.2. Simulation Setup and Grid Size Independence Study	139
AI.4. Results.....	141
AI.4.1. Effect of Channel Width Ratio (β).....	141
AI.4.2. Effect of the Capillary Number (Ca)	143
AI.4.3. Comparison between Experimental and Computational Results	144
AI.4.4. Regime Map.....	145
AI.4.5. Transition Region	147
AI.5. Discussion.....	147
AI.5.1. Equivalence to Squeezing and Dripping Regimes.....	147
AI.5.2. Mechanism of Droplet Breakup.....	153
AI.6. Application of Present Work in Droplet-based Microfluidics.....	156
AI.7. Conclusion	156
AI.8. Supplementary Information	157
AI.8.1. Droplet Generation	157
AI.8.2. Mother Droplet Length	158
AI.8.3. Average Shear Stress Calculation.....	159
AI.9. References.....	160
Appendix II - Microfluidic Valves for Selective On-chip Droplet Splitting at Multiple Sites ...	163
AII.1. Preface for Appendix II.....	164
AII.2. Introduction	164
AII.3. Method and Material	167
AII.3.1. Experimental Methods.....	167
AII.3.2. Simulation Setup and Grid Independence Study	167
AII.4. Results and Discussion.....	169
AII.4.1. Two Identical T-junctions	169
AII.4.2. Channel Flow Rate Examination.....	171
AII.4.3. Expansion Channel for 2 nd Junction	173
AII.4.4. Selective Droplet Breakup at Two Locations (Two Valve System Using Simulations)177	
AII.4.5. Selective Droplet Breakup at Two Locations (Two Valve System Using Experiments)180	
AII.5. Conclusion	182
AII.6. Microfabrication	182
AII.7. References	183

List of Tables

Table 2.1. Different regimes of splitting in a two-arm T-junction. Schematics are reprinted from ref.157, with the permission of AIP Publishing.....	15
Table 2.2. Different regimes of splitting in a one-arm T-junction. Schematics are reprinted figures with permission from ref. 93. Copyright (2006) by the American Physical Society...	16
Table 3.1. Different geometrical parameters were tested to characterize the valve.....	56
Table 5.1. Statistical analysis of sperm motility parameters. <i>P</i> values were calculated using one-way ANOVA based on at least 10 points for each range of radius of droplets, * $P \leq 0.05$, ** $P \leq 0.01$, *** $P \leq 0.001$ and NS denotes not significant.....	95
Table AI.1. Grid independence study. Error in ΔP and L_f with respect to the finest grid ($2 \mu m$) used.....	141
Table AII.1. Grid size independence study showing error in finger length (L_f) with respect to the finest grid.....	169

List of Figures

Figure 2.1. Different regimes of breakup, (a) squeezing, (b) dripping, (c) jetting, and (d) tip-multi-breaking regime in a flow focusing droplet generation method. (a) – (d) are reproduced from ref. 31 with permission from The Royal Society of Chemistry.....10

Figure 2.2. Different geometrical parameters which affect droplet splitting (a) - (e) Non-splitting regime (f) - (j) Splitting regime. (k) Dependency of splitting regime on capillary number and extension length. (l) Dependency of daughter droplet sizes on arms' length. (m) Dependency of daughter droplet sizes on arms' width. (a) – (l) are reprinted figures with permission from ref. 152. Copyright (2004) by the American Physical Society. (m) is reprinted figure with permission from ref. 154. Copyright (2013) by the American Physical Society...15

Figure 2.3. Different splitting regimes in (I) two-arm and (II) one-arm T-junctions (a) no-splitting (b) tunnel or retarded splitting (c) obstructed or direct splitting. (I) is reprinted from ref.157, with the permission of AIP Publishing. (II) is reprinted figure with permission from ref. 93. Copyright (2006) by the American Physical Society.....16

Figure 2.4. Four different techniques for symmetrically splitting of droplets. (a) Playing with the angle of the bifurcating junction¹⁵⁸, (b) using an obstacle in the center of the channel, (c) adding post to the junction and (d) connecting one of the outlets to the open tubing. (a) is reproduced with permission from Hsieh, et al. in ref.158. (b) is reprinted figure with permission from ref. 152. Copyright (2004) by the American Physical Society. (c) is reproduced from ref. 160 with permission from The Royal Society of Chemistry. (d) is reproduced from ref. 159 with permission from The Royal Society of Chemistry.....17

Figure 2.5. Combining passive and active methods for (a) symmetric droplet splitting without any external forces (b) controllable asymmetric droplet splitting by using electric fields, laser or integrated micro heater (c) droplet sorting by increasing any of mentioned forces (Electrical strength, duration of laser actuation or temperature). (a) – (c) are reprinted figures with permission from ref. 162. Copyright (2007) by the American Physical Society.....19

Figure 2.6. Newly introduced active splitting methods, (a) dielectrowetting targets a sessile droplet, (b) SAW halves a sessile droplet, (c) SAW splits moving droplet in a channel, (d) SAW

affects plug which approaches Y-junction, and (e) SAW works as a pipette for a plug passing through the bypass channel¹⁷⁰. (a) is reprinted figure with permission from ref. 166. © 2017 IEEE. (b) is reproduced from ref. 167 with permission from The Royal Society of Chemistry. (c) is reproduced from ref. 168 with permission from The Royal Society of Chemistry. (d) is reproduced from ref. 42 with permission from The Royal Society of Chemistry. (e) is reproduced from ref. 170 with permission from The Royal Society of Chemistry.....20

Figure 2.7. Passive fusion of microdroplets (a) without surfactant, (b) with surfactant, (c) with fusion junction, (d) with fusion chamber, (e) with pillars, (f) with storage chamber, and (g) with storage well¹⁸¹. (a) and (b) are reprinted from ref. 173 with permission from Elsevier. Copyright © 2015 Elsevier. (c) is reprinted with permission from ref. 174. Copyright 2007, Springer. (d) is reprinted figure with permission from ref. 176. Copyright (2008) by the American Physical Society. (e) is reproduced from ref. 37 with permission from The Royal Society of Chemistry. (f) is reprinted with permission from ref. 180. Copyright 2016, Springer. (g) is reproduced from ref. 181 with permission from The Royal Society of Chemistry.....23

Figure 2.8. Schematic of different actuation systems in active mechanical microvalves: (a) magnetic (b) electric (c) piezoelectric (d) bimetallic (e) thermopneumatic and (f) shape memory alloy microvalves. (a) – (f) are reproduced from ref. 186 with permission from © IOP Publishing Ltd. All rights reserved.....24

Figure 2.9. (a) Top and (b) – (d) Side views of different types of multi-layer valves and (e) different regimes of droplet break up by using multi-layer valves. (a) – (d) are reproduced from ref. 199 with permission from The Royal Society of Chemistry. (e) is reproduced from ref. 194 with permission from The Royal Society of Chemistry.....26

Figure 2.10. Using single-layer valves for different manipulation techniques (a) – (d) sorting, (e) merging, and (f) splitting of microdroplets. (a) – (d) are reproduced from ref. 42 with permission from The Royal Society of Chemistry.....27

Figure 3.1. Depiction of the selective droplet partitioning system. (a) Mother droplets are produced in a T-junction and passes the entrance of the bypass loop when the valve is off. Non-splitting regime dominates under these conditions. (b) The valve is actuated which results in deforming the channel wall and guiding more fluid into the secondary channel. The finger

length increases as a result of changing in flow resistance and curvature of the front of the droplet. (c) Under these conditions the mother droplet passes along the main channel after splitting has occurred.....41

Figure 3.2. Classification of splitting regimes by the frequency and size of mother droplets (a) Regime map shows four splitting regimes in the absence of valve on Oil Pressure-Water Pressure plane; (1) Non-splitting Regime with black square markers (2) Transition Regime with red circle markers (3) LESR (Low efficiency splitting regime) with blue triangle markers (4) HESR (High efficiency splitting regime) with green diamond markers (b) Images show the droplet behaviour in the entrance of bypass loop in the absence (i) - (iv) and presence of 800 mbar activated valve (v) - (viii). (c) Regime map shows four splitting regimes in the presence of activated valve on the pressure of 800 mbar on Oil Pressure-Water Pressure plane. (d) Transient lines follow the transition regions showing the transition from non-splitting to splitting regimes in four different valve pressures; 0 mbar, 800 mbar, 1000 mbar and 1100 mbar.....45

Figure 3.3. (a) Comparison between the pressure which is required to split droplets randomly and the pressure which is needed to split the first coming droplets for different inlet conditions (b) Experimental images for the indicated data points (i) - (v).....48

Figure 3.4. Plot shows the finger length as the function of frame numbers for small droplets (Oil Pressure = 800 mbar and Water Pressure = 500 mbar) and large droplets (Oil Pressure = 400 mbar and Water Pressure = 500 mbar) in the absence and presence of the valve that is actuated to 1000 mbar. (b) While in the absence of valve, finger reaches the maximum size of 74 μm (i) as valve is actuated finger reaches the maximum size of 174 μm (ii) for small droplets. On the other hand, for large droplets maximum finger lengths are 124 μm (iv) and 192 μm (v) in the absence and presence of actuated valve with the pressure of 1000 mbar.....49

Figure 3.5. Plot shows the relative volume of daughter droplet to the mother droplet for small droplets (Oil Pressure = 800 mbar and Water Pressure = 500 mbar) and large droplets (Oil Pressure = 400 mbar and Water Pressure = 500 mbar). (b) Contours are extracted images from numerical simulation for the Deformation = 36 μm related to the Valve Pressure = 600 mbar, (1) before and (2) after of droplet passing the entrance of bypass loop. (c) Two images from numerical simulation are shown, (1) before and (2) after splitting of the mother droplet, this

occurs for a deformation of 40 μm equivalent to an experimental valve pressure of 650 mbar, results show that 7% and 8% of mother droplet split numerically and experimentally. (d) Experimental images for the indicated data points (i) - (vi).....50

Figure 3.6. Schematic showing the setup used for selective droplet splitting using single layer microfluidic valves. The inlets and outlet of the microfluidic system is connected to a microfluidic flow control system (MFCSTM-EZ, Fluigent system); while the inlet of the valve control system is connected to a second Fluigent system to control the air pressure. This setup includes high speed camera, inverted microscope and two fluigent systems. These are connected to a computer for data collection.....53

Figure 3.7. The effect of the constriction position on the finger size. The operating conditions of the system are Oil Pressure = 400 mbar, Water Pressure = 500 mbar and Deformation = 36 μm . (a) Plot shows the finger interface vertical location over time comparing the effect of the constriction at the entrance and the constriction at the exit of the bypass channel on the finger size. (b) Contours are extracted images from numerical simulation, when Constriction = 36 μm is imposed at the entrance of the bypass channel at different time instances. (c) Four images from numerical simulation are shown for a constriction of 36 μm equivalent to an experimental valve pressure of 600 mbar that is imposed at the exit of the bypass channel.....54

Figure 3.8. The effect of valve pressure on the valve efficiency which is defined as the ratio of the number of split droplets in the bypass channel to the total number of droplets that pass the inlet of bypass loop (a) Four different pairs of oil and water pressures are studied here which is shown in the inset (b) Experimental images (i) - (v) show valve has different efficiencies at different valve pressures for the fixed inlet condition of Oil Pressure = 400 mbar and Water Pressure = 500 mbar.....54

Figure 3.9. Timelapse images of droplet passing the entrance of bypass loop with the constant inlet conditions of Oil Pressure = 400 mbar and Water Pressure = 500 mbar (a) In the absence of actuated valve (b) After the valve is actuated to the pressure of 600 mbar. (c) During the valve actuation when 650 mbar is imposed in the valve inlet.....55

Figure 3.10. Timelapse images of the droplet passing through the entrance of the bypass loop in the operating condition of Oil Pressure = 400 mbar, Water Pressure = 500 mbar and valve

pressure = 650 mbar which shows that the system is selective and on demand with the minimum possible actuation in the valve part.....55

Figure 3.11. Deformation of two valves with different membrane thicknesses under the $P = 100$ kPa (a) membrane thicknesses = $30 \mu\text{m}$ (b) membrane thicknesses = $50 \mu\text{m}$ ($Q_{\text{oil}} = 60 \mu\text{l/hr}$, $Q_{\text{water}} = 25 \mu\text{l/hr}$).....57

Figure 3.12. Visualization of valve actuation at different pressures for membrane with $30 \mu\text{m}$ thickness ($Q_{\text{oil}} = 60 \mu\text{l/hr}$, $Q_{\text{water}} = 25 \mu\text{l/hr}$).....57

Figure 4.1. Schematic of the microfluidic device to achieve selective droplet splitting and merging at multiple locations using eight single-layer microvalves. The microfluidic device generates four different coloured droplets mimicking four different chemicals in the upstream part of the chip, this is achieved using four valves located close to each of the channels carrying discontinuous phases. A zoomed-in view shows that downstream of the generation structures, there is a multiple site splitting and merging section of the chip. Here, the droplet can be split at any of four different locations each controlled by a separate microvalve, after splitting the daughter droplets are merged using a passive pillar-based approach.....62

Figure 4.2. Droplet generation part of the multi-splitting and merging system using two different approaches. (a) Schematic of the droplet generation part showing four valves controlling the flow of four discontinuous phases. (b) Blue and green droplets are generated, alternately. (c) Green and red droplets are generated, one after the other. (d) Four different coloured droplets are produced, sequentially. (e) - (h) Valve based droplet generation approach is used to create a red, blue, white and green droplet, respectively. Scale bars are $100 \mu\text{m}$65

Figure 4.3. Different Regimes of droplet splitting when droplets interact with four junctions placed one after the other. (a) Droplets split in all the four junctions. (b) Droplets split in the last three junctions. (c) Droplets split in the last two junctions. (d) There is no droplet splitting in all the four junctions: scale bars, $100 \mu\text{m}$67

Figure 4.4. Classification of different splitting regimes by the separation distance and the percentage of the flow rate entering each junction. (a) Schematic shows the separation distance

d1, d2, d3, d4. Regimes map is extracted based on (b) the average separation distance in each branch of the main channel, and (c) the percentage of the flow rate entering each branch divided by the total flow rate in the main channel, respectively. The dotted lines separate splitting and no splitting regimes.....68

Figure 4.5. Splitting of different coloured droplets at different locations using single-layer microfluidic valves. (a) Percentage of the relative daughter droplet volume against the deformation of the microchannel channel for all the four junctions. (b) The blue coloured droplet is split at the first junction when the valve is pressurised at 1800 mbar (deformation of 53 μm). (c) Splitting of the red coloured droplet at the second junction using valve pressurised at 1800 mbar. (d) Droplet splitting of the green coloured droplet at third junction using valve pressurised at 1800 mbar. (e) The white coloured droplet is split at the fourth junction when the valve is pressurised at 1800 mbar.....70

Figure 4.6. Splitting of different coloured droplets occurs whilst the valve is actuated. The two daughter droplets are merged within the chamber, the first being retarded by the pillar structures, after merging the total volume is such that the droplet is dragged out of the merging chamber. Merging of two different coloured droplets an equal volumetric ratio is shown at the (a) third and (b) first junctions. In the former, a single red daughter droplet is merged with a single clear one. For the latter two blue daughter droplets are merged with two clear droplets, Finally, (c) merging of an unequal number of droplets generated from two different samples is achieved, such that the mixing ratio is 1:2 (red: clear).....71

Figure 4.7. An image sequence demonstrating the merging of two different selected droplets (one clear and one red droplet) at the third junction. The clear droplet is split by transient actuation of the valve, resulting in the deposition of a daughter droplet in the merging chamber. Subsequent clear droplet passes without splitting due to timely deactivation of the valve. Finally, a single red droplet is selected and split, again a daughter droplet is formed and merges with the clear daughter droplet.....72

Figure 4.8. Flow rate distribution of multi-splitting and merging system. (a) The resistance network of a system considering the flow rate and hydrodynamic resistance of each branch without consideration of the presence of droplets in the system. (b) Schematic of the simplified microfluidic system in which same flow rate enters in four T-junctions with different width.

(c) Schematic of the actual microfluidic system in the presence of four merging chambers designed in such a way that same flow rate enters in four T-junctions with a similar width.....75

Figure 4.9. Characterisation of the single-layer microvalve. (a) Maximum deformation of the channel is plotted against different pressures that are applied to the single-layer valve. (b) Deformation of the channel is plotted against the time when the single-layer valve is fully pressurised to the pressure of 1800 mbar and fully depressurised, respectively. (c) Image sequence showing selectivity of the droplet splitting, red droplet arrives at the second junction and do not split at this junction, just before the second droplet arrives at this junction valve is actuated to split the droplet. Before the third droplet arrives at this junction valve is deactivated, and droplet does not split. Scale bar 100 μm76

Figure 5.1. Sperm motility at curved interfaces representing the soft and folded epithelial tissue in the female fallopian tube. (a) The female fallopian tube is a complex microenvironment composed of soft and highly folded epithelial tissue, forming confined lumens with radius of curvatures ranging from $\sim 20 \mu\text{m}$ to over $150 \mu\text{m}$. (b) Encapsulation of individual sperm in monodisperse droplets ranging in size from 30 to $140 \mu\text{m}$, mimicking the physiologically relevant range of curvatures in vivo. Time-lapse images and representative trajectories of sperm swimming in (c,d) aggressive attacking, (e,f) transition and (g,h) progressive surfaces aligned motility modes in 40 , 73 , and $110 \mu\text{m}$ -radius droplets, respectively. The colour of the instantaneous swimming trajectories corresponds to time, as shown in the legend in d. Orange dashed lines highlight the deviation between instantaneous trajectory and average path due to departing behavior. Scale bars, $50 \mu\text{m}$. Images were contrast-adjusted for clarity.....81

Figure 5.2. Characterization of sperm motility modes at curved interfaces. (a) Angle of attack, α , and the percentage of the 12 s tracked swimming trajectory in which the sperm is (b) attacking ($2^\circ < \alpha < 90^\circ$), (c) swimming parallel to ($-2^\circ < \alpha < 2^\circ$), and (d) departing ($\alpha < -2^\circ$) the interface in droplets ranging from 30 to $140 \mu\text{m}$ in radius. Values are reported as mean s.d. ($n \geq 10$), and P values were determined using one-way ANOVA, $*P \leq 0.05$, $**P \leq 0.01$, $***P \leq 0.001$83

Figure 5.3. Characterization of the temporal behavior of sperm in the attacking, transition, and progressive modes. (a) Representative variations of the angle of attack along the 12 s tracked swimming trajectories for sperm swimming in the attacking, transition, and progressive modes.

The horizontal red line indicates the threshold angle of attack of 2° for the sperm to align parallel to or depart from the interface. (b) Crossover frequency as a function of droplet radius. Values are reported as mean s.d. ($n \geq 10$), and P values were determined using one-way ANOVA, * $P \leq 0.05$, ** $P \leq 0.01$84

Figure 5.4. Sperm motility parameters at curved interfaces. (a) Curvilinear velocity (VCL), (b) average path velocity (VAP), (c) amplitude of lateral head displacement (ALH), and (d) beat cross frequency (BCF) for sperm swimming in droplets ranging in radius from $30 \mu\text{m}$ to $140 \mu\text{m}$. Values are reported as mean s.d. ($n \geq 10$), and P values were determined using one-way ANOVA, * $P \leq 0.05$, ** $P \leq 0.01$, *** $P \leq 0.001$ (see Table 5.1). (e) Schematic representation of the measured sperm motility parameters.....86

Figure 5.5. Theoretical model for estimating the angle of attack. (a) Angle of attack from experimental measurements as compared with theoretical values with fixed (dashed line) and varying (solid line) flagellar wave amplitude as a function of droplet radius. Schematic representation of the reference system and modeled sperm shown by the inset. (b) Experimentally measured flagellar wave amplitudes as a function of droplet radius. Values are reported as mean s.d. ($n=10$ per radius).....88

Figure 5.6. Sperm motility behavior at curved interfaces in microchannels that represent the increasing complexity of the female fallopian tube geometry. Overlaid trajectories of two representative sperm (head shown in red and blue) in microchannels that mimics the relevant range of curvatures in infundibulum, ampulla, and isthmus, with sperm exhibiting (a) head-on swimming behavior in the attacking mode, (b) a combination of head-on swimming and boundary following behavior in the transition mode, and (c) boundary-following behaviors in the progressive mode, respectively. Images were contrast-adjusted for clarity. Scale bars, $100 \mu\text{m}$90

Figure 5.7. Difference between average path and droplet radius for three different modes of sperm swimming in droplets with different size. The distance between the boundary of the surface and the circular average path of the sperm during the different swimming modes increases while the droplet size increases.....93

Figure 5.8. Temporal variations in the angle of attack for sperm in the attacking, transition, and progressive modes. Representative variations of the angle of attack along the 12 s tracked swimming trajectories for sperm swimming in droplets with radius ranging from (a) 30 μm to 40 μm , (b) 50 μm to 60 μm , (c) 70 μm to 80 μm , (d) 90 μm to 100 μm , (e) 110 μm to 120 μm , and (f) 130 μm to 140 μm . Sperm are swimming in the attacking mode in a, in the transition mode in b-d and in the progressive mode in e and f.....94

Figure 5.9. Schematic shows the setup used for droplet microfluidic based sperm motility analysing. The inlets and outlet of the droplet microfluidic system is connected to a microfluidic flow control system (MFCSTM-EZ, Fluigent system). Setup includes ORCA-Flash4.0 V3 Digital CMOS camera (Hamamatsu Photonics, Japan), inverted fluorescence microscope (Olympus IX83, Japan) and Fluigent systems, connected to a computer for data collection.....94

Figure 5.10. Theoretical model for calculating the angle of attack at curvatures. (a) Sperm with the conical envelope of the flagellar wave aligned with the curvature and (b) the schematic used to drive the theoretical model for the angle of attack.....95

Figure 6.1. Newly introduced intra droplet manipulation techniques using passive and active methods, (a) hydrodynamic, (b) electrical, (c) magnetic, and (d) acoustic have been used to concentrate and enrich particles inside droplets. (e) SAW has been used as a washing technique to exchange the droplet medium. (a) – (d) are reprinted with permission from ref. 366 Copyright (2018) American Chemical Society. (e) is reproduced from ref. 379 with permission from The Royal Society of Chemistry.....101

Figure 6.2. Depiction of the system integrating a single layer valve and a SAW actuation module for (a) intra-droplet particle encapsulation, (b) intra-droplet particle concentration, and (c) intra-droplet particle washing. Preliminary results show the capability of the system to encapsulate the droplet with SAW on and valve off. (d) Particles are moving freely inside the droplet before reaching the SAW exposed area. (e) SAW pushes the particles to the back (upstream side) and top side of the droplet. As a result, (f) the particles are captured in the daughter droplet and pushed out of the main stream into a secondary channel.....102

Figure AI.1. Schematic of the experimental setup used in the present work. Due to wetting properties of microfluidic chip de-ionized water is a discontinuous phase and oil is continuous phase.....137

Figure AI.2. (a) Problem definition shown by a schematic. The computational domain is shown by a dotted box and boundary conditions are shown at the inlet, outlet and wall (b) Zoomed in view of the entrance to the bypass channel and droplet shape before interaction with it. (c) Mesh is plotted in the region close to the entrance to the bypass channel.....138

Figure AI.3. Grid size independence study: Finger length (L_f) on the left-hand side of the Y-axis for different grid sizes (2 μm , 3 μm and 5 μm) on the X-axis at constant $\beta = 0.62$. Pressure drop (ΔP) in a microchannel on the right-hand side of the Y-axis for different grid sizes (2 μm , 3 μm , and 5 μm) on the X-axis when droplet interacts with the entrance of the bypass channel at constant $\beta = 0.62$140

Figure AI.4. High-speed visualization of the droplet interaction with the entrance of the bypass channel showing the transition from no droplet breakup to droplet break up at different time intervals. Results are plotted for three cases of β . (a) $\beta = 0.48$ [39] (b) $\beta = 0.77$ [39] (c) $\beta = 0.91$ [39]. Capillary number is kept almost constant in all cases ($Ca = 0.0028 \pm 0.0002$).....142

Figure AI.5. High-speed visualization of the droplet interaction with the entrance of a bypass channel showing the transition from no droplet breakup to droplet break up at different time intervals showing the effect of Ca (a) $Ca = 0.0022$ [39] (b) $Ca = 0.005$ [39] (c) $Ca = 0.037$ [39]. The ratio of channel width β is kept constant in all cases ($\beta = 0.48$).....143

Figure AI.6. Comparison between experimental and computational work at $\beta = 0.48$ and $Ca = 0.005$. (a) High-speed visualization of the droplet interaction with the entrance of a bypass channel. (b) Computed contours of the volume fraction of water [39]. (c) Isometric view of the iso-surface of the volume fraction of water at 0.5.....144

Figure AI.7. Comparison between experimental and computational work at $\beta = 0.63$ and $Ca = 0.007$. (a) High-speed visualization of the droplet interaction with the entrance of a bypass channel. (b) Computed contours of the volume fraction of water [39]. (c) Isometric view of the iso-surface of the volume fraction of water at 0.5.....145

Figure AI.8. (a) Regime map is showing contours of finger length (L_f) on Ca - β plane. A dotted line is shown to demarcate regions of droplet breakup and no droplet breakup. (b) Regime map showing contours of V_{ratio} on Ca - β plane.....146

Figure AI.9. (a) Dimensionless daughter droplet volume as a function of the capillary number showing equivalent squeezing and dripping regime. The dotted line shows the squeezing regime given by Menech et al. and a dash-dot line showing current work. (b) Contours of shear stress at different Ca in the equivalent dripping regime.....148

Figure AI.10. Evolution of finger length and ε with time. Finger Length (L_f) plotted on the left-hand of Y-axis and ε on the right-hand side of Y-axis Vs. stages of droplet interaction (evolution with time).....150

Figure AI.11. Schematic of the droplet interacting with the T-junction. Zoomed in view shows pressure notations inside and outside the droplet.....152

Figure AI.12. Evolution of average shear stress with time for Ca ranging from equivalent squeezing to the dripping regime. Contours at the top of the figure show average shear stress and corresponding stage of droplet interaction for given computed value.....152

Figure AI.13. Evolution of pressure built up with time for Ca ranging from equivalent squeezing to the dripping regime. Contours at the top show pressure built up and corresponding stage of droplet interaction for given computed value.....153

Figure AI.14. Evolution of $(F_R + F_\tau)$ and F_γ during various stages of the droplet interaction with the bypass channel. a) Forces acting on the trapped droplet (b) The case of droplet breakup (c) Case of no droplet breakup.....155

Figure AI.15. Comparison between dimensionless droplet length observed in experiments and model presented by Garstecki *et al.* [1]. The solid line is the curve showing predicted droplet size.....158

Figure AI.16. Mother droplet length Vs Number of experiments.....159

Figure AI.17. Contours of shear stress when droplet interacts with bypass channel. Black circle shows finger and bypass channel. Black dots in the gap are representative of locations where we computed shear stress.....159

Figure AII.1. Conceptual depiction of selective droplet breakup using microvalves at two locations. (a) The “mother” droplets are generated at upstream T-junction (not shown) and, as they pass down the main channel, interacts with the first and second junctions positioned adjacent to valves 1 and 2. When the valves are off, operating conditions are chosen such that no droplet breakup occurs at these junctions. (b) When the first valve is pressurized and deforms, the selected droplet breaks up and a small droplet enters the side branch, here it is depicted that a sample of the green and red fluids are selected, subsequently these can be passively merged in the branch (c) Similarly, the second valve also allows selective break up such that different reactions can be initiated in its merging station. The result is a system in which a range of reaction permutations can occur between different reagents.....166

Figure AII.2. Grid size independence study showing finger length (L_f) vs minimum grid size (ΔS) for droplet interaction with the first and second junction.....168

Figure AII.3. A schematic of microfluidic system design with upstream droplet generation section followed by two stage droplet division section. Mother droplets are produced upstream and are made to interact with identical droplet division junctions.....170

Figure AII.4. High-speed visualization, at a capillary number (Ca) of 0.01, of a mother droplet interacting with the (a) first and (b) second junctions. In which a finger is seen to develop in the

branch and either break into a droplet or retract. The discrepancy, between the two junctions, of the maximum length of the finger length (c) and the (d) percentage of the volume of the mother droplet which breaks into a daughter droplet is seen across the Ca range tested.....170

Figure AII.5. The Resistance network of the microfluidic system with the associated flow rate distribution of the continuous phase, without considering the resistance of the droplets.....172

Figure AII.6. A schematic of a microfluidic system with upstream droplet generation section followed by droplet division section, designed such that the behavior at each splitting junction is balanced. To achieve this the second junction consists of a section of channel with the original width, followed by an expansion which drops the overall resistance of the branch...173

Figure AII.7. High-speed visualization of droplet interaction with straight channel branching from the first junction and the expansion channel stemming from the second junction. Five regimes are observed: (a) No droplet breakup in both junctions, (b) Breakup in the first junction, (c) Breakup in first junction onset of breakup in the second junction, (d) Breakup in both the junctions. (e) Intermittent breakup in both the junctions.....174

Figure AII.8. The finger length for four regimes of droplet interaction is plotted against Ca . The finger length from regime e (intermittent breakup regime) is not plotted as it is not consistent across each droplet. The dots below the regime letters indicates whether break up at the first (red) and second (green) junction occurs.....175

Figure AII.9. The evolution of finger length measured in the first and second junction for both the designs (symmetric and expansion channel) as a function of time under the same flow conditions ($Ca = 0.0055$). Case of symmetric design second junction yields no breakup while all other cases represent breakup.....176

Figure AII.10. High-speed visualization of droplet interacting with the first T-junction and expansion channel, which yields the same volume of daughter droplets at both the junctions. This lies between regime 3 and 4.....176

Figure AII.11. Comparison between experimental and 3D numerical simulations at $Ca = 0.011$. (a) Contours of the volume fraction of the continuous and discontinuous phase. (b) High-speed visualization of the droplet interaction with the first and second junction.....177

Figure AII.12. Percentage efficiency of droplet breakup in the first junction against deformation at the entrance of the first junction calculated using numerical simulations. Bottom inset shows a top view of the 3D numerical simulation without deformation at the entrance of first junction resulting in no breakup. The top inset shows a top view of the 3D numerical simulation with deformation of $50\mu\text{m}$ at the entrance of first junction resulting in a breakup.179

Figure AII.13. Percentage efficiency of droplet breakup in the second junction and expansion channel against deformation near the entrance of the second junction calculated using numerical simulations. Bottom inset shows a top view of the 3D numerical simulation with deformation of $60\mu\text{m}$ for symmetric second junction resulting in no breakup. The top inset shows a top view of the 3D numerical simulation with deformation of $60\mu\text{m}$ for expansion channel resulting in a breakup.....179

Figure AII.14. High-speed visualization showing the interaction of droplets with two junctions in the presence and absence of valve actuation. (a) Actuation of valve for the first junction (b) Actuation of the valve for the second junction with the valve away from the entrance of second junction (c) Actuation of the valve for the second junction with the valve at the entrance of second junction (d) Actuating both the valves simultaneously.....181

Figure AII.15. Percentage efficiency of droplet breakup vs valve deformation for (a) first junction (b) second junction with two valve locations.....182

Chapter 1

Introduction

1.1. Motivation

Miniaturisation of mechanical and electrical components is one of the most promising technological advancements of the twenty-first century that has led to significant conservation of material, energy and manufacturing costs. Due to the recent rapid increase in energy demand worldwide, reducing energy loss using microelectromechanical systems (MEMS) has become increasingly important for design and operation engineers in developing novel engineering systems. In recent decades, numerous studies have been undertaken on microelectromechanical systems (MEMS); these studies focused on finding new techniques not only to save material and costs, but also to achieve higher efficiency in both operation and performance. MEMS have been widely used in different branches of science and technology, ranging from new techniques for cooling electronic components to novel blood pressure sensors for biomedical sciences^{1,2}. When it comes to working with fluids, the structure and size of MEMS devices necessitate the use of fluidic systems with volumes ranging from microliter to picolitre, which resulted in the development of a new field, small-scale fluid mechanics or microfluidics³. Here, the savings are primarily in terms of reagent volumes, in addition other advantages emerge due to the size scale being in the order of a single cell, and the visualisation possibilities this offer.

Microfluidics is the science and technology of studying, utilising, and controlling fluids that are microlitre scale in volume and are mainly limited to microstructures of 1 to 1000 microns in size. Modern micro-scale engineering technologies have the potential to revolutionise various branches of science and industry by offering new capabilities and providing numerous advantages over their traditional macroscale counterparts. There are several important advantages in microfluidics that include smaller sample and reagents volumes, improved reaction rate, higher sensitivity, portability, possibility of parallelisation, and lower cost. These enhancement properties make microfluidics beneficial for on-chip reactions and mixing in which different chemical reactions, non-chemical mixing and molecular synthesis can be achieved by miniaturising huge chemical reactors and traditional macroscale mixers into small but efficient microreactors and micromixers⁴⁻⁶. With respect to biomedical applications, microfluidics has shown promise in understanding cell biology⁷⁻¹⁰, cancer cell detection^{11,12}, assisted reproductive technology (ART)^{13,14}, and single cell analysis^{15,16} by operating in precisely monitored and controlled chemical and physical microenvironments. Microfluidics includes various domains from paper-based microfluidics¹⁷ and open microfluidics¹⁸ to digital microfluidics¹⁷ and droplet microfluidics¹⁹. As an example, digital microfluidics is one of the

main domains of microfluidics which is about handling and manipulation of a single sessile microdroplet on a planar platform²⁰. Although many of the advancements using microfluidics have taken place in a single-phase flow, two-phase flow microfluidics, and specifically droplet microfluidics has gained significant attention during the last two decades²¹. Droplet microfluidics involves the use of two immiscible fluid phases, with one phase forming microdroplets in the other phase, to provide a high throughput method for encapsulating and manipulating cells and reagents in controlled microenvironments of femtoliter to nanoliter in volume.

1.2. Thesis Overview

This thesis focuses on the application of microfluidics for on-chip reaction and cell biology study by developing microvalve and droplet manipulation techniques. The thesis investigates various droplet manipulation techniques using microvalves to offer lab-on-a-chip devices that could be miniaturised substitutes of traditional laboratory assays for high throughput industrial reactions. Specifically, droplet generation, splitting and merging will be demonstrated using single-layer microvalves in Chapter 3 and Chapter 4. In order to also illustrate the application of droplet microfluidics for single-cell analysis, the thesis also presents a new method in Chapter 5 for the encapsulation of individual sperm in microdroplets of controlled size and studying sperm motility characteristics. Specifically, high throughput droplet generation techniques are integrated with an advanced imaging and analysis system in order to gain a better understanding of the biophysics of sperm interactions with the curved microenvironment of the female fallopian tube *in vivo*.

Chapter 2 reviews the current state of literature in the field of droplet microfluidics and the applications of microfluidic manipulation techniques (splitting and merging) for on-chip reaction, high throughput screening and cell biology study. This chapter highlights new opportunities in the field and illustrates current research gaps in the field, focusing on the research aims of this PhD thesis.

Chapter 3 investigates one of the most important manipulation techniques of droplet microfluidics, droplet splitting. Utilising a novel single-layer valve, selectivity, efficiency and response time of splitting of droplets are improved in this chapter. A bypass loop is designed to split incoming droplets selectively, thus turning the droplet or on-chip test tube into an on-

chip pipette. The results are analysed to support the explanation of the splitting phenomenon in the entrance of the bypass loop. The ability to switch between non-splitting regime and splitting regime whenever needed with the minimum external force is essential for high throughput screening and is demonstrated in this chapter. Flexibility of polydimethylsiloxane (PDMS) is utilised in this chapter to show that with minimum external force and without any complexity in design or microfabrication process, a single-layer microvalve is able to actuate the microchannel and split the isolated chemicals with full controllability and selectivity. The presented system has the potential to replicate automated pipetting technologies currently used on a larger scale. Combining droplet microfluidic splitting manipulation techniques and microvalve technology to make a matrix of droplets can be of benefit in pharmaceutical tests where diseased carrying cells are tested against the proposed drugs to search for positive reactions. The integration of this manipulation technique with other manipulation techniques such as generation and merging by using the presented microvalve can result in producing a combinatorial library of chemicals for further screening which is presented in Chapter 4. This work was published in *Sensors and Actuators B: Chemical*²².

Chapter 4 expands upon the work presented in Chapter 3 by the integration of the selective valve-induced droplet splitting with valve-induced on-chip droplet generation and merging. In this chapter, a method is presented to integrate the three most important droplet manipulation techniques (droplet generation, splitting and merging) selectively on the same microfluidic chip using eight single-layer microvalves. As a means of manipulating droplets in a microfluidic system, single-layer microvalves provide a simple and bio-compatible method. In this chapter, the sequential generation of different droplet types is demonstrated by using an activation/deactivation of four microvalves located in close proximity to the four discontinuous phase inlets. These generated droplets are split selectively at four junctions using partial closure of valves located at each junction. Finally, using pillars to merge droplets in different permutations and combinations, the ability of the method to make a matrix of products with different concentrations from an array of ingredients is demonstrated. Moreover, fast reaction kinetics studies could be performed by the integration generation, splitting and merging of microdroplets using this platform on a chip. This work has been submitted for publication.

Chapter 5 describes the results obtained from a high-throughput droplet generation device for single cell biology and sperm study. The female fallopian tube in the reproductive tract is lined with a highly complex convoluted epithelium surrounding a lumen that progressively narrows.

The influence of this increasing geometrical complexity on sperm behaviour as they move through this environment is unknown. Through the use of droplet microfluidics, we contain a single sperm in droplets ranging from 30 μm to 140 μm in radius, and observe the resulting sperm swimming characteristics. It is revealed for the first time that curvatures activate a dynamic response mechanism in sperm to switch from a progressive surface-aligned motility mode at low curvatures to an aggressive surface-attacking mode at high curvatures. In the attacking mode, the sperm head is consistently aligned at 70° with respect to the interface and swims $\sim 35\%$ slower, spending 1.66-fold longer time at the interface than progressive mode. Our experimental results and mathematical modelling also reveal that hydrodynamic effects lead to an active response mechanism in sperm to decrease their flagellar wave amplitude by up to 66% at high curvatures, potentially by activating an intercellular regulation mechanism such as switch-inhibition mechanism. The gathered data reveals that surface curvature within the fallopian tube alters sperm motion from a faster surface aligned locomotion in distal regions to a prolonged physical contact between sperm and the epithelial tissue close to the sight of fertilisation. This work has been submitted for publication.

Finally, Chapter 6 summarises the main conclusions and outcomes of the thesis and presents potential directions for future studies.

Chapter 2

Literature Review and Research Aims

2.1. Preface for Chapter 2

In chapter 2, a detailed and comprehensive literature review will be given to present the studies in the field of microfluidics-based microsystems with the focus on droplet microfluidics, microvalves and droplet microfluidics applications in the fields of on-chip reactions, high throughput screening and cell biology. In the second section of this chapter, droplet microfluidics will be briefly introduced and the importance of this field of science will be discussed. The literature review will then focus on a thorough analysis and critical comparison of different microdroplet generating and splitting manipulation techniques in sections 3 and 4. In section 5, fusion phenomenon is presented and different techniques which can intensify the coalescence of microdroplets are briefly discussed. This is followed by a review of microvalves with a focus on multi-layer and single-layer pneumatic valves in section 6. The range of applications obtained from the microfluidic platforms with the focus on using microdroplets manipulation techniques for on-chip reactions, high throughput screening, and cell biology studies are then discussed in sections 7 and 8. Finally, section 9, summarises the gap in the literature and introduces the problem statement of this PhD study and its significance and impact.

2.2. Droplet Microfluidics

One of the newly introduced methods for the improvement of high throughput screening^{23,24}, chemical reactions^{25,26}, and single cell biology study^{23,27} is droplet microfluidics. Droplet microfluidics also provides opportunities to transport live cells and microorganisms ranging in size from 5 to 500 micrometer^{28,29}. Droplet microfluidics involves the use of two immiscible fluid phases, such that one (dispersed or discontinuous phase) forms droplets in a volume range between femtoliters and nanoliters within the other (continuous phase) with the production rate of even more than 100 kHz^{30,31}. Different methods have been used to generate these streams of microdroplets, including T-junction³² and flow-focusing^{33,34} which will be studied in detail in the next section. These isolated microdroplets can be equated to test tubes if the lab is brought onto a chip, as samples are physically and chemically isolated from surroundings and each other, so each of these isolated microdroplets can be used as a microreactor for on-chip reactions and nanoparticle synthesis^{35,36}. Different droplet manipulation techniques were invented during the last two decades to give scientists the ability to form, handle and utilize droplet microfluidics for different purposes including droplet generating³⁷⁻³⁹, splitting^{22,40,41},

merging⁴²⁻⁴⁴, trapping⁴⁵⁻⁴⁷, sorting⁴⁸⁻⁵⁰, mixing⁵¹⁻⁵³ and sensing⁵⁴⁻⁵⁶. The first three mentioned techniques (droplet generation, splitting, merging) will be discussed in detail in the next three sections of this chapter since these techniques were examined and extended in the experiments within this PhD thesis.

2.3. Generation of Microdroplets

Droplet microfluidics generation techniques, in which a constant flow of buffer and sample meet at a microfluidic junction, create monodisperse droplets at rapid speed⁵⁷ and is the foundation of other droplet manipulation techniques⁵⁸. Generally, to enable the chip to do other manipulation techniques like splitting, merging, trapping and intra-droplet manipulation techniques, it is necessary to first generate microdroplets from the same or different dispersed phases on demand on the same chip or bring them to the inlet of the main chip with tubes from the generation chip after their formation, which shows that without generation, other droplet manipulations techniques are almost impossible. Also, droplet generation has a wide range of application from nanoparticles fabrication⁵⁹ and cell encapsulation⁶⁰ to emulsions⁶¹ and foams⁶² and drug delivery research⁶³. Hence, before studying any other manipulation techniques, it is best to first review different regimes and methods of droplet generations in detail.

In the mechanism of generation or formation of microdroplets, different production regimes can be observed including squeezing^{64,65}, squeezing–dripping transition⁶⁶, dripping^{65,67}, jetting^{67,68}, tip-streaming⁶⁹, and tip-multi-breaking⁷⁰. Capillary number is used as a dimensionless parameter to demarcate the physical boundaries between these regimes. Capillary number is defined as the ratio of viscous forces over surface tension ($Ca = \mu v / \gamma$) where μ (Pa s) is the viscosity of the continuous phase, v (m s^{-1}) is the average flow velocity of the continuous phase, and γ (N m^{-1}) is the surface tension between the continuous and dispersed phases⁷¹.

Starting from the lowest capillary number ($Ca \leq 0.015$), where the shear force is negligible, the squeezing regime occurs. Droplet formation in this regime is mostly influenced by the pressure imposed by the continuous phase⁷¹. Here, the interface between the continuous and dispersed phases grows until it blocks the whole width of the channel. As a result, there is a build-up of

pressure upstream which finally overcomes the interfacial tension, the interface ruptures and large non-spherical droplets or plugs are created which occupy the whole width of the channel^{72,73}. In the squeezing regime, the channel geometry and the relative flow rate between continuous and dispersed phases play key roles in generation process and droplet volume^{37,74,75}, however, the relative viscosity between the continuous and dispersed phases or other physical properties of two fluids are of less importance^{71,76}. Here, the generated droplets have a larger volume in comparison to other generation regimes³⁷.

Increasing the Capillary number of the continuous phase results in a confined transition regime between squeezing and dripping regimes ($0.015 \leq Ca \leq 0.02$)^{65,71,72}, in which both surface tension and shear forces are of great importance^{65,75}. In this intermediate regime, the interface between the continuous and dispersed phases obstructs the channel partially and provisionally during the generation of microdroplets^{66,77-79}. For $0.02 \leq Ca$, the dominance of shear force, enforces the dispersed phase to break up and creates the droplet before the protrusion of fluid emerging from the side channel blocks the main channel (Dripping regime)^{32,71}. As a result, droplets are spherical and smaller in size in comparison to squeezing and transition regimes (Figure 2.1b). However, the production rate, stability and monodispersity are much higher than other generation regimes which make this regime an excellent candidate for high throughput screening, drug delivery and cancer therapy^{80,81}. Here, the size of generated droplets is highly dependent on the capillary number and fully independent of the relative flow rate^{74,82}.

By further increase of the flow rate of either the continuous phase or dispersed phase, a jet consisting of the dispersed phase is shaped in the middle of the channel (Figure 2.1c). This jet stream breaks up downstream and creates highly monodisperse droplets (Jetting regime) as a result of Rayleigh-Plateau instabilities^{67,83,84}, which can be used in single-cell protease detection⁸⁵, fibre synthesis⁸⁶, and wafer die marking⁸⁷. Creeping flow condition in the tip-streaming regime results in shaping the very thin cone jet⁸⁸, which finally splits to tiny monodisperse droplets as small as a micron or even sub-micrometer⁸⁹⁻⁹¹. These sub-micrometer droplets have an increasing demand in emulsions and nanoparticle productions⁶⁹. Tip-multi-breaking regime is very similar to tip-streaming regime unless the cone jet is unsteady in tip-multi-breaking regime. So, droplets production is not continuous but rather sequential (Figure 2.1d). As a result, trains of polydisperse droplets are shaped one after the other which gradually increase in size from the back to the front of the train⁹². These trains of droplets are well suited to use in multi-volume droplet digital PCR⁹³, smart biosensors or drug delivery applications⁹⁴.

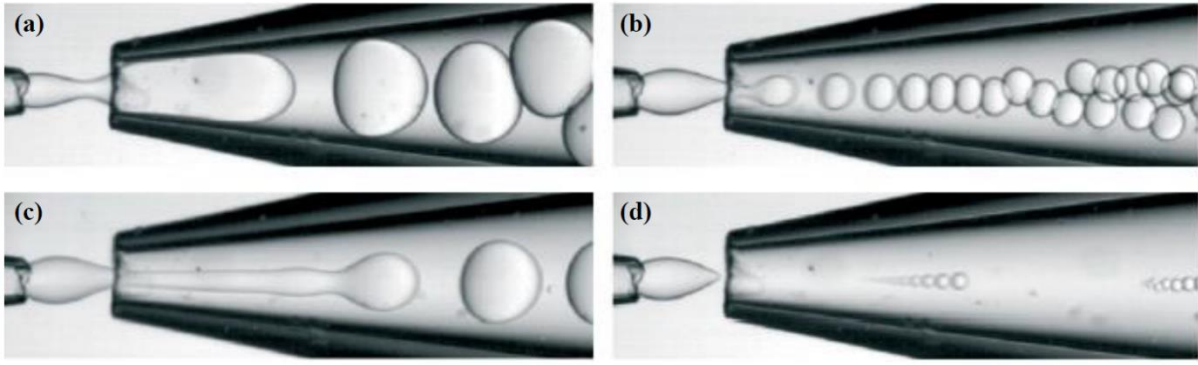


Figure 2.1. Different regimes of breakup, (a) squeezing, (b) dripping, (c) jetting, and (d) tip-multi-breaking regime in a flow focusing droplet generation method³⁷. (a) – (d) are reproduced from ref. 31 with permission from The Royal Society of Chemistry.

Microfluidic based droplet generation methods can be grouped into active or passive techniques, depending on whether any external force field is used to form the droplets (active)³⁸ or only the microchannel geometry and inherent fluid forces play roles on droplet formation (passive)^{37,80}, which will be discussed in detail in the next two subsections.

2.3.1. Passive Droplets Generation

Passive droplet generation methods, which make use of selective channel geometries without any external force are fast, low-cost, on demand and simple in in operation, therefore they are usually preferred for single cell isolation and analysis⁹⁵. The three most widely used geometrical configurations for passive droplet generation are cross-flowing³², flow focusing^{33,34}, and co-flowing⁹⁶.

Pioneered by scientists at California Institute of Technology, cross-flowing was the first geometrical configuration that was used to generate microdroplets on demand³². In this method, dispersed-phase stream meets the continuous-phase stream in an arbitrary angle ($0^{\circ} < \theta \leq 180^{\circ}$). If the two streams intersect perpendicularly ($\theta = 90^{\circ}$) or in an acute intersection angle ($0^{\circ} < \theta \leq 90^{\circ}$), it is also called a T-junction. Otherwise, it is called head-on junction for $\theta = 180^{\circ}$ and Y-junction for $90^{\circ} < \theta \leq 180^{\circ}$. Since T-junction is the simplest and most common passive droplet generation methods, all the parameters that play an effective role in droplet generation such as Capillary number, surface tension, relative dimensions of channels and relative pressure imposed in two inlets, are widely studied and well-established for T-junction⁹⁷ or other cross-flowing generation methods^{76,98,99}. More complicated versions of T-junctions have also been

introduced and developed more recently to increase the monodispersity and diversity of generated droplets and functionality of the system for especially mass production in chemical and biological assays including double T-junction¹⁰⁰, parallel dual T-junctions¹⁰¹, K-junction^{102,103}, V-junction^{104,105} and block and break generation system¹⁰⁶. As an example, in a double T-junction system, the second dispersed stream is introduced into the main channel from the second arm, located opposite to the first arm which carries the first dispersed stream, as such two different coloured droplets are produced alternately from two different reagents¹⁰⁰. It is also worth mentioning that among all different generation regimes (squeezing, squeezing–dripping transition, dripping, jetting, tip-streaming, and tip-multi-breaking) only the first four have been observed in the cross-flowing generation method³⁷.

Simultaneously invented by two different groups working independently of each other in flow focusing droplet generation method, two continuous-phase streams come to the generation junction from opposite directions while one dispersed-phase stream meets them perpendicularly. A small orifice is also added after the junction from which two immiscible fluids flow out^{33,34}. Different factors play roles in droplet generation regimes and droplet size in flow focusing including flow rate or pressure imposed in the inlets, interfacial tension, density, contact angle and viscosity. This droplet generation method is preferred when sensitive biological or pharmaceutical samples need to be loaded into the microfluidic droplets due to its improved monodispersity, high throughput, and higher frequency of droplet formation⁵⁸.

Initially introduced by scientists at Harvard university in the beginning of the twenty-first century, the co-flowing approach is very similar to flow focusing in terms of physics of droplet generation¹⁰⁷. The difference is, here, two streams of continuous phases and one stream of dispersed phase meet in parallel instead of meeting perpendicularly in the generation junction. Two streams of continuous phases flow in the outer cylindrical channel while one stream of a dispersed phase flows in the same direction in the inner cylindrical channel in a way that these two cylindrical channels are co-axial, so co-flowing can offer rotational symmetry⁹⁶. Droplet generation using co-flowing has a wide range of applications including formation of emulsions and bubbles¹⁰⁸. In emulsion studies, flow focusing droplet generation in the modified version of microcapillary device, can be integrated with co-flow method to generate monodisperse double emulsion droplets using one-step approach¹⁰⁹⁻¹¹¹.

2.3.2. Active Droplets Generation

While formation of the same sized droplets on demand (monodispersity) is of great interest in diverse applications including high throughput biological screening¹¹², emulsions¹¹³, drug delivery¹¹⁴ and single cell analysis⁹⁵, having great control over the polydispersity index to generate different ranges of droplets on demand is also useful to improve the performance of biological and chemical assays. As an example, quantitative and accurate detection of genetic targets can be achieved using programmable pneumatic micropumps⁹³. Therefore, having additional control over the size of produced droplets to create a more complex droplet patterns, necessitates the use of external forces to generate microdroplets, although active methods are costlier and more complicated.

Electrical field as a direct current was the first external force implemented on a chip to actively generate microdroplets in which water and oil phases play roles as conductor and insulator, respectively¹¹⁵. Later on, electrochemical¹¹⁶, magnetic¹¹⁷⁻¹¹⁹, centrifugal¹²⁰⁻¹²³, optical¹²⁴⁻¹²⁶, thermal¹²⁷⁻¹²⁹ and mechanical forces were integrated on different device geometries (T-junction, flow focusing, step emulsification and co-flowing) to improve the selectivity, functionality, and frequency in generation of microdroplets. Mechanical vibration¹³⁰⁻¹³², off-chip valves¹³³⁻¹³⁵, surface acoustic wave (SAW)¹³⁶⁻¹³⁹, piezoelectric actuator¹⁴⁰⁻¹⁴², or on-chip microvalves¹⁴³⁻¹⁴⁵ are different types of mechanical controls which have been used until now to generate microdroplets. While the mechanism of the generation in the first three introduced mechanical methods is based on the modification of the fluid pressure, in the last two mechanical methods, channel deformation and blockage help to improve the selectivity of droplet generation.

As an example of using non-mechanical forces to generate microdroplets, nanoscale ferromagnetic or ferrimagnetic can be diluted in the continuous or dispersed phases such as the magnetic field can affect the generation mechanism by creating a magnetic drag¹⁴⁶. Here, the size of droplets and the frequency of generation are dependent to the device geometry, direction and location of the applied magnetic field, and the flow rate^{37,147}. Integration of temperature sensor and microheater at the orifice of flow focusing device can adjust not only the droplet size but also the generation regime¹²⁸. Also, optical methods including focused pulsed laser is efficient in generation droplets especially monodisperse droplets in the scale of sub-micrometer or even picoliter with the high generation frequency of 10 kHz^{124,148}. While Capillary number

is the most important dimensionless number in the study of thermal and optical droplet generation methods, magnetic bond number also plays a key role in magnetic generation study since it represents the relative importance of magnetic force over surface tension¹⁴⁷.

As an example of using mechanical forces to have extra control over the production time and droplet size, interdigital transducer (IDT) was integrated with both flow focusing¹³⁸ and T-junction¹³⁹. The acoustic wave generated by a SAW device, travels through the continuous phase, affects the interface between the continuous and dispersed phases, and also increases the pressure in the inlet of continuous phase. As a result, generation frequency is increased but the generated droplet size is decreased. Focused interdigital transducers (FIDT) were also implemented on the modified T-junction to control the frequency of production of one single¹³⁷ or confined number of droplets (2-5 droplets)¹³⁶. The size and number of generated droplets and the frequency of generation are the function of SAW power and duration of pulse and capillary number¹³⁷. SAW offers the biocompatible and contactless technique for droplet generation. However, the complexity in fabrication and bonding the IDTs on PDMS, the cost of equipment, and limitation due to the pulse modulation capabilities of signal generators¹⁴⁹ are the most obvious disadvantages of this active droplet generation method which creates the need to look for other active methods that are of lower cost and less complicated but also biocompatible and on demand for cell biology study.

2.4. Fission of Microdroplets

In a very complex world-to-chip droplet microfluidic interconnection technology, which use each unique droplet as a vessel for different reagents and chemicals, the ability to halve or divide the plugs or larger droplets to smaller tiny droplets is highly requested, especially when concentration, separation and dilution of particles in droplets is of interest. The controllable ability to split droplets when combined with generation and merging mechanism, helps microfluidic researchers to solve the long-lasting issue of having a combinatorial library of chemicals, ingredients and drugs in high throughput screening. A symmetric breaking up of droplets is desirable when splitting is used to increase the production rate of droplets, maximize the capacity of the device, or produce one set of equal size droplets as a backup control experiment^{19,150-153}. However, when a controllable volume or concentration of chemicals inside a droplet is required in pharmaceutical or chemical industries, an asymmetric splitting of

droplets is more of interest¹⁵⁴⁻¹⁵⁶. It seems that most of the methods used to generate droplets can be adopted to split them as well. For instance, decreasing the width of the orifice in flow focusing junction can also be used for splitting the plug to tiny droplets⁵⁸. Droplet splitting can be categorized into passive, active and combined methods which are discussed in detail in the following next two subsections.

2.4.1. Passive Droplets Fission

Passive manipulation techniques utilize interactive effects between dispersed phase, continuous phase and channel structures without using any external fields or forces. On the first attempt to passively split the droplets, simple bifurcating junctions were designed and tested to show the effectiveness of different geometrical parameters on the splitting mechanism¹⁵⁷. Based on the findings of this study, there is a critical extension length (ratio between the length of the mother droplet and the circumference of the main channel) above which all mother droplets split and below which the splitting/non-splitting regime is controlled only by the capillary number. Here, splitting happens when the shear force which is controlled by the channel design, overcomes the interfacial tension. As shown in Figure 2.2, a mother droplet with the length of l_0 and velocity of v (a,f) enters (b,g) and expands at the T-Junction. Below the critical line, the mother droplet (c) fully extends and then (d) penetrates alternately into the two equal-size secondary channels. Above this critical line, longer droplets with higher velocity (h) break and then each of the produced daughter droplets moves to one of the daughter channels¹⁵⁷. It has also been shown that the relative size of two daughter droplets can be controlled by the relative resistance (length or width) of two daughters' microfluidic channels. The results show that the longer or wider the arm is existed; the larger the daughter droplet is produced¹⁵⁷⁻¹⁶⁰.

Even though the phenomenon of droplet splitting for large or moderate capillary numbers in T-junctions was widely described in the literature, only a few studies have focused on the small capillary numbers which are more applicable in the microfluidic world^{99,161,162}. Tables 2.1 and 2.2 briefly classify different regimes of droplet splitting in two different types of T-junctions (two-arm and one-arm). It is worthwhile to mention that in both cases there is a critical length for droplets above which all droplets break up (Figure 2.3). This critical length is not only linked with but also fully controlled by the geometry of the channel. Therefore, it can be concluded that all long droplets split independently from the channel velocity. Short or

medium-sized droplets can be split or not, depending on the velocity in the secondary channel or capillary number^{99,162}.

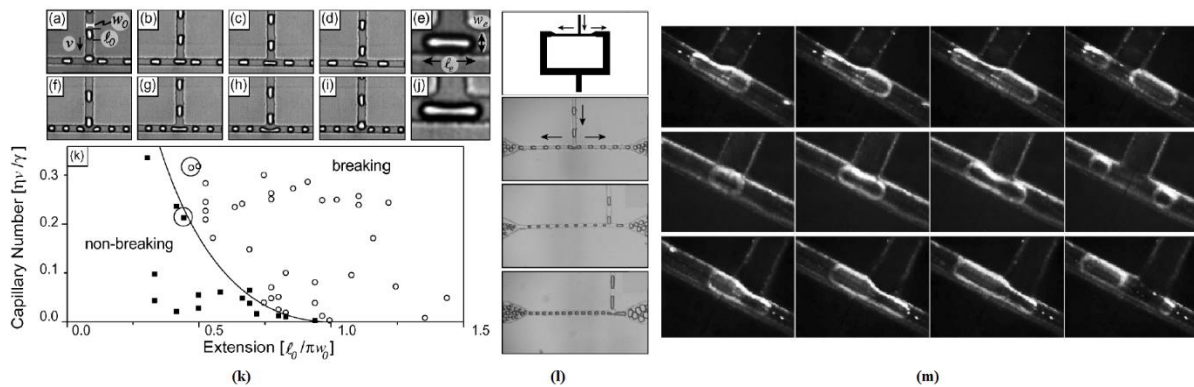
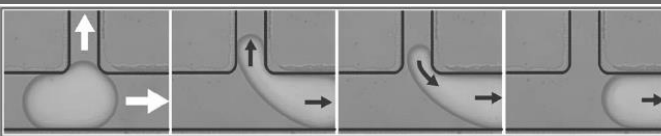
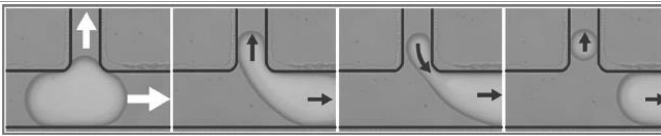
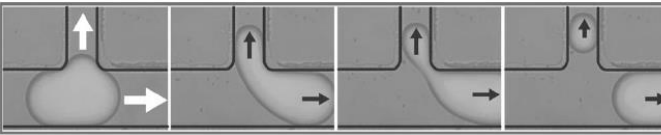


Figure 2.2. Different geometrical parameters which affect droplet splitting (a) - (e) Non-splitting regime¹⁵⁷ (f) - (j) Splitting regime¹⁵⁷. (k) Dependency of splitting regime on capillary number and extension length¹⁵⁷. (l) Dependency of daughter droplet sizes on arms' length¹⁵⁷. (m) Dependency of daughter droplet sizes on arms' width¹⁵⁹. (a) – (l) are reprinted figures with permission from ref. 152. Copyright (2004) by the American Physical Society. (m) is reprinted figure with permission from ref. 154. Copyright (2013) by the American Physical Society.

Table 2.1. Different regimes of splitting in a two-arm T-junction¹⁶². Schematics are reprinted from ref.157, with the permission of AIP Publishing.

Regime	Explanation	Schematic
(a) No Splitting	Short droplets at low velocities penetrate into one of the arms. The droplet could block the arm or leave the tunnel open when passing the arm.	
(b) Tunnel Splitting	Gap always exists between the medium-size droplets and walls. Droplets stretched under viscous force, followed by fully extending and symmetric splitting.	
(c) Obstructed Splitting	Long droplets block the bifurcating channels. No tunnel forms. A circular-shaped neck forms and narrows gradually until splitting occurs.	

Table 2.2. Different regimes of splitting in a one-arm T-junction⁹⁹. Schematics are reprinted figures with permission from ref. 93. Copyright (2006) by the American Physical Society.

Regime	Explanation	Schematic
(a) Retreat Without Splitting	After the initial penetration of a short finger into an arm, the tunnel opens in which a thin layer of oil is sandwiched between the wall and droplet. Droplet regains its shape and continues its path after finger retreating.	
(b) Retarded Splitting	During the finger's retreat, breakup occurs and the daughter droplet separates and is sucked into the daughter channel.	
(c) Direct Splitting	Long finger penetrates into a secondary channel. The bridge between this finger and main plug gradually narrows and finally the daughter droplet is split from the plug.	

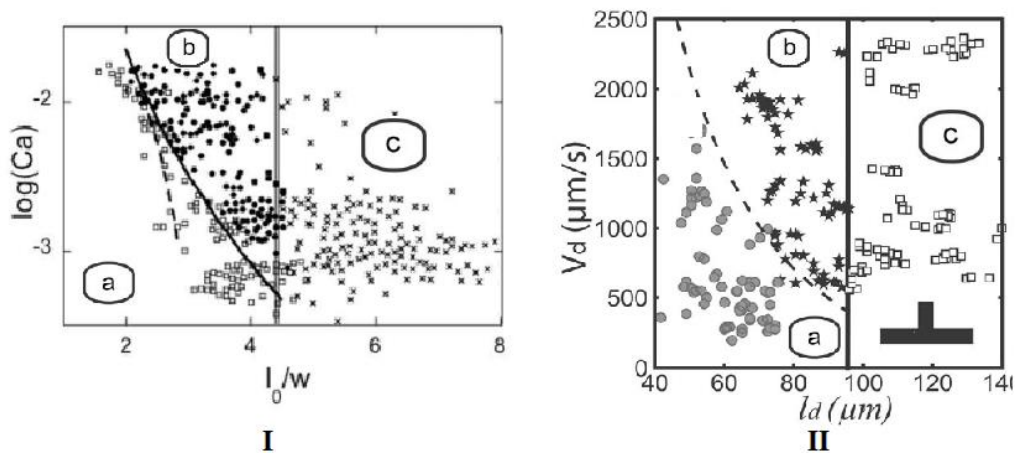


Figure 2.3. Different splitting regimes in (I) two-arm and (II) one-arm T-junctions (a) no-splitting (b) tunnel or retarded splitting (c) obstructed or direct splitting^{99,162}. (I) is reprinted from ref.157, with the permission of AIP Publishing. (II) is reprinted figure with permission from ref. 93. Copyright (2006) by the American Physical Society.

A new device with multiple bifurcating junctions was developed based on the introduced theory in the previous paragraphs, as another passive technique for splitting of droplets¹⁵⁷. Although multiple bifurcating T-junctions with equal-length daughter channels resulted in successfully splitting a big plug into 16 tiny droplets¹⁵⁷, asymmetric splitting was observed due to pressure drop and high surface tension in a microchannel¹⁵⁰. In the same study, the square PDMS obstacle was placed in the centre of the microchannel to split the mother droplet to two equal-size daughter droplets (Figure 2.4b)¹⁵⁷. Asymmetric droplet splitting has also been achieved by changing the distance between the PDMS obstacle and the center line of the microchannel¹⁵⁷. A sorting technique should be added here to separate the unequal-size daughter droplets from each other, which is the drawback of this geometrical-based splitting method¹⁵⁷. Adding surfactants to the main fluid is also an efficient way to reduce the relatively high surface tension between the continuous and dispersed phases (Oil and Water). Besides, using daughter channels with decreasing cross section area helps droplets to maintain their extension, but it interrupts the symmetry of splitting¹⁵⁰.

Changing the angle of bifurcating junction from 90° in T-Junction to 45° in Y-Junction (Figure 2.4a), adding a pointy structure to the bifurcating junction (Figure 2.4c), and connecting one of the outlets of the daughter channels to an open tubing while fluid was withdrawn from other daughter channels with the equal rate (Figure 2.4d), were three other successful ideas implemented by researchers in order to split mother droplet into daughter droplets with the same size^{157,163-165}.

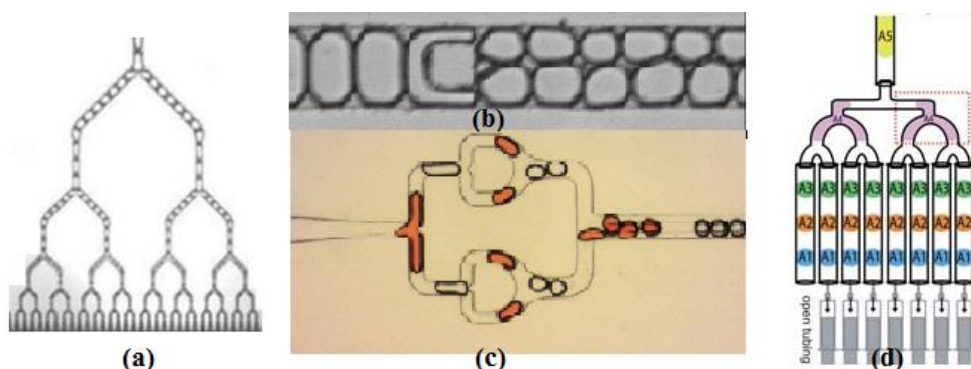


Figure 2.4. Four different techniques for symmetrically splitting of droplets. (a) Playing with the angle of the bifurcating junction¹⁶³, (b) using an obstacle in the center of the channel¹⁵⁷, (c) adding post to the junction¹⁶⁵ and (d) connecting one of the outlets to the open tubing¹⁶⁴. (a) is reproduced with permission from Hsieh, et al. in ref.158. (b) is reprinted figure with permission from ref. 152. Copyright (2004) by the American Physical Society. (c) is reproduced from ref. 160 with permission from The Royal Society of Chemistry. (d) is reproduced from ref. 159 with permission from The Royal Society of Chemistry.

Discussed literature review in this section showed that like other manipulation techniques, passive splitting has been proven possible. However, as it was shown in Figure 2.3, controllable passive splitting only worked within a narrow range of operating conditions depending on the geometry of microchannels. Besides, passive methods are highly affected by fabrication faults and downstream disturbance which makes it worthwhile to integrate or replace them with active splitting methods depending on the application. Hence, in the next subsection of this literature review, active and combined droplet splitting methods are critically discussed.

2.4.2. Active and Combined Droplets Fission

As previously discussed, passive droplet splitting techniques are cheap and simple due to their working principle based on a combination of flow condition with the geometry of designs. However, in more complex high throughput screening research, especially where selectivity of the device is highly desired, active methods seem to be more useful despite their higher cost and complexity. The majority of droplet microfluidic manipulation studies specifically for splitting of microdroplets used passive techniques, with the exception of some mostly new studies, which applied active or combined methods.

Adding an electrical field to the simple bifurcating junction can induce and polarize the neutral mother droplet and split it into two negative and positive daughter droplets, each penetrating to one of the daughter channels or arms. It was found that the size of these oppositely charged daughter droplets changes with an increase in the electrical field and there is an optimum electric field strength, above which no splitting happens and the mother droplet is entirely sucked into one of the daughter channels based on the electric field direction¹¹⁵. Like an electrical field, other active methods such as electrostatic potential wells and laser can be used to break up the droplets when they are combined with passive methods. While without any laser, droplets split symmetrically at the T-junction which has a pointed structure, adding laser beam to one side of the pointy structure increases the local surface tension on the droplet, guiding it to penetrate more to the other side. The longer the laser actuation is induced in one daughter channel, the smaller the daughter droplets are. There is a critical duration of laser actuation, beyond which the droplet completely switches to the opposite daughter channel^{125,166,167}. A similar trend has been observed for breakup mechanism by using an integrated micro heater placed under one of the secondary channels. A viscosity gradient is produced by heating the fluid which results in decreasing the viscosity, hydrodynamic

resistance and surface tension and finally sucking the continuous phase and droplets into the heated channel. Again, here, there is the optimum temperature above which droplet completely penetrates into the heated daughter channel. Vaporizing the fluid, especially in the low-pressure area, and changing the continuity of droplets due to high temperature are amongst the drawbacks of the heating-based splitting method^{168,169}. This ability of the electrical, heating and laser-based splitting, improves the controllability over the sizes of daughter droplets in comparison to the pure passive splitting (Figure 2.5). However, damaging live cells and reagents is the most evident demerit of these combined manipulation techniques for microdroplet splitting.

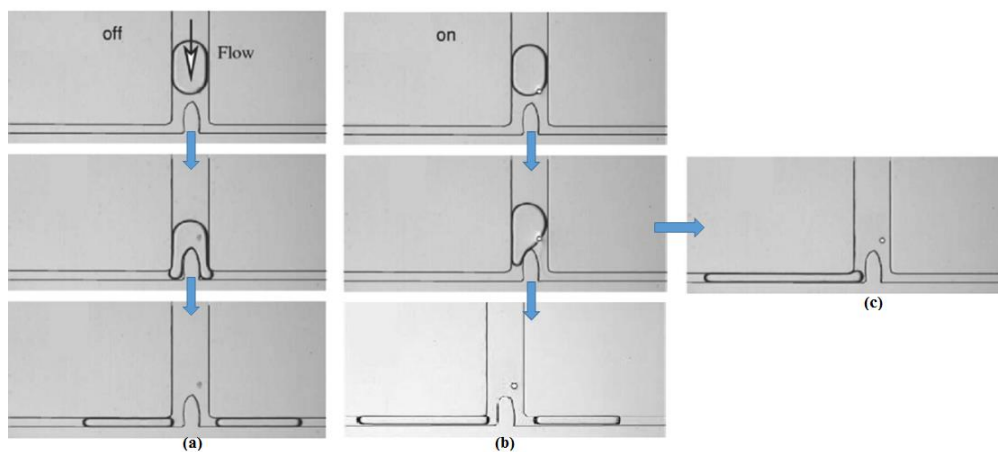


Figure 2.5. Combining passive and active methods for (a) symmetric droplet splitting without any external forces (b) controllable asymmetric droplet splitting by using electric fields, laser or integrated micro heater (c) droplet sorting by increasing any of mentioned forces (Electrical strength, duration of laser actuation or temperature)^{115,125,166-169}. (a) – (c) are reprinted figures with permission from ref. 162. Copyright (2007) by the American Physical Society.

The flexibility and functionality of Electrowetting-on-Dielectric (EWOD) and Dielectrowetting for droplet actuation were successfully tested for droplet splitting (Figure 2.6a). In these methods, constantly energizing the outer electrodes excite surfaces on the two sides of the droplet, while the electrode beneath the surface of the droplet's central line is deactivated after a certain period of activity. Therefore, the droplet is drawn towards its sides and halved^{170,171}.

Despite the cost and complexity of equipment, Surface Acoustic Waves (SAW) have been implemented in the splitting mechanism of droplets, recently¹⁷²⁻¹⁷⁵. Using a pair of off-axis IDTs, SAW was directly applied on the two ends of a sessile droplet to break it up (Figure

2.6b). Depending on the SAW power and excitation time of each IDT and relative impedances or power between them, different behaviors were observed. While insufficient input power only extends the droplet towards the sides or rotates it, similar and different input energy levels of two IDTs can symmetrically and asymmetrically break up the droplet, respectively. Similar to the other active mechanisms, the overcritical SAW energy level can only translate or reflect the droplets which is more useful in sorting manipulation technique¹⁷². A very similar approach was used to split the moving water droplet flows into the oil actuated by slanted-finger interdigitated transducer (Figure 2.6c).

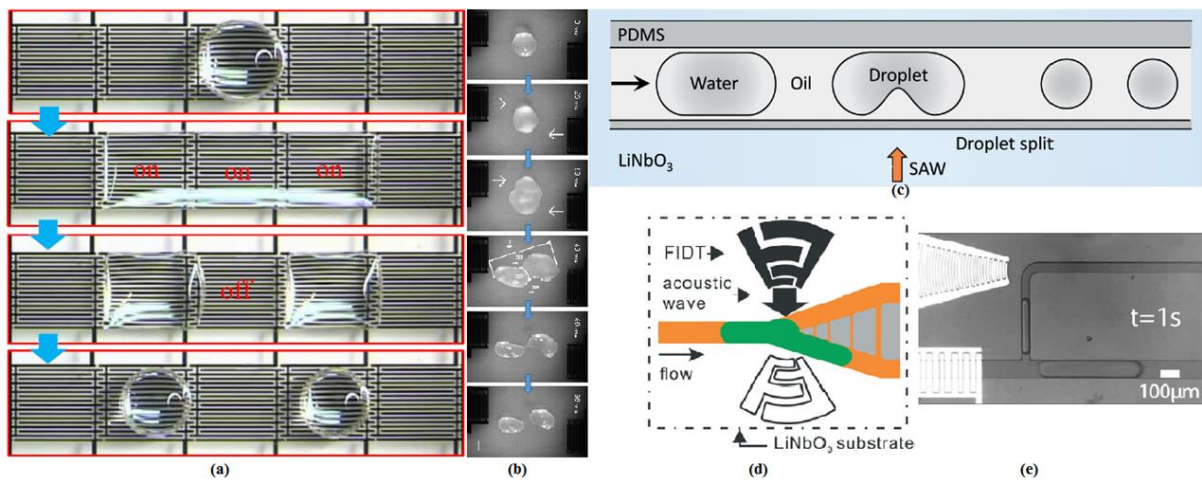


Figure 2.6. Newly introduced active splitting methods, (a) dielectrowetting targets a sessile droplet¹⁷¹, (b) SAW halves a sessile droplet¹⁷², (c) SAW splits moving droplet in a channel¹⁷³, (d) SAW affects plug which approaches Y-junction¹⁷⁴, and (e) SAW works as a pipette for a plug passing through the bypass channel¹⁷⁵. (a) is reprinted figure with permission from ref. 166. © 2017 IEEE. (b) is reproduced from ref. 167 with permission from The Royal Society of Chemistry. (c) is reproduced from ref. 168 with permission from The Royal Society of Chemistry. (d) is reproduced from ref. 42 with permission from The Royal Society of Chemistry. (e) is reproduced from ref. 170 with permission from The Royal Society of Chemistry.

Droplets splitting/non-splitting regimes and the ratio of daughter droplets was controlled by the capillary number of fluids, applied voltage and the region of the droplet targeted by SAW¹⁷³. Splitting and steering of a moving droplet in the presence of travelling SAW was investigated while the mother droplet approached the Y-junction (Figure 2.7d). In the absence of SAW, symmetric breaking up was observed due to the symmetric geometry of daughter channels whereas applying SAW leads to asymmetric splitting or fully steering droplets to one of the daughter channels depending on the power level¹⁷⁴. Finally, pipetting from a moving plug in the design in which a by-pass loop was added as a secondary channel to the main channel was recently investigated (Figure 2.6e). Without using SAW, only a small finger

penetrates into the secondary channel and no pipetting occurs. Actuation of the upper part of the loop using SAW, pushes the continuous phase fluid in the secondary channel and increases the pressure difference between the main and secondary channels and affects the interface between the main and secondary streams of fluid. The higher the SAW power and the longer the actuation duration are, the larger the finger is formed which is finally split from the main channel and penetrated to the by-pass loop. Adding a capacitive sensor to the chip system improves the controllability and selectivity of the introduced pipetting mechanism¹⁷⁵.

While it seems that SAW is more versatile and bio-compatible than other active methods for fission, the cost and complexity of operational instruments make it worthwhile to search for a reasonable-cost substitution active method for droplet splitting which is one of the aims of this PhD study.

2.5. Fusion of Microdroplets

While splitting seems to be an effective method for separating, concentrating, portioning, and diluting particles in droplets, merging two or more droplets plays a pivotal role in mixing chemicals and ingredients and accelerating biological or chemical reaction between them^{19,155,176}. Because each microdroplets that could be merged can work as an isolated capsule, droplet microfluidic also supplies a unique environment for studying fast organic reactions¹⁷⁷. Like fission of microdroplets, geometry of the microchannel as well as velocity of fluid has an effect on fusion. However, other parameters such as capillary number, viscosity, impact velocities and wetting properties play an important role here, which makes merging phenomenon analysis more sophisticated in comparison to other manipulation techniques¹⁷⁸.

Two reviews on the merging phenomenon of microdroplets were recently published and widely studied the mechanisms that play an effective role in fusion^{176,178}. The latter presented a theory termed the drainage model in order to explain the coalescence of microdroplets in the presence or absence of surfactants. Based on this theory, in the absence of any surfactant, there exists a thin layer of continuous phase between two separate droplets which prevents them from being merged. The thinner the drainage film is, the more probable the coalescence can occur. As soon as this thin film fades away and two droplets touch or become close enough to each other, the intermolecular forces become strong enough to tear up interfaces between the droplets and merge them (Figure 2.7a). It was also found that there is a critical capillary number below

which merging is more likely to occur. On the other hand, in the presence of surfactants, Marangoni flow is induced in the opposite direction to the film drainage due to irregularity in the surface tension of the interface. Besides, bipolar surfactant molecules which coated the interfaces of droplets repel each other and intensify the stability of droplets. These two effects cooperate with each other to delay the film drainage and droplet fusion in the presence of surfactants (Figure 2.7b)¹⁷⁸.

2.5.1. Passive Droplets Fusion

Like droplet generation, splitting and other droplet manipulation techniques, unspontaneous fusion of microdroplets can be subcategorized into passive and active merging, which are briefly discussed in this and the following subsections. Adding fusion T-junction, fusion chamber, pillars or by-pass channel to the microchannels, modified the geometrical designs and facilitated droplet merging as shown in Figure 2.7c-e. These modifications decrease the velocity of the first droplet that reaches the channel, due to an expansion in the designed channel or other geometrical restrictions and give the following droplet sufficient chance to come and touch the first droplet. A thin film between two trapped daughter droplets prevents the merging of two droplets. Within a short time, this thin film drains out, and two daughter droplets merge and the newly formed droplet continues its journey downstream towards the exit of the channel^{43,179-183}.

Trapping which is another important manipulation technique can be employed to catch targeted droplets in a storage chamber or wells (Figure 2.7f-g)¹⁸⁴⁻¹⁸⁶. When trapping is followed by flushing the system with a pure continuous phase that does not have any surfactant, merging can easily happen without using any external forces¹⁸⁶.

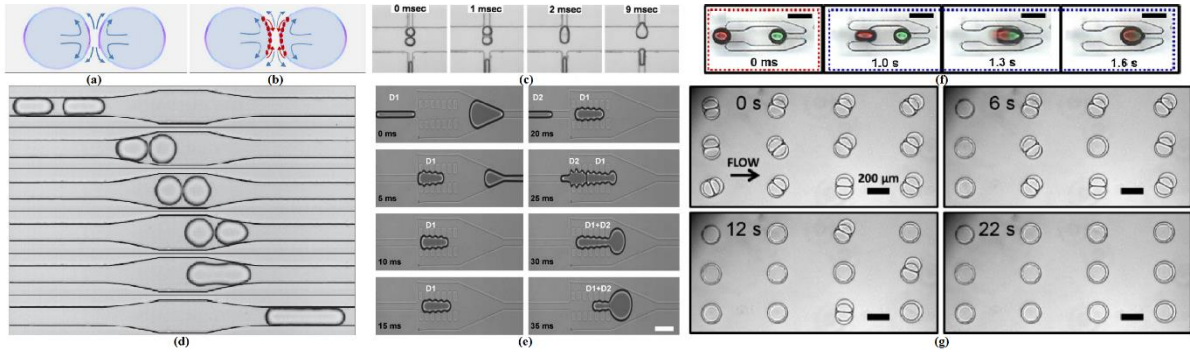


Figure 2.7. Passive fusion of microdroplets (a) without surfactant¹⁷⁸, (b) with surfactant¹⁷⁸, (c) with fusion junction¹⁷⁹, (d) with fusion chamber¹⁸¹, (e) with pillars⁴³, (f) with storage chamber¹⁸⁵, and (g) with storage well¹⁸⁶. (a) and (b) are reprinted from ref. 173 with permission from Elsevier. Copyright © 2015 Elsevier. (c) is reprinted with permission from ref. 174. Copyright 2007, Springer. (d) is reprinted figure with permission from ref. 176. Copyright (2008) by the American Physical Society. (e) is reproduced from ref. 37 with permission from The Royal Society of Chemistry. (f) is reprinted with permission from ref. 180. Copyright 2016, Springer. (g) is reproduced from ref. 181 with permission from The Royal Society of Chemistry.

2.5.2. Active Droplets Fusion

While passive fusion manipulation techniques are highly applicable in the absence of surfactant, when surfactants are present, external forces assist in overcoming the increased stability of the interface to merge droplets. Among different active methods, electrocoalescence is the most common for droplet fusion. As it is obvious from its name, electrocoalescence is the coalescence of droplets under the effect of a variable electric field^{115,187-190}. While electric forces were used widely as an active method for droplet merging, other possible external forces such as dielectrowetting¹⁷⁰⁻¹⁷² or surface acoustic waves^{42,44} have been recently applied to merge the droplets. Additional equipment used in introduced active techniques encourage researchers to search for cheaper and simpler methods for unspontaneous merging of droplets which can be integrated with active manipulation techniques for generating and splitting microdroplets.

2.6. Microvalves

In this part of the literature review, pneumatic valves, their different types and their importance in the lab-on-a-chip (LOC) droplet manipulation techniques will be introduced.

Conventionally, valves have been used for controlling, blocking, minimizing, guiding, or alternatively switching the flow of fluid into specific directions within complex engineered structures. As miniaturization of every mechanical component came into use in the last decades, the idea that valves could be miniaturized and work as microactuators revolutionized droplet manipulation techniques. While based on their initial mode, microvalves can be categorized into mostly open, mostly close and bistable microvalves, classifying them based on existence (active) or non-existence (passive) of any external force is more useful¹⁹¹. In passive microvalves, the pressure difference between the inlet and outlet of the valve controls the flow rate without any external actuation. Passive microvalves are subdivided to mechanical/check valves and non-mechanical/capillary valves which are considered as a micropumps in some literatures¹⁹²⁻¹⁹⁴. On the other hand, an autonomous actuation system is used to control the flow rate in the main microfluidic channel by using active microvalves. Mechanical (magnetic, electric, piezoelectric or thermal), non-mechanical (electrochemical, phase change, bistable) or external (rheological, modular, pneumatic) actuation systems which can be used to open and close the microvalves are the basis of subdividing active valves into different subcategories¹⁹¹. Based on the topic of this PhD project, we only critically focused on the pneumatic valves which are one of the most useful valves in the microfluidic world due to its simplicity, ease of fabrication, high-power density, bio-compatibility, reasonable-cost experimental setup and versatility^{195,196}. Besides, pneumatic valves can be controlled electronically, allowing several independent microvalves to work simultaneously and automatically¹⁹⁷.

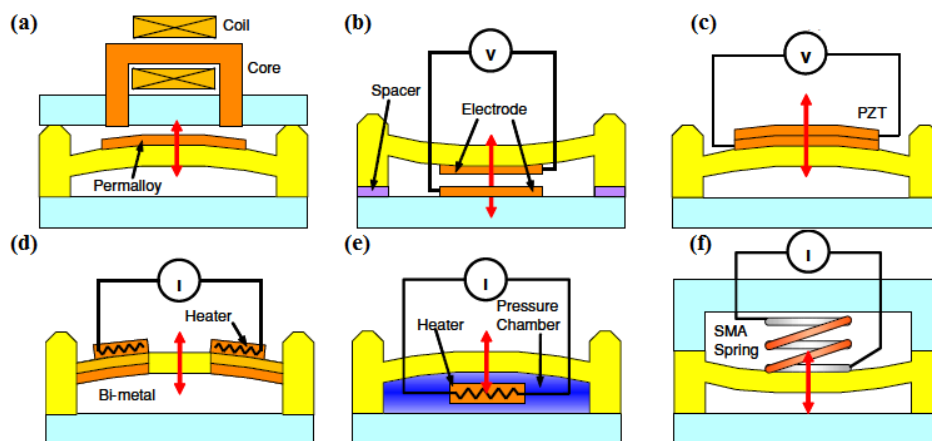


Figure 2.8. Schematic of different actuation systems in active mechanical microvalves: (a) magnetic (b) electric (c) piezoelectric (d) bimetallic (e) thermopneumatic and (f) shape memory alloy microvalves¹⁹¹. (a) – (f) are reproduced from ref. 186 with permission from © IOP Publishing Ltd. All rights reserved.

2.6.1. Multi-Layer Pneumatic Valves

Initially introduced by the Quake group, these types of valves have been also referred to as Quake valves¹⁹⁸. Since then, multi-layer valves have been broadly used to controllably generate^{199,200}, split¹⁹⁹, sort⁵⁰, merge²⁰⁰ and mix^{201,202} either droplets or cells. As is easily understood from its name, flow and control channels have been manufactured in two different layers and then have been positioned on top of each other, with a shared thin flexible horizontal membrane in between them; thus, they are labelled as a multi-layer valve. Increasing the pressure of gas or liquid in the control layer actuates the membrane which results in compressing and finally blocking the flow channel¹⁹⁸. Similarly, applying negative pressure in the control channel moves the membrane in the opposite direction and expands the flow channel due to the suction effect²⁰³.

Multi-layer valves can be subdivided into push-down valves, push-up valves, push-up and push-down valves and sieve valves (Figure 2.9a-d). The control channel passes over and below the flow channel in the push-down and push-up valves, respectively. However, the control channel lies in between two flow channels in the push-up and push-down valves. While in the first three mentioned valves, a tight seal and true valving has been achieved due to the rounded profile of the flow channel, the sieve valves have failed to be fully closed due to the rectangular shape of the flow channel. Hence, when the complete sealing of the channel without any leakage is needed, push-up and push-down multi-layer valves are the best possible choices²⁰⁴.

Multi-layer valves showed their capability in splitting of microdroplets in which different regimes of splitting in the microfluidic channels are controlled by the difference between the valving pressure induced in the control channel and the overall pressure in the flow channel. As shown in Figure 2.9e, at a small valving pressure, expanding the flow channel towards the control channel results in a no-splitting regime. Above a critical pressure, a constriction regime is shaped which leads to splitting a mother droplet into two different sized daughter droplets, a small satellite droplet which is attached to a bigger daughter droplet. An increment in the valving pressure decreases the size and increases the number of daughter droplets, respectively. Finally, above another critical pressure, the flow channel is completely blocked by the valve, making both the microdroplet of dispersed phase and the continuous phase unable to pass through it¹⁹⁹.

Multi-layer valves suffer from sophisticated fabrication and designing processes. Flow layer and control layer have different concentrations of the curing agent in PDMS, therefore they should be cured separately. The necessity for aligning different PDMS layers by hand under the microscope on top of each other or by using a mask aligner and specific photoresist add at least one challenging step to the fabrication process²⁰⁴. Besides, carefully fitting the control layer and the flow layer in the designing step is required in order to escape from overlapping. Any partial change in the control layer may lead to the redesign or a vital change in the flow layer and vice versa, which consumes extra time, cost and energy²⁰⁵. These drawbacks encouraged researchers to look for a substitution for multi-layer valves which is the subject of the next subsection of this literature review.

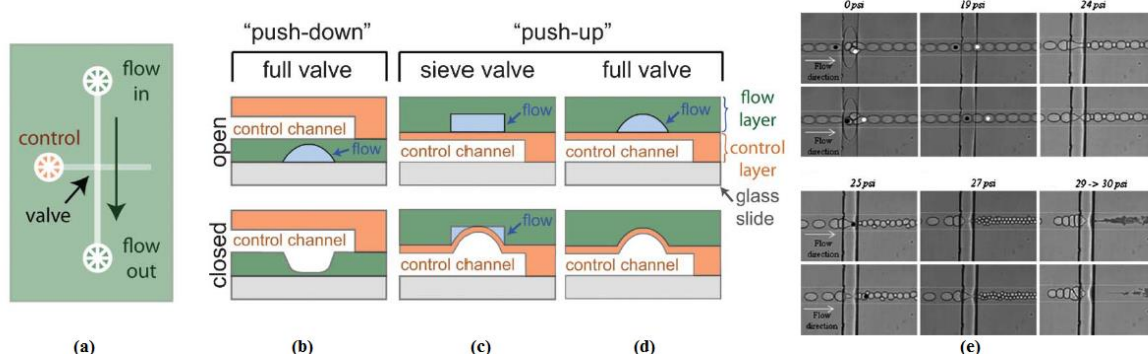


Figure 2.9. (a) Top and (b) – (d) Side views of different types of multi-layer valves²⁰⁴ and (e) different regimes of droplet break up by using multi-layer valves¹⁹⁹. (a) – (d) are reproduced from ref. 199 with permission from The Royal Society of Chemistry. (e) is reproduced from ref. 194 with permission from The Royal Society of Chemistry.

2.6.2. Single-Layer Pneumatic Valves

Pioneered by scientists at Wisconsin–Madison University, single-layer valves integrates ease of fabrication and simplicity of single-layer devices with the controllability and versatility of the pneumatic valves^{206,207}. Followed by Harvard university scientists, this valve perfectly showed its high efficiency to generate¹⁴⁵ and sort^{208,209} droplets. In contrast to multi-layer valves here, a thin layer of elastomeric membrane lies vertically between the control and flow layers^{145,208,209}. Like sieve multi-layer valves, single layer valves suffer from leakage mostly via the corners of the channel. Even when fully actuated by air, they do not close completely, due to the rectangular profile of the flow channel. However, new innovations to use them at both sides of the channel as a pincer or to fabricate them using dual-sided molding method reduce the leakage to a negligible amount and makes them a suitable substitution of multi-

layervalves in DNA synthesis and other biological applications where leak-tight microvalve seem to be an urgent priority²¹⁰⁻²¹³.

In many manipulation techniques, only a certain change in flow rate or pressure in the main stream without complete blockage is required, therefore the two key advantages of single-layer valves (simplicity in structure, and eased of fabrication) result in choosing them as the best candidate for generating, sorting, splitting and merging of microdroplets without adding any supplementary steps in the design or fabrication. The versatility of the single layer valve allowed researchers to test them in different designs for droplet manipulation techniques, some of which are schematized in Figure 2.10^{48,208,209,211,214-219}.

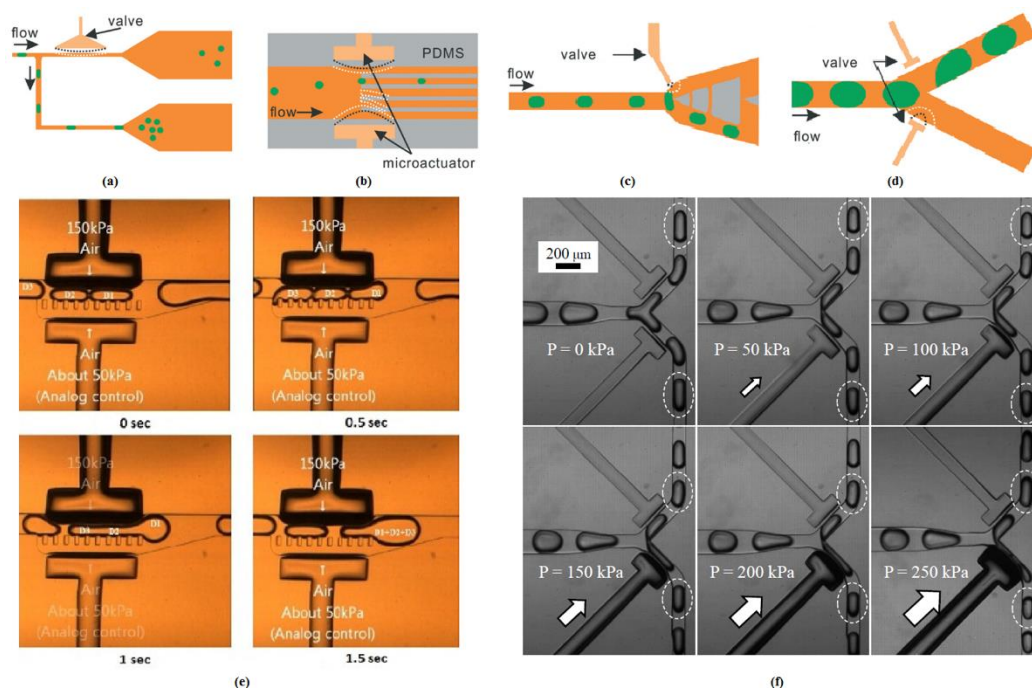


Figure 2.10. Using single-layer valves for different manipulation techniques (a) – (d) sorting⁴⁸, (e) merging²¹⁸, and (f) splitting²¹⁹ of microdroplets. (a) – (d) are reproduced from ref. 42 with permission from The Royal Society of Chemistry.

Adding a pair of single layer valve opposite to each other after the orifice of a flow focusing junction results in membrane deformation when it is needed, which gives the user excellent control over the size of droplets and frequency of generation^{145,220}. In the sorting manipulation technique, as shown in Figure 2.10a, while without applying external pressure via microvalve, the fluid tends to carry droplets to the upper chamber due to its lower resistance, actuating the valve blocks the upper chamber and deflects the droplet to the lower chamber with higher resistance²⁰⁸. A similar trend has successfully been tested for sorting droplets approaching the

bifurcation Y-junction (Figure 2.10c)²⁰⁹. Single-layer valves also showed their excellent ability to guide droplets to the different subchannels which branches from one main channel with thin PDMS walls in between them. Regulating the relative pressure between two different microactuators can block all subchannels except one, which gives droplets no choice but to flow to the targeted subchannel (Figure 2.10b)²¹⁵.

Although sorting and generation of microdroplets were investigated sufficiently by using a single layer valve as an actuator, there was only one study found in the literature, which focused on the merging manipulation technique in spite of its importance in making a combination of droplets for on chip reactions. Hydrodynamically controlling the pressure on the sides of two parallel channels by using two single-layer valves successfully resulted in merging of two or three droplets. Pillar arrays were placed between the main and side channels to give researchers the capability to decrease the flow rate and trap droplets for the purpose of merging. While the valve which is placed close to the main channel controls the velocity of droplets, the space between the droplets and the number of trapped and finally merged droplets were a function of the pressure differences between two valves during the actuation (Figure 2.10e)²¹⁸.

Despite the significance of droplet splitting in high throughput screening, only one work was found in the literature review, which successfully reported the single-layer microvalve's ability on the splitting mechanism of droplets as depicted in Figure 2.10f. When valves are turned off, symmetric splitting is observed due to the same hydrodynamic resistance of two daughter channels branched from the main channel at the Y-junction. Applying pressure to one of the valves actuates the membrane and increases the resistance of the connected subchannel. Therefore, the size of the daughter droplet decreased in that branch. The more deformation is imposed by one of the microvalves, a larger difference is observed between the resistance of two daughter channels and the size of two daughter droplets. Results obtained from the experiments showed that the relative size of daughter droplets is a function of the main flow rate, pressure difference between two valves and the relative size of subchannels and microvalves. Although the high-pressure injection into one of the microvalves cannot completely seal off the affected microchannel due to its rectangular shape, it can completely divert the droplet to the other branch. Therefore, the presented design has the high efficiency for both splitting and sorting of microdroplets as shown in Figure 2.10d,²¹⁹. However, selectivity (here meaning the splitting of only the targeted droplet), which is one of the most

important challenges in the microfluidic world using droplet manipulation techniques couldn't be achieved in their work which remains a research gap, and the topic of this PhD study.

2.7. Droplet Microfluidics for On-chip Reactions and High Throughput Screening

One of the most important applications of the multidisciplinary science of droplet microfluidics is in the field of pharmaceutical science^{221,222}. Pharmaceutical companies mostly benefit from drug and vaccine discovery, delivery and screening research by means of High Throughput Screening (HTS). This technology enables testing of different compounds, chemicals, antibodies or reagents in different concentrations on a patient's diseased cells or organs so as to search for a positive reaction between them. In these types of experiments usually a giant matrix of possible combinations of the drug is experimented and applied on cells which are infected with cancer, diabetes, HIV, kidney or other diseases²²³. Rather too much time, energy and money need to be consumed to fully test such a large matrix of combinations to extract the unique array with the specific combination as a final product which can be either a drug or a vaccine. Routinely, plates that consist of a matrix of wells and reagents are used for HTS reaction. Ingredients are transferred to the plates by pipetting robots that are integrated to robotic arms. Bulky and high-priced equipment that needs to be used in HTS, led researchers to think about miniaturization. Maximizing the number of tests per sample, enhancing the reliability of HTS and optimising the total cost of equipment can be achieved by reducing the volumes of ingredients when miniaturisation is applied for HTS²²⁴. Faster heat and mass transfer result in easier regulation of the compound's temperature and its concentration in smaller samples²²⁵. Finally, improved detection sensitivity is achieved due to less background noise. Despite all these advantages, miniaturized microliter systems have limitations due to the relatively low accuracy of robotic pipetting equipment and evaporation that occurs in these open systems^{226,227}.

These disadvantages of miniaturised HTS techniques can be minimised effectively by using droplet microfluidic devices in which chemicals, cells and reagents are usually encapsulated in picolitre droplets in an immiscible fluid (for instance, the diseased cell or big molecules like graphene oxides or carbon nanotubes can be trapped in water droplets as a dispersed phase, which is usually made within an oil carrier continuous phase). These closed systems offer

single cell analysis capabilities at increased throughputs and lower costs due to the inherent nature of miniaturization process. There is no evaporation problem in these enclosed systems^{23,228}. Also, since the system is static, there is no concern about accuracy of moving equipment and having a pipetting error²²⁸. However, the selective combination of multiple samples which is required in HTS still remains elusive. This means that one reaction between two different sample types, happens several times in these systems because of the similarity of droplets in each channel before any merging and mixing occurs. Therefore, the major issue in droplet microfluidic-based HTS systems is the ordered formation of a droplet matrix which needs selectivity in manipulation techniques.

Some researchers have previously made their best effort to solve this long-lasting problem. A 1 by n vector of droplets was formed by incorporating parallel channels within a multi-layered microfluidic device to form different concentrations in produced droplets^{229,230}. A new robot system so-called Serial Sample Loading (SSL) platform was recently used to shift the inlet of the microdevice so that the droplets of desired chemical contents could be siphoned through a well-controlled process^{231,232}. On the first attempt to form an m by n matrix of droplets, the custom-designed SSL platform was used to generate the primary vector of microdroplets. Then, multi-layer valve's actuation resulted in a reaction between the droplets of this vector with another set of droplets which was provided from multiple secondary inlets. As a result, the matrix of microdroplets was produced²³¹. As another good example, a Polyether Ether Ketone (PEEK) cross, was used to collect different droplet streams into a single container. Then, a matrix of microdroplets was produced by merging different types of droplets distributed in a vessel with a primary vector of droplets created by an SSL platform²³³.

While these pioneering works have been vital to improve on-chip HTS, they cannot be easily implemented to trace and analyse the products generated from merging of distinct libraries of reagents reacting with distinct sample sets. Besides, they are far away from commercialization due to their slow and uncontrollable working procedure. Hence, one of the aims in this PhD project is to offer a method that has the capability of dispensing the correct chemicals in a definable sequence of locations, allowing many controllable reaction permutations. At the first step, it will be necessary to have an accurate control in different droplet production and manipulation techniques on a single chip²³⁴⁻²³⁸. Among all different manipulation techniques, it seems that droplet generating, splitting and merging are the most desired ones that should cooperate with each other to form a combinatorial library for on-chip reactions. The aim of this

PhD project is to incorporate single-layer valve capability with all these manipulation methods to achieve the desired matrix of products from different ingredients at different concentrations with higher speed and selectivity in comparison to previous studies. This integration is an important step towards commercialisation of on-chip high throughput reaction and screening.

2.8. Droplet Microfluidics for Single Cell Biology Study

Microfluidics has shown promise in life science applications, particularly for manipulating, capturing and analyzing cells at the single cell level, as the basic units of life^{15,239}. Conventionally in cell biology, to study a particular cell behaviour, a collection of cells is cultured in the same condition which is suitable for their growth, and then that behaviour is statistically calculated by taking an average between dozens of data extracted from the population of individual cells. However, it was proven that, this method can only resolve the cell behaviour at the population level and fails to fully capture critical details and unique characteristics of cells at the single cell level – an important consideration when studying rare cells and minority sub-populations of cells^{240,241}. These drawbacks encouraged researchers to look for a substitution for the traditional methods to study cell biology, especially when analysis of cell-to-cell heterogeneity and disclosing the hidden subpopulations of cells is important²⁴². As a simple example, the variation of rare tumour cells behaviour from the average behaviour of the group of cells is of great interest in cancer research and drug development^{243,244}, which necessitate the use of new methods including microfluidics^{245,246} for single cell culture^{9,247}, isolation²⁴⁸⁻²⁵⁰, manipulation²⁵¹ and analysis^{252,253}.

Microdroplets is well suited for biological single cell analysis⁹⁵ as the size of individual diseased cells in the human body and the drug molecules needed to cure them are usually in the order of microns²⁵⁴. Droplet microfluidics which involves the use of continuous and dispersed fluid phases, such that the dispersed phase forms droplets within the continuous phase can be used to make these microdroplets for *in vitro* studies. This compartmentalization in droplets with volumes as small as picolitre (1 pL to 10 nL), and within which evaporation does not occur,²³ has proven to be an advanced and high throughput approach for understanding the behaviour of microscopic live microorganism^{255,256} and single cell analysis^{95,257,258}.

To have the high efficiency in high throughput single cell analysis and manipulation, each produced droplet should encapsulate only one single cell. To achieve this, none of the droplets should contain either zero or more than one cell. In a sample containing suspended matter, the number of particulate matter per droplet is stochastic and described by Poisson statistics²⁵⁹. But, the number of droplets containing only a single cell or efficiency of encapsulation, can be maximized by (i) matching the criteria of one cell per volume of generated droplet with the concentration of the sample flow, (ii) using different hydrodynamic approach²⁶⁰, or (iii) playing with the geometry of channel²⁶¹⁻²⁶³. However, with these traditional methods, encapsulation efficiency never reaches more than 80%. Entrapment of one live cell in one droplet in a closed droplet microfluidic system reduces the sample contamination, maintains the viability and enables droplet microfluidic as an excellent test tube to study antibody secretion and/or digital polymerase chain reactions^{95,264}. Recently, the newly introduced method of microgel technology showed its high capability in the improvement of encapsulation efficiency to more than 90%. Here, instead of water, hydrogel is used as a dispersed phase and then hydrogel droplets are emulsified by a dispersed phase (oil and biocompatible surfactant) and being cross-linked to form microgels^{265,266}.

Integration of cell encapsulation technologies with droplet generation and manipulation technologies gives researchers a great chance for single cell manipulation and analysis²⁵¹ including single cell nucleic acid sequencing^{267,268}, single cell metabolite analysis^{269,270} and single cell protein detection^{24,271,272}. Besides, additionally maintaining good cell viability over of 9 and 2 hours for TCR T cells²⁹ and zebrafish²⁸ after the transportation and sorting of cells using microdroplets respectively, shows the ability of droplet microfluidic to handle both very small cells^{29,273} and also larger organisms^{28,274,275} in the broad range of 5-500 micrometer.

The possibility of studying and analysing individual cells in droplet microfluidics provides a promising opportunity to study natural fertilization as one of the most unique biological phenomena that happens at the single cell level and as a result of sperm interactions with micro-curvatures of the female fallopian tube²⁷⁶ – a research gap which is the topic of this PhD study. The last project of this PhD thesis is about the role of the interface curvature on sperm behavior using droplet microfluidics. Sperm motility is crucial to natural fertilisation, where sperm has to travel thousands of body lengths to reach the egg¹³. The geometry of the fallopian tube is highly confined with lots of curved surfaces that can guide the sperm to the site of fertilisation. The distance between the folded lumens in the fallopian tube is as small as 100 μm ²⁷⁷. When

the sperm penetrates deeper inside the fallopian tube into isthmus, ampulla and infundibulum, these surfaces become narrower and more complicated. Sperm interactions with the microconfined structures was studied before,²⁷⁸; however, sperm motility at soft and curved interfaces that represents the in vivo environment is still unexplored. Here, for the first time, the interaction mechanisms of sperm with soft curved interfaces is resolved and quantified using droplet microfluidics. Enabled through the integration of droplet generation and cell encapsulation techniques, the results of the last main chapter of this PhD thesis can bring new insights into the biophysics of sperm migration through the female reproductive tract.

2.9. Conclusion and Research Aims

As mentioned in the introduction and supported by the critical literature review, there is no successful work found in the literature to make a matrix of droplets with sufficient speed, functionality and controllability that can be integrated onto a commercialized microchip. Therefore, the ordered formation of an m by n matrix of droplets is still the main challenge among droplet microfluidic researchers. In theory, it seems that with consecutive implementing introduced droplet manipulation techniques – generating, splitting and merging - in an innovative design, this long-lasting unsolved problem can be solved. This proposed device may be a right successor for the first generation of droplet matrix generators which were previously introduced^{231,233}. No work in the literature has used pneumatic single layer valves to integrate generating, splitting and merging in one microchip. In the next two chapters of this PhD project, it will be demonstrated that the single-layer valve can be one of the best choices among different active methods for selective generating, splitting and merging of microdroplets. Here, some parameters of these manipulation techniques, including response time, selectivity and durability, are aimed to be improved by using the single-layer valve technology due to its simplicity in design and ease of fabrication. Since each of the generated microdroplets can provide an isolated environment for chemicals and reagents, this device with generating, splitting and merging abilities can be regarded as a starting point for the new generation of miniaturized lab-on-a-chip devices with the selectivity capability for on chip reaction in different concentrations.

Apart from the abovementioned research goals in the previous paragraph, high-throughput droplet manipulation techniques that are developed in this PhD are used for single cell biology

and sperm study. The female fallopian tube is covered with highly folded and convoluted epithelial tissue with confined lumens narrowing towards the egg^{277,279}. However, how this increasing geometrical complexity and subsequent hydrodynamic effects regulate sperm behaviour is poorly understood. Sperm motion and accumulation on flat solid surfaces have been studied extensively over the past decade¹³, resulting in an improved fundamental understanding of sperm motion and demonstrating new opportunities for high-quality sperm selection. However, understanding sperm behaviour at soft curved interfaces, relevant to the in vivo environment which is key to understanding sperm attachment/detachment mechanisms in the female fallopian tube and the role of tract geometry on promoting sperm capacitation and fertilisation ability, as the sperm cell approaches the egg, still remains unknown. To begin to understand this challenge, using droplet microfluidics generation and encapsulation techniques, sperm behaviour at soft curved interfaces ranging in radius from 30 to 140 μm – a range relevant to the in vivo environment will be studied in the last main chapter of this PhD project.

Chapter 3

Selective Droplet Splitting Using Single Layer Microfluidic Valves

3.1. Preface for Chapter 3

Droplet microfluidics, with its small-scale isolated samples, offers huge potential in the further miniaturisation of high throughput screening. The challenge is to deliver multiple samples in a manner such that reactions can be performed in numerous permutations. In this chapter, we investigate the use of single layer valves to break up individual droplets selectively. This splitting of large droplets, allows the main sample volume to navigate around the chip, with smaller daughter droplets being removed at desired locations. As such, the mother droplet is no longer an isolated sample akin to an on-chip test tube, but rather a mobile sample delivery system akin to an on-chip pipette. The partitioning takes place at the entrance to a bypass loop of the main channel. Under normal operating conditions the droplet passes the entrance intact, however, when a valve located at the entrance to the bypass loop is actuated, the geometry changes causes the droplet to split. In this chapter, we analyse this transition in behaviour for a range of oil and water inlets, and valve actuation pressures, showing that the valve can be actuated such that the next droplet to pass the bypass loop will be split, but subsequent droplets will not be.

This chapter was published as a journal article in *Sensors and Actuators B: Chemical* and reproduced from ref. 16 with permission from Elsevier. Copyright © 2020 Elsevier²². The candidate was the first author in this work and played the primary role in designing the research, performing the experiments, analysing the data, and writing the paper. Additional authors for the work include Mr. Sagar N Agnihotri, Dr. Muhsincan Sesen, Prof. Rajneesh Bhardwaj, and Prof. Adrian Neild. Their contributions were central to the publication of this work and are gratefully acknowledged and appreciated.

Furthermore, the candidate presented the results of this work in the 23rd International Conference on Miniaturized Systems for Chemistry and Life Sciences in Basel, Switzerland in October 2019, and was awarded the MicroTAS 2019 Travel Grant by the Applied Sciences (MDPI) and the Chemical and Biological Microsystems Society.

Two additional contributions were inspired by the idea of this work. The first work was published in *Physical Review Applied* for which the candidate was the second author; this work is included in Appendix I⁴⁰. The second work was published in the journal of *Langmuir* and the candidate was the second author for this work; this work is included in Appendix II⁴¹.

The work that is introduced in this chapter is further developed in the next chapters of this thesis. This work lies in the intersection of two fields of microfluidics; droplet microfluidics splitting techniques and microvalves. This new droplet splitting system is easy to fabricate and operate since it uses single layer microvalves that make it ideal for integration with other droplet manipulation techniques. In the next chapter it will be demonstrated that the integration of the valve induced selective splitting that is introduced here with two other manipulation techniques can lead to controlled droplet interaction. A short review of droplet fission and microvalves, and the working principle of the proposed device are presented in this chapter followed by a detailed analysis of experimental results, discussion, methodology and supplementary information.

3.2. Introduction

Droplet microfluidics are enclosed systems in which two immiscible phases are used, such that samples and reagents can be encapsulated in picolitre droplets within a continuous buffer where evaporation does not occur²³. This partitioning of samples into isolated droplets, the lab-on-a-chip equivalent of a micro well plate, has been widely used for single cell analysis²⁸⁰. Single cells can be captured and analysed in such microenvironments, allowing information to be gathered at the individual cell level across a whole population of cells. Other applications include nanoparticle production²⁸¹, creating micro structures for drug delivery vessels²⁸², and conducting high throughput screening^{23,229}. The latter, would allow a new platform for conducting the type of combinatorial library reactions currently performed using microtiter plates. Here, banks of reagents are reacted with each other in numerous permutations, however, the plates cannot undergo further miniaturisation due to issues with pipette dispensing accuracy and evaporation^{226,283}. Two phase droplet microfluidics provides an evaporation free environment so picolitres can be handled²³. However, there are challenges around dispensing, or more specifically, the delivery of small sample volumes such that different chemicals can be reacted together in the desired combinations⁸⁰.

The standard, passive tools for droplet microfluidics, such as droplet generation at channel junctions cause the same behaviour to occur repeatedly, for example, the partition of a sample flow into multiple droplets when merged with an immiscible buffer flow at a T-junction³². However, for the selective combination of multiple samples in different permutations, the

challenge is to direct different samples to different locations at will so that an ordered matrix of droplets can be formed. Whilst there have been considerable successes in this direction^{229,230,232}, there is still a need to develop improved methods to actively interact with single fluid samples to create^{32,66,284-286}, merge^{42,43,287,288} or divide^{173,175,289,290} a droplet when desired.

The introduction of different samples onto a chip in relatively large volumes has been achieved by mechanical movement of the inlet connected to the channel between sample reservoirs²³². The ability to halve or divide these plugs into daughter droplets would allow the controlled delivery of each sample into certain locations around a fluidic network. The ability to selectively subdivide becomes analogous to pipetting and dispensing from a well plate to another¹⁷⁵, when combined with droplet merging mechanism, permutations of reactions can be performed from a library of samples.

A symmetric breaking-up of droplets, i.e. into two equal volumes, is desirable when splitting is used to increase the production rate of droplets, maximize the capacity of the device, or produce one set of equal size droplet for a control experiment^{19,150}. However, when a controllable volume or concentration of chemicals inside the droplet is required in pharmaceutical or chemical industries, an asymmetric breaking up of droplets is required¹⁵⁴. Methods for performing droplet splitting can be categorized into passive, active and combined methods.

Passive manipulation techniques utilize interactive effects between dispersed phase, continuous phase and channel structures without using any external fields. Methods include using a narrow orifice in a flow focusing junction which can cause the splitting of a plug into much smaller droplets⁵⁸, the addition of a mid-channel obstacle¹⁵⁷ or bifurcating the channel^{157,165}, as such, it can be seen that passive droplet splitting techniques need to simply be designed into the geometry of the chip, however, they act equally on all droplets without the possibility of selectivity.

A degree of control can be gained by the addition of active mechanisms to these passive geometric features. For example by adding an electrical field at a simple bifurcating junction can alter the relative size of the daughter droplets created¹¹⁵. Other methods include the use of electrostatic potential wells, a laser¹²⁵ or micro-heaters¹⁶⁸. Whilst these methods improve the controllability of daughter droplet size there are some potential issues with biocompatibility.

Other methods have used Electrowetting-on-Dielectric (EWOD) and Dielectrowetting to control the splitting in a bifurcation through contact line control^{170,291} and surface acoustic waves (SAW) which have been used to apply forces on the interface between the immiscible fluids to split and steer droplets^{173,174,289}. Finally, the droplet as pipette concept has been shown by altering the flow field locally at a bifurcation using acoustic streaming created by surface acoustic waves, this allows the splitting of a droplet¹⁷⁵. While SAW is more versatile and bio-compatible than other active methods for fission, the cost and complexity of operational instruments make it worthwhile to search for an alternative active method for droplet splitting. Another problem with SAW devices is that the speed of splitting of droplets is limited by the weak forces which can be generated. To address these issues here, we present an alternative method, using pneumatic valves, which is of more reasonable cost and 20 times faster.

Microvalves fabricated in deformable, multilayer, PDMS structures have been used to control on-chip fluid flows since their conception¹⁹⁸. These pneumatic valves offer simplicity, ease of fabrication, high-power density, bio-compatibility and versatility^{195,292}, and multiple valves can be controlled independently and simultaneously¹⁹⁷. Their ability to control fluid behaviour has also meant they have been applied to two phase systems; generating^{199,200}, sorting⁵⁰ and merging²⁰⁰ has been achieved. In most cases, the deformation of the channel geometry caused by valve operation causes a number of droplets to demonstrate altered behaviour, whether that is droplet size upon generation or toggling between merging and non-merging events. This is also the case for a previous study on multilayer valve usage for control of droplet splitting¹⁹⁹, in which the size of batches of daughter droplets was controlled.

In addition to multilayer valves, a simpler single layer valve (horizontal valve) design has been developed^{206,207}, this design incorporates the control and flow channels on one layer of PDMS, separated by a thin, and therefore deformable, membrane. These valves have been used for droplet formation¹⁴⁵, sorting^{208,209}, merging²¹⁸ and splitting²¹⁹. In the latter, it was shown that the size of two daughter droplets could be tuned by the relative actuation of two valves at the exits of a Y-junction. In both the previous studies on droplet splitting, using double¹⁹⁹ or single²¹⁹ layer valves, the emphasis has been on the repetition of multiple events, such that all droplets passing through a junction are split in the same way. Besides, a large deformation, potentially reducing device durability by causing inaccuracies or even channel damage⁴⁸, was required to steer all droplets to a waste outlet with no ability to split selectively²¹⁹. Rather than looking at the steady state condition²¹⁹, here, we examine the transient case, and study what

happens at the onset of valve actuation, with the interest in causing selective droplet splitting, targeting an individual droplet. Our system works close to the transition regime where a slight change in pressure induced by the valve can initiate splitting thereby improving device durability by preventing channel damage.

It is possible to introduce mother droplets into a microfluidic system in which each contain different chemicals. Our motivation is to develop a method through which these mother droplets can be selectively split. By doing this, we establish a way in which small samples of selected reagents can be delivered to sites at which reactions can take place. The inclusion of multiple such reaction sites would allow multiple permutations of reactions to take place, just as takes place in a microwell plate at a much larger scale. To establish this selective splitting capability, we study a simplified system, one in which each mother droplet contains the same sample, and in which the daughter droplets are not merged together; what we focus on is the selective nature of droplet splitting. That is, we examine the actuation conditions which ensure the first droplet after actuation is split. The valves are used to alter the geometry of the system at the site of entry into a bypass channel, the deformation allows the transient transition between non-splitting and splitting events, so demonstrating, under the identified operating conditions, the selectivity of our approach.

3.3. Working Principle

The microchannel network consists of components for droplet generation and droplet splitting section (see Figure 3.6 for more details). It is envisaged that for future usage of the splitting technology we have developed, each droplet will be of a different chemical, produced by moving a nozzle between samples off chip²³², or by individual droplet formation²²⁹. However, for this system, designed to test the capability of the splitting technology, a standard droplet generation approach was taken, and this consists of a T-junction, fed by oil and water. The width of both the continuous and dispersed inlet channels is $100\ \mu\text{m}$ with a height of $133.8\ \mu\text{m}$, the result is monodisperse, high throughput droplet generation³². Once the droplets are formed on the chip, the next feature is the bypass channel at which we seek to demonstrate selective droplet subdivision. This division part as shown in Figure 3.1a, consists of the main channel bifurcating at a standard T-junction, where the width of the secondary channel is half that of the main channel. This asymmetry in channel dimensions makes it possible to have different

regimes of splitting without the actuation of the valve which is located at this junction. The effect of the ratio of the width of the bypass channel to the main channel from value 0.35 to 0.91 on the splitting regimes of droplets and size of daughter droplets was well studied recently. As the ratio of the bypass channel to the main channel was increased, the regime was shifted from the non-splitting to the splitting and further increase in this ratio, caused larger finger to penetrate into the bypass channel and larger daughter droplets to split from the mother droplets. The knife edge that separates, splitting and non-splitting regime at different ratio of width of the bypass channel to main channel was examined in that study. Taking the ratio of the width of the bypass channel to the main channel as 0.5, the bypass system is operated at the knife edge between a splitting and non-splitting condition and the valve can be activated selectively in order to tip the balance in favour of the splitting event⁴⁰. The thinner branched channel subsequently rejoins the main channel; hence we term it a bypass loop. In future, we envisage that reactions of daughter droplets split from mother droplets containing different chemicals will take place within this bypass loop by use of standard merging techniques⁴³.

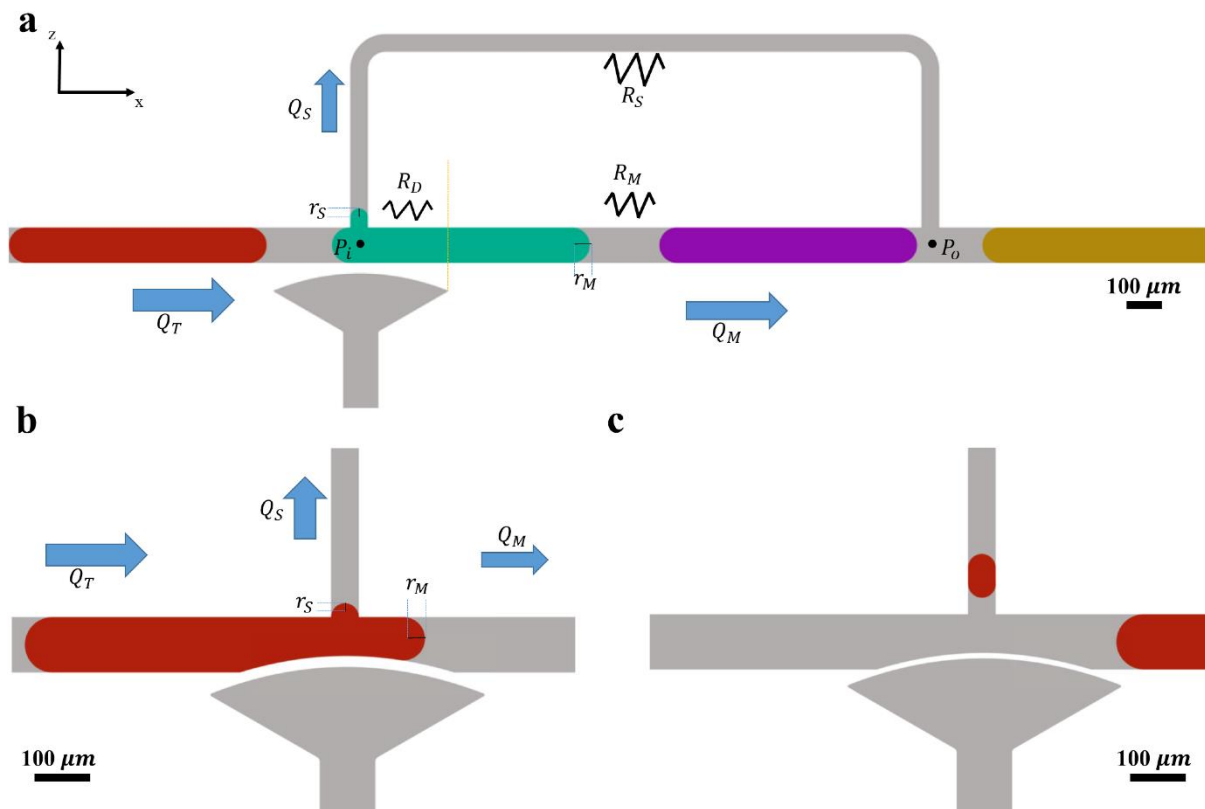


Figure 3.1. Depiction of the selective droplet partitioning system. (a) Mother droplets are produced in a T-junction and passes the entrance of the bypass loop when the valve is off. Non-splitting regime dominates under these conditions. (b) The valve is actuated which results in deforming the channel wall and guiding more fluid into the secondary channel. The finger length increases as a result of changing in flow resistance and curvature of the front of the droplet. (c) Under these conditions the mother droplet passes along the main channel after splitting has occurred.

Double^{50,197-200,292} and single^{145,206-209} layer valve design have been described in the literature. Here, we do not need to fully seal the valve, rather just alter the channel geometry, hence a single layer valve is ideal. In this type of valve, a membrane, consisting of a thin layer of soft PDMS, is located in a vertical plane between the main channel and a valve actuation chamber. Once pressurised, the valve actuation chamber causes the membrane to deform into the main channel, hence changing the channels physical geometry. After running and analysing a series of experiments, a mushroom-shaped valve (with 500 μm length of the head) with membrane thickness 30 μm was selected with a PDMS mix ratio of 20:1.

The microfluidic chip design as can be seen in Figure 3.1a, consists of the main and secondary channels. The hydrodynamic resistance and the pressure drop of a rectangular channel can be calculated by the equations below²⁹³,

$$R = \frac{12\mu L}{\omega h^3 \left[1 - 0.63\left(\frac{h}{\omega}\right)\right]} \quad (3.1)$$

$$\Delta P = RQ \quad (3.2)$$

where, ω , h and L denote width, height and length of the rectangular channel, respectively. In addition, Q , R and ΔP represent flow rate, resistance and pressure drop. So, in our design, the narrower and longer secondary channel (subscript S) has higher resistance and lower flow rate rather than the main channel (subscript M) due to the equality in differences between the pressure of the inlet (P_i) and pressure of the outlet (P_o) of the loop.

$$P_o - P_i = \Delta P_M = \Delta P_S \quad (3.3)$$

Based on the fact that for a series resistance network, the total resistance equals the sum of the individual resistances and by applying equation (3.2) into equation (3.3):

$$(R_D + R_M)Q_M = R_S Q_S \quad (3.4)$$

where, the subscript D denotes the resistance passes the deformable valve. In addition, mass conservation of the fluid gives:

$$Q_T = Q_M + Q_S \quad (3.5)$$

where, Q_T denotes the total flow.

By applying equation (3.4) into equation (3.5), equation (3.6) derives as:

$$Q_S = Q_T \left[1 + (R_S / (R_D + R_M))\right]^{-1} \quad (3.6)$$

In the absence of the droplet and before valve actuation, the pressure balance between the main and the high resistance secondary channel ensures that most of the flow passes through the main channel. Based on equation (3.1), actuating the valve decreases the width of the entrance of the loop and so increases the hydrodynamic resistance of the deformable part of the main channel, R_D . This causes more fluid to pass via the secondary channel.

When two different phases are present in the microfluidic channel, additional pressure changes occur over the interfaces between continuous and dispersed phases due to the surface tension²⁹⁴.

$$\Delta P = RQ + 2\gamma H \quad (3.7)$$

where, γ and H are the interfacial tension between the two phases and mean curvature of the interface, respectively. The mean curvature of interface is the inverse of radius of curvature based on Young-Laplace equation^{99,294}.

By substituting equation (3.7) in equation (3.3), equation (3.8) derives as:

$$(R_D + R_M)Q_M + 2\gamma H_M = R_S Q_S + 2\gamma H_S \quad (3.8)$$

where, $H_M = 1/r_M$ and $H_S = 1/r_S$. r_M and r_S are the radius of the front interface of the mother droplet and the radius of the interface of finger, respectively (Figure 3.1a,b). Finally, replacing equation (3.8) in equation (3.5) results in:

$$Q_S = (Q_T - [2\gamma(H_S - H_M)])[1 + (R_S/(R_D + R_M))]^{-1} \quad (3.9)$$

Hence, in the presence of droplets, upon actuation of the valve two effects promote a higher flow rate in the bypass channel. These are the change in flow resistance and the change in the curvature of the front of the droplet. In the latter, as the droplet passes the constriction the curvature of the front interface in the main channel, H_M is increased (Figure 3.1b). To confirm this, Figure 3.7a shows the results of the numerical analysis for the system operating at Oil Pressure = 400 mbar and Water Pressure = 500 mbar at different time instances. We placed a constriction, similar in size to the operating valve, opposite the entrance to the bypass channel in one model (Figure 3.7b), and opposite its exit in a second model (Figure 3.7c). In the latter, only the flow resistance change will be relevant to the finger length created in the entrance of the bypass channel. Whilst in the former the radius change of the front interface will also play a role. When we plotted the finger length as a function of time in Figure 3.7a, we saw an

increase of 50% in the finger length when the constriction was at the entrance to the bypass for $t_{ij} \cong 0.005s$ confirming the additional effect of the deformed interface of the droplet on finger size.

Under certain flow conditions, when there is no valve actuation, we can expect the droplet to pass along the main channel intact, a finger into the bypass channel will develop, but it will then retract and the droplet will not split. However, when the valve is actuated, we can expect the two effects identified here to increase the flow into the bypass channel, and hence increase the finger length. This gives the possibility of using the valve to move from a non-splitting condition (Figure 3.1a) to a splitting condition (Figure 3.1c) for the droplet.

3.3. Results and discussion

We first explore the operating conditions when the valve is not activated, showing that depending on the inlet pressure of the oil and water phases, the droplets formed may or may not split at the entrance to the bypass channel. In Figure 3.2a the two inlet pressures were varied independently between 0 and 900 mbar; four regimes were observed in the splitting behaviour. *Non-splitting regime* for the case that none of the droplets which passed through the inlet of the loop is split, a *transition regime* in which less than 10% of droplets are split, and *low efficiency splitting regime* (LESR) and *high efficiency splitting regime* (HESR) in which between 10% and 50% and more than 50% of droplets are split, respectively. An increase in water inlet pressure, whilst oil inlet pressure is constant, gives rise to larger mother droplets, as can be seen by comparing Figure 3.2b i and ii. Whilst, at higher oil pressure, and a fixed water pressure, smaller droplets are formed, as shown in Figure 3.2b ii and iii. If the ratio between the pressure in the dispersed and continuous phases is fixed, then the mother droplet size is fixed, this can be seen from Figure 3.2b i and iii, and is also true for Figure 3.2b ii and iv. However, based on the same comparison between Figure 3.2b i and iii, and Figure 3.2b ii and iv, increasing the pressure of inlets while the relative pressure ratio of inlets is kept constant, increases the speed of same sized droplets (from 7300 $\mu\text{m/s}$ for case i to 15600 $\mu\text{m/s}$ for case iii and from 9600 $\mu\text{m/s}$ for case ii to 18300 $\mu\text{m/s}$ for case iv) and decreases the distance between following mother droplets. It should be noted here that whilst the splitting outcome of i and iii is the same (splitting does not occur), this is not true for the latter, case ii does not split, whilst iv does. Clearly, splitting events are not dictated by droplet size alone. In case iv,

daughter droplets are created each time a mother droplet passes the entrance to the bypass, as such multiple droplets are seen in the bypass channel, this gives an indication of the relatively slow speed of fluid motion in the bypass compared to the main channel.

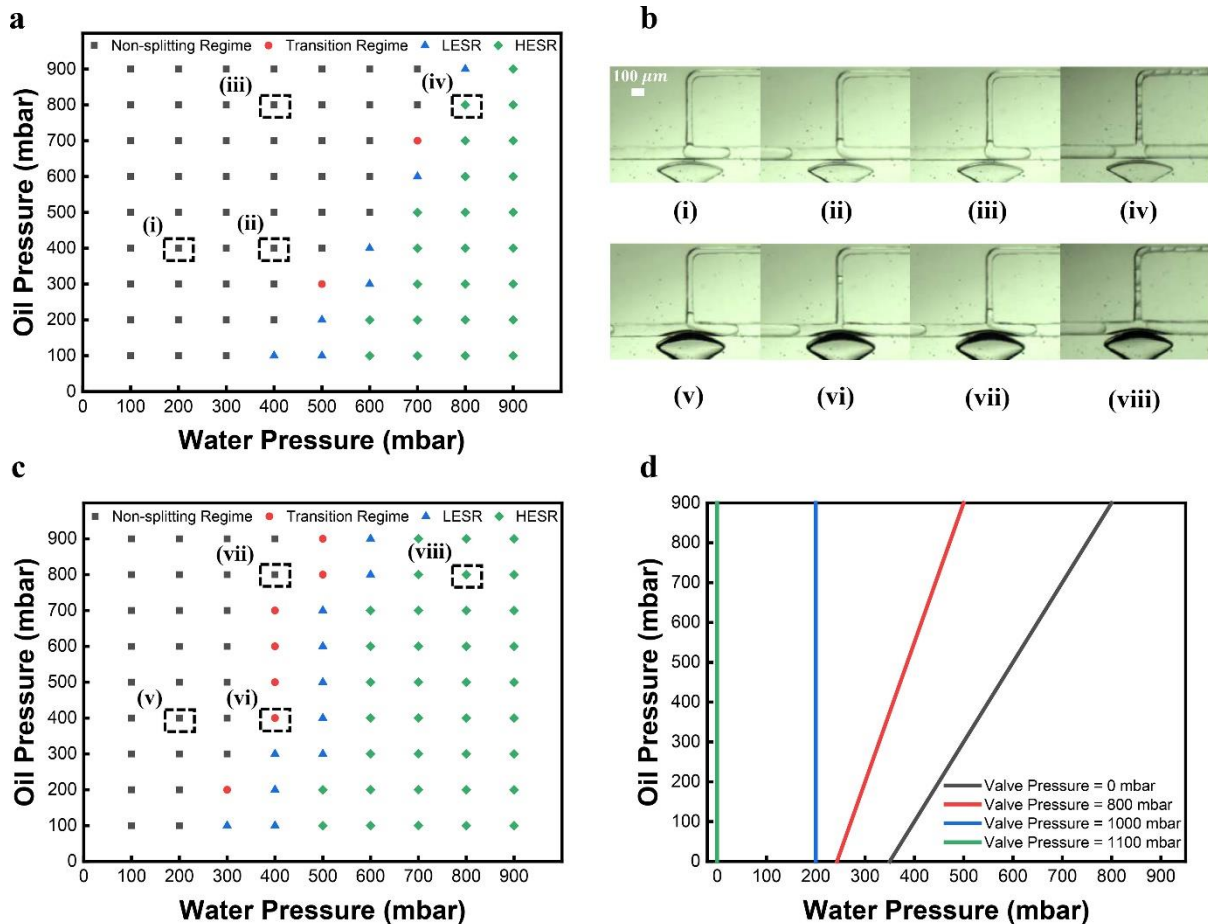


Figure 3.2. Classification of splitting regimes by the frequency and size of mother droplets (a) Regime map shows four splitting regimes in the absence of valve on Oil Pressure-Water Pressure plane; (1) Non-splitting Regime with black square markers (2) Transition Regime with red circle markers (3) LESR (Low efficiency splitting regime) with blue triangle markers (4) HESR (High efficiency splitting regime) with green diamond markers (b) Images show the droplet behaviour in the entrance of bypass loop in the absence (i) - (iv) and presence of 800 mbar activated valve (v) - (viii). (c) Regime map shows four splitting regimes in the presence of activated valve on the pressure of 800 mbar on Oil Pressure-Water Pressure plane. (d) Transient lines follow the transition regions showing the transition from non-splitting to splitting regimes in four different valve pressures; 0 mbar, 800 mbar, 1000 mbar and 1100 mbar.

To explore the effect of the valve, the same pressure ranges are tested for each inlet, however, the valve is also pressurised at 800 mbar. Again, splitting behaviour is characterised using the same four regime descriptions, the results are shown in Figure 3.2c. Here, the transition regime has shifted leftward (towards lower water pressures). What we observe from the experiments

is that in each case, the finger length formed is significantly larger than that of the non-activated valve case. Comparison between Figure 3.2b ii and vi shows that actuating the valve to 800 mbar results in breaking up some of the droplet, whilst for the unactuated valve no splitting was observed. To relate this shift in behaviour to the valve actuation pressure, the data from further experiments with two additional valve pressures have been summarised by simply plotting a line following the transition region for each case in Figure 3.2d. It can be seen that with increasing valve pressure, as the channel constricts further, the transient regime is shifted further towards low water pressures. When a valve pressure of 1100 mbar is used, the droplets are split in all cases. This initial data set clearly shows that we can control the breakup region by actuating the valve.

In Figure 3.2, the regimes are classified by the water pressure and oil pressure, this classification is explored further in Figure 3.8a, in which the valve efficiency is shown as a function of valve pressure for a range of different inlet pressure conditions (the inset shows the location of these conditions on the same axes used in Figure 3.2d). The valve efficiency is defined as the ratio of the number of split droplets in the bypass channel to the total number of droplets that pass the inlet to this loop. In each case, it can be seen that, for a fixed set of inlet conditions, increasing the actuation pressure of the valve increases the efficiency up to 1000 mbar. Above this valve pressure, some of the daughter droplets, that are formed, re-enter the main channel via the entrance of the bypass loop. This seems to occur as the deformation is such that the main channel is narrower than the bypass channel.

The data plotted in Figure 3.8a shows that for the same continuous phase inlet condition (Oil Pressure = 500 mbar), increasing the water pressure increased the valve efficiency, this is because larger mother droplets are formed at the droplet generation T-junction. When these larger mother droplets interact with the entrance to the bypass channel, longer fingers are formed in the entrance and so even in the absence of the valve, they are closer to the condition at which splitting occurs. Hence a small bulge in the valve is required to switch regime, such that splitting occurs. The opposite trend is observed if the oil pressure is increased, whilst the water pressure is kept constant (Water Pressure = 500 mbar). It should be noted here that the efficiency never goes above 67% in the experiments conducted. In the context of splitting every droplet, this would be a poor outcome. However, in the application of selective delivery of individual daughter droplets, the key feature is the repeatability of the splitting of the first droplet. Conceptually, the droplet of interest would be identified, and the valve actuated, what

is desirable is that this, and only this droplet is then split i.e. selective breakup of a droplet. Next, we examine the notion of selectivity in this context.

Specifically, we wish to split the first droplet after actuation, it can be arranged that each droplet contains a different chemical, hence selective splitting gives the ability to pipette specific chemicals into reactions sites. In the absence of valve actuation, the pressure imposed in the inlets of continuous and dispersed phases can be fully controlled and brought near the transition line between non-splitting and splitting, one set of conditions to achieve this are Oil Pressure = 400 mbar and Water Pressure = 500 mbar. Figure 3.9a shows images of operation under these conditions, and demonstrates that increasing the pressure of valve, increases the maximum finger length, such that at a specific valve pressure, here 600 mbar, droplets randomly start to break up (Figure 3.9b). In the case shown, the sixth droplet which passes after valve actuation was split. This breaking up happens during the retreating of the droplet to the main channel and can be considered as a retarded breakup⁹⁹.

Again, this is not desirable when selectivity is of interest. However, if the valve pressure is further increased by between 50-100 mbar and subsequently the width of deformation is increased by 4-8 μm , the result is that the first droplet is split. An example of this repeatable effect is shown in Figure 3.9c. Once the daughter droplet is in the bypass channel, subsequent droplets do not split, so the valve efficiency, as detailed in Fig. Figure 3.8, remains low, but the desired droplet is split. This occurs as the presence of the daughter droplet in the bypass channel causes a change in the pressure balances. This could be rectified by changing the design of the bypass channel, for example, if the droplets are well spaced, then the speed of valve deflation can be slower than the interspacing time between droplets. Figure 3.3a demonstrates this effect over a wider range of conditions, here the valve pressure required to randomly split a droplet is compared to the slightly higher value required to ensure the first droplet during valve actuation is split. It can be seen that the increase required, in the valve pressure, is no more than 100 mbar. Images of droplet behaviour are shown for different cases of valve pressure in Figure 3.3b.

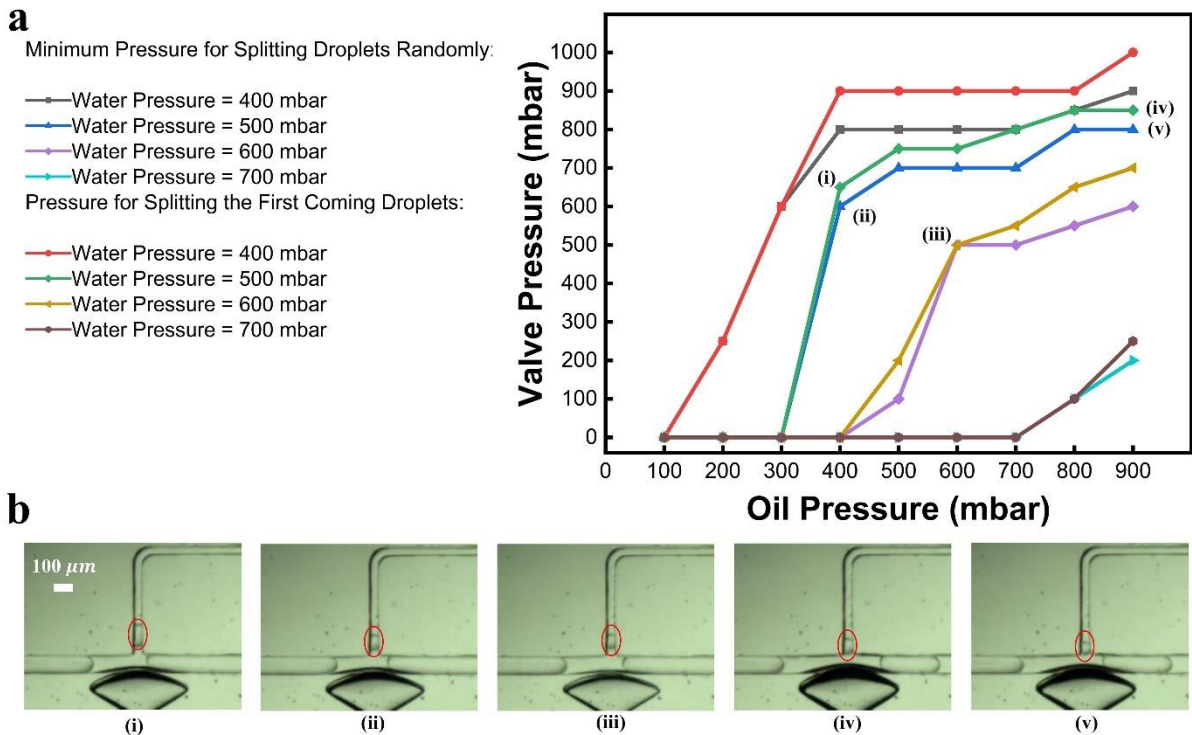


Figure 3.3. (a) Comparison between the pressure which is required to split droplets randomly and the pressure which is needed to split the first coming droplets for different inlet conditions (b) Experimental images for the indicated data points (i) - (v).

To confirm this, Figure 3.10 shows the valve operating at 650 mbar for Oil Pressure = 400 mbar and Water Pressure = 500 mbar at different time instances. The data shows that exactly the first mother droplet which passed the loop during actuation of valve splits, subsequently for the duration of time in which the daughter droplet is in the loop, no further mother droplet splits. This shows that the valve can split targeted droplets, hence is selective, provided the correct actuation pressure is used. In addition, it can be seen that the time response of the valve is around 0.05s which makes it at least 20 times faster than an earlier SAW actuated droplet splitting system¹⁷⁵.

To examine the size of the daughter droplet formed, Figure 3.4a measures the length of the finger drawn into the bypass channel, it can be seen from the range of conditions examined that the length of the finger grows continuously with time as the mother droplets passes the bypass entrance. This occurs with or without valve actuation. Comparison between Figure 3.4a i and ii shows that when valve is actuated with 1000 mbar pressure, the maximum finger size is approximately increased by 135% for these small mother droplets, while for larger mother droplets only 55% increment in size has been observed by comparison between Figure 3.4a iii and v. The corresponding finger lengths are shown in Figure 3.4b.

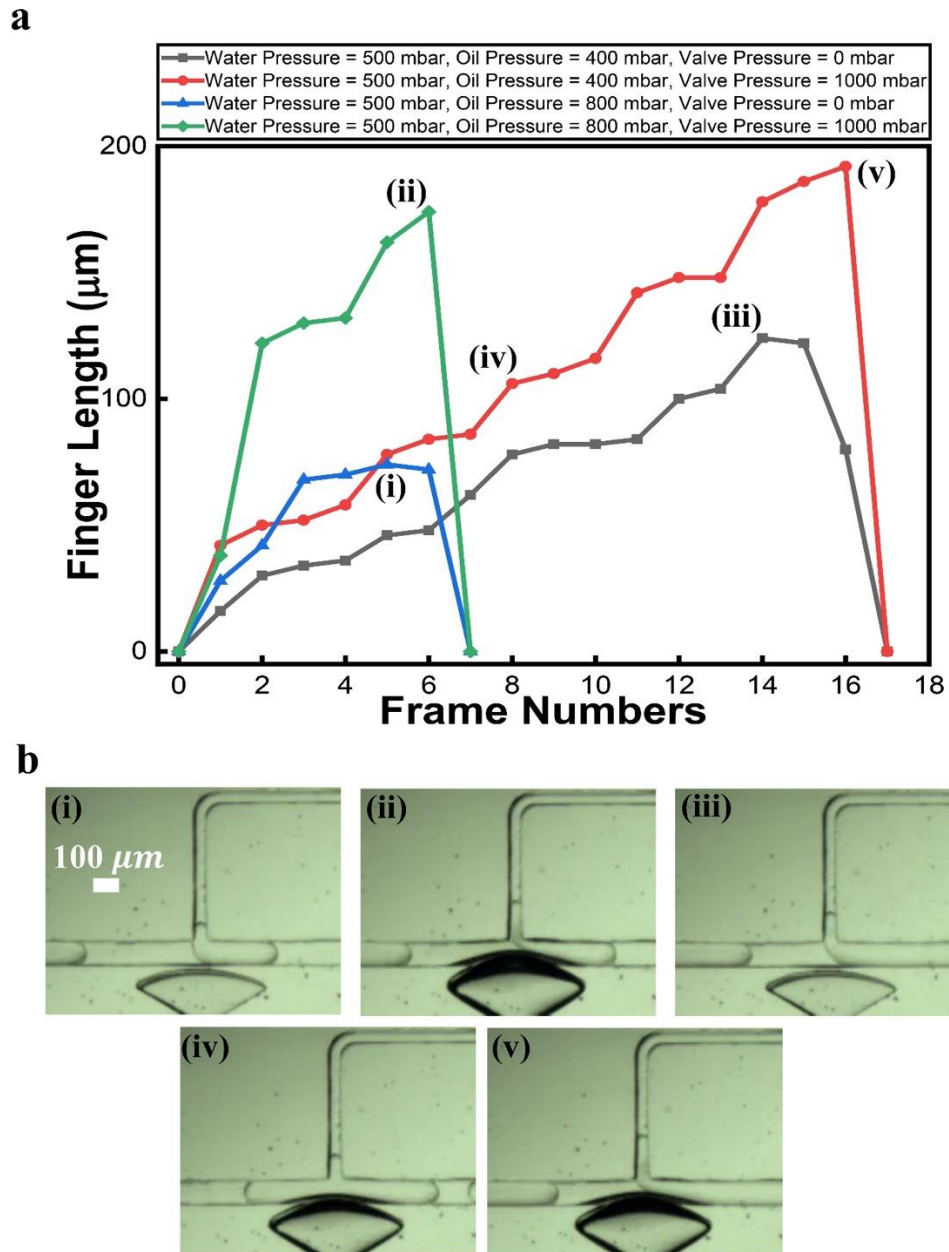


Figure 3.4. Plot shows the finger length as the function of frame numbers for small droplets (Oil Pressure = 800 mbar and Water Pressure = 500 mbar) and large droplets (Oil Pressure = 400 mbar and Water Pressure = 500 mbar) in the absence and presence of the valve that is actuated to 1000 mbar. (b) While in the absence of valve, finger reaches the maximum size of $74 \mu\text{m}$ (i) as valve is actuated finger reaches the maximum size of $174 \mu\text{m}$ (ii) for small droplets. On the other hand, for large droplets maximum finger lengths are $124 \mu\text{m}$ (iv) and $192 \mu\text{m}$ (v) in the absence and presence of actuated valve with the pressure of 1000 mbar.

As a result of this lesser effect on the finger length for the larger droplets, the range of daughter droplet sizes that can be produced are smaller. Figure 3.5a shows the relative volume of daughter droplet to the mother droplet versus the valve pressure for two inlet conditions which produce different mother droplet volumes. The droplet breakup with different relative volumes obtained at different valve pressures, indicated in Figure 3.5a, and predicted by the numerical

simulations shown in Figure 3.5b,c, are shown in Figure 3.5d. It can be seen in Figure 3.5a that the range of relative volume of daughter droplets are up to approximately 10% for larger droplets and 20% for the smaller mother droplets. The maximum ratio is split from the main droplet when valve is working in the optimum pressure of 1000 mbar. This demonstrates that inlet pressures, which control mother droplet volume can be used to set the range of daughter droplet volumes which can be produced. For example, if a narrow range is required which shows little variation with valve pressure, and hence is robust to fluctuations, then longer droplets should be used. Whilst for the ability to dispense droplets of different sizes a shorter mother droplet is desirable.

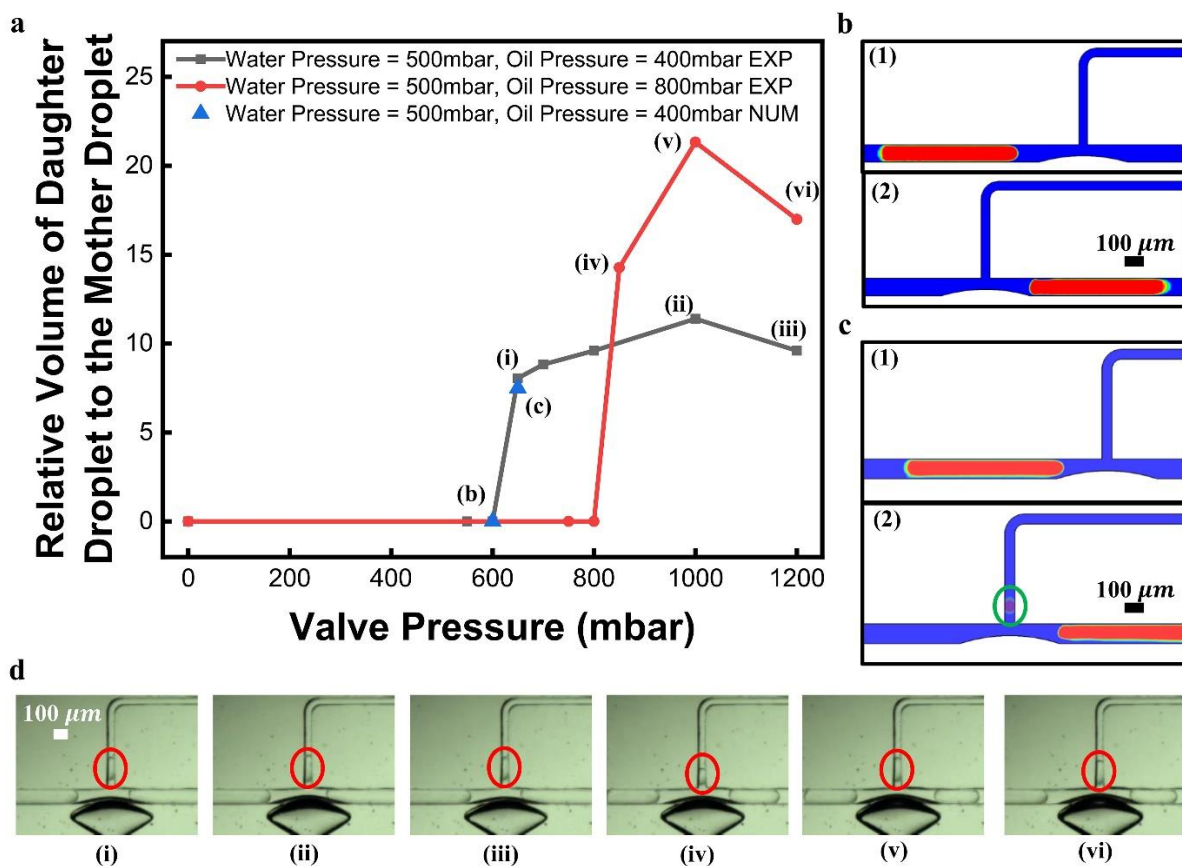


Figure 3.5. Plot shows the relative volume of daughter droplet to the mother droplet for small droplets (Oil Pressure = 800 mbar and Water Pressure = 500 mbar) and large droplets (Oil Pressure = 400 mbar and Water Pressure = 500 mbar). (b) Contours are extracted images from numerical simulation for the Deformation = $36 \mu\text{m}$ related to the Valve Pressure = 600 mbar, (1) before and (2) after of droplet passing the entrance of bypass loop. (c) Two images from numerical simulation are shown, (1) before and (2) after splitting of the mother droplet, this occurs for a deformation of $40 \mu\text{m}$ equivalent to an experimental valve pressure of 650 mbar, results show that 7% and 8% of mother droplet split numerically and experimentally. (d) Experimental images for the indicated data points (i) - (vi).

3.4. Conclusions

As a novel, selective and compact high throughput screening system, our system uses a single layer valve to split droplets on demand. A microfabricated membrane is pressurised to deform precisely which selectively breaks up desired droplets. Control over the pressure of two inlets and one valve simultaneously, gives users the ability to completely dictate the range of droplets that can be produced in the new splitting system. The effect of pressure induced in the valve on the daughter droplet sizes was also numerically investigated which qualitatively validated the trend observed experimentally and the results was used to back up the underlying physics of proposed system. Being cheap, simple, high speed and selective, are some of the advantages of our newly-introduced splitting system. In addition to the biocompatibility of the selective droplet partitioning system, the slight change in pressure induced by the valve, prolongs the device durability and prevents channel damage. When our splitting technique is combined with the traditional merging system, it can be used as a high throughput system for combinatorial library purposes. More studies for the evaluation of the effect of ejected daughter droplets on the pressure in the main and secondary channels needs to be done to show that successive bypass loops can be used as independent units for on demand splitting and merging.

3.5. Methodology

3.5.1. Microfabrication

The microchannels were formed in polydimethylsiloxane (PDMS), using a master mold fabricated by standard lithography, electron beam evaporation and dry etching techniques. To characterizing the valve, PDMS channels with different stiffnesses were prepared by changing the mix ratio. The usual ratio of PDMS is 10 parts (by weight) Dow Corning Sylgard 184 Silicone Elastomer base mixed with 1-part (by weight) Dow Corning Sylgard 184 Silicone Elastomer Curing Agent, however, to form more flexible structures 20:1 and 25:1 were also used, the latter being the limit in terms of room condition curing. After curing, the PDMS was peeled off the silicon mold, access holes for inlets and outlet were punched, and then it was exposed to an air plasma for 18 seconds. It was bonded to a clean glass slide because its surface was activated.

3.5.2. Experimental Set-up

The inlets and outlet of the microfluidic network were connected to a microfluidic flow control system (MFCSTM-EZ, Fluigent system) by using polytetrafluoroethylene (PTFE) tubing. Further tubing connected the inlet of the valve control channel to a second Fluigent system to control the air pressure in the microvalve. Two different Fluigent systems were used in the main and control channels to avoid fluctuation in pressures. A synthetic oil (3MTM NovecTM) was used as a continuous phase in which 2% surfactant (Pico-SurfTM 1, Sphere Fluidics, UK) was added, while Milli-Q water was used as a dispersed phase. A camera (Pixelink PL-B782U, Ottawa, Canada) was mounted on an inverted microscope (Olympus CKX53, Tokyo, Japan) to record videos and images from the chip (see Figure 3.6 for more details).

3.5.3. Image Processing

The recorded images and videos were analysed using a custom code written in MATLAB[®] by the authors. Two successive frames of the videos were used to track the movement of the interface between the continuous and dispersed phases in x direction (with reference to Figure 3.1a) to calculate the mother droplet velocity. The volumes of the mother and daughter droplets were also measured by pixel counting and multiplying the resulting area by the height of channel ($133.8 \mu\text{m}$). The deformation of the channel wall due valve actuation was measured by edge detection.

3.5.4. Numerical Methods

To probe the flow physics of the system, a numerical model was utilized. The simulation used a finite volume method with the PISO (Pressure-implicit with splitting of operators) in ANSYS Fluent[®] v15 to numerically solve the 3D Navier-Stokes equation. In addition, a VOF (Volume-of-Fluid) method was used to trace the liquid-liquid interface and examine the droplet behaviour at the entrance of the microfluidic bypass loop. A mother droplet with the same volume and velocity as those in experiments was placed, initially, upstream of the inlet to the bypass loop. The outlet was set to atmospheric pressure while a no slip boundary condition was imposed on all walls. The continuous phase density and dynamic viscosity were set at 1614 kg m^{-3} and 1.24 mPa s , respectively, while for the dispersed phase these values were selected as 998.2 kg m^{-3} and 1.003 mPa s , respectively. A contact angle of 135° between the two phases at the PDMS wall was extracted from the experimental video frames and used in the simulation.

The surface tension between the continuous and dispersed phases was set to 18.5 mN/m. To numerically simulate the splitting mechanism at the valve, the dimensions of the deformed valves during the experiments was measured by edge detection and imposed in the model as a bulge in the channel wall.

3.6. Supplementary Information

3.6.1. Supplementary Figures

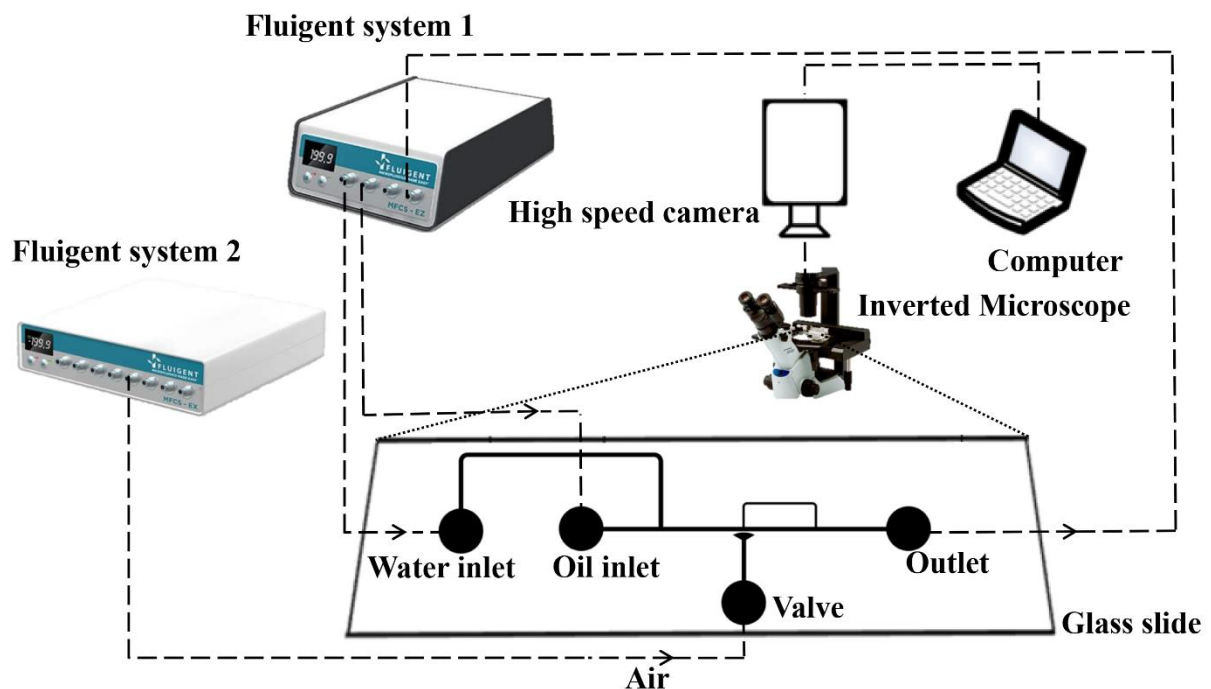


Figure 3.6. Schematic showing the setup used for selective droplet splitting using single layer microfluidic valves. The inlets and outlet of the microfluidic system is connected to a microfluidic flow control system (MFCS™-EZ, Fluigent system); while the inlet of the valve control system is connected to a second Fluigent system to control the air pressure. This setup includes high speed camera, inverted microscope and two fluigent systems. These are connected to a computer for data collection.

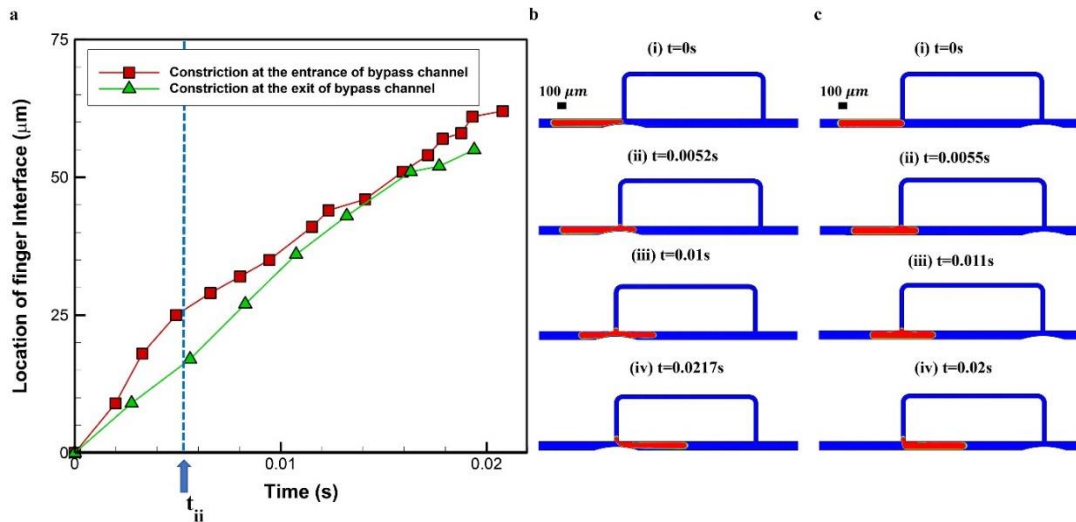


Figure 3.7. The effect of the constriction position on the finger size. The operating conditions of the system are Oil Pressure = 400 mbar, Water Pressure = 500 mbar and Deformation = $36 \mu m$. (a) Plot shows the finger interface vertical location over time comparing the effect of the constriction at the entrance and the constriction at the exit of the bypass channel on the finger size. (b) Contours are extracted images from numerical simulation, when Constriction = $36 \mu m$ is imposed at the entrance of the bypass channel at different time instances. (c) Four images from numerical simulation are shown for a constriction of $36 \mu m$ equivalent to an experimental valve pressure of 600 mbar that is imposed at the exit of the bypass channel.

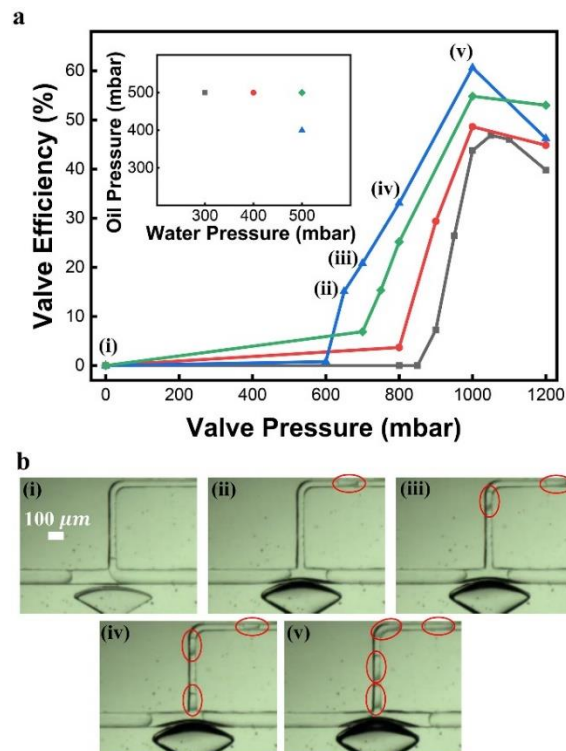


Figure 3.8. The effect of valve pressure on the valve efficiency which is defined as the ratio of the number of split droplets in the bypass channel to the total number of droplets that pass the inlet of bypass loop (a) Four different pairs of oil and water pressures are studied here which is shown in the inset (b) Experimental images (i) - (v) show valve has different efficiencies at different valve pressures for the fixed inlet condition of Oil Pressure = 400 mbar and Water Pressure = 500 mbar.

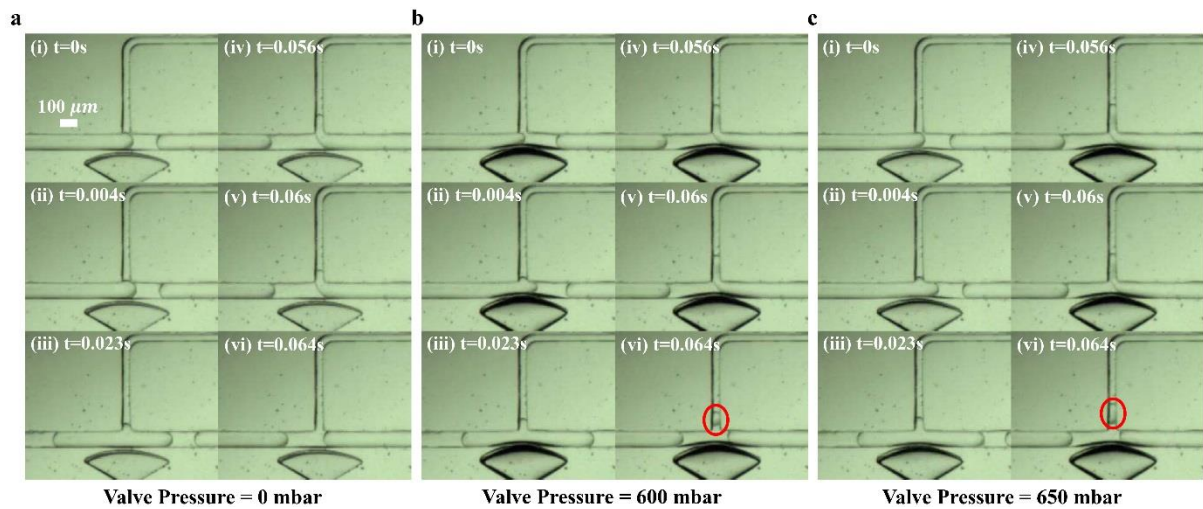


Figure 3.9. Timelapse images of droplet passing the entrance of bypass loop with the constant inlet conditions of Oil Pressure = 400 mbar and Water Pressure = 500 mbar (a) In the absence of actuated valve (b) After the valve is actuated to the pressure of 600 mbar. (c) During the valve actuation when 650 mbar is imposed in the valve inlet.

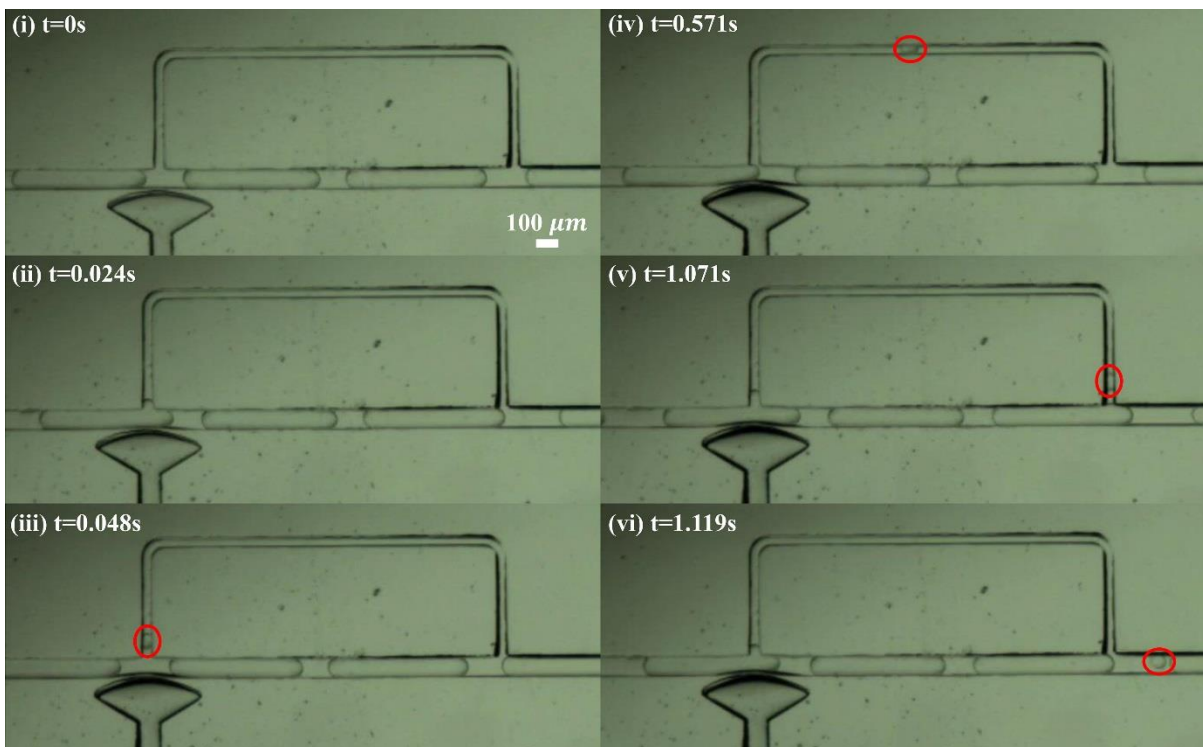


Figure 3.10. Timelapse images of the droplet passing through the entrance of the bypass loop in the operating condition of Oil Pressure = 400 mbar, Water Pressure = 500 mbar and valve pressure = 650 mbar which shows that the system is selective and on demand with the minimum possible actuation in the valve part.

3.6.2. Valve Characterization

Single layer valves with different geometrical parameters were designed and tested. Dimension and shape of valves as well as thickness of membranes were changed to find the best pair that can be easily fabricated and sufficiently actuated without any leakage. Table. 3.1 summarises the geometrical parameters, advantages and disadvantages of single-layer valves and membranes with different geometrical parameters that were tested. The membrane is a thin layer of soft PDMS, which lies horizontally between the valve and main channel. Also, PDMS with different stiffness were tested in which the ratio of the curing agent was gradually increased from 10% to 25%.

Table 3.1. Different geometrical parameters were tested to characterize the valve.

Valve type	T-shaped valve	Normal deformation
	Tulip-shaped valve	Normal deformation
	Mushroom-shaped valve	More deformation
Valve size (Length/width)	Small (500 μm/50 μm)	Easily bonded
	Large (1000 μm /50 μm)	not easily bonded
Membrane thickness	Thin (30 μm)	Mostly bonded with enough deformation
	Normal (50 μm)	Always bonded with less deformation
	Thick (80 μm)	No deformation
PDMS Stiffness (Weight ratio of curing agent to the PDMS)	Very Stiff (1/10)	No deformation
	Stiff (1/15)	less deformation
	Soft (1/20)	More deformation
	Very Soft (1/25)	Hard for punching and tubing

From previous studies, it was found that after actuating PDMS with the single-layer valve, usually a convex deformation is shaped in the microchannel^{48,218}. Therefore, it was hypothesised that if the head of the valve is curved, more actuation can be observed, especially in the splitting zone. After running experiments and analysing the experimental data, more actuation was observed when the mushroom-shaped valve was actuated as predicted. As another example, the maximum deformation of two membranes with different thicknesses was shown in Figure 3.11. While 20% of the main channel was deformed by using membrane with 50 μm thickness in the channel with 100 μm width, membrane with 30 μm thickness was deformed for about 50 μm with the same pressure of 100 kPa. Therefore, the thinner the membrane, the more deformation was observed in the main microchannel, although the very thin (<30 μm) membrane suffers from a fabrication problem. On the other hand, membranes

with thickness of more than $80\ \mu\text{m}$ did not show any deformation under valve actuation. The Effect of external pressure on the deformation of the valve is visualized in the Figure 3.12. The more external pressure was applied, the more deformation was observed in the microchannel.

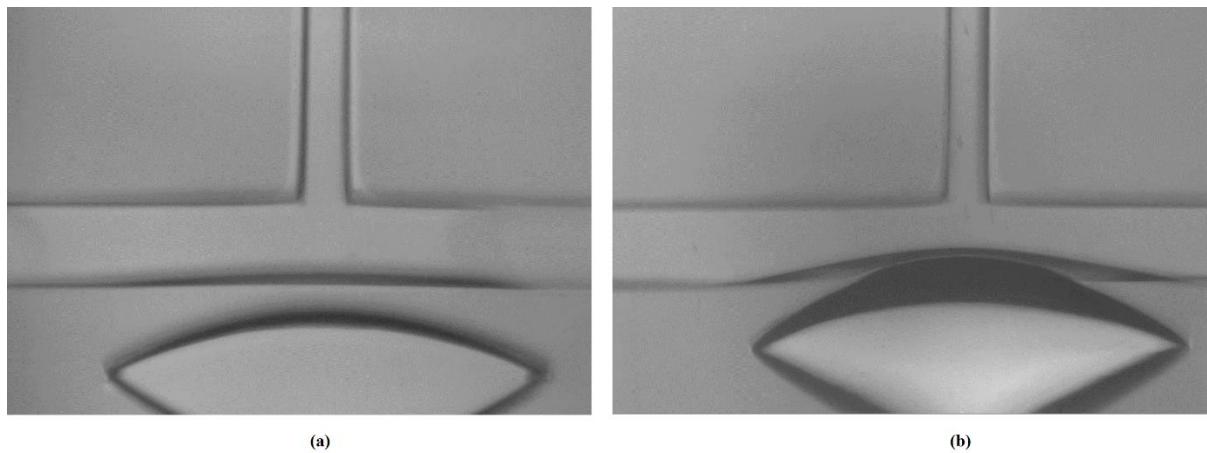


Figure 3.11. Deformation of two valves with different membrane thicknesses under the $P = 100\ \text{kPa}$ (a) membrane thicknesses = $30\ \mu\text{m}$ (b) membrane thicknesses = $50\ \mu\text{m}$ ($Q_{\text{oil}} = 60\ \mu\text{l/hr}$, $Q_{\text{water}} = 25\ \mu\text{l/hr}$).

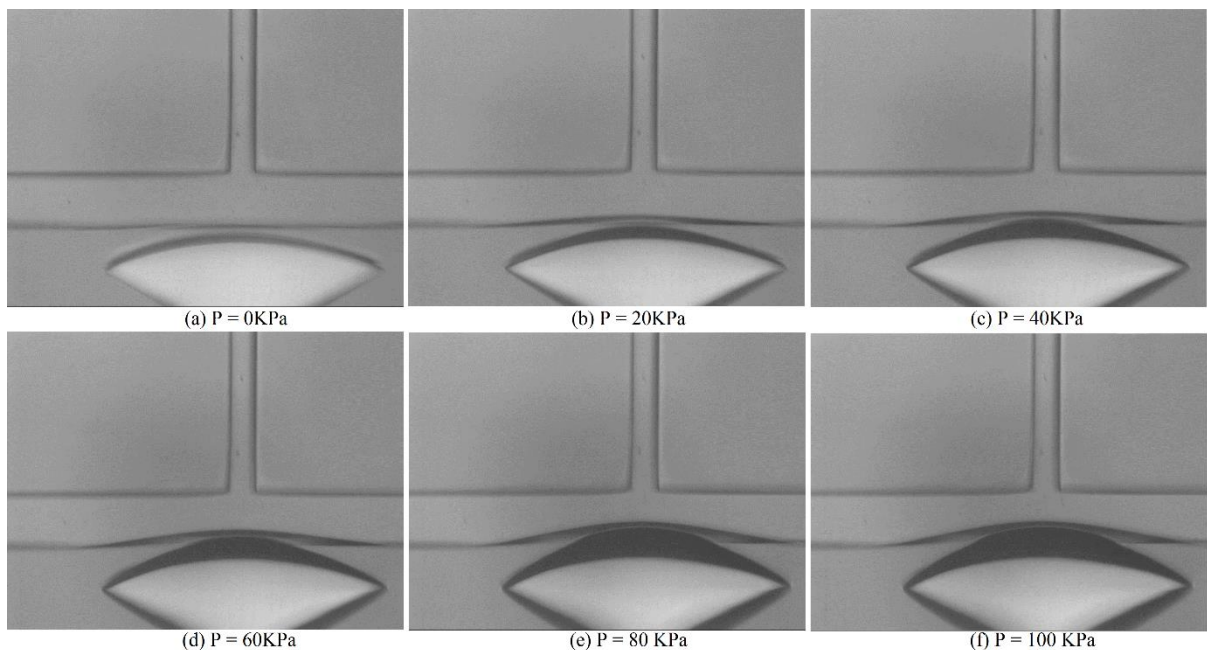


Figure 3.12. Visualization of valve actuation at different pressures for membrane with $30\ \mu\text{m}$ thickness ($Q_{\text{oil}} = 60\ \mu\text{l/hr}$, $Q_{\text{water}} = 25\ \mu\text{l/hr}$).

Based on the preliminary characterisation experiments, it is concluded that when the mushroom-shaped valve with $500\ \mu\text{m}$ length and $50\ \mu\text{m}$ width of the head is utilised to actuate $30\ \mu\text{m}$, both factors of ease of bonding and sufficient actuating for splitting are satisfied without any leakage. Hence, in the splitting experiments this combination of single layer valve with membrane was utilised.

Chapter 4

Controlled Droplet Manipulation and Interaction using Single Layer Microvalves

4.1. Preface for Chapter 4

The miniaturisation of high-throughput screening on the microfluidic chip from existing microtiter plates and robotic dispensing reduces the volume of samples and reagents required in the drug discovery studies. In this chapter, we demonstrate a selective multisite splitting and merging system to perform the type of permutations of reactions required for high-throughput screening. Our approach uses multiple single-layer microfluidic valves as they offer simplicity, ease of operation, biocompatibility and high-speed operation. These valves are used both to control the generation of droplets and the location of splitting. In the former the valves are used to completely block some channels, in the latter they create a more modest variation in local geometry. The generated droplets act as a vessel which transports different samples around the chip, these vessels can then be subdivided at splitting locations, just as a pipette can be used to dispense a fraction of its total volume. The split droplets enter a merging channel, in which daughter droplets of different types and sizes can be reacted together. In this chapter, based on the methods developed in Chapter 3, we demonstrate the merging of different droplet types in different concentrations at four merging locations, so laying the foundations for a valve driven method for high-throughput screening on a chip.

This chapter has been submitted for publication to *Sensors and Actuators B: Chemical*, and is currently under review. The candidate was the shared co-first author in this work. The candidate and the other co-first author (Mr. Sagar N Agnihotri) played primary roles in designing the research, performing the experiments, analysing the data, and writing the paper. While the candidate was in charge of the valving and selective droplet splitting system, the other co-first author (Mr. Sagar N Agnihotri) worked on the droplet merging and generation parts in this integrated system. Additional authors for the work include Prof. Rajneesh Bhardwaj, and Prof. Adrian Neild. Their contributions were central to the publication of this work and are gratefully acknowledged and appreciated. This chapter was inspired by the previous work presented in Chapter 3 (published as lead-author journal article in *Sensors and Actuators B: Chemical*²²) and previous contributions included in Appendix I⁴⁰ and II⁴¹ (published as second author journal articles in *Physical Review Applied*⁴⁰ and *Langmuir*⁴¹, respectively).

This work is the stepping stone towards a high throughput screening for drug discovery in multi splitting and merging system using microvalves. Integration of other manipulation techniques

such as generation, merging and trapping with the selective splitting that was introduced in the previous chapter by using the single layer microvalve and duplicate the microfluidic loop can result in producing a combinatorial library of chemicals for drug screening. The presented system has the potential to replicate automated pipetting technologies currently used on a larger scale and in four loops. In this chapter; a review of different droplet manipulation methods, fabrication and methodology are presented. This is followed by a thorough characterisation of the three different manipulation techniques (Generation, splitting and merging) in the integrated system via detailed analysis of experimental results, discussion and supplementary information.

4.2. Introduction

Droplet-based microfluidics involves the generation of monodisperse droplets of nanolitre to femtoliter volumes separated by an immiscible carrier fluid. The carrier fluid isolates each droplet; hence different samples or reagents can be encapsulated in droplets without cross-contamination. These systems provide accurate droplet volumes, reliable droplet manipulation, faster reaction times, and a reduction in the cost of samples. Droplet-based microfluidics offers evaporation free environment and the ability to handle small volumes. As such, droplet-based microfluidics finds applications in various fields such as single-cell analysis^{280,295}, protein crystallization^{296,297}, nanoparticle production^{182,281}, inorganic chemistry²⁹⁸, chemical and biological assays^{299,300}, clinical diagnosis^{301,302}, reaction kinetics³⁰³ and high throughput screening (HTS)^{23,225,229}. However, to use droplet microfluidics for HTS, there are challenges around dispensing different samples and reagents at multiple locations to achieve the desired combinations. Especially, as one of the key features of continuous droplet production methods^{32,33,75} is their ability to generate thousands of identical droplets, this repetitiveness and homogeneity is not directly compatible with the requirements of HTS of creating a multitude different permutation and outcomes.

For on-chip HTS, the ability of a pipette to be loaded with a sample and dispense it in sub-volumes into desired wells of a titre plate needs to be replicated. As such one approach is to generate different droplets from different chemicals with temporal control (akin to pipette loading), split the generated droplets selectively at multiple locations (akin to pipette dispensing) and merge the split droplets on the chip at will. Some of these tasks, such as the production of droplet pairs^{101,304,305}, splitting^{99,157} and merging^{42,43}, have been individually

demonstrated. Indeed, a variety of methods have been established for on-chip droplet manipulation⁸⁰, including both passive and active approaches. Passive approaches use features in the chip design or operation such as changes in channel geometry¹⁵⁷, use of pillars^{43,288}, gravity³⁰⁶, surface properties³⁰⁷ to interact identically with every passing droplet. However, for selective droplet interaction, active methods are required. Here, external activation is selectively applied to specific droplets to achieve the desired outcome. This activation can be thermal or take the form of externally generated force fields, for example, using surface acoustic waves^{137,173,175}, electrostatic^{115,308}, or magnetic³⁰⁹ effects, lasers¹²⁵, and microheaters¹⁶⁸. Alternatively, the activation of single-layer microfluidic valves^{206,208,209} provides a mechanism to alter channel dimensions and hence selectively change droplet behaviour.

Single-layer microvalves provide a biocompatible method of rapidly (~0.05s) locally altering channel geometry for droplet splitting^{22,41}. They consist of a thin deformable membrane of PDMS separating a dead-end channel from the sample carrying microchannel. The deformation of the membrane is achieved by applying pressure in the dead-end channel. The valves can operate in a binary manner, in which the channel is either open or fully closed, or, instead, a pressure-dependent constriction of the main channel can be utilised. The latter can be used for droplet manipulations, provided flow conditions are chosen such that a small alteration of flow conditions switch behaviour, for example, from a droplet remaining intact event to a droplet splitting event⁴⁰. These valves have been used for both selective and non-selective operations. For example, non-selective droplet generation¹⁴⁵ and merging²¹⁸, and selective splitting⁴¹ and sorting²⁰⁹. Each time, however, the operations have been investigated in a specialised chip, rather than being integrated on a single device to deliver full functionality.

Our motivation in this study is to form droplets of different chemicals on-chip and then to split and merge them at multiple locations, simultaneously and selectively. The combination of these droplet manipulations techniques allows permutations of different combination of droplets to be merged at a range of different concentrations. To achieve this integrated functionality, we use eight single-layer valves and four pillar-induced merging chambers, as shown in Figure 4.1. The system has the potential to conduct screening on-chip, using smaller volumes and without the evaporation issues faced by standard microtiter plates.

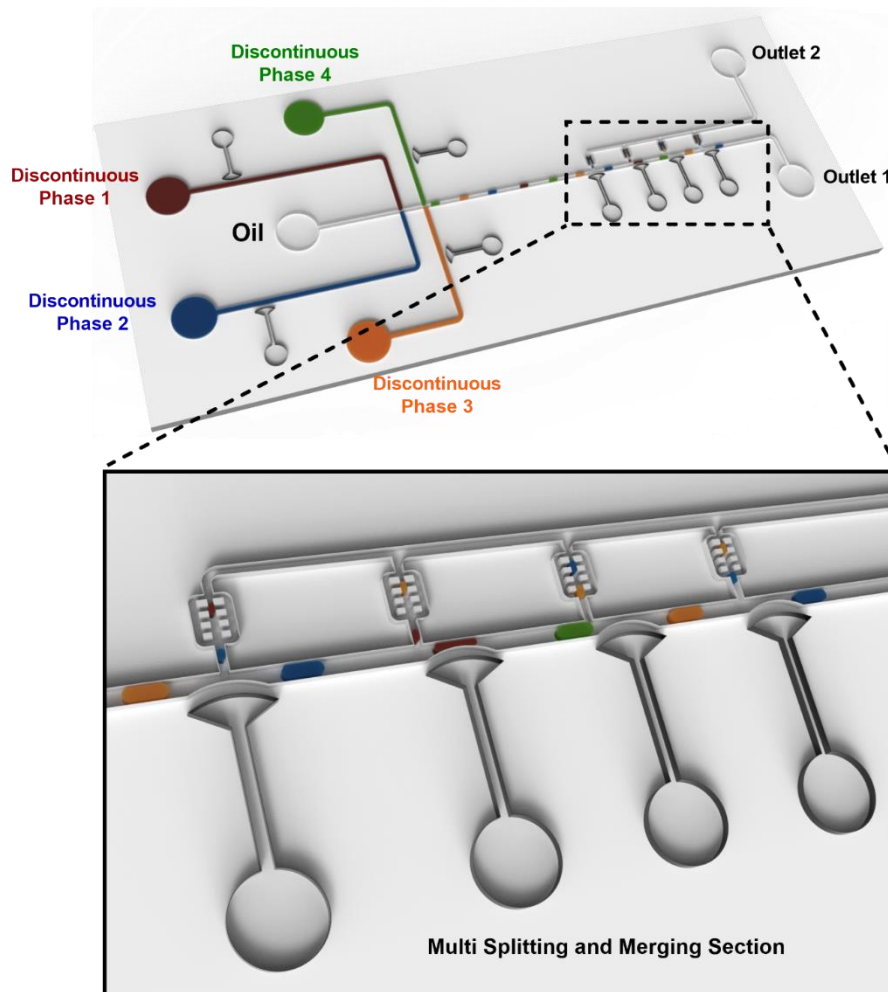


Figure 4.1. Schematic of the microfluidic device to achieve selective droplet splitting and merging at multiple locations using eight single-layer microvalves. The microfluidic device generates four different coloured droplets mimicking four different chemicals in the upstream part of the chip, this is achieved using four valves located close to each of the channels carrying discontinuous phases. A zoomed-in view shows that downstream of the generation structures, there is a multiple site splitting and merging section of the chip. Here, the droplet can be split at any of four different locations each controlled by a separate microvalve, after splitting the daughter droplets are merged using a passive pillar-based approach.

4.3. Methods and Materials

Polydimethylsiloxane (PDMS) is used to fabricate the microchannel using a master mould. To fabricate the mould, we used standard lithography on a 4-inch silicon wafer spin-coated with negative photoresist (SU8-3050) to a height of 130 μm . The PDMS and curing agent mixture (20:1 ratio) are poured over the prepared mould, degassed and heated on a hotplate at 70 $^{\circ}\text{C}$ for 3 hours. After curing, the PDMS replica is peeled off the mould, holes are punched for inlets and outlets. The PDMS replica is bonded onto a glass slide by exposure to an oxygen plasma

for 18 seconds. A pressure-driven pump (MFCSTM-EZ, Fluigent systems) was used to control the air pressure in the single-layer pneumatic valves (8 in number, each with a membrane thickness of 35 μm), and a second system was used to control the pressure of the discontinuous phase (4 in number). A syringe pump was used to pump the continuous phase (olive oil unless otherwise stated). Mili-Q water with food-grade dye was used as the discontinuous phase. Videos and images were recorded using a camera (Pixelink PL-B782U, Ottawa, Canada) mounted on an inverted microscope (Olympus CKX53, Tokyo, Japan).

The design of the chip (Figure 4.1) involves valves located close to junctions leading to merging chambers. The operation of these valves causes partial constriction of the channel such that the flow properties at each junction change. Droplets will be selectively partitioned, using these valves, so that the desired daughter droplets can be delivered to the required merging chamber. Earlier work shows that for having droplets split at all four junctions simultaneously, flow conditions need to be such that a passing droplet almost splits even when the valve is not activated. The geometry needed to achieve these conditions is found using an electric circuit analogy³¹⁰ as described in the supplementary information. It must be noted that the flow resistances, used for this analysis, are calculated in the absence of droplets in the system. Hence, when droplets are present, deviations from these ideal conditions must be expected. The experimental work, however, shows that by starting at this idealised analysis which assumes no *a priori* knowledge of operation conditions, droplets can be successfully split at will at each location.

4.4. Results and Discussion

The concept of the device is that different chemicals (here coloured aqueous samples) will be introduced into the main channel in the form of droplets, each separated by the continuous oil phase. As these droplets get to the junctions leading to the merging chambers, they can be selectively split, resulting in the deposition of a small sample volume into the merging chamber. In this way, droplets of different compositions can be split at different chambers so that the desired permutation of reactions is enabled. Subsequently, the merged droplet volume is larger than the capacity of the merging chamber, and so it moves into the exit channel, and the merging chamber is ready for renewed operation. This requires selective droplet production, selective droplet splitting and daughter droplet merging. These tasks will first be examined and characterised in isolation. For droplet generation, different methods of obtaining

droplet pairs and quartets will be examined using both passive and active approaches. Whilst for droplet splitting, the passive operation is first investigated in order to seek suitable operating conditions. Then using these conditions, selective splitting is achieved by active use of the valves at all four junctions. Finally, these operations are used in conjunction with the merging pillars to demonstrate the delivery of different daughter droplet combinations to each merging chamber, hence the mixing of different permutations of the droplet types is achieved.

4.4.1. Droplet Generation

To deliver droplets of different compositions, a continuous oil phase is flowed through the microfluidic chip using a syringe pump, in addition, four other channels (each delivering a different fluid type) introduces the dispersed phases. In these experiments, the dispersed phases used were pure water, and water mixed with red, blue and green food dye.

A schematic of the droplet generation part of the chip is shown in Figure 4.2a. It consists of four side channels, each carrying a different dispersed phase, which all join a single main channel carrying the continuous phase. The arrangement is such that the side channels join as opposing pairs, one from either side of the main channel. A single-layer microfluidic valve is located on each of the side channels. Droplet generation can be passive, in which case these valves are not used, or active. For active operations, these valves are pressurised, as required, by a Fluigent system to 1800 mbar. This causes the PDMS membrane to deform such that the channel is entirely blocked. Hence the valves can be used in binary mode, such that flow can either continue along the side channel resulting in droplet formation, or the flow can be stopped and with it the droplet generation. Figure 4.2b,c show pairs of channels operating in passive mode, by application of equal pressure to the inlet of the side channels alternate droplets are formed. If this is extended to all four channels, again with equal applied pressure, sequences of the four different droplets can be formed (Figure 4.2d), but with lower reliability.

For active production, three of the valves are actuated simultaneously so that flow results in just one of the side channels. By altering which valve remains inactivated the type of droplet produced is changed. Figure 4.2e-h shows the generation of undyed, green, blue and white coloured droplets. In these experiments, a continuous flow rate of $2 \mu\text{l}/\text{min}$ is used, selected for its compatibility with the splitting part of the chip. At this flow rate, and with the side channels pressurised to 100 mbar, a droplet is produced every 60 ms. A plot of the deformation of the

valve membrane over time during activation and deactivation is shown in the supplementary information, the cycle of deactivation and reactivation (as required to allow and subsequently prevent flow along the side channel) takes approximately 50 ms. As such this method can switch from droplets of one type to other in just 110 ms, meaning that, currently, a minimum of 2 droplets of one type could be produced. Each of these droplets is 3 nl in size, and acts as transport entities delivering the various samples around the chip and past the entry to each merging chamber, at each of which the droplet can be split down to the reaction volume. A process equivalent of nanoliter pipetting of a sample into a reaction vessel.

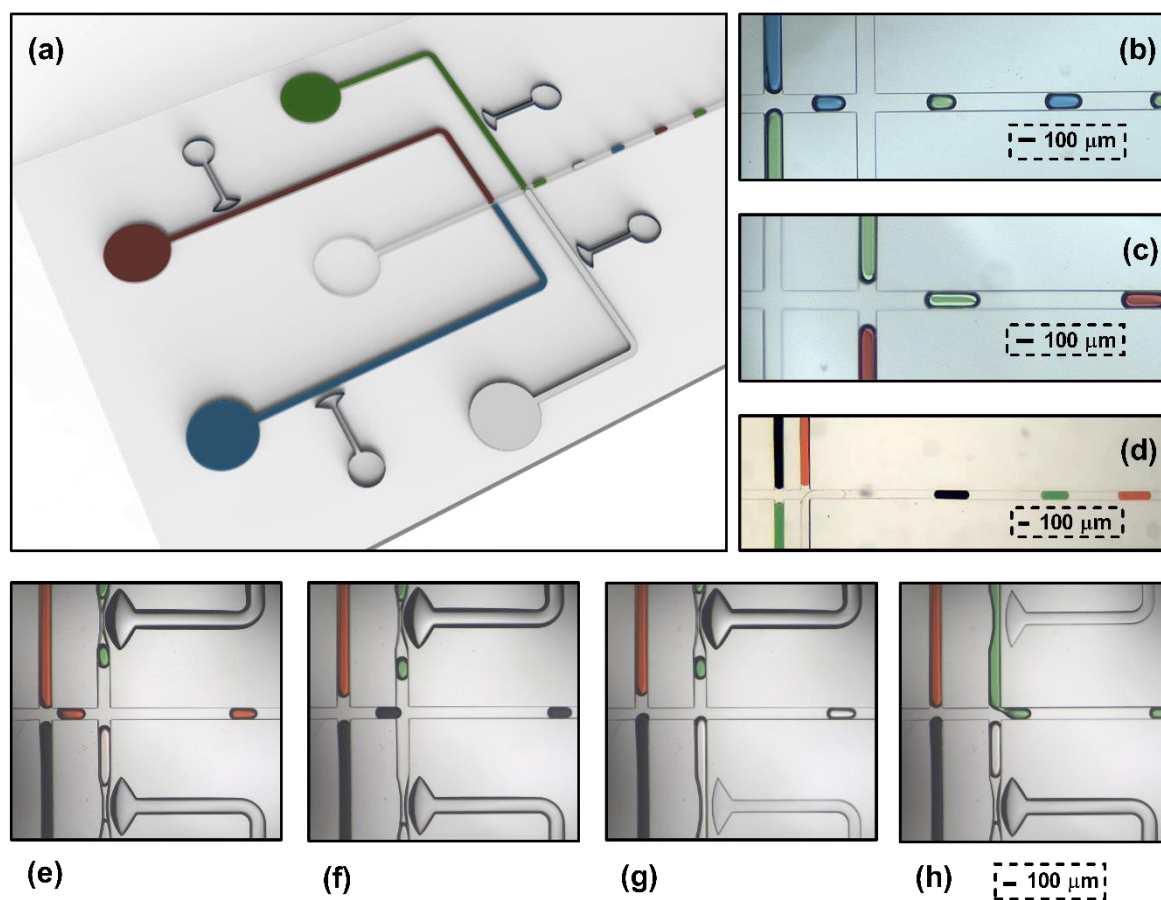


Figure 4.2. Droplet generation part of the multi-splitting and merging system using two different approaches. (a) Schematic of the droplet generation part showing four valves controlling the flow of four discontinuous phases. (b) Blue and green droplets are generated, alternately. (c) Green and red droplets are generated, one after the other. (d) Four different coloured droplets are produced, sequentially. (e) - (h) Valve based droplet generation approach is used to create a red, blue, white and green droplet, respectively. Scale bars are 100 μm.

4.4.2. Droplet Splitting

Droplets will be split at the junctions to the merging chambers by use of four valves along the main channel. In contrast to the use of valves for the droplet generation stage, here they will not be used in a binary manner. Instead, rather than ceasing flow along the main channel, which would simply divert the droplet in its entirety into the merging chamber, the valve will be partially activated. Enough deformation will be applied to change the division of flow at the junction, pulling more of the droplet into the channel heading to the merging chamber. As a droplet passes a junction in which the flow splits, a finger of the droplet enters the channel with the lower flow. A change in the flow conditions which increases that finger length can cause the finger to pinch off so that the formation of a daughter droplet occurs.

As the valves only act to change local flow conditions, rather than completely block one channel, there is a need to make the change required to transition between behaviours as small as possible. To this end, we first start by analysing the flow conditions when no valve actuation is imposed. The system has been designed such that the flow into the channels at each of the junctions is the same. This provides an idealised starting point for balancing the conditions at each junction, however, the addition of droplets into the system causes alterations to the flow resistances in the system, the inclusion of which into the design process would require no prior knowledge of how the system was to be used and, hence, lose the flexibility of operation being sought.

First, we examine the interaction of the mother droplet with each junction, in the absence of actuation, to obtain a flow regime in which splitting does not occur at any junction. Figure 4.3 shows different regimes of interaction across a relatively modest range of capillary numbers, 0.006 to 0.009 (calculated from the flow in the main channel before interacting with the first junction). In this experiment only the flow rate of the dispersed phase, hence the range of Ca (calculated using the combined flow rate of the dispersed and continuous phase) is modest. We started with the regime where we observed droplet splitting at all the four junctions, and we called this as regime 1 (Figure 4.3a). In this regime the flow rate of the dispersed phase is the highest of all of the regimes, the separation distance between consecutive droplets is the smallest, and the size of the mother droplet is the largest ($230 \pm 10 \mu\text{m}$). As we decreased the flow rate of the dispersed phase gradually, an increase in separation distance and a decrease in the size of the mother droplet ($210 \pm 10 \mu\text{m}$) occurred. Resulting in splitting occurring only in

the last three junctions, termed, here, as regime 2 (Figure 4.3b). In this regime, the size of the daughter droplet generated becomes larger at each successive junction, there is no droplet splitting at the first junction. With the further reduction of the dispersed phase flow rate (droplet size: $190 \pm 10 \mu\text{m}$), droplet splitting in the last two junctions is observed, regime 3 (Figure 4.3c) Finally, with a further decrease in the flow rate of the dispersed phase, no droplet splitting occurred, regime 4 (Figure 4.3d). In this regime separation distance is maximum while the size of the mother droplet is minimum ($175 \pm 10 \mu\text{m}$). To have selective droplet splitting at all the four junctions, regime 4 is the only useful regime as it provides a common outcome of no droplet splitting at all of the four junctions.

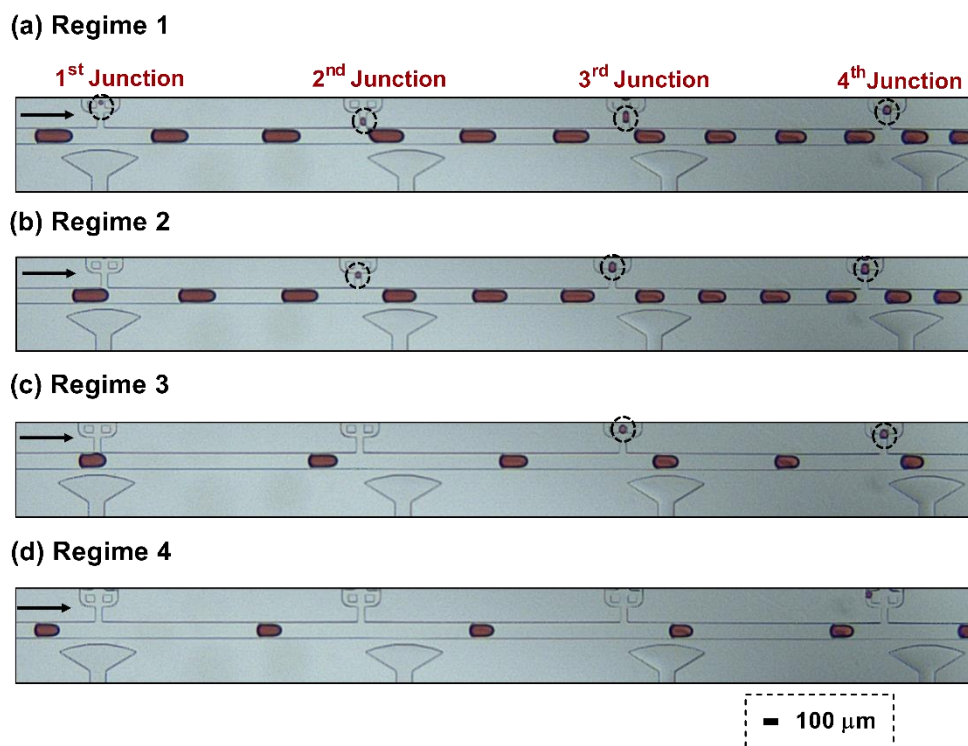


Figure 4.3. Different Regimes of droplet splitting when droplets interact with four junctions placed one after the other. (a) Droplets split in all the four junctions. (b) Droplets split in the last three junctions. (c) Droplets split in the last two junctions. (d) There is no droplet splitting in all the four junctions: scale bars, $100 \mu\text{m}$.

The percentage of flow rate entering each channel branching from at the junctions is shown in Figure 4.4. In experiments, we calculated actual flow rate entering each of the junctions by finding out the velocity before and after that junction. The change in the velocity is used to calculate the relative flow rate values in each of the junctions during the experiments. Figure 4.4b shows that there is a critical separation distance at which splitting is observed. The presence of droplets in the channels adds a finite hydrodynamic resistance to the branch in which they are present. Hence, a lower number of droplets in the system will allow the system

to function in a manner closer to the idealised design (which ignores this effect). The number of droplets present in a particular branch is inversely proportional to the separation distance. Hence, a decrease in d_1 causes an increase in the resistance of that channel, as such, it is the separation distance in each branch which causes deviations in the flow rate away from the ideal, and so causes four different regimes (rather than two, one with all junctions splitting and one with none).

A line is also plotted (Figure 4.4c) distinguishing those cases in which splitting occurred (above 15%) and those in which it did not (below 15%). The geometry of microfluidic chip is designed using resistive network analysis in such a way that same amount of flow rate enters each of the junctions. In this analysis, we do not consider presence of droplets to simplify the equations. We solved 4 equations to find 4 unknowns (dimensions of the last 3 junctions and the flow rate entering the junctions). We calculated this value of 15% flow rate by solving these equations. In ideal case, in the absence of droplets, 15% of flow rate should enter each junction, hence, to have same output (either splitting or no splitting) at each junction, 15% of flow should enter each junction. Ideally, in regime 4, the regime in which selectivity can be imposed, this percentage would be identical in each junction and would lie very close to the 15% value. It can be seen in regime 4, the variation is small, much reduced from the regimes in which different behaviour is observed at each of the junctions.

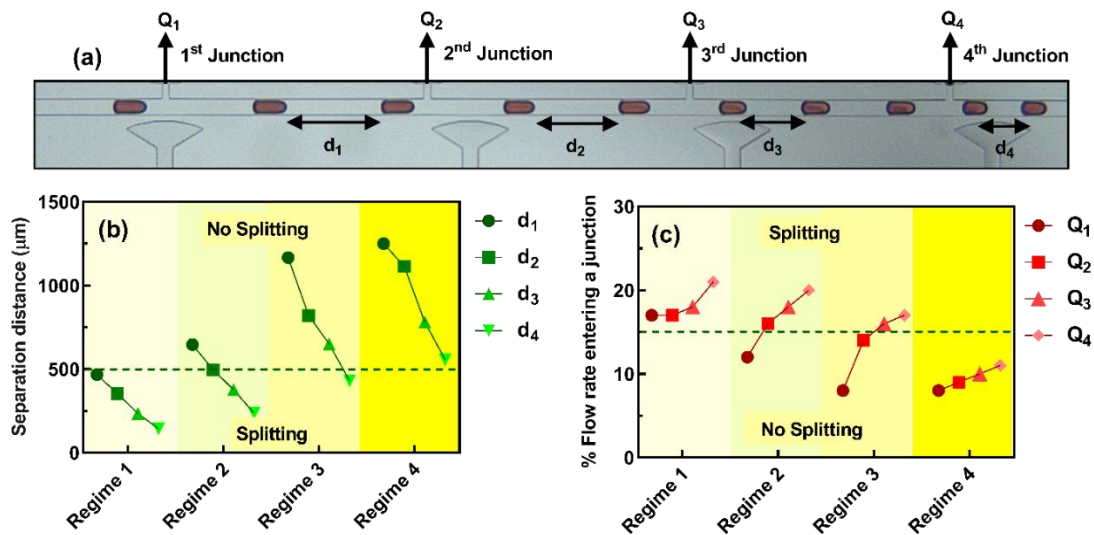


Figure 4.4. Classification of different splitting regimes by the separation distance and the percentage of the flow rate entering each junction. (a) Schematic shows the separation distance d_1, d_2, d_3, d_4 . Regimes map is extracted based on (b) the average separation distance in each branch of the main channel, and (c) the percentage of the flow rate entering each branch divided by the total flow rate in the main channel, respectively. The dotted lines separate splitting and no splitting regimes.

4.4.3. Selective Droplet Splitting Using Valves at Four Junctions

To demonstrate the splitting of different coloured droplets at the different junctions, we operated the microfluidic system in regime 4, where there is no droplet splitting at all the four junctions in the absence of valve actuation. At each junction, we pressurise the valve systematically from 0 to 1800 mbar (corresponding deformation of 53 μm) to investigate whether a daughter droplet is formed and measure its volume. Daughter droplet formation and size at each junction increases as we pressurise the valve. When we pressurise the valve, deformation in the main channel causes the resistance in the main channel to increase, which leads to droplet splitting at a junction. We observed that for maximum deformation, the ratio of daughter to mother droplet volume is smallest for the first junction and increases in each subsequent junction. This variation in droplet volume can be attributed to the fact that in regime 4, flow rate entering the fourth junction is higher than the other junctions, as shown in Figure 4.4c. The maximum relative volume of the daughter droplet formed in the fourth junction is close to 25%, while in the first junction it is close to 10% for a membrane deformation of 53 μm . The solid line shown in Figure 4.5a shows that the deformation required to achieve 10% of the relative volume of daughter droplet that is formed in each junction. So, this system can split a droplet equally at four junctions with the help of a valve placed at each junction pressurised unequally. We also demonstrated selectivity of droplet splitting at each junction by splitting a blue, red, green and clear droplet at the 1st, 2nd, 3rd and 4th junctions respectively (Figure 4.5b-e).

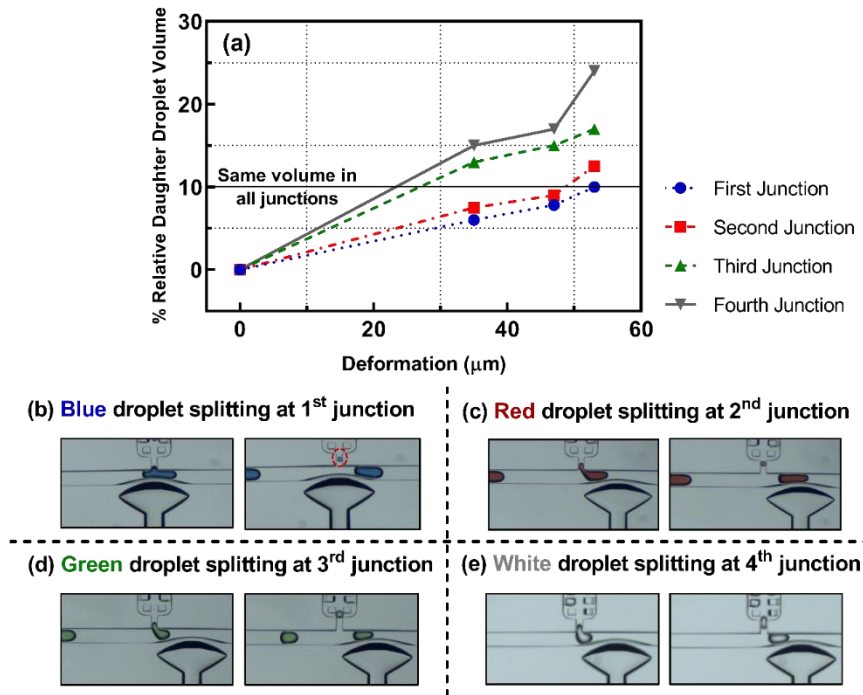


Figure 4.5. Splitting of different coloured droplets at different locations using single-layer microfluidic valves. (a) Percentage of the relative daughter droplet volume against the deformation of the microchannel channel for all the four junctions. (b) The blue coloured droplet is split at the first junction when the valve is pressurised at 1800 mbar (deformation of 53 µm). (c) Splitting of the red coloured droplet at the second junction using valve pressurised at 1800 mbar. (d) Droplet splitting of the green coloured droplet at third junction using valve pressurised at 1800 mbar. (e) The white coloured droplet is split at the fourth junction when the valve is pressurised at 1800 mbar.

4.4.4. Droplet Merging

Four merging chambers with pillars⁴³ were integrated into the system so that the split droplets can be merged as would be required for the onset of a chemical reaction.

First, we demonstrate that the location of splitting can be selected and that merging ensues. Here, droplets of two types are produced alternately and continuously by applying equal pressure to the sources of the two dispersed phases (the valves in the generation section of the chip remaining inactive). As the droplets pass active valves, they all split, the site of splitting is selected by choice of which valve is actuated but the droplet that should split is not selected. Each daughter droplet enters the merging chamber, and merges, when the capacity of the chamber is reached they are dragged along the exit channel. Depending on the size of the daughter droplet this can cause the merging of two droplets, Figure 4.6a (1 red + 1 white), as shown at junction three, or four droplets, Figure 4.6b (2 white + 2 blue) shown for junction

one. In these experiments, when operated, both valves were pressurised to 1800 mbar. Hence smaller droplets were produced at the first junction than the third.

In Figure 4.6b three droplets are merged, two clear and one red, hence the concentration of the merged droplet is altered from the 1:1 ratio shown previously. Again, here the droplets which are split are not chosen selectively, rather the location at which they are split. In this case, the valve is pressurised until it splits three droplets and then depressurised, the droplets being generated passively as an alternating stream. As the volume of the daughter droplet is dependent on the pressure applied to the valve, two droplets of different sizes can also be merged to control concentration. However, this requires the pressure applied to the single valve to be rapidly altered, hence there is a useful simplicity to the approach shown.

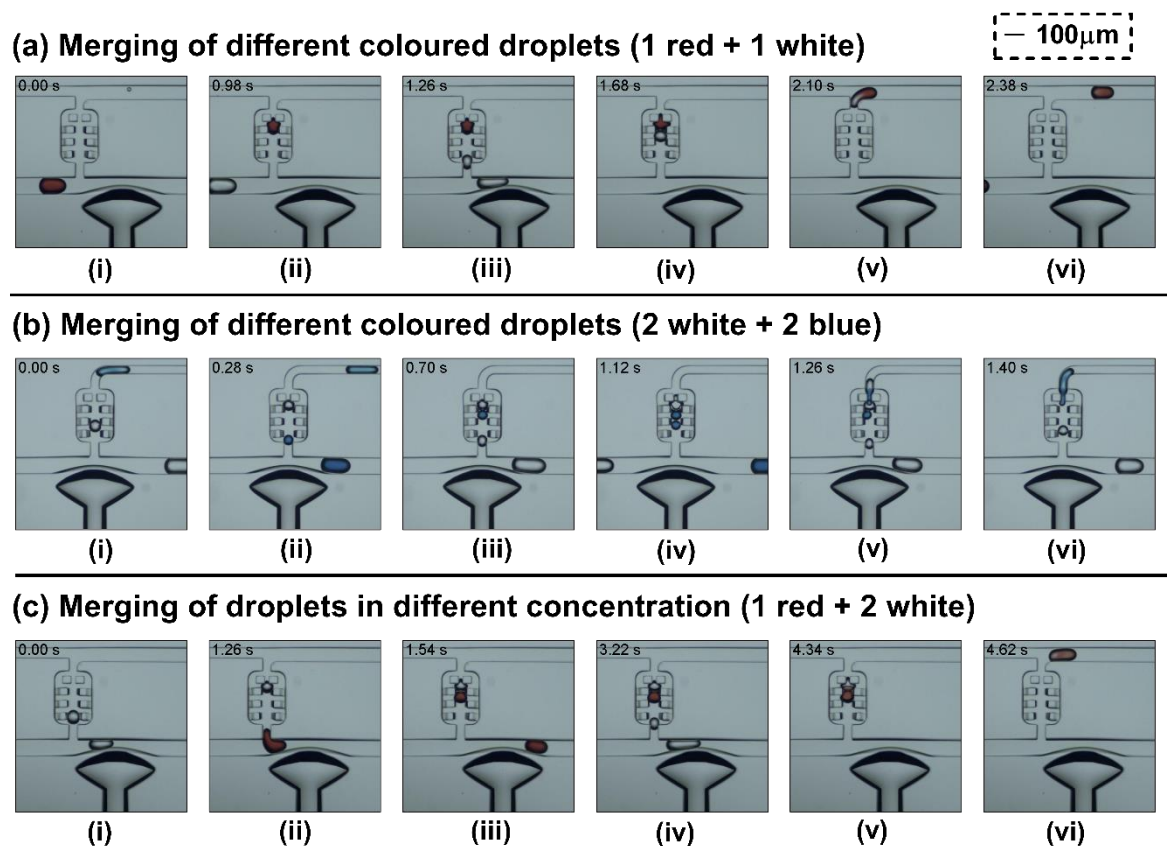


Figure 4.6. Splitting of different coloured droplets occurs whilst the valve is actuated. The two daughter droplets are merged within the chamber, the first being retarded by the pillar structures, after merging the total volume is such that the droplet is dragged out of the merging chamber. Merging of two different coloured droplets an equal volumetric ratio is shown at the (a) third and (b) first junctions. In the former, a single red daughter droplet is merged with a single clear one. For the latter two blue daughter droplets are merged with two clear droplets, Finally, (c) merging of an unequal number of droplets generated from two different samples is achieved, such that the mixing ratio is 1:2 (red: clear).

Finally, we demonstrate the selective splitting of droplets, here the location of splitting is dictated by the choice of the valve being operated, and in addition the droplet is selected by the transient nature of valve actuation. In Figure 4.7 a single clear droplet is selected out of a stream and split. With the daughter droplet remaining trapped in the merging chamber. Subsequently, a single red droplet out of a stream was split, such that when its daughter droplet enters the merging chamber, it merges with the clear daughter droplet.

This demonstrates the ability of single-layer valves to control the introduction of relatively large sample volumes onto the chip, and then to split these droplets and deposit nanoliter volumes into a merging chamber. For the splitting process selectivity is achieved both spatially, as local geometric deformation is used such that splitting occurs at just one valve, and temporally such that splitting of a single selected droplet is obtained. Taken together this approach can be used to subdivide droplets, generated on chip as performed here or introduced after off chip production, and mix them in different combinations at multiple sites.

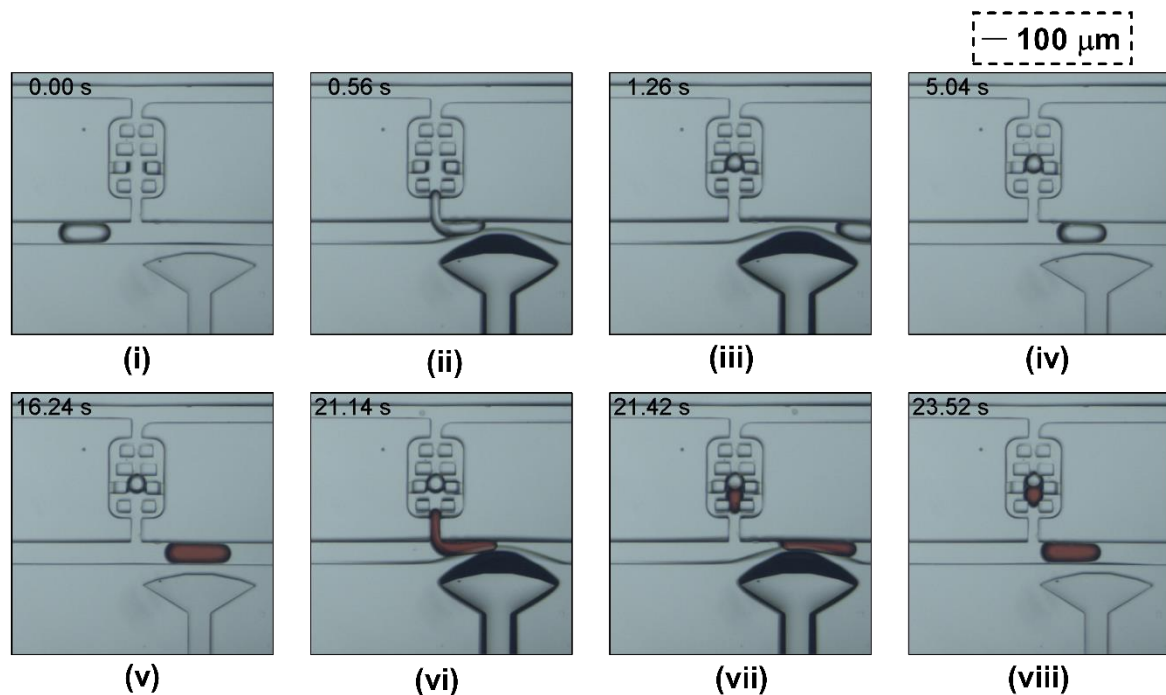


Figure 4.7. An image sequence demonstrating the merging of two different selected droplets (one clear and one red droplet) at the third junction. The clear droplet is split by transient actuation of the valve, resulting in the deposition of a daughter droplet in the merging chamber. Subsequent clear droplet passes without splitting due to timely deactivation of the valve. Finally, a single red droplet is selected and split, again a daughter droplet is formed and merges with the clear daughter droplet.

4.5. Conclusions

Temporal and spatial control has been demonstrated over droplet splitting behaviour on a chip. Through the introduction of different chemicals in a controlled sequence of mother droplets, here generated on the chip, samples pass through the main channel of the chip. As they pass branches in the channel, each leading to a merging channel, the droplets can be split selectively, causing deposition of that sample into the merging chamber, just as a pipette dispenses into a micro titre well at much higher volumes. This level of control offers the ability to react samples in multiple permutations. When the merging has occurred, the reaction droplets exit each chamber along a single, common exit channel, allowing the potential for subsequent analysis of the reactions to occur at a single observation site along the exit channel. Our method, using single-layer valves, unveils an easy technique for selective splitting and merging at multiple locations and offers reduced chemical waste and rapid analysis times for sample reagent studies, which makes it an ideal candidate for closed channel microfluidic high throughput screening.

4.6. Supplementary Information

4.6.1. Channel Flow Rate Examination

We analysed the system to have the same flow rate entering all the four junctions, as finger length of the droplet forming in each junction is dependent on flow rate entering in that particular junction. To achieve this, we used electric circuit analogy, where current is equivalent to flow rate (Q), a potential difference is equivalent to the pressure drop and resistance is equivalent to the hydrodynamic flow resistance of the microchannel. This analysis is used for the initial design of the microfluidic circuit, and design is further modified based on actual experiments performed on the chip. To predict channel flow rate with the least complexity, we only considered the presence of continuous phase and did not consider droplets and pillared merging chambers.

Figure 4.8a shows the microfluidic network with hydrodynamic resistances and flow rate entering in all the branches. The hydrodynamic resistance is calculated using equation below:

$$R = \frac{12\mu l}{wh^3 \left[1 - 0.63 \left(\frac{h}{w} \right) \right]} \quad (4.1)$$

$$R = al$$

$$\text{Where } a = \frac{12\mu}{wh^3 \left[1 - 0.63 \left(\frac{h}{w} \right) \right]}$$

w , h , l , μ represent the width, height, length of the channel and viscosity of the continuous phase, respectively. Here, we need to find the width of branches 5,7,8,10,11 and flow rate Q_1 in terms of Q . We have similar width for branches 5 and 7, 8 and 10, 11 and 13. Hence $a_5 = a_7, a_8 = a_{10}, a_{11} = a_{13}$.

Applying Kirchhoff's loop law for 1st junction and converting it in terms of a and l , we get:

$$a_5 l_5 Q_1 = (R_2 + R_3 + R_4) Q_1 - R_2 Q$$

$$a_5 l_5 + R_2 Q^* = (R_2 + R_3 + R_4) \quad (4.2)$$

$$\text{Where } Q^* = \left(\frac{Q}{Q_1} \right)$$

Similarly, applying Kirchhoff's law for 2nd and 3rd junctions, we get:

$$a_8 l_8 - a_5 (2l_7 + l_5) + R_6 Q^* = 2R_6 \quad (4.3)$$

$$a_{11} l_{11} - a_8 (3l_{10} + l_8) + R_9 Q^* = 3R_9 \quad (4.4)$$

Both outlets are subjected to atmospheric conditions, so we can write:

$$(P_A - P_K) = (P_A - P_J)$$

$$R_3 + R_4 + 2a_5 l_7 + 3a_8 l_{10} + 4a_{11} l_{13} = (R_2 + R_6 + R_9 + R_{12}) Q^* - (R_2 + 2R_6 + 3R_9 + 4R_{12}) \quad (4.5)$$

Now, we have four equations (4.2, 4.3, 4.4, and 4.5) and four unknowns (a_5, a_8, a_{11}, Q^*), solving these equations we get, $W_5=65\mu\text{m}$, $W_8=87\mu\text{m}$, $W_{11}=120\mu\text{m}$, $Q_1=0.1436Q$.

Geometry with these dimensions is shown in Figure 4.8b; this geometry is used as the initial design to conduct the experiments. Several experiments were conducted to modify the initial design further to include the effects of droplets and merging chamber in the microfluidic system. Figure 4.8c shows the modified microfluidic chip design.

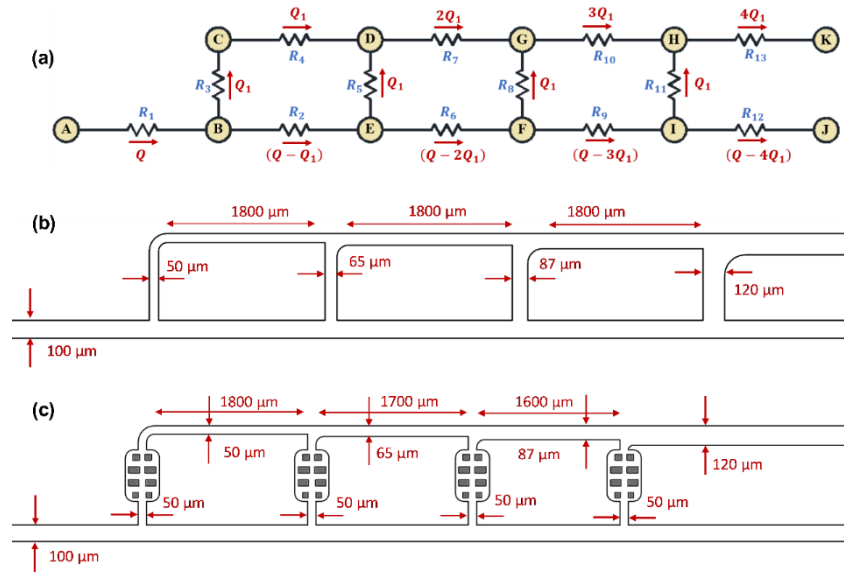


Figure 4.8. Flow rate distribution of multi-splitting and merging system. (a) The resistance network of a system considering the flow rate and hydrodynamic resistance of each branch without consideration of the presence of droplets in the system. (b) Schematic of the simplified microfluidic system in which same flow rate enters in four T-junctions with different width. (c) Schematic of the actual microfluidic system in the presence of four merging chambers designed in such a way that same flow rate enters in four T-junctions with a similar width.

4.6.2. Characterisation of Single-Layer Microvalves

Two critical parameters for the working of multi splitting and merging microfluidic system are the deformation caused by the valve in elastic PDMS and the time required for pressurising/depressurising of the valve. To find out more details about these two parameters set of experiments have been conducted by varying the pressure in the valve, these results are shown in Figure 4.9a,b. Figure 4.9a shows the plot of maximum deformation in PDMS against the valve pressure. We gradually increased the pressure in single-layer microfluidic valve from 0 mbar to 1800 mbar using Fluigent system. The deformation as a result of pressurising the valve is in the form of semi ellipse. Semi minor axis of this deformation is useful, as it will determine the volume of daughter droplet generated; hence it is plotted on Y-axis. When we gradually increase the valve pressure, deformation increases, maximum deformation for the pressure of 1800 mbar was observed to be 53 μm , which means it blocks more than 50 % of the main channel due to contraction. In the next set of experiments, we figured out the time required by the valve to achieve maximum deformation (Figure 4.9b). When the valve is pressurised at 1800 mbar, we captured the image sequence of deformation at 266 fps and plotted deformation against time. We observed that time required to attain maximum deformation is close to 20 ms. In the next set of experiments, we depressurised the valve from 1800 mbar to 0 mbar. We observed that time required for the channel wall to come back to its

original shape is close to 30 ms, which makes the total time required for pressurising and depressurising the valve to be 50 ms. Hence, the present microfluidic system can split the moving droplets with the frequency around 20 Hz. Figure 4.9c shows the selectivity of droplet splitting with the help of image sequences. As the first droplet approaches the junction, the valve is depressurised, which does not cause the droplet to split. Before next droplet arrives at the junction valve is actuated at 1800 mbar which causes elastic PDMS membrane to deform, and droplet splits at the junction. The valve is depressurised again, and the membrane comes back to the usual position, which allows the next droplet to pass the junction without splitting.

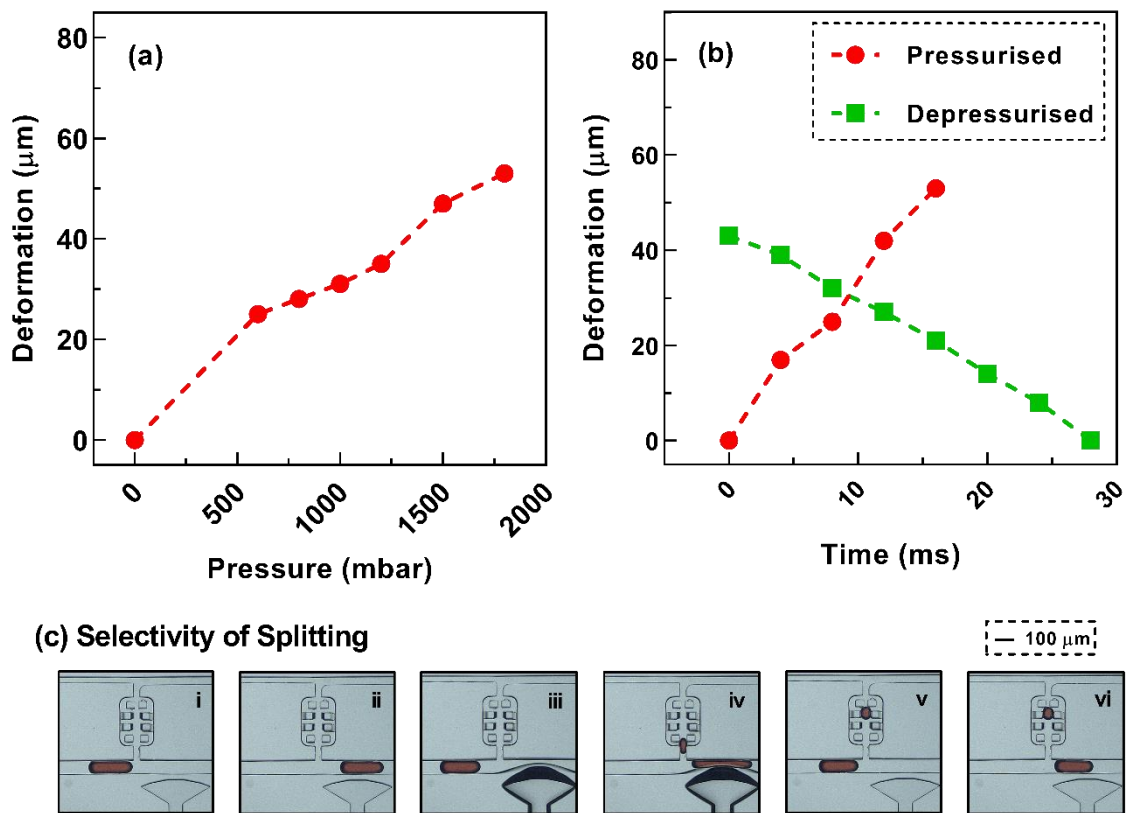


Figure 4.9. Characterisation of the single-layer microvalve. (a) Maximum deformation of the channel is plotted against different pressures that are applied to the single-layer valve. (b) Deformation of the channel is plotted against the time when the single-layer valve is fully pressurised to the pressure of 1800 mbar and fully depressurised, respectively. (c) Image sequence showing selectivity of the droplet splitting, red droplet arrives at the second junction and do not split at this junction, just before the second droplet arrives at this junction valve is actuated to split the droplet. Before the third droplet arrives at this junction valve is deactivated, and droplet does not split. Scale bar 100 μm .

Chapter 5

Curvature in the Reproductive Tract Alters Sperm-surface Interactions

5.1. Preface for Chapter 5

The possibility of studying and analysing individual cells in droplet microfluidics offers a promising opportunity to study natural fertilisation as one of the most unique biological phenomena that happens at the single cell level and as a result of sperm interactions with micro-curvatures of the female fallopian tube. The last project of this PhD thesis studies the role of the interface curvature on sperm behaviour using droplet microfluidics. The fallopian tube is lined with a highly complex folded epithelium surrounding a lumen that progressively narrows. To study the influence of this labyrinthine complexity on sperm behaviour, we use droplet microfluidics to create soft curved interfaces over a range corresponding to the *in vivo* environment. In this chapter, we reveal a dynamic response mechanism in sperm, switching from a progressive surface-aligned motility mode at low curvatures, to an aggressive surface-attacking mode at high curvatures ($<50 \mu\text{m}$ -radius). Sperm in the attacking mode swim $\sim 35\%$ slower, spend 1.66-fold longer at the interface and have a 66% lower beating amplitude than in the progressive mode. These findings demonstrate that surface curvature within the fallopian tube alters sperm motion from a faster surface aligned locomotion in distal regions to a prolonged physical contact with the epithelium near the site of fertilisation, the latter being known to promote capacitation and fertilisation competence.

This chapter has been submitted for publication to Nature Communication, and is currently awaiting revision. The candidate was the first author in this work and played the primary role in designing the research, performing the experiments, analysing the data, and writing the paper. Additional authors for the work include Ms. Melati Abdul Halim, Mr. Sagar N Agnihotri, Prof. Moira K. O'Bryan, Prof. Adrian Neild and Dr. Reza Nosrati. Their contributions were central to the publication of this work and are gratefully acknowledged and appreciated.

In this chapter; a short overview about sperm migration through the uterine tubes, a review of microfluidics for sperm analysis, and droplet microfluidic for cell biology study are presented in the introduction. This is followed by sperm motility modes and kinematics of sperm motility via a detailed analysis of experimental results. Finally, the chapter is concluded with a thorough discussion, methods and supplementary information.

5.2. Introduction

Sperm migration through the female reproductive tract is crucial for fertilization³¹¹⁻³¹³. The natural selection process *in vivo* is mainly achieved in the fallopian tube, where anatomical features and physiological conditions guide the sperm to the site of fertilization^{277,311}. The fallopian tube is lined with complex labyrinthine epithelium which forms crevice-like lumens which narrow towards the egg^{277,279,314} (Figure 5.1a) thus intensifying the role of hydrodynamic interactions in sperm function^{277,311,315}. The interaction of spermatozoa with these complex epithelial surfaces is thought to provide geometrical guidance, increase the chance of survival³¹⁶⁻³¹⁸, trigger sperm attachment/detachment mechanisms³¹⁹, stimulate capacitation³¹⁶ (a physiological change in sperm to enable fertilization competence) and play a key role in the timing of fertilization^{311,320}. It is known that chemical signalling, via oviductal secretory fluids³²¹⁻³²³, and surface effects influence sperm motion^{315,324-326}. However, how the physiology and anatomy of the, soft, curved epithelial surfaces in the fallopian tube regulates sperm dynamics and confers guidance is still poorly understood.

Sperm motion *in vivo* is influenced by confinement and surface proximity^{313,327}, whereby hydrodynamic forces^{328,329} and steric repulsion^{325,330} cause the cell to follow boundaries and accumulate at interfaces^{327,331,332}. Over the past 10 years, sperm motion and accumulation at flat solid surfaces have been studied extensively using advanced microscopy methods^{315,333-335}, mathematical modelling^{327,336-338}, and microfluidics^{312,339-341}. The results have been an improved fundamental understanding of sperm locomotion, demonstrating new swimming modes³⁴², and new opportunities for high-quality sperm selection³⁴³⁻³⁴⁶. However, in these previous studies, the *in vivo* environment is modelled *in vitro* by confinement using solid flat surfaces. Whilst, the lumens within the fallopian tube are curved, with radii of curvature on the order of 10 to 100 μm (ref. ²⁷⁷), formed via soft epithelial surfaces. The mechanical properties of this epithelium (with elasticity and stiffness of 10-10³ Pa) is considerably different to the rigid flat surfaces in common laboratory dishes or microfabrication materials that are six orders of magnitude stiffer (e.g. polystyrene, polydimethylsiloxane or glass have elasticity and stiffness of 10⁶-10⁹ Pa)^{347,348}.

Droplet microfluidics is well suited to the generation of soft curved interfaces of controlled shape and size³⁴⁹ for studying sperm behaviour, providing an environment that closely mimics the architecture and mechanical properties of the female fallopian tube. In these systems, immiscible

fluid phases form droplets of one phase within the other⁸⁰. This compartmentalization in droplets has proved a breakthrough in the biomedical area for applications in high-throughput drug screening^{22,41,80}, tissue and protein engineering^{272,350}, and single cell analysis⁹⁵. For example, droplets containing cells have previously been used to transport live organisms including yeast and zebrafish embryos^{28,274}. Retention of zebrafish embryo viability for up to two hours during transportation shows the capability of droplet microfluidics to handle cells as large as 500 μm in diameter²⁸. Individual live cells have also been isolated in droplets to study protein expression and antibody secretion in a well-controlled and monitored vessel^{195,264}. Such single cell encapsulation of live cells in droplet microfluidics points to an opportunity to study sperm dynamics at curved liquid-liquid interfaces, representing a more physiologically relevant interface than solid flat surfaces.

Here, using droplet microfluidics (Figure 5.1b), we observe and quantify sperm behaviour at soft curved interfaces using individual sperm encapsulated in droplets (ranging in size from 30 μm to 140 μm). We find that surface curvature triggers a dynamic response mechanism in sperm to switch from a progressive surface-aligned motility mode at smaller curvatures (*i.e.* larger droplets $>100 \mu\text{m}$ in radius) to an aggressive surface-attacking motility mode at bigger curvatures (*i.e.* smaller droplets $<50 \mu\text{m}$ in radius). In the aggressive attacking mode, sperm swim at an acute angle (to the normal of the tangent) and are constantly in contact with the interface, spending $0.037 \pm 0.007 \text{ s } \mu\text{m}^{-1}$ at the surface – for a 1.66-fold longer period of time than a sperm in the progressive motility mode. Using a theoretical model, we reveal that hydrodynamic effects lead to an active response mechanism in sperm to decrease their flagellar wave amplitude by up to 66% at larger curvatures (smaller droplets). These findings highlight the role of changes in mammalian fallopian tube geometry^{277,311} to either guide the sperm towards the site of fertilization or facilitate sperm-egg interaction. Specifically, the lower curvature of the epithelial tissue in the isthmus encourages a surface aligned motility mode for sperm navigation, while higher curvatures in the ampulla activates an aggressive-surface attacking motility mode to encourage sperm-epithelial cell contact thus facilitating sperm capacitation and ultimately fertilization potential.

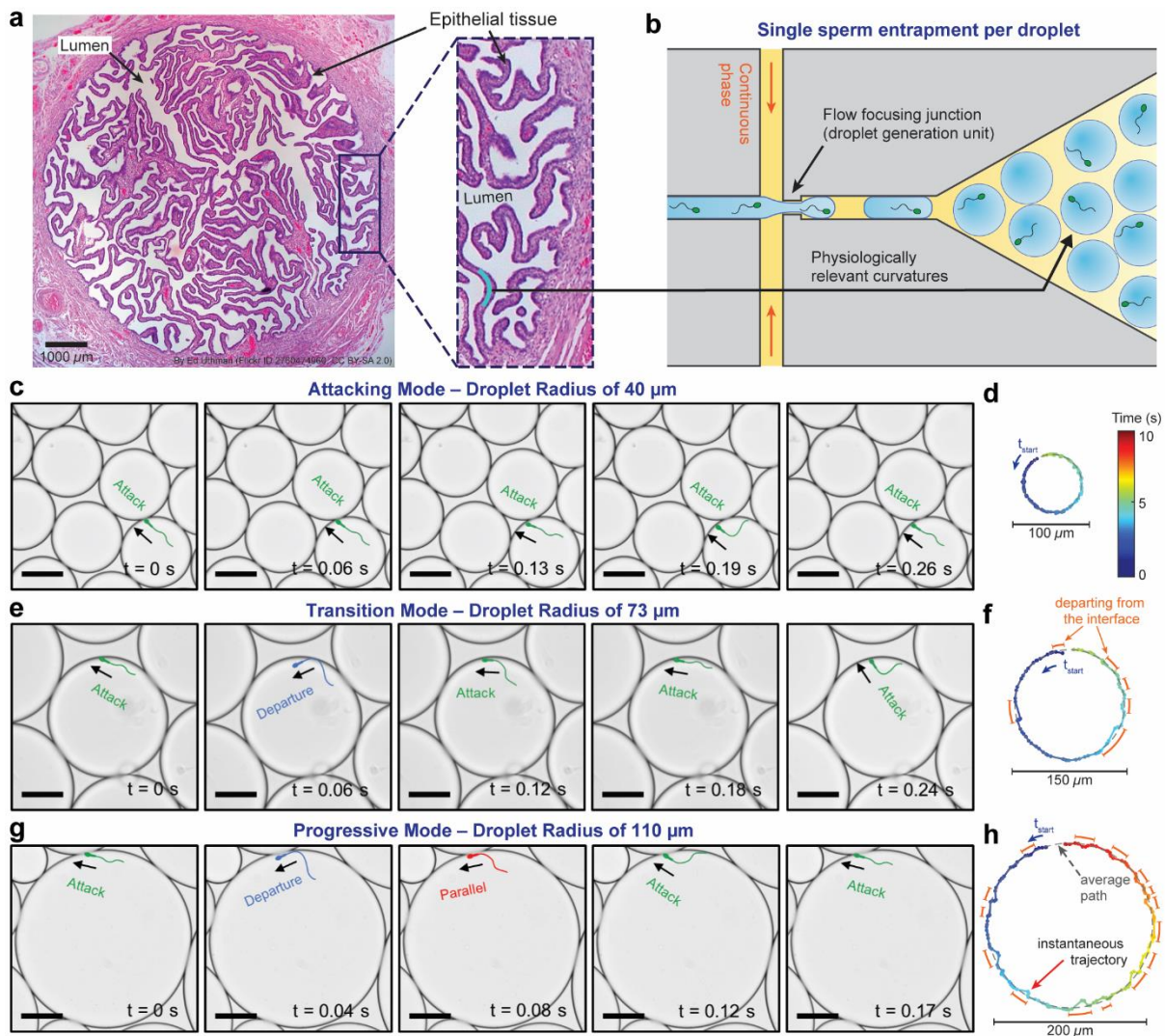


Figure 5.1. Sperm motility at curved interfaces representing the soft and folded epithelial tissue in the female fallopian tube. (a) The female fallopian tube is a complex microenvironment composed of soft and highly folded epithelial tissue, forming confined lumens with radius of curvatures ranging from $\sim 20 \mu\text{m}$ to over $150 \mu\text{m}$. (b) Encapsulation of individual sperm in monodisperse droplets ranging in size from 30 to $140 \mu\text{m}$, mimicking the physiologically relevant range of curvatures *in vivo*. Time-lapse images and representative trajectories of sperm swimming in (c,d) aggressive attacking, (e,f) transition and (g,h) progressive surfaces aligned motility modes in 40 , 73 , and $110 \mu\text{m}$ -radius droplets, respectively. The colour of the instantaneous swimming trajectories corresponds to time, as shown in the legend in d. Orange dashed lines highlight the deviation between instantaneous trajectory and average path due to departing behavior. Scale bars, $50 \mu\text{m}$. Images were contrast-adjusted for clarity.

5.3. Results

5.3.1. Sperm Motility Modes at Physiologically Relevant Curvatures

Individual bull sperm were encapsulated in droplets with radii ranging from 30 to 140 μm , and imaged for 12 s (Figure 5.1b; Methods). This range of droplet size represents the complex epithelial tissue in the female fallopian tube where the curvature of folded lumens varies from 20 to over 150 μm in radius (Figure 5.1a). In smaller droplets with <50 μm -radius, sperm were observed to swim consistently in contact with and almost normal to the interface in an ‘aggressive attacking mode’ (Figure 5.1c). In this attacking mode, sperm always followed the droplet boundary to swim along a perfect circle that was only 0.9 ± 0.3 μm smaller in radius than the droplet radius ($n=10$; Figure 5.7), by constantly pushing against the interface the instantaneous swimming trajectory was confined close to the average path (Figure 5.1d; Methods). In larger droplets, ranging in radius from 50 to 100 μm , sperm were still swimming pushing against the interface, but were observed to intermittently depart from, or align parallel to, the interface, swimming in a ‘transition mode’ (Figure 5.1e,f). For droplets >100 μm in radius, in contrast to the attacking mode, sperm were observed to routinely align parallel to, or depart from, the interface (Figure 5.1g) in a ‘progressive surface aligned motility mode’. In the progressive mode, sperm swam freely along a circular average path that was up to 4.3 ± 0.9 μm smaller in radius than the droplet ($n=10$; Figure 5.7), with the instantaneous swimming trajectory oscillating around the average path (Figure 5.1h). These results demonstrate that surface curvature alters sperm motion, guiding progressive motility at lower curvatures, and promoting increased and prolonged surface contact at higher curvatures.

We characterized the swimming behavior of sperm at curved interfaces (Figure 5.2) by tracking sperm for 12 s in droplets ranging in radius from 30 μm to 140 μm . With respect to the orientation of sperm at the interface, Figure 5.2a shows the average angle between the longitudinal axis of sperm and the tangent line to the droplet, hereafter referred to as the angle of attack, α . For droplets with radius smaller than 100 μm , the angle of attack exhibited a negative correlation with the droplet size. Specifically, the angle of attack decreased significantly by 54% from 70° to 32° by increasing the droplet radius from 30 μm to 100 μm , respectively, and then plateaued at 30° for larger droplets. For a pusher microswimmer such as sperm, both the conical envelope of the flagellar wave^{334,338}, and the hydrodynamic flow field around the tail^{351,352} interact with the interface to define the angle of attack. At curvatures

smaller than 100 μm in radius, the interaction between sperm flagellum and the elevated surface upstream of the sperm head was significant, amplifying both the hydrodynamic effects and the steric repulsion to align the cell at an acute angle with respect to the interface. However, a curvature larger than 100 μm in radius essentially acts as a flat surface to guide the sperm, with the conical envelope of the flagellar wave almost aligned with the surface, resulting in an angle of attack of $\sim 30^\circ$.

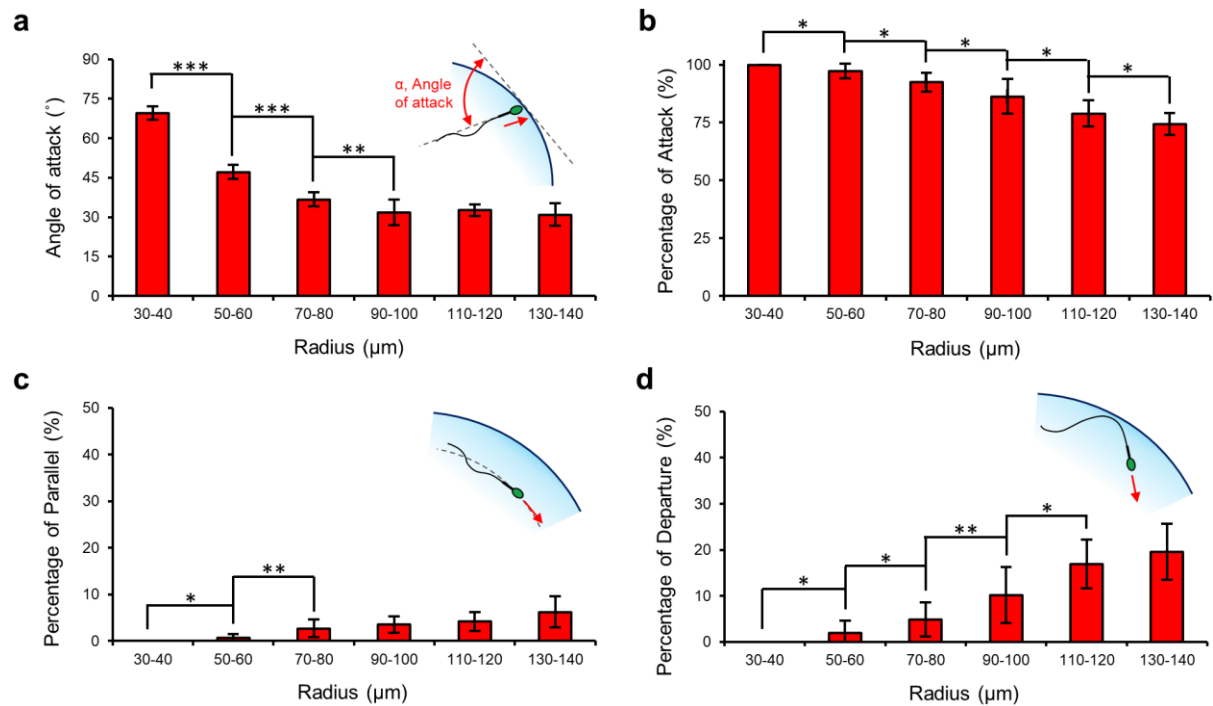


Figure 5.2. Characterization of sperm motility modes at curved interfaces. (a) Angle of attack, α , and the percentage of the 12 s tracked swimming trajectory in which the sperm is (b) attacking ($2^\circ < \alpha < 90^\circ$), (c) swimming parallel to ($-2^\circ < \alpha < 2^\circ$), and (d) departing ($\alpha < -2^\circ$) the interface in droplets ranging from 30 to 140 μm in radius. Values are reported as mean \pm s.d. ($n \geq 10$), and P values were determined using one-way ANOVA, $*P \leq 0.05$, $**P \leq 0.01$, $***P \leq 0.001$.

In the attacking mode (specifically, for curvatures smaller than 50 μm in radius), sperm consistently (100% of the 12 s-tracked trajectory) aligned at an acute angle with the interface ($29^\circ < \alpha < 90^\circ$) to attack and swim in contact with the interface (Figure 5.2), with the angle of attack always greater than 66° . Notably, the range of curvature in the attacking mode is relevant to that of the later part of the female fallopian tube in ampulla, close to the site of fertilization, where physical contact between sperm and the epithelial surface is necessary for capacitation³¹⁶. In the transition and progressive motility modes, the tendency of sperm to attack the interface decreased linearly ($R^2=0.98$, $P \leq 0.001$ with Pearson correlation) with

increasing droplet size (Figure 5.2b) from 97% in 50 μm -radius droplets to 74% in 140 μm -radius droplets. In contrast, the tendency of the sperm to swim parallel with ($-2^\circ < \alpha < 2^\circ$) or depart from ($\alpha < -2^\circ$) the interface increased from 1% and 2% in 50 μm -radius droplets to 6% and 20% in 140 μm -radius droplets, respectively (Figure 5.2c,d). The results indicate that sperm exhibit a greater tendency to attack and swim in contact with the surface at higher curvatures, whilst at lower curvatures the sperm navigate along the interface.

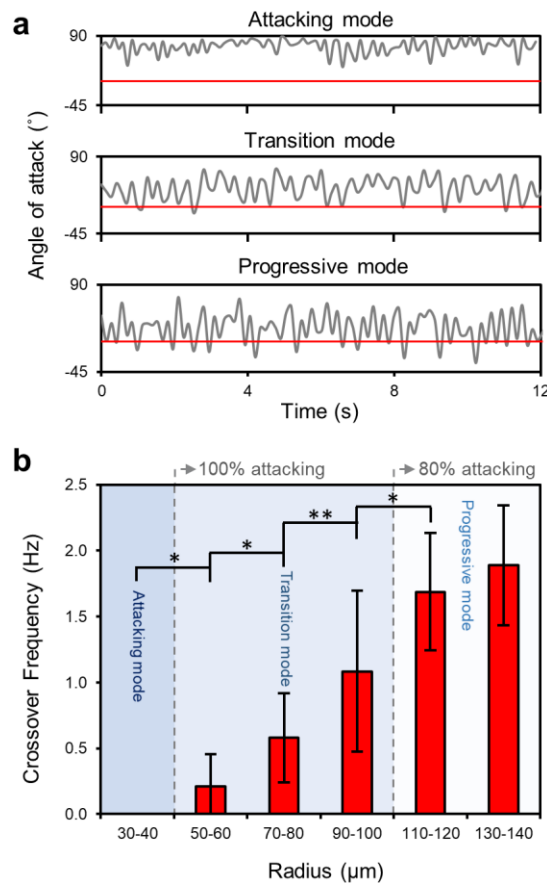


Figure 5.3. Characterization of the temporal behavior of sperm in the attacking, transition, and progressive modes. (a) Representative variations of the angle of attack along the 12 s tracked swimming trajectories for sperm swimming in the attacking, transition, and progressive modes. The horizontal red line indicates the threshold angle of attack of 2° for the sperm to align parallel to or depart from the interface. (b) Crossover frequency as a function of droplet radius. Values are reported as mean \pm s.d. ($n \geq 10$), and P values were determined using one-way ANOVA, $*P \leq 0.05$, $**P \leq 0.01$.

Figure 5.3 quantifies the temporal behaviour of sperm to crossover from an attacking orientation to a parallel or departing orientation. The crossover frequency was zero for sperm in the attacking mode, and increased significantly ($R^2=0.98$, $P \leq 0.001$ with Pearson correlation) in the transition and progressive modes, from 0.2 Hz in 50 μm -radius droplets to 1.7 Hz in 120

μm -radius droplets (Figure 5.3b). Sperm exhibited sustained attacking behaviour (radius of curvature $<50 \mu\text{m}$) to align at acute angle with the interface for the whole 12 s of the tracked trajectory (Figure 5.3a), with small variation in the angle of attack and without any tendency to crossover to parallel or departing orientation (Figure 5.3b). However, in the transition mode, sperm showed an intermittent behaviour, switching from a sharp angle of attack to a parallel or departing orientation at irregular time intervals (happening once per every 1 s to 4 s, depending on the radius of curvature). In the progressive mode, this behaviour became more stable and sperm exhibited an alternating behaviour to regularly crossover between attacking and non-attacking orientations every $679 \pm 433 \text{ ms}$ ($n=20$), regularly detaching from the interface. Notably, the modulus of the angle of attack was always smaller than 90° in all the swimming modes, demonstrating that the motion around the interface is unidirectional, hence, the sperm is effectively guided along the interface.

5.3.2. Kinematics of Sperm Motility at Curvatures

Figure 5.4 details the key motility parameters for sperm swimming in attacking, transition and progressive modes as a function of droplet radius. The measured curvilinear velocity (VCL) and average path velocity (VAP) of sperm in the attacking mode (droplet radius $<50 \mu\text{m}$) were significantly lower by at least 24% and 31% (Figure 5.4a,b, $P \leq 0.01$), respectively, compared with sperm in the transition mode (in 50 to 110 μm droplets). VCL and VAP slightly increased in the transition mode for sperm in larger droplets, and plateaued at $88.56 \mu\text{m s}^{-1}$ and $73.55 \mu\text{m s}^{-1}$ for sperm in the progressive mode (droplet radius $>110 \mu\text{m}$). The results demonstrate that sperm in the attacking mode are 35% slower than sperm in the progressive mode, prolonging the physical interaction between sperm head and the interface by 185% at tight curvatures. Similar to VCL and VAP, the amplitude of lateral head displacement (ALH) and beat cross frequency (BCF) were also significantly lower, by 66% (decreasing from over $8.61 \mu\text{m}$ to $2.94 \mu\text{m}$, $P \leq 0.001$) and 61% (decreasing from over 4.17 Hz to 1.62 Hz , $P \leq 0.01$) in the attacking mode compared to the progressive mode (Figure 5.4c,d), demonstrating a highly restricted flagellar motion and a significant reduction in head oscillation in the attacking mode. These reductions in beating amplitude and frequency contribute to a reduction in the progressive velocity³⁵³. The increased proximity to the interface at tight curvatures ($<50 \mu\text{m}$ in radius) dampens the flagellar motion, due to increased drag coefficients and friction^{353,354} to reduce the ALH and restrict the instantaneous swimming path close to the average path (Figure 5.4e).

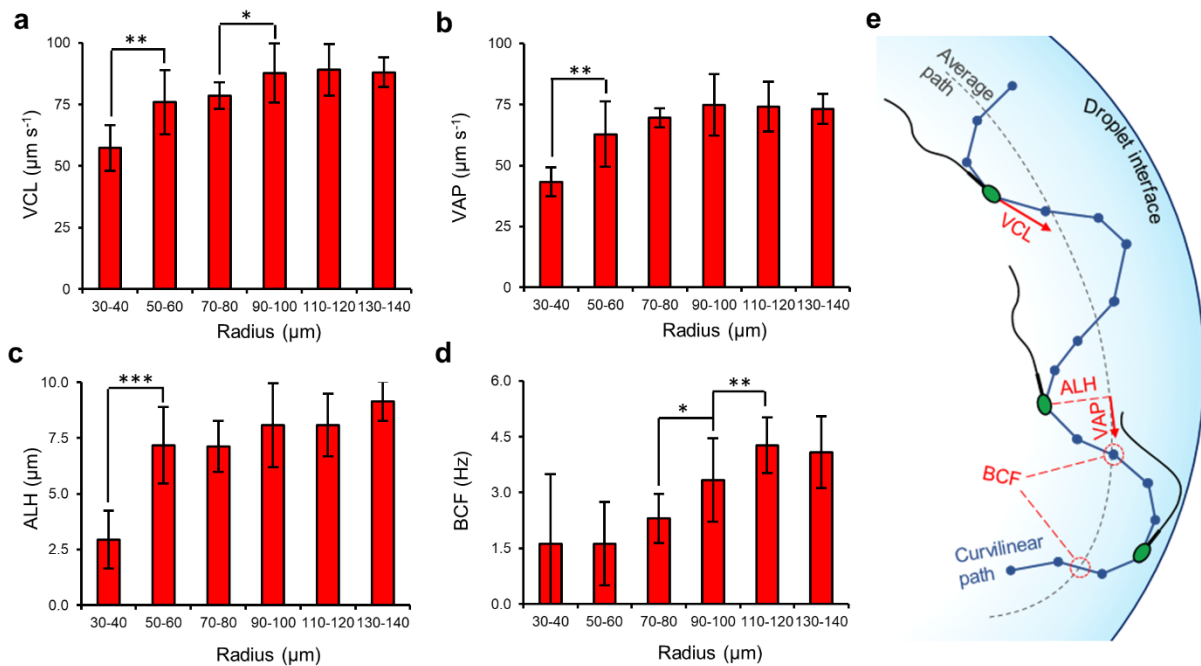


Figure 5.4. Sperm motility parameters at curved interfaces. (a) Curvilinear velocity (VCL), (b) average path velocity (VAP), (c) amplitude of lateral head displacement (ALH), and (d) beat cross frequency (BCF) for sperm swimming in droplets ranging in radius from 30 μm to 140 μm . Values are reported as mean \pm s.d. ($n \geq 10$), and P values were determined using one-way ANOVA, $*P \leq 0.05$, $**P \leq 0.01$, $***P \leq 0.001$ (see Table 5.1). (e) Schematic representation of the measured sperm motility parameters.

5.4. Discussion

We used droplet microfluidics to study sperm behavior at soft curved interfaces, closely mimicking the curvature²⁷⁷ and mechanical properties^{347,348} of folded epithelial tissue within the female fallopian tube. Our results reveal that hydrodynamic effects activate a response mechanism in sperm to switch from a ‘progressive motility’ mode at low curvatures ($>100 \mu\text{m}$ in radius) to a distinct ‘aggressive surface-attacking motility’ mode at tight curvatures ($<50 \mu\text{m}$ in radius). In the attacking mode, the sperm head is aligned at an acute angle and is consistently in contact with the interface. In strong contrast to the progressive mode observed at low curvatures and planar surfaces, where sperm routinely align parallel or depart from the interface. Sperm also exhibit a ‘transition motility mode’ at moderate curvatures (ranging in radius from 50 μm to 100 μm), with mixed characteristics of progressive and attacking modes. The average angle of attack for sperm in the attacking mode was found to be 70° , which reduced significantly by 54% in the progressive mode and plateaued at $\sim 30^\circ$. Several factors, associated with short-range steric interactions^{330,351} and long-range hydrodynamic effects^{336,352}, contribute to orient the sperm at curvatures, including: (i) contact interactions between sperm tail and the elevated curved surface upstream of sperm, (ii) increased drag coefficients and friction

experienced by the sperm due to nearby boundaries^{353,354} particularly upstream of the cell, and (iii) the interaction between the hydrodynamic flow field around the sperm tail and the elevated interface on the two sides of sperm^{336,355}. Due to these interactions, in the aggressive attacking mode, sperm always (100% of the trajectories) swim at an acute attack angle, relatively normal to the interface. However, in the progressive mode, sperm exhibit a lower tendency to attack the interface (lower than 77% of the trajectories), rather they more routinely align parallel (5%) or depart (18%) the interface every 679 ± 433 ms.

To fully interpret the experimental results, we developed a simple theoretical model to estimate the angle of attack using similarity of triangles (see Supplementary Information). For a sperm of length l and beating amplitude of δ with the conical envelope of the flagellar wave aligned with a curvature of radius R , the angle of attack can be estimated as:

$$\alpha = \sin^{-1} \frac{\sqrt{\delta^2 + l^2}}{2R} + \tan^{-1} \left(\frac{\delta}{l} \right) \quad (5.1)$$

From our experimental measurements for sperm freely swimming near a planar surface, the total length of bull sperm was $\sim 70 \mu\text{m}$, beating with a relatively fixed flagellar wave amplitude of $\sim 15 \mu\text{m}$ at the end of the tail, in agreement with previous studies³⁵⁶⁻³⁵⁸.

Figure 5.5 compares the experimentally measured angle of attacks with estimated values obtained from the theoretical model. While following almost the same trend, for fixed δ of $15 \mu\text{m}$, the theoretical model deviates considerably from experimental results, over estimating the angle of attack by 13% for $39 \mu\text{m}$ droplets and under estimating the angle of attack by 10% for $131 \mu\text{m}$ droplets. To understand whether this discrepancy is attributed to the influence of curvature on sperm motility behavior, we measured the amplitude of flagellar wave for sperm in droplets of different curvatures (Figure 5.5b). The results reveal that sperm decrease their flagellar wave amplitude by 66% at high curvatures (from $20.9 \mu\text{m}$ in $131 \mu\text{m}$ -radius droplets to $7.2 \mu\text{m}$ in $39 \mu\text{m}$ -radius droplets), with the results from a theoretical model with varying δ in full agreement with experimental measurements (Figure 5.5a). The effect of high curvatures to reduce the flagellar wave amplitude, as also suggested by lower ALH values, contributes to reduce the swimming velocity by 35% in the attacking mode, and to prolong the physical interaction between the sperm head and the interface by up to 185%. This correlation highlights

the potential importance of attacking mode for sperm in regions of the fallopian tube where physical interaction between sperm and the epithelial tissue is crucial for capacitation³¹⁶.

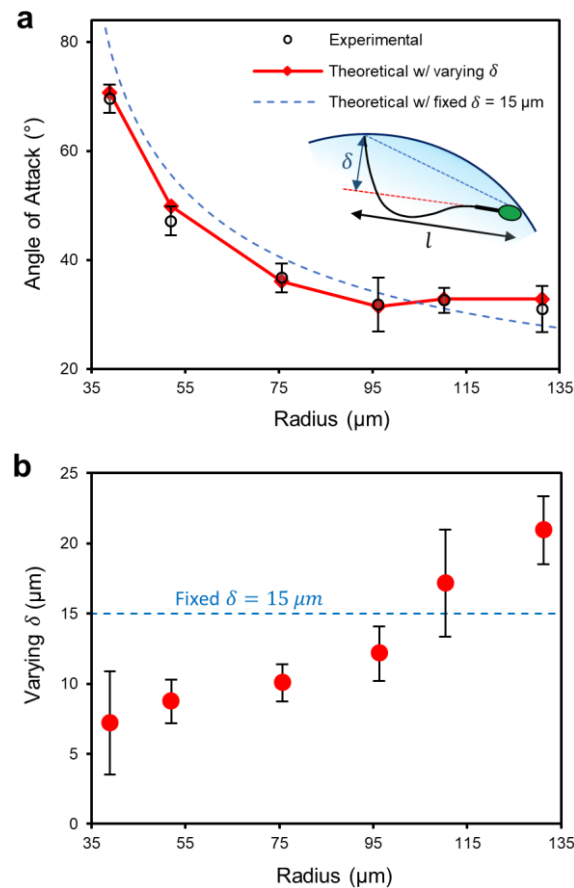


Figure 5.5. Theoretical model for estimating the angle of attack. (a) Angle of attack from experimental measurements as compared with theoretical values with fixed (dashed line) and varying (solid line) flagellar wave amplitude as a function of droplet radius. Schematic representation of the reference system and modeled sperm shown by the inset. (b) Experimentally measured flagellar wave amplitudes as a function of droplet radius. Values are reported as mean \pm s.d. ($n=10$ per radius).

The flagellar wave in sperm is generated by the ATP-activated dynein motors attached to the 9+2 microtubules within outer nine microtubules of the axoneme at the central core of the flagellum³¹². The outer nine microtubule doublets are connected to each other by nexin links and to the central pair of microtubules via radial spokes. Dynein arms sequentially slide each of the outer microtubules over the neighboring doublet, which bend the flagellum due to spatial restrictions imposed by the radial spokes and nexin links, forming the flagellar wave^{312,359}. The flagellar waveform is defined by balancing the active sliding forces of the dynein motors with hydrodynamic forces and passive forces due to the axoneme and accessory structures surrounding the axoneme^{353,360}. Our results indicate that, in the attacking mode at tight

curvatures, the increased hydrodynamic drag and additional spatial restrictions (steric interactions) create a force imbalance to regulate the flagellar wave and reduce the beat amplitude, potentially by also activating an intercellular regulation mechanism. Dynamic constraints of sperm head and tail have been shown to increase the intercellular sliding force of dynein arms^{361,362}, and reduce the sliding amplitude due to the large drag experienced by the flagellum³⁶³. In response to change in the medium viscosity^{364,365}, a signal coordinated through radial spokes has been suggested as an intercellular response mechanism for regulating dynein sliding forces and power production. The increase hydrodynamic drag for sperm at tight curvatures may cause a similar effect to activate this intercellular mechanism. Our results are also in agreement with the switch-inhibition mechanism that suggests force imbalance on the two sides of the flagellum is required to inhibit dynein arms on one side of the cell and drive the flagellar wave³⁶⁶. At tight curvatures with sperm oriented almost normal to the interface, the hydrodynamic forces and steric interactions on the two sides of sperm are balanced more effectively (as compared with sperm at bigger curvatures), mainly due to almost identical proximity of sperm to elevated interfaces on the two sides, and therefore, act to reduce the bend in flagellar wave based on the switch-inhibition mechanism.

With respect to reproduction, our findings reveal the role of increasing geometrical complexity and confinement of the female fallopian tube in natural fertilization^{277,313}. As sperm progress through the fallopian tube, from uterotubal junction (300 μm in radius) to isthmus and ampulla, the tract becomes highly folded and confined with epithelial lumens narrowing towards the site of fertilization (curvatures increasing from >150 to <20 μm -radius in size), exposing sperm to epithelial surfaces of higher curvatures^{277,313,326}. The isthmus, in the beginning part of the fallopian tube, includes a thick muscular layer²⁷⁷, resulting in a simple geometry with relatively large radius of curvatures in the folded epithelial tissue. These low curvatures encourage progressive and transition modes to enable faster locomotion towards the site of fertilization. However, the increased curvature of the epithelial lumens in ampulla and infundibulum, closer to the site of fertilization, encourage the aggressive attacking mode to increase the physical contact between sperm and the epithelial tissue and to prolong this interaction, increasing the chance of sperm survival³¹⁶⁻³¹⁸ and stimulating capacitation³¹⁶.

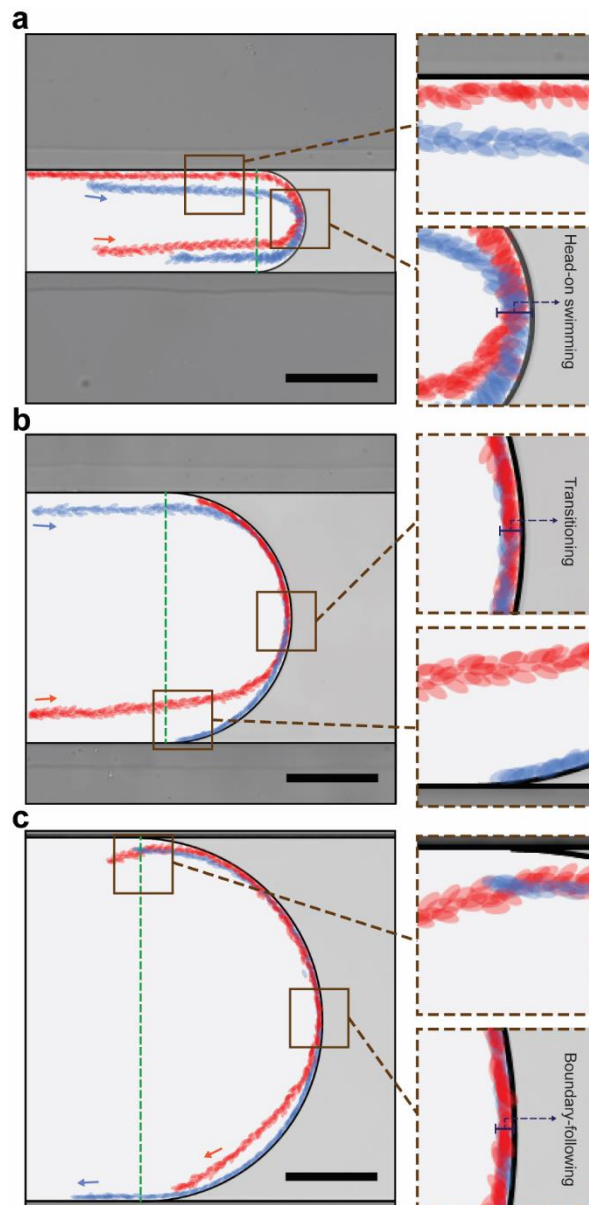


Figure 5.6. Sperm motility behavior at curved interfaces in microchannels that represent the increasing complexity of the female fallopian tube geometry. Overlaid trajectories of two representative sperm (head shown in red and blue) in microchannels that mimics the relevant range of curvatures in infundibulum, ampulla, and isthmus, with sperm exhibiting (a) head-on swimming behavior in the attacking mode, (b) a combination of head-on swimming and boundary following behavior in the transition mode, and (c) boundary-following behaviors in the progressive mode, respectively. Images were contrast-adjusted for clarity. Scale bars, 100 μm .

To better highlight the role of surface curvature on regulating sperm behavior with respect to natural fertilization, when a straight swimmer faces a curvature, Figure 5.6 shows overlaid trajectories of sperm in microchannels of different sizes, with curvatures that mimic relevant ranges of curvature in infundibulum, ampulla, and isthmus. In a 390 μm wide microchannel (radius of curvature of 195 μm), that is relevant to the geometry of the isthmus, sperm swim freely in the progressive mode along the interface by exhibiting the boundary-following

behaviour³³¹, and a relatively fast locomotion (Figure 5.6c), spending only $0.022 \pm 0.001 \text{ s } \mu\text{m}^{-1}$ at the curvature. The overlaid trajectory was confined within $5 \pm 1 \text{ } \mu\text{m}$ of the curvature, almost equal to the length of the minor axis of sperm head³⁵⁸, confirming a directed locomotion with a relatively parallel head orientation. In a smaller microchannel with $110 \text{ } \mu\text{m}$ in width (radius of curvature of $55 \text{ } \mu\text{m}$), relevant to upstream regions of ampulla and infundibulum, sperm swim in the attacking mode by exhibiting a head-on interface swimming behavior (Figure 5.6a), spending as high as $0.037 \pm 0.007 \text{ s } \mu\text{m}^{-1}$ at the curvature – for a 1.66-fold longer period of time than a sperm in the progressive mode. The thickness of overlaid sperm heads along the trajectory was $10 \pm 1 \text{ } \mu\text{m}$, almost equal to the length of the major axis of sperm head³⁵⁸, confirming a head-on aggressive surface interaction.

Taken together, these findings show that the increasing geometrical complexity of the female fallopian tube alters sperm motion to guide the locomotion at lower curvatures but to increase and prolong surface contact at higher curvatures, enabling sperm capacitation and fertilization closer to the site of fertilization. These finding also provides new insights into how surface curvature can be used to guide the locomotion for sperm selection applications or to increase surface interactions for understanding sperm attachment/detachment mechanisms. Motility of sperm at curvatures could also be relevant to the behavior of other pusher type microorganisms and eukaryotic microswimmers at curvatures, such as *E. coli*³³⁶, and motile *Caulobacter crescentus*³⁶⁷, particularly to understand their transport process in higher organisms.

5.5. Methods

5.5.1. Sperm Sample Preparation

Bull semen was purchased in straws (ABS Australia) and stored in liquid nitrogen tank until used. Prior to the experiment, bull semen was thawed in $37 \text{ } ^\circ\text{C}$ water bath for 5 minutes and removed from the straw using an artificial insemination syringe. The sample was then washed using a physiologically relevant HEPES-buffered salt solution (117 mM NaCl, 5.3 mM KCl, 2.3 mM CaCl_2 , 0.8 mM MgSO_4 , 0.8 mM $\text{Na}_2\text{H}_2\text{PO}_4$, 5.5 mM D-Glucose, 0.03 mM Phenol Red, 4 mM NaHCO_3 , 21 mM HEPES, 0.33 mM Na Pyruvate, 21.4 mM Na Lactate, supplemented with 1 mg ml^{-1} polyvinyl alcohol) via centrifugation at 200 g for 12 min, and then resuspended in 200 μl of pre-warmed buffer. Washed sperm sample were diluted to a concentration determined, by Poisson statistics³⁶⁸, to ensure the maximum probability of encapsulating single sperm in each droplet.

5.5.2. Device Fabrication

A mask for a polydimethylsiloxane (PDMS) microfluidic device master mold was designed in AutoCAD software. The device comprises two inlets, one outlet, a 100 μm flow focusing junction for droplet generation and an expansion chamber (Figure 5.1b; Figure 5.9). The expansion chamber was designed to reduce the progression speed of the droplets and so holding them in place for long-term imaging. The master mold was fabricated by patterning Hexamethyldisilazane and AZ[®] nLOF 2035 negative photoresist on a silicon wafer and then selectively etching the silicon using Oxford Plasma Lab100 System to achieve a desired depth of 62 μm . The top layer of the device was fabricated in PDMS (Silgard 184; Dow Corning, MI, USA) with 10:1 mixing ratio, and cured for 4 hours at 70°C on a hotplate. The inlet and outlet ports were then punched in the cured PDMS. Finally, the PDMS layer was bonded to a glass slide using an oxygen plasma.

5.5.3. Experimental Procedure

A standard droplet microfluidic generation technique (flow focusing junction) was used, in which a constant flow of buffer and sample meet at a microfluidic junction resulting in monodisperse droplets encapsulating single sperm⁵⁸. A synthetic and biocompatible oil (3M[™] Novec[™]) was used as the continuous phase in which 2% of a biocompatible surfactant (Pico-Surf[™] 1, Sphere Fluidics, UK) was added to avoid droplets from merging with each other. A pressure pump (MFCST[™]-EZ, Fluigent system) was used to adjust the inlet pressures for both the dispersed (sperm & buffer) and continuous phases (oil and surfactant). After producing the droplets, the outlet pressure was adjusted so that the droplets stayed static in the expansion chamber where they were imaged. Between experiments, the ratio of the two inlet pressures was adjusted such that droplets of different sizes were generated. It is noteworthy that, due to the 62 μm height of the channel and relatively large size of the droplets, each droplet is essentially a flattened disk rather than a sphere and sperm motion is mainly limited into a two-dimensional (2D) plane, allowing for straight-forward visualization in 2D.

5.5.4. Microscopy

An inverted fluorescence microscope (Olympus IX83, Japan) equipped with an ORCA-Flash4.0 V3 Digital CMOS camera (Hamamatsu Photonics, Japan) and a stage incubator was used to capture 20 \times magnification images of sperm in bright-field imaging modes at 15 and 25 frames per second.

5.5.5. Image Analysis

The image processing software ImageJ was used to measure size of the droplets, process images, and manually track sperm, measure the flagellar wave amplitude (δ), and angle of attack (α). The location of sperm head was tracked manually in each droplet for 12 s (10 sperm were tracked in each case). A custom-written script in Matlab was then used to analyse the motility parameters for the tracked sperm and reconstruct the swimming trajectory. The motility parameters were defined according to World Health Organisation (WHO) guidelines³⁶⁹ as: (i) curvilinear velocity (VCL): time-average velocity of the sperm head along its instantaneous trajectory; (ii) average path velocity (VAP): time average velocity of the sperm following its average trajectory; (iii) amplitude of lateral displacement (ALH): time-average deviation of the sperm head from its average path; (iv) beat cross frequency (BCF): the frequency at which the instantaneous sperm trajectory crosses the average path trajectory. The angle of attack, α , was also measured manually as the angle between sperm axis and the tangent line to the droplet. A statistical analysis was performed using one-way ANOVA between each two groups, where P less than 0.05 was considered significant (* $P \leq 0.05$, ** $P \leq 0.01$, *** $P \leq 0.001$).

5.6. Supplementary Information

5.6.1. Supplementary Figures

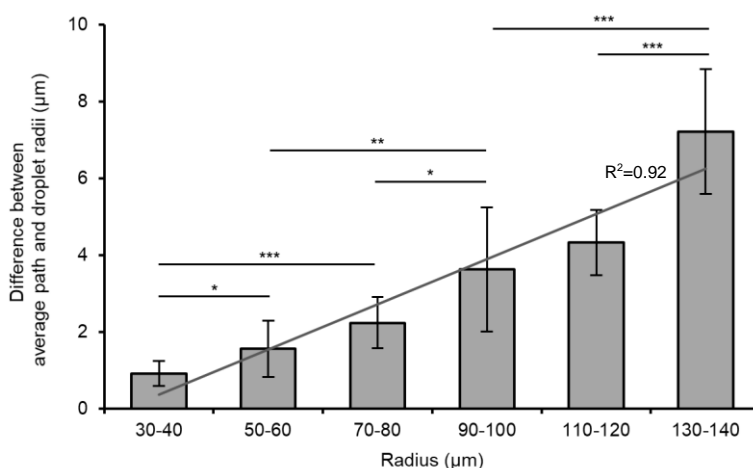


Figure 5.7. Difference between average path and droplet radius for three different modes of sperm swimming in droplets with different size. The distance between the boundary of the surface and the circular average path of the sperm during the different swimming modes increases while the droplet size increases.

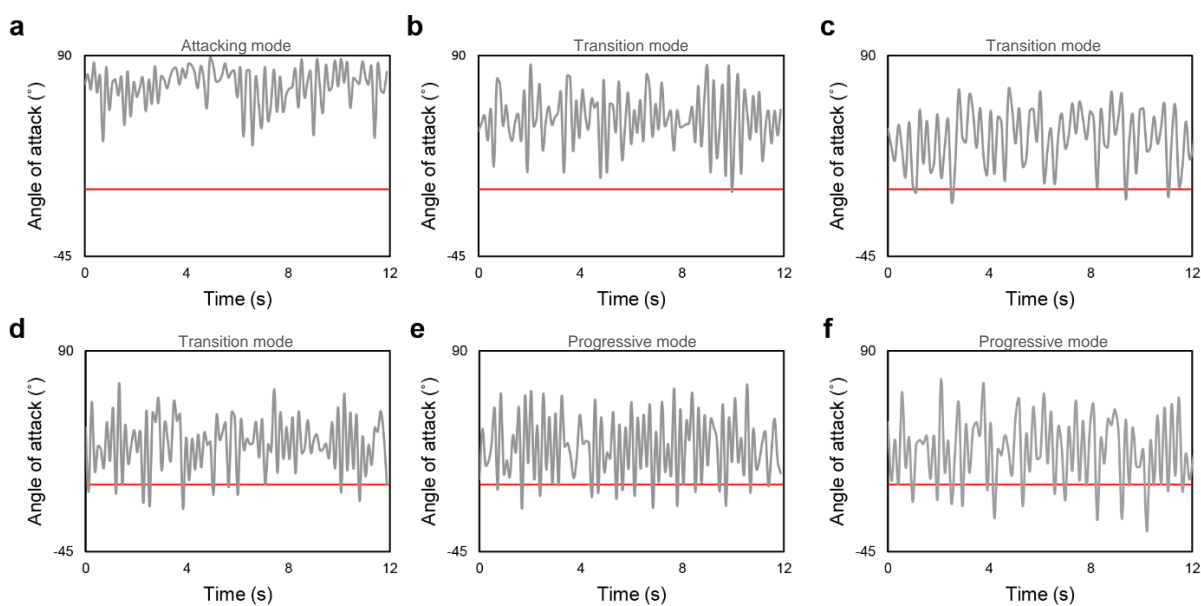


Figure 5.8. Temporal variations in the angle of attack for sperm in the attacking, transition, and progressive modes. Representative variations of the angle of attack along the 12 s tracked swimming trajectories for sperm swimming in droplets with radius ranging from (a) 30 μm to 40 μm , (b) 50 μm to 60 μm , (c) 70 μm to 80 μm , (d) 90 μm to 100 μm , (e) 110 μm to 120 μm , and (f) 130 μm to 140 μm . Sperm are swimming in the attacking mode in a, in the transition mode in b-d and in the progressive mode in e and f.

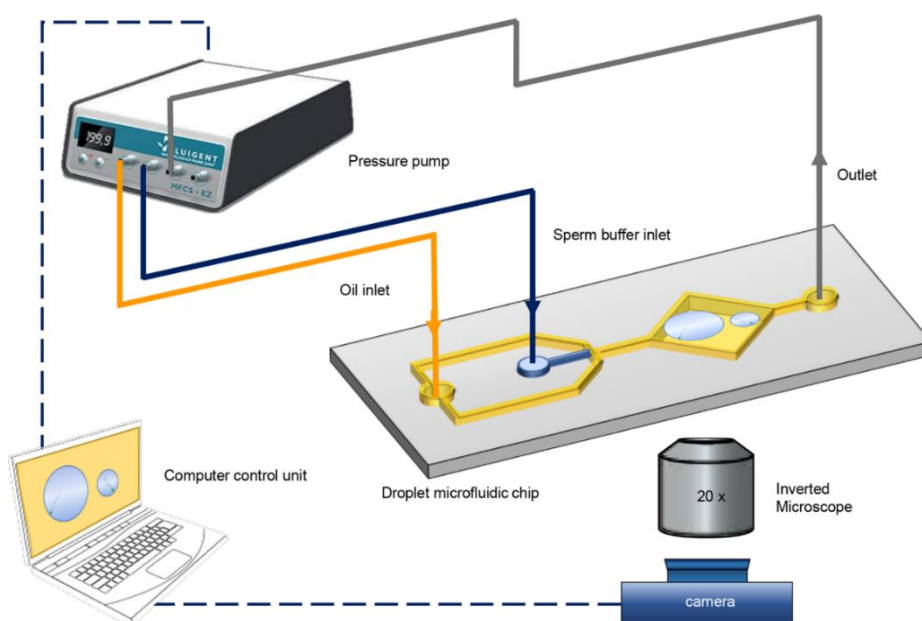


Figure 5.9. Schematic shows the setup used for droplet microfluidic based sperm motility analysing. The inlets and outlet of the droplet microfluidic system is connected to a microfluidic flow control system (MFC5TM-EZ, Fluigent system). Setup includes ORCA-Flash4.0 V3 Digital CMOS camera (Hamamatsu Photonics, Japan), inverted fluorescence microscope (Olympus IX83, Japan) and Fluigent systems, connected to a computer for data collection.

5.6.2. Supplementary Table

Table 5.1. Statistical analysis of sperm motility parameters. P values were calculated using one-way ANOVA based on at least 10 points for each range of radius of droplets, * $P \leq 0.05$, ** $P \leq 0.01$, *** $P \leq 0.001$ and NS denotes not significant.

Group	a	b	c	d	e	f									
Radius of Droplet	30-40	50-60	70-80	90-100	110-120	130-140									
Parameter\Group	a,b	a,c	a,d	a,e	a,f	b,c	b,d	b,e	b,f	c,d	c,e	c,f	d,e	d,f	e,f
VCL	**	***	***	***	***	NS	*	**	*	*	**	*	NS	NS	NS
VAP	**	***	***	***	***	NS	*	*	*	NS	NS	NS	NS	NS	NS
ALH	***	***	***	***	***	NS	NS	NS	**	NS	*	**	NS	NS	NS
BCF	NS	NS	*	**	**	NS	**	***	***	*	***	***	**	NS	NS
Angle of attack	***	***	***	***	***	***	***	***	***	**	*	**	NS	NS	NS
Percentage of attack	*	***	***	***	***	*	***	***	***	*	***	***	*	**	*
Percentage of parallel	*	***	***	***	***	**	***	***	***	NS	NS	*	NS	*	NS
Percentage of departure	*	**	***	***	***	*	**	***	***	**	***	***	*	*	NS
Crossover Frequency	*	***	***	***	***	*	***	***	***	**	***	***	*	*	NS

5.6.3. Theoretical Model for the Angle of Attack

A theoretical model was developed based on similarity of triangles to obtain the angle of attack, α , for sperm of length l with a beating amplitude of δ at a curved interface with a radius of curvature of R (Figure 5.10).

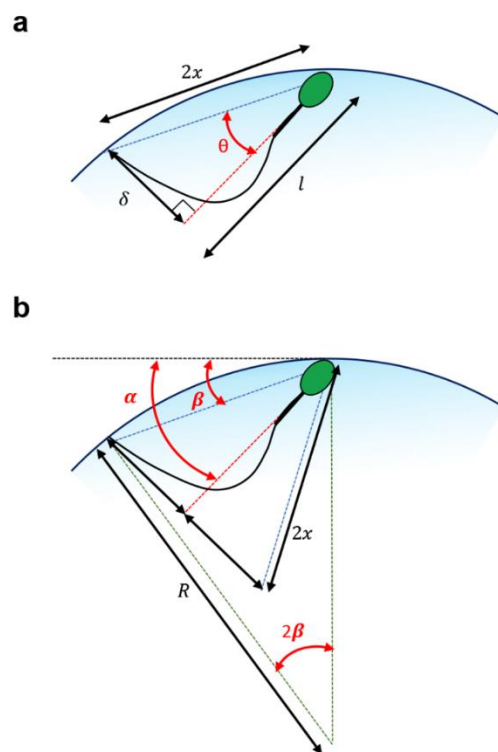


Figure 5.10. Theoretical model for calculating the angle of attack at curvatures. (a) Sperm with the conical envelope of the flagellar wave aligned with the curvature and (b) the schematic used to drive the theoretical model for the angle of attack.

The hypotenuse of the right-angle triangle formed by δ and l in Figure 5.10 is identified as $2x$ and can be described as:

$$2x = \sqrt{\delta^2 + l^2} \quad (5.2)$$

$$x = \frac{\sqrt{\delta^2 + l^2}}{2} \quad (5.3)$$

The angle between the longitudinal axis of sperm and the edge of the flagellar envelope, θ , is:

$$\tan \theta = \tan^{-1}(\delta/l) \quad (5.4)$$

Therefore, the angle between the radii of the curvature formed by the conical envelope, 2β , is:

$$\beta = \sin^{-1}(x/R) \quad (5.5)$$

$$\sin \beta = \frac{\sqrt{\delta^2 + l^2}}{2R} \quad (5.6)$$

Since $\alpha = \beta + \theta$, the angle of attack can be obtained as a function of δ , l , and R as:

$$\alpha = \sin^{-1} \frac{\sqrt{\delta^2 + l^2}}{2R} + \tan^{-1} \left(\frac{\delta}{l} \right) \quad (5.7)$$

Chapter 6

Conclusions and Future Work

6.1. Thesis Contributions

This thesis described applications of microfluidic technologies for on-chip reaction and single cell study using droplet microfluidic manipulation techniques.

6.1.1. Droplet Manipulation Techniques for High Throughput Reactions

Pharmaceutical industries use high-throughput screening (HTS) for drug discovery. Droplet based microfluidics offers a promising alternative for on-chip HTS, replacing the conventional robotic dispensing techniques and microliter plates. The droplet manipulation platforms presented in Chapter 3 and Chapter 4 are able to perform selective permutations and combinations required for HTS using active bio-compatible methods. Our valve based microfluidic device integrated three droplet manipulation techniques to deliver the capability of selective combination of reagents on a chip.

In Chapter 3, selective droplet splitting using single-layer microvalves is demonstrated for the first time. This platform allows to control 3 different inlet pressures using 2 different pressure control Fluigent systems. In this chapter, a splitting regime map was demonstrated based on a series of experiments with oil and water inlet pressures ranging from 100 to 900 mbar, both in the absence and presence of the valve. Operating the device near the critical conditions of splitting when the valve is off was found to be necessary if efficient usage of the pneumatic valve is of interest. In this case, with only minimum force, fission of the droplet can be achieved, and the device can be used several times with minimum damage. Finding the critical condition for shifting from non-splitting to splitting regimes provides an opportunity to increase the durability of the system, since a large deformation of the channel walls affects device durability and causes inaccuracies or even channel damage⁴⁸. It was also found that there is a minimum pressure from which droplets start to split randomly. At pressures around 50-100 mbar higher than this minimum pressure, selective splitting of droplets was observed, which is favourable based on the purpose of this PhD study. The results indicate that the splitting of the first droplet is influenced by changes in the hydraulic resistance of the main channel and also changes in the radius of the front interface of the droplet. Finally, the system showed that by controlling 3 different pressures simultaneously, we can split any volume of desired droplets on demand.

In Chapter 4, we developed a platform for producing a combinatorial library of chemicals for on-chip screening by integrating the selective splitting methods developed in Chapter 3 with selective droplet generation, merging and trapping. This system replicated pipetting technologies currently used in four microfluidic bypass loops. The system was thoroughly characterised to provide further insights into controlled droplet manipulation and interaction techniques. The data obtained from Chapter 4 formed a basis that allows for the development of rapid and controllable splitting, trapping and merging manipulation techniques for pharmaceutical applications. Splitting a plug into small droplets and having the ability to merge, trap and release them on demand assist researchers to make simple, portable lab-on-a-chip devices in which a combinatorial library of the droplets can be rapidly produced and analysed. Depending on the application, this advanced platform also has the potential to integrate with other manipulation techniques like sensing, mixing and intra-droplet manipulation techniques.

6.1.2. Understanding Sperm Behaviour at Soft Curved Interfaces using Microdroplets

The possibility of single-cell encapsulation in droplet microfluidics provides a unique opportunity to understand mammalian reproduction. The role of soft and highly folded epithelial tissue (*i.e.* lots of curved interfaces) on sperm motion through the female reproductive tract and the natural selection process is still unknown. Specifically, we still need to understand how changes in hydrodynamic effects near curved surfaces influence sperm flagellar waveform, the orientation of sperm with respect to the interface, and the resulting motility characteristics.

In Chapter 5, leveraging droplet microfluidics, we used liquid-liquid interfaces to study sperm behaviour near soft curved surfaces. Droplets with diameters ranging from 60 μm to over 300 μm were produced using the flow focusing droplet generation method to match the range of curvatures sperm experience *in vivo*. Individual sperm were trapped in droplets and the swimming behaviour of sperm near the interface was captured using high-speed microscopy. The gathered data revealed that sperm exhibit distinct motility characteristics as a result of the curvature that they are interacting with to swim in the attacking, transition or progressive motility modes. In the progressive motility mode at larger radii of curvatures, the sperm

routinely departs from the interface before returning to it, and alternates between these two states. In the attacking mode at small radii of curvatures, the sperm swims with its head pushing against the interface and remains constantly in contact with curved surface. The results demonstrated for the first time that hydrodynamic effects trigger a dynamic response mechanism in sperm to decrease their flagellar wave amplitude by up to 66% at bigger curvatures (smaller droplets) to swim in the aggressive attacking mode. This switch from a progressive surface-aligned motility mode at smaller curvatures to an aggressive surface-attacking motility mode at bigger curvatures highlights the role of an increasing complexity of the fallopian tube to either guide the sperm towards the egg or facilitate sperm-egg interaction. This aggressive attacking mode is essential for sperm capacitation and fertilisation competence. Beyond these contributions to the field of fertility, sperm behaviour at curvatures is instructive in developing an understanding of the motility of other pusher type microorganisms and eukaryotic microswimmers at curvatures, such as *E. coli* and motile *Caulobacter crescentus*.

6.2. Future Work

Droplet microfluidics has shown promise for the manipulation and control of particles and live cells like tumor cells inside microdroplets^{74,370}. Manipulation of cells inside droplets can be categorised into in-droplet cell encapsulation³⁷¹, in-droplet cell concentration (enrichment)³⁷²⁻³⁷⁹, in-droplet cell sorting^{374,380,381} and in-droplet cell washing^{382,383}. Similar to droplet manipulation techniques, different passive^{371,377} and active^{372-376,378-383} methods were employed to manipulate cells inside droplets. While in passive methods only hydrodynamic forces are used for internal droplet manipulation^{371,377}, active methods take advantages of electrical³⁷⁹, magnetic^{378,382}, and acoustic^{372-376,380,381,383} forces to manipulate the encapsulated cells and particles as well the droplet which encapsulates them. As a successful example of intra-droplet manipulation techniques, magnetic force was used in a CAR-Wash module to selectively enrich a green fluorescent protein from cell lysate³⁸². Although the CAR-Wash module has been shown to successfully exchange the medium containing the protein, not enough control was achieved over the number of cells encapsulated per droplets³⁸².

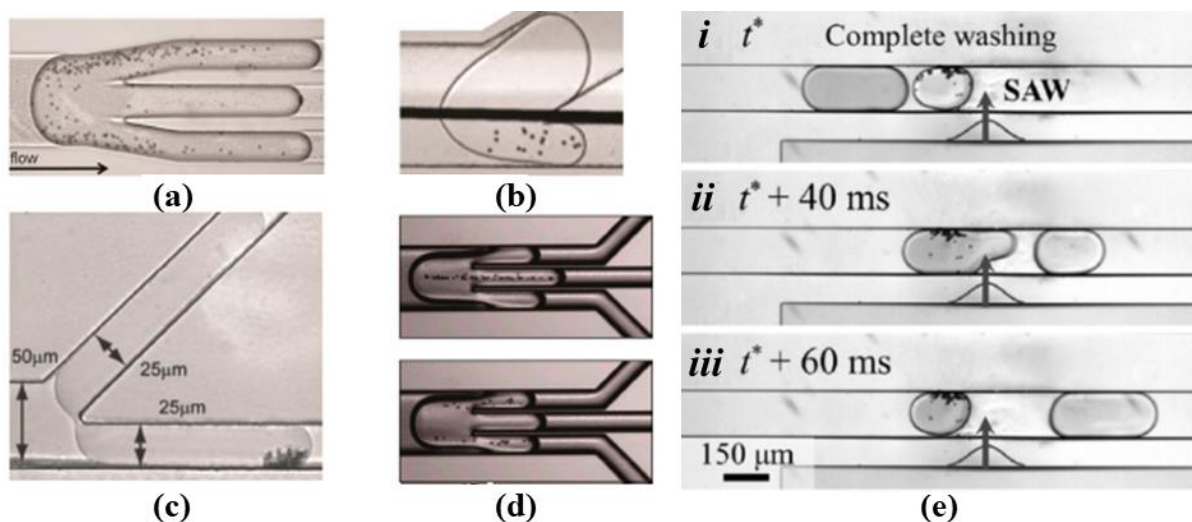


Figure 6.1. Newly introduced intra droplet manipulation techniques using passive and active methods, (a) hydrodynamic³⁷⁷, (b) electrical³⁷⁹, (c) magnetic³⁷⁸, and (d) acoustic³⁷² have been used to concentrate and enrich particles inside droplets. (e) SAW has been used as a washing technique to exchange the droplet medium³⁸³. (a) – (d) are reprinted with permission from ref. 366 Copyright (2018) American Chemical Society. (e) is reproduced from ref. 379 with permission from The Royal Society of Chemistry.

As an example of using acoustic forces, surface acoustic wave-driven acoustic radiation forces have been used to simultaneously split the droplets and to enrich³⁸³ or sort³⁷⁴ the particles inside the droplets. It was also shown that washing can be achieved using SAW by splitting the droplet that contains microparticles and then merging the split droplet with another droplet to exchange the medium of dispersed phase³⁸³. However, in this method, serial droplet splitting and merging is required to fully exchange the medium.

A new technique for encapsulation (Figure 6.2a), concentration (Figure 6.2b) and washing (Figure 6.2c) of particles inside droplets can be achieved by integrating the selective partitioning method (introduced in Chapter 3) with internal droplet manipulation techniques using surface acoustic waves. This method leverages all the useful capabilities of droplet microfluidics, microvalve technology and acoustofluidics to enable simultaneous manipulation of cell and droplets. Currently, the candidate is working to develop this system for both non-selective and selective intra-droplet manipulation.

To achieve non-selective but efficient cell encapsulation, the pressure imposed on the continuous and dispersed phases is carefully tuned to split all the passing mother droplets. Particles have random and free movement inside the droplet before reaching the SAW actuation area or when the SAW is off (Figure 6.2d). However, under SAW actuation at optimum power

(a power that affects particle movements but not the droplet), the particles were pushed upstream of the flow while the droplet moves downstream (Figure 6.2e) – resulting in particle enrichment at the upstream side of the droplet. The droplets are then split using a T-junction, with the particles trapped in the daughter droplets (Figure 6.2f). Using this method, our preliminary results demonstrate up to 70% encapsulation efficiency (the average number of particles trapped in the daughter droplet over the total number of particles in the mother droplet). The candidate is currently working on the device design and SAW actuation parameters (input power and frequency) to increase the encapsulation efficiency to over 90%.

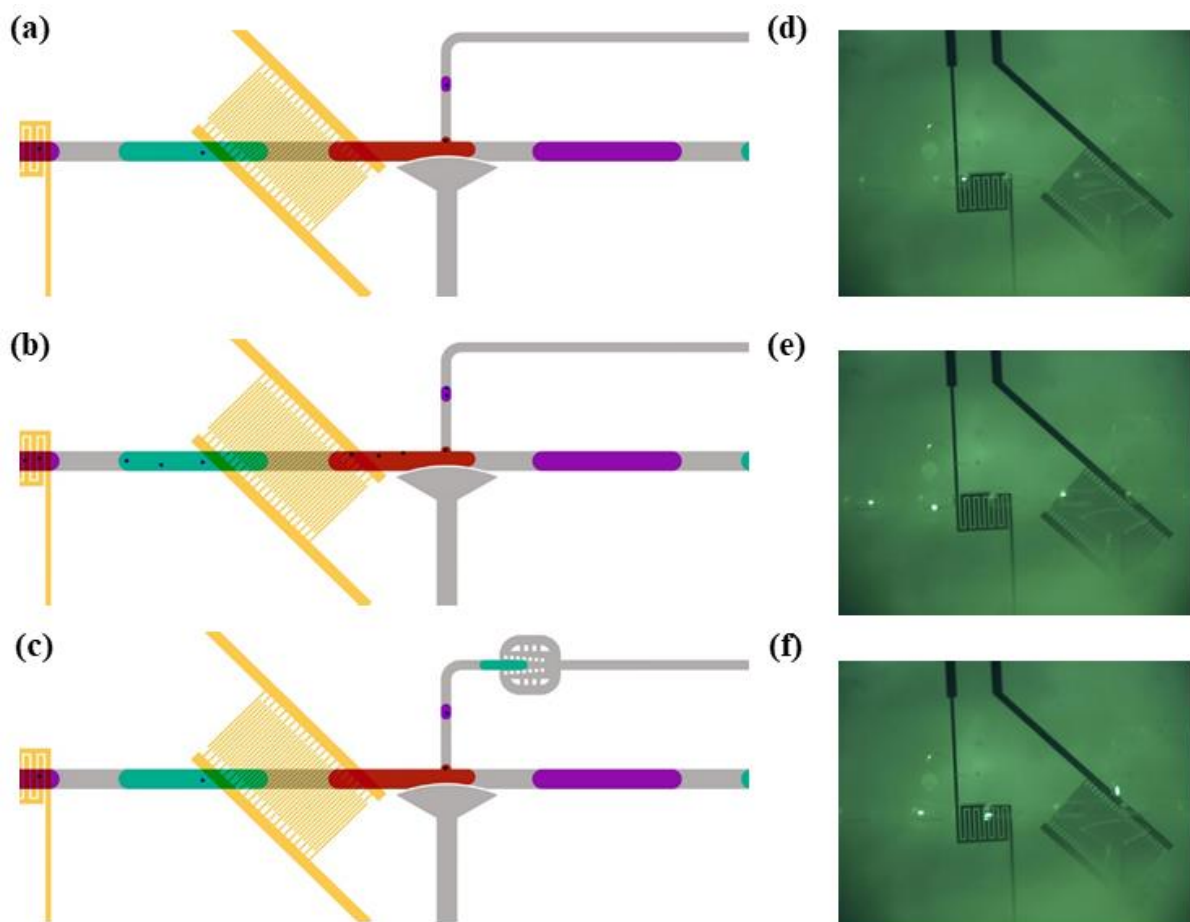


Figure 6.2. Depiction of the system integrating a single layer valve and a SAW actuation module for (a) intra-droplet particle encapsulation, (b) intra-droplet particle concentration, and (c) intra-droplet particle washing. Preliminary results illustrate the capability of the system to encapsulate the droplet with SAW on and valve off. (d) Particles are moving freely inside the droplet before reaching the SAW exposed area. (e) SAW pushes the particles to the back (upstream side) and top side of the droplet. As a result, (f) the particles are captured in the daughter droplet and pushed out of the main stream into a secondary channel.

To achieve selective cell encapsulation, the SAW actuation module and a single-layer microvalve operate simultaneously. Here, a transition regime between splitting and non-splitting is imposed such that the mother droplets are not split in the junction but instead long fingers are formed as they pass the junction. While SAW is continuously on, the valve is then activated to split the targeted droplet, and then the split daughter droplet containing particles is transferred out of the main stream to a separate outlet (Figure 6.2a). If the mother droplet contains more than one particle, SAW affects all of them and as a result all particles move to the split daughter droplet and intra-droplet cell concentration or enrichment is achieved (Figure 6.2b).

To achieve intra-droplet cell washing, two droplets of different colours (green and purple) were generated one after the other in the droplet generation section, based on the method presented in Chapter 4. We then pressurised the valve to the relatively high-pressure of 2000 mbar just before the first droplet not containing the cell reaches the junction. Using the pressurised valve, the green coloured droplet is split with a 25% relative volume of daughter to mother droplets, and the daughter droplet is then trapped in a merging chamber (Figure 6.2c). The valve pressure is then decreased to 500 mbar before the next droplet reaches the junction. Following that, the red droplet containing the particle approaches the junction and splits as well to generate the small red daughter droplet encapsulating the particles (with a 5% relative volume of daughter to mother droplet), which also gets trapped in the merging chamber. A thin film between two trapped daughter droplets prevents the merging of the two different coloured droplets. In a short time, this thin film drains out, and two daughter droplets merge and washing occurs. This newly formed droplet contains 85% of the green medium and 15% of the purple medium, demonstrating a one-step washing procedure with a higher efficiency than previously introduced SAW-induced washing methods³⁸³. This method of enriching and washing encapsulated particles/cells is beneficial to pharmaceutical applications where diseased carrying cells need to be tested against a proposed drug. This project offers significant innovation in droplet microfluidics technology using single-layer microvalve and surface acoustic waves, and presents a stepping stone to make microchips for commercialised drug discovery and cancer treatment purposes. It is expected that the result of this work, an extension of the techniques developed in this thesis, will be very beneficial to chemists and pharmacologists as it finds a broad range of applications in microfluidics, chemistry, cancer treatment and high throughput screening.

In terms of the knowledge gained from studying sperm swimming in proximity of the curved interface offered by droplet encapsulation, a new method of characterising sperm cell behaviour has been established; future work will examine how this behaviour is related to fertilisation outcomes. Specifically, as the fallopian tube is the result of an evolutionary process to ensure the best sperm reach the egg, understanding how these swimming behaviours allow migration through this complex structure will increase understanding of this process. In addition, examining whether some cells exhibit these behaviours to a higher extent than others could act as a sorting mechanism which is more in tune with the natural sort performed *in vivo*.

Bibliography

- 1 Judy, J. W. Microelectromechanical systems (MEMS): fabrication, design and applications. *Smart materials and Structures* **10**, 1115 (2001).
- 2 Maluf, N. & Williams, K. *Introduction to microelectromechanical systems engineering*. (Artech House, 2004).
- 3 Verpoorte, E. & De Rooij, N. F. Microfluidics meets MEMS. *Proceedings of the IEEE* **91**, 930-953 (2003).
- 4 Lee, C.-Y., Chang, C.-L., Wang, Y.-N. & Fu, L.-M. Microfluidic mixing: a review. *International journal of molecular sciences* **12**, 3263-3287 (2011).
- 5 Yao, X., Zhang, Y., Du, L., Liu, J. & Yao, J. Review of the applications of microreactors. *Renewable and Sustainable Energy Reviews* **47**, 519-539 (2015).
- 6 Bayareh, M., Ashani, M. N. & Usefian, A. Active and passive micromixers: a comprehensive review. *Chemical Engineering and Processing-Process Intensification* **147**, 107771 (2020).
- 7 Salieb-Beugelaar, G. B., Simone, G., Arora, A., Philippi, A. & Manz, A. Latest developments in microfluidic cell biology and analysis systems. *Analytical chemistry* **82**, 4848-4864 (2010).
- 8 Hung, P. J., Lee, P. J., Sabounchi, P., Lin, R. & Lee, L. P. Continuous perfusion microfluidic cell culture array for high-throughput cell-based assays. *Biotechnology and bioengineering* **89**, 1-8 (2005).
- 9 Mehling, M. & Tay, S. Microfluidic cell culture. *Current opinion in Biotechnology* **25**, 95-102 (2014).
- 10 Velve-Casquillas, G., Le Berre, M., Piel, M. & Tran, P. T. Microfluidic tools for cell biological research. *Nano today* **5**, 28-47 (2010).
- 11 Chen, J., Li, J. & Sun, Y. Microfluidic approaches for cancer cell detection, characterization, and separation. *Lab on a Chip* **12**, 1753-1767 (2012).
- 12 Xu, Y. *et al.* Aptamer-based microfluidic device for enrichment, sorting, and detection of multiple cancer cells. *Analytical chemistry* **81**, 7436-7442 (2009).
- 13 Nosrati, R. *et al.* Microfluidics for sperm analysis and selection. *Nature Reviews Urology* **14**, 707-730 (2017).
- 14 Kashaninejad, N., Shiddiky, M. J. A. & Nguyen, N. T. Advances in microfluidics-based assisted reproductive technology: From sperm sorter to reproductive system-on-a-chip. *Advanced Biosystems* **2**, 1700197 (2018).

- 15 Yin, H. & Marshall, D. Microfluidics for single cell analysis. *Current opinion in biotechnology* **23**, 110-119 (2012).
- 16 Lecault, V., White, A. K., Singhal, A. & Hansen, C. L. Microfluidic single cell analysis: from promise to practice. *Current opinion in chemical biology* **16**, 381-390 (2012).
- 17 Berthier, J. *Micro-drops and digital microfluidics*. (William Andrew, 2012).
- 18 Berthier, J., Brakke, K. A. & Berthier, E. *Open microfluidics*. (John Wiley & Sons, 2016).
- 19 Teh, S.-Y., Lin, R., Hung, L.-H. & Lee, A. P. Droplet microfluidics. *Lab on a Chip* **8**, 198-220 (2008).
- 20 Samiei, E., Tabrizian, M. & Hoorfar, M. A review of digital microfluidics as portable platforms for lab-on a-chip applications. *Lab on a Chip* **16**, 2376-2396 (2016).
- 21 Zhao, C.-X. & Middelberg, A. P. Two-phase microfluidic flows. *Chemical Engineering Science* **66**, 1394-1411 (2011).
- 22 Raveshi, M. R., Agnihotri, S. N., Sesen, M., Bhardwaj, R. & Neild, A. Selective droplet splitting using single layer microfluidic valves. *Sensors and Actuators B: Chemical* **292**, 233-240 (2019).
- 23 Brouzes, E. *et al.* Droplet microfluidic technology for single-cell high-throughput screening. *Proceedings of the National Academy of Sciences* **106**, 14195-14200 (2009).
- 24 Weng, L. & Spoonamore, J. E. Droplet Microfluidics-Enabled High-Throughput Screening for Protein Engineering. *Micromachines* **10**, 734 (2019).
- 25 Song, H., Chen, D. L. & Ismagilov, R. F. Reactions in droplets in microfluidic channels. *Angewandte chemie international edition* **45**, 7336-7356 (2006).
- 26 Churski, K., Korczyk, P. & Garstecki, P. High-throughput automated droplet microfluidic system for screening of reaction conditions. *Lab on a Chip* **10**, 816-818 (2010).
- 27 Mazutis, L. *et al.* Single-cell analysis and sorting using droplet-based microfluidics. *Nature protocols* **8**, 870 (2013).
- 28 Son, S. U. & Garrell, R. L. Transport of live yeast and zebrafish embryo on a droplet (“digital”) microfluidic platform. *Lab on a chip* **9**, 2398-2401 (2009).
- 29 Segaliny, A. I. *et al.* Functional TCR T cell screening using single-cell droplet microfluidics. *Lab on a Chip* **18**, 3733-3749 (2018).
- 30 Leman, M., Abouakil, F., Griffiths, A. D. & Tabeling, P. Droplet-based microfluidics at the femtolitre scale. *Lab on a Chip* **15**, 753-765 (2015).

- 31 Shim, J.-u. *et al.* Ultrarapid generation of femtoliter microfluidic droplets for single-molecule-counting immunoassays. *Acs Nano* **7**, 5955-5964 (2013).
- 32 Thorsen, T., Roberts, R. W., Arnold, F. H. & Quake, S. R. Dynamic pattern formation in a vesicle-generating microfluidic device. *Physical review letters* **86**, 4163 (2001).
- 33 Anna, S. L., Bontoux, N. & Stone, H. A. Formation of dispersions using “flow focusing” in microchannels. *Applied physics letters* **82**, 364-366 (2003).
- 34 Dreyfus, R., Tabeling, P. & Willaime, H. Ordered and disordered patterns in two-phase flows in microchannels. *Physical review letters* **90**, 144505 (2003).
- 35 Frenz, L. *et al.* Droplet-based microreactors for the synthesis of magnetic iron oxide nanoparticles. *Angewandte Chemie International Edition* **47**, 6817-6820 (2008).
- 36 Zhao, C.-X., He, L., Qiao, S. Z. & Middelberg, A. P. Nanoparticle synthesis in microreactors. *Chemical Engineering Science* **66**, 1463-1479 (2011).
- 37 Zhu, P. & Wang, L. Passive and active droplet generation with microfluidics: a review. *Lab on a Chip* **17**, 34-75 (2017).
- 38 Chong, Z. Z. *et al.* Active droplet generation in microfluidics. *Lab on a Chip* **16**, 35-58 (2016).
- 39 Chen, J.-S. & Jiang, J.-H. Droplet microfluidic technique: microdroplets formation and manipulation. *Chin J Anal Chem* **8**, 60567-60567 (2012).
- 40 Agnihotri, S. N., Raveshi, M. R., Bhardwaj, R. & Neild, A. Droplet Breakup at the Entrance to a Bypass Channel in a Microfluidic System. *Physical Review Applied* **11**, 034020 (2019).
- 41 Agnihotri, S. N., Raveshi, M. R., Bhardwaj, R. & Neild, A. Microfluidic Valves for Selective on-Chip Droplet Splitting at Multiple Sites. *Langmuir* **36**, 1138-1146 (2020).
- 42 Sesen, M., Alan, T. & Neild, A. Microfluidic on-demand droplet merging using surface acoustic waves. *Lab on a Chip* **14**, 3325-3333 (2014).
- 43 Niu, X., Gulati, S. & Edel, J. B. Pillar-induced droplet merging in microfluidic circuits. *Lab on a chip* **8**, 1837-1841 (2008).
- 44 Sesen, M., Fakhfour, A. & Neild, A. Coalescence of Surfactant-Stabilized Adjacent Droplets Using Surface Acoustic Waves. *Analytical chemistry* **91**, 7538-7545 (2019).
- 45 Huebner, A. *et al.* Static microdroplet arrays: a microfluidic device for droplet trapping, incubation and release for enzymatic and cell-based assays. *Lab on a Chip* **9**, 692-698 (2009).
- 46 Wang, W., Yang, C. & Li, C. M. On-demand microfluidic droplet trapping and fusion for on-chip static droplet assays. *Lab on a Chip* **9**, 1504-1506 (2009).

- 47 Simon, M. G., Lin, R., Fisher, J. S. & Lee, A. P. A Laplace pressure based microfluidic trap for passive droplet trapping and controlled release. *Biomicrofluidics* **6**, 014110 (2012).
- 48 Xi, H.-D. *et al.* Active droplet sorting in microfluidics: a review. *Lab on a Chip* **17**, 751-771 (2017).
- 49 Cao, Z. *et al.* Droplet sorting based on the number of encapsulated particles using a solenoid valve. *Lab on a Chip* **13**, 171-178 (2013).
- 50 Chen, Y. *et al.* Microfluidic droplet sorting using integrated bilayer micro-valves. *Applied Physics Letters* **109**, 143510 (2016).
- 51 Paik, P., Pamula, V. K. & Fair, R. B. Rapid droplet mixers for digital microfluidic systems. *Lab on a Chip* **3**, 253-259 (2003).
- 52 Paik, P., Pamula, V. K., Pollack, M. G. & Fair, R. B. Electrowetting-based droplet mixers for microfluidic systems. *Lab on a Chip* **3**, 28-33 (2003).
- 53 Schertzer, M., Ben-Mrad, R. & Sullivan, P. E. Using capacitance measurements in EWOD devices to identify fluid composition and control droplet mixing. *Sensors and Actuators B: Chemical* **145**, 340-347 (2010).
- 54 Jahn, I. *et al.* Surface-enhanced Raman spectroscopy and microfluidic platforms: challenges, solutions and potential applications. *Analyst* **142**, 1022-1047 (2017).
- 55 Nguyen, N.-T., Lassemono, S. & Chollet, F. A. Optical detection for droplet size control in microfluidic droplet-based analysis systems. *Sensors and actuators B: Chemical* **117**, 431-436 (2006).
- 56 Jakiela, S., Makulska, S., Korczyk, P. M. & Garstecki, P. Speed of flow of individual droplets in microfluidic channels as a function of the capillary number, volume of droplets and contrast of viscosities. *Lab on a Chip* **11**, 3603-3608 (2011).
- 57 Xu, J., Li, S., Tan, J., Wang, Y. & Luo, G. Preparation of highly monodisperse droplet in a T-junction microfluidic device. *AIChE journal* **52**, 3005-3010 (2006).
- 58 Seemann, R., Brinkmann, M., Pfohl, T. & Herminghaus, S. Droplet based microfluidics. *Reports on progress in physics* **75**, 016601 (2011).
- 59 Madadelahi, M., Ghazimirsaeed, E. & Shamloo, A. Design and fabrication of a two-phase diamond nanoparticle aided fast PCR device. *Analytica chimica acta* **1068**, 28-40 (2019).
- 60 Wu, L., Chen, P., Dong, Y., Feng, X. & Liu, B.-F. Encapsulation of single cells on a microfluidic device integrating droplet generation with fluorescence-activated droplet sorting. *Biomedical microdevices* **15**, 553-560 (2013).

- 61 Nabavi, S. A., Vladislavljević, G. T., Gu, S. & Ekanem, E. E. Double emulsion production in glass capillary microfluidic device: Parametric investigation of droplet generation behaviour. *Chemical Engineering Science* **130**, 183-196 (2015).
- 62 Quell, A., Elsing, J., Drenckhan, W. & Stubenrauch, C. Monodisperse polystyrene foams via microfluidics—A novel templating route. *Advanced Engineering Materials* **17**, 604-609 (2015).
- 63 Lee, S. *et al.* in *2015 37th Annual International Conference of the IEEE Engineering in Medicine and Biology Society (EMBC)*. 3541-3544 (IEEE).
- 64 Gupta, A. & Kumar, R. Effect of geometry on droplet formation in the squeezing regime in a microfluidic T-junction. *Microfluidics and Nanofluidics* **8**, 799-812 (2010).
- 65 Xu, J. H., Li, S., Tan, J. & Luo, G. Correlations of droplet formation in T-junction microfluidic devices: from squeezing to dripping. *Microfluidics and Nanofluidics* **5**, 711-717 (2008).
- 66 Glawdel, T., Elbuken, C. & Ren, C. L. Droplet formation in microfluidic T-junction generators operating in the transitional regime. I. Experimental observations. *Physical Review E* **85**, 016322 (2012).
- 67 Fu, T., Wu, Y., Ma, Y. & Li, H. Z. Droplet formation and breakup dynamics in microfluidic flow-focusing devices: from dripping to jetting. *Chemical engineering science* **84**, 207-217 (2012).
- 68 Sauret, A. & Shum, H. C. Beating the jetting regime. *International Journal of Nonlinear Sciences and Numerical Simulation* **13**, 351-362 (2012).
- 69 Jeong, W.-C. *et al.* Controlled generation of submicron emulsion droplets via highly stable tip-streaming mode in microfluidic devices. *Lab on a Chip* **12**, 1446-1453 (2012).
- 70 Zhu, P., Kong, T., Kang, Z., Tian, X. & Wang, L. Tip-multi-breaking in capillary microfluidic devices. *Scientific reports* **5**, 11102 (2015).
- 71 De Menech, M., Garstecki, P., Jousse, F. & Stone, H. A. Transition from squeezing to dripping in a microfluidic T-shaped junction. *journal of fluid mechanics* **595**, 141-161 (2008).
- 72 Liu, H. & Zhang, Y. Droplet formation in a T-shaped microfluidic junction. *Journal of applied physics* **106**, 034906 (2009).
- 73 Christopher, G. & Anna, S. Passive breakup of viscoelastic droplets and filament self-thinning at a microfluidic T-junction. *Journal of Rheology* **53**, 663-683 (2009).
- 74 Salomon, R. *et al.* Droplet-based single cell RNAseq tools: a practical guide. *Lab on a Chip* **19**, 1706-1727 (2019).

- 75 Garstecki, P., Fuerstman, M. J., Stone, H. A. & Whitesides, G. M. Formation of droplets and bubbles in a microfluidic T-junction—scaling and mechanism of break-up. *Lab on a Chip* **6**, 437-446 (2006).
- 76 Shui, L., Mugele, F., van den Berg, A. & Eijkel, J. C. Geometry-controlled droplet generation in head-on microfluidic devices. *Applied physics letters* **93**, 153113 (2008).
- 77 Glawdel, T., Elbuken, C. & Ren, C. L. Droplet formation in microfluidic T-junction generators operating in the transitional regime. II. Modeling. *Physical Review E* **85**, 016323 (2012).
- 78 Glawdel, T. & Ren, C. L. Droplet formation in microfluidic T-junction generators operating in the transitional regime. III. Dynamic surfactant effects. *Physical Review E* **86**, 026308 (2012).
- 79 Christopher, G. F., Noharuddin, N. N., Taylor, J. A. & Anna, S. L. Experimental observations of the squeezing-to-dripping transition in T-shaped microfluidic junctions. *Physical Review E* **78**, 036317 (2008).
- 80 Sesen, M., Alan, T. & Neild, A. Droplet control technologies for microfluidic high throughput screening (μ HTS). *Lab on a Chip* **17**, 2372-2394 (2017).
- 81 Bardin, D. *et al.* High-speed, clinical-scale microfluidic generation of stable phase-change droplets for gas embolotherapy. *Lab on a Chip* **11**, 3990-3998 (2011).
- 82 Moon, S.-K., Cheong, I. W. & Choi, S.-W. Effect of flow rates of the continuous phase on droplet size in dripping and jetting regimes in a simple fluidic device for coaxial flow. *Colloids and Surfaces A: Physicochemical and Engineering Aspects* **454**, 84-88 (2014).
- 83 Utada, A. S., Fernandez-Nieves, A., Stone, H. A. & Weitz, D. A. Dripping to jetting transitions in coflowing liquid streams. *Physical review letters* **99**, 094502 (2007).
- 84 Kovalchuk, N. M., Sagisaka, M., Steponavicius, K., Vigolo, D. & Simmons, M. J. Drop formation in microfluidic cross-junction: jetting to dripping to jetting transition. *Microfluidics and Nanofluidics* **23**, 103 (2019).
- 85 Jing, T. *et al.* Jetting microfluidics with size-sorting capability for single-cell protease detection. *Biosensors and Bioelectronics* **66**, 19-23 (2015).
- 86 Nunes, J., Tsai, S., Wan, J. & Stone, H. A. Dripping and jetting in microfluidic multiphase flows applied to particle and fibre synthesis. *Journal of physics D: Applied physics* **46**, 114002 (2013).
- 87 ZHANG, L., HU, H. & CAO, Y. Droplet Generation of Microfluidic Jetting and Its Applications [J]. *Nanotechnology and Precision Engineering* **1** (2012).

- 88 Marín, A., Campo-Cortés, F. & Gordillo, J. Generation of micron-sized drops and bubbles through viscous coflows. *Colloids and Surfaces A: Physicochemical and Engineering Aspects* **344**, 2-7 (2009).
- 89 Gañán-Calvo, A. M., González-Prieto, R., Riesco-Chueca, P., Herrada, M. A. & Flores-Mosquera, M. Focusing capillary jets close to the continuum limit. *Nature Physics* **3**, 737-742 (2007).
- 90 Basaran, O. A. & Suryo, R. The invisible jet. *Nature Physics* **3**, 679-680 (2007).
- 91 Castro-Hernández, E., Campo-Cortés, F. & Gordillo, J. M. Slender-body theory for the generation of micrometre-sized emulsions through tip streaming. *Journal of fluid mechanics* **698**, 423-445 (2012).
- 92 Zhu, P. *et al.* Droplet breakup in expansion-contraction microchannels. *Scientific reports* **6**, 21527 (2016).
- 93 Zeng, Y., Shin, M. & Wang, T. Programmable active droplet generation enabled by integrated pneumatic micropumps. *Lab on a Chip* **13**, 267-273 (2013).
- 94 Guzowski, J., Gizynski, K., Gorecki, J. & Garstecki, P. Microfluidic platform for reproducible self-assembly of chemically communicating droplet networks with predesigned number and type of the communicating compartments. *Lab on a Chip* **16**, 764-772 (2016).
- 95 Joensson, H. N. & Andersson Svahn, H. Droplet microfluidics—A tool for single-cell analysis. *Angewandte Chemie International Edition* **51**, 12176-12192 (2012).
- 96 Cramer, C., Fischer, P. & Windhab, E. J. Drop formation in a co-flowing ambient fluid. *Chemical Engineering Science* **59**, 3045-3058 (2004).
- 97 Lagus, T. P. & Edd, J. F. A review of the theory, methods and recent applications of high-throughput single-cell droplet microfluidics. *Journal of Physics D: Applied Physics* **46**, 114005 (2013).
- 98 Steegmans, M. L., Schroën, K. G. & Boom, R. M. Characterization of emulsification at flat microchannel Y junctions. *Langmuir* **25**, 3396-3401 (2009).
- 99 Ménétrier-Deremble, L. & Tabeling, P. Droplet breakup in microfluidic junctions of arbitrary angles. *Physical Review E* **74**, 035303 (2006).
- 100 Zheng, B., Tice, J. D. & Ismagilov, R. F. Formation of droplets of alternating composition in microfluidic channels and applications to indexing of concentrations in droplet-based assays. *Analytical chemistry* **76**, 4977-4982 (2004).
- 101 Frenz, L., Blouwolff, J., Griffiths, A. D. & Baret, J.-C. Microfluidic production of droplet pairs. *Langmuir* **24**, 12073-12076 (2008).

- 102 Lin, R., Fisher, J. S., Simon, M. G. & Lee, A. P. Novel on-demand droplet generation for selective fluid sample extraction. *Biomicrofluidics* **6**, 024103 (2012).
- 103 Rhee, M., Liu, P., Meagher, R. J., Light, Y. K. & Singh, A. K. Versatile on-demand droplet generation for controlled encapsulation. *Biomicrofluidics* **8**, 034112 (2014).
- 104 Ding, Y., i Solvas, X. C. & DeMello, A. “V-junction”: a novel structure for high-speed generation of bespoke droplet flows. *Analyst* **140**, 414-421 (2015).
- 105 Tangen, U., Sharma, A., Wagler, P. & McCaskill, J. S. On demand nanoliter-scale microfluidic droplet generation, injection, and mixing using a passive microfluidic device. *Biomicrofluidics* **9**, 014119 (2015).
- 106 van Steijn, V. *et al.* Block-and-break generation of microdroplets with fixed volume. *Biomicrofluidics* **7**, 024108 (2013).
- 107 Umbanhowar, P., Prasad, V. & Weitz, D. A. Monodisperse emulsion generation via drop break off in a coflowing stream. *Langmuir* **16**, 347-351 (2000).
- 108 Taassob, A., Manshadi, M. K. D., Bordbar, A. & Kamali, R. Monodisperse non-Newtonian micro-droplet generation in a co-flow device. *Journal of the Brazilian Society of Mechanical Sciences and Engineering* **39**, 2013-2021 (2017).
- 109 Utada, A. S. *et al.* Monodisperse double emulsions generated from a microcapillary device. *Science* **308**, 537-541 (2005).
- 110 Utada, A. *et al.* Dripping, jetting, drops, and wetting: The magic of microfluidics. *Mrs Bulletin* **32**, 702-708 (2007).
- 111 Yoon, D. H., Nozaki, Y., Tanaka, D., Sekiguchi, T. & Shoji, S. Integration of Horizontal and Vertical Microfluidic Modules for Core-Shell Droplet Generation and Chemical Application. *Micromachines* **10**, 613 (2019).
- 112 Chang, C. B., Wilking, J. N., Kim, S. H., Shum, H. C. & Weitz, D. A. Monodisperse emulsion drop microenvironments for bacterial biofilm growth. *Small* **11**, 3954-3961 (2015).
- 113 Priest, C., Herminghaus, S. & Seemann, R. Generation of monodisperse gel emulsions in a microfluidic device. *Applied physics letters* **88**, 024106 (2006).
- 114 Xu, Q. *et al.* Preparation of monodisperse biodegradable polymer microparticles using a microfluidic flow-focusing device for controlled drug delivery. *Small* **5**, 1575-1581 (2009).
- 115 Link, D. R. *et al.* Electric control of droplets in microfluidic devices. *Angewandte Chemie International Edition* **45**, 2556-2560 (2006).

- 116 Tang, S. Y. *et al.* Liquid-metal microdroplets formed dynamically with electrical control of size and rate. *Advanced Materials* **28**, 604-609 (2016).
- 117 Kahkeshani, S. & Di Carlo, D. Drop formation using ferrofluids driven magnetically in a step emulsification device. *Lab on a Chip* **16**, 2474-2480 (2016).
- 118 Tan, S. H. & Nguyen, N.-T. Generation and manipulation of monodispersed ferrofluid emulsions: The effect of a uniform magnetic field in flow-focusing and T-junction configurations. *Physical Review E* **84**, 036317 (2011).
- 119 Yan, Q., Xuan, S., Ruan, X., Wu, J. & Gong, X. Magnetically controllable generation of ferrofluid droplets. *Microfluidics and Nanofluidics* **19**, 1377-1384 (2015).
- 120 Schuler, F. *et al.* Centrifugal step emulsification applied for absolute quantification of nucleic acids by digital droplet RPA. *Lab on a Chip* **15**, 2759-2766 (2015).
- 121 Schuler, F. *et al.* Digital droplet PCR on disk. *Lab on a Chip* **16**, 208-216 (2016).
- 122 Haerberle, S., Zengerle, R. & Ducrée, J. Centrifugal generation and manipulation of droplet emulsions. *Microfluidics and Nanofluidics* **3**, 65-75 (2007).
- 123 Kar, S., Joshi, S., Chaudhary, K., Maiti, T. K. & Chakraborty, S. Generation of droplets to serpentine threads on a rotating compact-disk platform. *Applied Physics Letters* **107**, 244101 (2015).
- 124 Park, S.-Y., Wu, T.-H., Chen, Y., Teitell, M. A. & Chiou, P.-Y. High-speed droplet generation on demand driven by pulse laser-induced cavitation. *Lab on a Chip* **11**, 1010-1012 (2011).
- 125 Baroud, C. N., de Saint Vincent, M. R. & Delville, J.-P. An optical toolbox for total control of droplet microfluidics. *Lab on a Chip* **7**, 1029-1033 (2007).
- 126 de Saint Vincent, M. R., Chraïbi, H. & Delville, J.-P. Optical flow focusing: Light-induced destabilization of stable liquid threads. *Physical Review Applied* **4**, 044005 (2015).
- 127 Tan, S.-H., Murshed, S. S., Nguyen, N.-T., Wong, T. N. & Yobas, L. Thermally controlled droplet formation in flow focusing geometry: formation regimes and effect of nanoparticle suspension. *Journal of Physics D: Applied Physics* **41**, 165501 (2008).
- 128 Nguyen, N.-T. *et al.* Thermally mediated droplet formation in microchannels. *Applied Physics Letters* **91**, 084102 (2007).
- 129 Yeh, C.-H., Chen, K.-R. & Lin, Y.-C. Developing heatable microfluidic chip to generate gelatin emulsions and microcapsules. *Microfluidics and nanofluidics* **15**, 775-784 (2013).

- 130 Sauret, A., Spandagos, C. & Shum, H. C. Fluctuation-induced dynamics of multiphase liquid jets with ultra-low interfacial tension. *Lab on a Chip* **12**, 3380-3386 (2012).
- 131 Li, J., Mittal, N., Mak, S. Y., Song, Y. & Shum, H. C. Perturbation-induced droplets for manipulating droplet structure and configuration in microfluidics. *Journal of Micromechanics and Microengineering* **25**, 084009 (2015).
- 132 Cheung Shum, H., Varnell, J. & Weitz, D. A. Microfluidic fabrication of water-in-water (w/w) jets and emulsions. *Biomicrofluidics* **6**, 012808 (2012).
- 133 Moon, B.-U., Jones, S. G., Hwang, D. K. & Tsai, S. S. Microfluidic generation of aqueous two-phase system (ATPS) droplets by controlled pulsating inlet pressures. *Lab on a Chip* **15**, 2437-2444 (2015).
- 134 Zhou, H. & Yao, S. A facile on-demand droplet microfluidic system for lab-on-a-chip applications. *microfluidics and nanofluidics* **16**, 667-675 (2014).
- 135 Yu, M., Hou, Y., Zhou, H. & Yao, S. An on-demand nanofluidic concentrator. *Lab on a Chip* **15**, 1524-1532 (2015).
- 136 Brenker, J. C., Collins, D. J., Van Phan, H., Alan, T. & Neild, A. On-chip droplet production regimes using surface acoustic waves. *Lab on a Chip* **16**, 1675-1683 (2016).
- 137 Collins, D. J., Alan, T., Helmerson, K. & Neild, A. Surface acoustic waves for on-demand production of picoliter droplets and particle encapsulation. *Lab on a Chip* **13**, 3225-3231 (2013).
- 138 Schmid, L. & Franke, T. SAW-controlled drop size for flow focusing. *Lab on a Chip* **13**, 1691-1694 (2013).
- 139 Schmid, L. & Franke, T. Acoustic modulation of droplet size in a T-junction. *Applied physics letters* **104**, 133501 (2014).
- 140 Cheung, Y. N. & Qiu, H. Droplet pinch-off in acoustically actuated flow-focusing devices. *Journal of micromechanics and microengineering* **22**, 125003 (2012).
- 141 Ziemecka, I. *et al.* Monodisperse hydrogel microspheres by forced droplet formation in aqueous two-phase systems. *Lab on a Chip* **11**, 620-624 (2011).
- 142 Shemesh, J., Nir, A., Bransky, A. & Levenberg, S. Coalescence-assisted generation of single nanoliter droplets with predefined composition. *Lab on a chip* **11**, 3225-3230 (2011).
- 143 Wu, H.-W., Huang, Y.-C., Wu, C.-L. & Lee, G.-B. Exploitation of a microfluidic device capable of generating size-tunable droplets for gene delivery. *Microfluidics and nanofluidics* **7**, 45-56 (2009).

- 144 Raj, A., Halder, R., Sajeesh, P. & Sen, A. Droplet generation in a microchannel with a controllable deformable wall. *Microfluidics and Nanofluidics* **20**, 102 (2016).
- 145 Abate, A. R., Romanowsky, M. B., Agresti, J. J. & Weitz, D. A. Valve-based flow focusing for drop formation. *Applied Physics Letters* **94**, 023503 (2009).
- 146 Liu, J., Tan, S.-H., Yap, Y. F., Ng, M. Y. & Nguyen, N.-T. Numerical and experimental investigations of the formation process of ferrofluid droplets. *Microfluidics and nanofluidics* **11**, 177-187 (2011).
- 147 Nguyen, N.-T. & Tan, S.-H. in *Microdroplet Technology* 51-75 (Springer, 2012).
- 148 Xiong, S. *et al.* Droplet generation via a single bubble transformation in a nanofluidic channel. *Lab on a Chip* **15**, 1451-1457 (2015).
- 149 Collins, D. J. *et al.* Acoustic tweezers via sub-time-of-flight regime surface acoustic waves. *Science advances* **2**, e1600089 (2016).
- 150 Adamson, D. N., Mustafi, D., Zhang, J. X., Zheng, B. & Ismagilov, R. F. Production of arrays of chemically distinct nanolitre plugs via repeated splitting in microfluidic devices. *Lab on a Chip* **6**, 1178-1186 (2006).
- 151 Hatch, A. C. *et al.* 1-Million droplet array with wide-field fluorescence imaging for digital PCR. *Lab on a chip* **11**, 3838-3845 (2011).
- 152 De Menech, M. Modeling of droplet breakup in a microfluidic T-shaped junction with a phase-field model. *Physical Review E* **73**, 031505 (2006).
- 153 Afkhami, S., Leshansky, A. & Renardy, Y. Numerical investigation of elongated drops in a microfluidic T-junction. *Physics of Fluids* **23**, 022002 (2011).
- 154 Tan, Y.-C., Fisher, J. S., Lee, A. I., Cristini, V. & Lee, A. P. Design of microfluidic channel geometries for the control of droplet volume, chemical concentration, and sorting. *Lab on a Chip* **4**, 292-298 (2004).
- 155 Yang, C.-G., Xu, Z.-R. & Wang, J.-H. Manipulation of droplets in microfluidic systems. *TrAC Trends in Analytical Chemistry* **29**, 141-157 (2010).
- 156 Scheiff, F., Mendorf, M., Agar, D., Reis, N. & Mackley, M. The separation of immiscible liquid slugs within plastic microchannels using a metallic hydrophilic sidestream. *Lab on a Chip* **11**, 1022-1029 (2011).
- 157 Link, D., Anna, S. L., Weitz, D. & Stone, H. Geometrically mediated breakup of drops in microfluidic devices. *Physical review letters* **92**, 054503 (2004).
- 158 Bedram, A. & Moosavi, A. Droplet breakup in an asymmetric microfluidic T junction. *The European Physical Journal E: Soft Matter and Biological Physics* **34**, 1-8 (2011).

- 159 Samie, M., Salari, A. & Shafii, M. B. Breakup of microdroplets in asymmetric T junctions. *Physical Review E* **87**, 053003 (2013).
- 160 Bedram, A., Moosavi, A. & Hannani, S. K. Analytical relations for long-droplet breakup in asymmetric T junctions. *Physical Review E* **91**, 053012 (2015).
- 161 Hoang, D., Portela, L., Kleijn, C., Kreutzer, M. & Van Steijn, V. Dynamics of droplet breakup in a T-junction. *Journal of Fluid Mechanics* **717** (2013).
- 162 Jullien, M.-C., Tsang Mui Ching, M.-J., Cohen, C., Menetrier, L. & Tabeling, P. Droplet breakup in microfluidic T-junctions at small capillary numbers. *Physics of Fluids* **21**, 072001 (2009).
- 163 Hsieh, A. *et al.* in *The Eleventh international conference on miniaturized systems for chemistry and life sciences (uTAS 2007)*, Paris, France. 346-348.
- 164 Clausell-Tormos, J., Griffiths, A. D. & Merten, C. A. An automated two-phase microfluidic system for kinetic analyses and the screening of compound libraries. *Lab on a Chip* **10**, 1302-1307 (2010).
- 165 Um, E., Rogers, M. E. & Stone, H. A. Combinatorial generation of droplets by controlled assembly and coalescence. *Lab on a Chip* **13**, 4674-4680 (2013).
- 166 de Ruiter, R. *et al.* Electrostatic potential wells for on-demand drop manipulation in microchannels. *Lab on a Chip* **14**, 883-891 (2014).
- 167 Baroud, C. N., Delville, J.-P., Gallaire, F. & Wunenburger, R. Thermocapillary valve for droplet production and sorting. *Physical Review E* **75**, 046302 (2007).
- 168 Ting, T. H. *et al.* Thermally mediated breakup of drops in microchannels. *Applied Physics Letters* **89**, 234101 (2006).
- 169 Yap, Y.-F. *et al.* Thermally mediated control of liquid microdroplets at a bifurcation. *Journal of Physics D: Applied Physics* **42**, 065503 (2009).
- 170 Cho, S. K., Moon, H. & Kim, C.-J. Creating, transporting, cutting, and merging liquid droplets by electrowetting-based actuation for digital microfluidic circuits. *Journal of microelectromechanical systems* **12**, 70-80 (2003).
- 171 Geng, H., Feng, J., Stabryla, L. M. & Cho, S. K. in *Micro Electro Mechanical Systems (MEMS), 2017 IEEE 30th International Conference on*. 113-116 (IEEE).
- 172 Collignon, S., Friend, J. & Yeo, L. Planar microfluidic drop splitting and merging. *Lab on a chip* **15**, 1942-1951 (2015).
- 173 Jung, J. H., Destgeer, G., Ha, B., Park, J. & Sung, H. J. On-demand droplet splitting using surface acoustic waves. *Lab on a Chip* **16**, 3235-3243 (2016).

- 174 Sesen, M., Alan, T. & Neild, A. Microfluidic plug steering using surface acoustic waves. *Lab on a Chip* **15**, 3030-3038 (2015).
- 175 Sesen, M., Devendran, C., Malikides, S., Alan, T. & Neild, A. Surface acoustic wave enabled pipette on a chip. *Lab on a Chip* **17**, 438-447 (2017).
- 176 Gu, H., Duits, M. H. & Mugele, F. Droplets formation and merging in two-phase flow microfluidics. *International journal of molecular sciences* **12**, 2572-2597 (2011).
- 177 Whitesides, G. M. The origins and the future of microfluidics. *Nature* **422**, 368-373 (2006).
- 178 Feng, S., Yi, L., Zhao-Miao, L., Ren-Tuo, C. & Gui-Ren, W. Advances in microdroplets coalescence using microfluidics. *Chinese Journal of Analytical Chemistry* **43**, 1942-1954 (2015).
- 179 Tan, Y.-C., Ho, Y. L. & Lee, A. P. Droplet coalescence by geometrically mediated flow in microfluidic channels. *Microfluidics and Nanofluidics* **3**, 495-499 (2007).
- 180 Liu, K., Ding, H., Chen, Y. & Zhao, X.-Z. Droplet-based synthetic method using microflow focusing and droplet fusion. *Microfluidics and Nanofluidics* **3**, 239-243 (2007).
- 181 Bremond, N., Thiam, A. R. & Bibette, J. Decompressing emulsion droplets favors coalescence. *Physical review letters* **100**, 024501 (2008).
- 182 Hung, L.-H. *et al.* Alternating droplet generation and controlled dynamic droplet fusion in microfluidic device for CdS nanoparticle synthesis. *Lab on a Chip* **6**, 174-178 (2006).
- 183 Yoon, D. H. *et al.* Active microdroplet merging by hydrodynamic flow control using a pneumatic actuator-assisted pillar structure. *Lab on a Chip* **14**, 3050-3055 (2014).
- 184 Jin, S. H., Jeong, H.-H., Lee, B., Lee, S. S. & Lee, C.-S. A programmable microfluidic static droplet array for droplet generation, transportation, fusion, storage, and retrieval. *Lab on a Chip* **15**, 3677-3686 (2015).
- 185 Lee, S., Kim, H., Won, D.-J., Lee, J. & Kim, J. On-demand, parallel droplet merging method with non-contact droplet pairing in droplet-based microfluidics. *Microfluidics and Nanofluidics* **20**, 1 (2016).
- 186 Tullis, J., Park, C. L. & Abbyad, P. Selective fusion of anchored droplets via changes in surfactant concentration. *Lab on a Chip* **14**, 3285-3289 (2014).
- 187 Eow, J. S. & Ghadiri, M. Drop-drop coalescence in an electric field: the effects of applied electric field and electrode geometry. *Colloids and Surfaces A: Physicochemical and Engineering Aspects* **219**, 253-279 (2003).

- 188 Ahn, K., Agresti, J., Chong, H., Marquez, M. & Weitz, D. Electrocoalescence of drops synchronized by size-dependent flow in microfluidic channels. *Applied Physics Letters* **88**, 264105 (2006).
- 189 Priest, C., Herminghaus, S. & Seemann, R. Controlled electrocoalescence in microfluidics: Targeting a single lamella. *Applied Physics Letters* **89**, 134101 (2006).
- 190 Mousavichoubeh, M., Ghadiri, M. & Shariaty-Niassar, M. Electro-coalescence of an aqueous droplet at an oil–water interface. *Chemical Engineering and Processing: Process Intensification* **50**, 338-344 (2011).
- 191 Oh, K. W. & Ahn, C. H. A review of microvalves. *Journal of micromechanics and microengineering* **16**, R13 (2006).
- 192 Woias, P. Micropumps—past, progress and future prospects. *Sensors and Actuators B: Chemical* **105**, 28-38 (2005).
- 193 Laser, D. J. & Santiago, J. G. A review of micropumps. *Journal of micromechanics and microengineering* **14**, R35 (2004).
- 194 Zhang, C., Xing, D. & Li, Y. Micropumps, microvalves, and micromixers within PCR microfluidic chips: advances and trends. *Biotechnology advances* **25**, 483-514 (2007).
- 195 De Volder, M. & Reynaerts, D. Pneumatic and hydraulic microactuators: a review. *Journal of Micromechanics and microengineering* **20**, 043001 (2010).
- 196 Au, A. K., Lai, H., Utela, B. R. & Folch, A. Microvalves and micropumps for BioMEMS. *Micromachines* **2**, 179-220 (2011).
- 197 Yetisen, A. K. *et al.* Art on the Nanoscale and Beyond. *Advanced Materials* **28**, 1724-1742 (2016).
- 198 Unger, M. A., Chou, H.-P., Thorsen, T., Scherer, A. & Quake, S. R. Monolithic microfabricated valves and pumps by multilayer soft lithography. *Science* **288**, 113-116 (2000).
- 199 Choi, J.-H., Lee, S.-K., Lim, J.-M., Yang, S.-M. & Yi, G.-R. Designed pneumatic valve actuators for controlled droplet breakup and generation. *Lab on a Chip* **10**, 456-461 (2010).
- 200 Zeng, S., Li, B., Su, X., Qin, J. & Lin, B. Microvalve-actuated precise control of individual droplets in microfluidic devices. *Lab Chip* **9**, 1340-1343, doi:10.1039/b821803j (2009).
- 201 Streets, A. M. *et al.* Microfluidic single-cell whole-transcriptome sequencing. *Proceedings of the National Academy of Sciences* **111**, 7048-7053 (2014).

- 202 Liu, J., Williams, B. A., Gwartz, R. M., Wold, B. J. & Quake, S. Enhanced signals and fast nucleic acid hybridization by microfluidic chaotic mixing. *Angewandte Chemie* **118**, 3700-3705 (2006).
- 203 Lin, Y.-H. *et al.* A negative-pressure-driven microfluidic chip for the rapid detection of a bladder cancer biomarker in urine using bead-based enzyme-linked immunosorbent assay. *Biomicrofluidics* **7**, 024103 (2013).
- 204 Fordyce, P., Diaz-Botia, C., DeRisi, J. & Gomez-Sjoberg, R. Systematic characterization of feature dimensions and closing pressures for microfluidic valves produced via photoresist reflow. *Lab on a Chip* **12**, 4287-4295 (2012).
- 205 Hulme, S. E., Shevkoplyas, S. S. & Whitesides, G. M. Incorporation of prefabricated screw, pneumatic, and solenoid valves into microfluidic devices. *Lab on a Chip* **9**, 79-86 (2009).
- 206 Sundararajan, N., Kim, D. & Berlin, A. A. Microfluidic operations using deformable polymer membranes fabricated by single layer soft lithography. *Lab on a Chip* **5**, 350-354 (2005).
- 207 Lee, S., Chan, J. C., Maung, K., Rezler, E. & Sundararajan, N. Characterization of laterally deformable elastomer membranes for microfluidics. *Journal of Micromechanics and Microengineering* **17**, 843 (2007).
- 208 Abate, A. & Weitz, D. Single-layer membrane valves for elastomeric microfluidic devices. *Appl Phys Lett* **92**, 243509 (2008).
- 209 Abate, A. R., Agresti, J. J. & Weitz, D. A. Microfluidic sorting with high-speed single-layer membrane valves. *Applied Physics Letters* **96**, 203509 (2010).
- 210 Ochs, C. J. & Abate, A. R. Rapid modulation of droplet composition with pincer microvalves. *Lab on a Chip* **15**, 52-56 (2015).
- 211 Kim, H., Lee, S. & Kim, J. Hydrodynamic trap-and-release of single particles using dual-function elastomeric valves: design, fabrication, and characterization. *Microfluidics and nanofluidics* **13**, 835-844 (2012).
- 212 Hansson, J., Hillmering, M., Haraldsson, T. & van der Wijngaart, W. Leak-tight vertical membrane microvalves. *Lab on a Chip* **16**, 1439-1446 (2016).
- 213 Hansson, J., Hillmering, M., Haraldsson, T. & Van Der Wijngaart, W. in *Micro Electro Mechanical Systems (MEMS), 2015 28th IEEE International Conference on.* 563-565 (IEEE).

- 214 Yoon, D., Wakui, D., Sekiguchi, T. & Shoji, S. in *Proceedings of the 14th International Conference on Miniaturized Systems for Chemistry and Life Sciences, Groningen, The Netherlands*.
- 215 Yoon, D. H., Wakui, D., Nakahara, A., Sekiguchi, T. & Shoji, S. Selective droplet sampling using a minimum number of horizontal pneumatic actuators in a high aspect ratio and highly flexible PDMS device. *RSC Advances* **5**, 2070-2074 (2015).
- 216 Kim, H. & Kim, J. A microfluidic-based dynamic microarray system with single-layer pneumatic valves for immobilization and selective retrieval of single microbeads. *Microfluidics and nanofluidics* **16**, 623-633 (2014).
- 217 Jamshaid, A., Yoon, D., Sekiguchi, T. & Shoji, S. Active size controlled droplet generation device using horizontal pneumatic microvalves. *Proc. MMB*, 8-9 (2013).
- 218 Jamshaid, A., Igaki, M., Yoon, D. H., Sekiguchi, T. & Shoji, S. Controllable active micro droplets merging device using horizontal pneumatic micro valves. *Micromachines* **4**, 34-48 (2013).
- 219 Yoon, D. H., Ito, J., Sekiguchi, T. & Shoji, S. Active and precise control of microdroplet division using horizontal pneumatic valves in bifurcating microchannel. *Micromachines* **4**, 197-205 (2013).
- 220 Hsiung, S.-K., Chen, C.-T. & Lee, G.-B. Micro-droplet formation utilizing microfluidic flow focusing and controllable moving-wall chopping techniques. *Journal of Micromechanics and Microengineering* **16**, 2403 (2006).
- 221 Damiati, S., Kompella, U. B., Damiati, S. A. & Kodzius, R. Microfluidic devices for drug delivery systems and drug screening. *Genes* **9**, 103 (2018).
- 222 Kaushik, A. M., Hsieh, K. & Wang, T. H. Droplet microfluidics for high-sensitivity and high-throughput detection and screening of disease biomarkers. *Wiley Interdisciplinary Reviews: Nanomedicine and Nanobiotechnology* **10**, e1522 (2018).
- 223 Macarron, R. *et al.* Impact of high-throughput screening in biomedical research. *Nature reviews Drug discovery* **10**, 188-195 (2011).
- 224 Szymański, P., Markowicz, M. & Mikiciuk-Olasik, E. Adaptation of high-throughput screening in drug discovery—toxicological screening tests. *International journal of molecular sciences* **13**, 427-452 (2012).
- 225 Dittrich, P. S. & Manz, A. Lab-on-a-chip: microfluidics in drug discovery. *Nature reviews Drug discovery* **5**, 210-218 (2006).
- 226 Berg, M. *et al.* Evaluation of liquid handling conditions in microplates. *Journal of biomolecular screening* **6**, 47-56 (2001).

- 227 Janzen, W. P. *High throughput screening: methods and protocols*. (Springer Science & Business Media, 2002).
- 228 Hertzberg, R. P. & Pope, A. J. High-throughput screening: new technology for the 21st century. *Current opinion in chemical biology* **4**, 445-451 (2000).
- 229 Kang, D.-K. *et al.* 3D droplet microfluidic systems for high-throughput biological experimentation. *Analytical chemistry* **87**, 10770-10778 (2015).
- 230 Niu, X., Gielen, F. & Edel, J. B. A microdroplet dilutor for high-throughput screening. *Nature chemistry* **3**, 437-442 (2011).
- 231 Zec, H., Rane, T. D. & Wang, T.-H. Microfluidic platform for on-demand generation of spatially indexed combinatorial droplets. *Lab on a Chip* **12**, 3055-3062 (2012).
- 232 Gielen, F. *et al.* A fully unsupervised compartment-on-demand platform for precise nanoliter assays of time-dependent steady-state enzyme kinetics and inhibition. *Analytical chemistry* **85**, 4761-4769 (2013).
- 233 Theberge, A. B. *et al.* Microfluidic platform for combinatorial synthesis in picolitre droplets. *Lab on a chip* **12**, 1320-1326 (2012).
- 234 Babahosseini, H., Misteli, T. & DeVoe, D. L. Microfluidic on-demand droplet generation, storage, retrieval, and merging for single-cell pairing. *Lab on a chip* **19**, 493-502 (2019).
- 235 Shen, F., Li, Y., Liu, Z. & Li, X. Study of flow behaviors of droplet merging and splitting in microchannels using Micro-PIV measurement. *Microfluidics and nanofluidics* **21**, 66 (2017).
- 236 Chiu, Y.-L., Yadav, R. A. K., Huang, H.-Y., Wang, Y.-W. & Yao, D.-J. Unveiling the Potential of Droplet Generation, Sorting, Expansion, and Restoration in Microfluidic Biochips. *Micromachines* **10**, 756 (2019).
- 237 Teo, A. J., Tan, S. H. & Nguyen, N.-T. On-demand droplet merging with an AC electric field for multiple-volume droplet generation. *Analytical Chemistry* **92**, 1147-1153 (2019).
- 238 Babahosseini, H., Padmanabhan, S., Misteli, T. & DeVoe, D. L. A programmable microfluidic platform for multisample injection, discretization, and droplet manipulation. *Biomicrofluidics* **14**, 014112 (2020).
- 239 Bhagat, A. A. S. *et al.* Microfluidics for cell separation. *Medical & biological engineering & computing* **48**, 999-1014 (2010).
- 240 Zhu, Z. & Yang, C. J. Hydrogel droplet microfluidics for high-throughput single molecule/cell analysis. *Accounts of chemical research* **50**, 22-31 (2017).

- 241 Qin, Y. *et al.* A Self-Digitization Dielectrophoretic (SD-DEP) Chip for High-Efficiency Single-Cell Capture, On-Demand Compartmentalization, and Downstream Nucleic Acid Analysis. *Angewandte Chemie International Edition* **57**, 11378-11383 (2018).
- 242 Fritzsche, F. S., Dusny, C., Frick, O. & Schmid, A. Single-cell analysis in biotechnology, systems biology, and biocatalysis. *Annual review of chemical and biomolecular engineering* **3**, 129-155 (2012).
- 243 Hodzic, E. Single-cell analysis: Advances and future perspectives. *Bosnian journal of basic medical sciences* **16**, 313 (2016).
- 244 Navin, N. *et al.* Tumour evolution inferred by single-cell sequencing. *Nature* **472**, 90 (2011).
- 245 Chen, Y. *et al.* Rare cell isolation and analysis in microfluidics. *Lab on a Chip* **14**, 626-645 (2014).
- 246 Pratt, E. D., Huang, C., Hawkins, B. G., Gleghorn, J. P. & Kirby, B. J. Rare cell capture in microfluidic devices. *Chemical engineering science* **66**, 1508-1522 (2011).
- 247 Ni, M. *et al.* Cell culture on MEMS platforms: a review. *International journal of molecular sciences* **10**, 5411-5441 (2009).
- 248 Gross, A. *et al.* Technologies for single-cell isolation. *International journal of molecular sciences* **16**, 16897-16919 (2015).
- 249 Hu, P., Zhang, W., Xin, H. & Deng, G. Single cell isolation and analysis. *Frontiers in cell and developmental biology* **4**, 116 (2016).
- 250 Zeb, Q., Wang, C., Shafiq, S. & Liu, L. in *Single-Cell Omics* 101-135 (Elsevier, 2019).
- 251 Gao, D., Jin, F., Zhou, M. & Jiang, Y. Recent advances in single cell manipulation and biochemical analysis on microfluidics. *Analyst* **144**, 766-781 (2019).
- 252 Wang, D. & Bodovitz, S. Single cell analysis: the new frontier in 'omics'. *Trends in biotechnology* **28**, 281-290 (2010).
- 253 Heath, J. R., Ribas, A. & Mischel, P. S. Single-cell analysis tools for drug discovery and development. *Nature reviews Drug discovery* **15**, 204 (2016).
- 254 Zagnoni, M. & Cooper, J. M. in *Methods in cell biology* Vol. 102 23-48 (Elsevier, 2011).
- 255 Chen, Q. *et al.* Controlled assembly of heterotypic cells in a core-shell scaffold: organ in a droplet. *Lab on a Chip* **16**, 1346-1349 (2016).
- 256 Wlodkowic, D. & Cooper, J. M. Tumors on chips: oncology meets microfluidics. *Current opinion in chemical biology* **14**, 556-567 (2010).

- 257 Chen, Q. & Lin, J.-M. in *Microfluidics for Single-Cell Analysis* 119-141 (Springer, 2019).
- 258 Du, G., Fang, Q. & den Toonder, J. M. Microfluidics for cell-based high throughput screening platforms—A review. *Analytica chimica acta* **903**, 36-50 (2016).
- 259 Collins, D. J., Neild, A., Liu, A.-Q. & Ai, Y. The Poisson distribution and beyond: methods for microfluidic droplet production and single cell encapsulation. *Lab on a Chip* **15**, 3439-3459 (2015).
- 260 Chabert, M. & Viovy, J.-L. Microfluidic high-throughput encapsulation and hydrodynamic self-sorting of single cells. *Proceedings of the National Academy of Sciences* **105**, 3191-3196 (2008).
- 261 Edd, J. F. *et al.* Controlled encapsulation of single-cells into monodisperse picolitre drops. *Lab on a Chip* **8**, 1262-1264 (2008).
- 262 Ramji, R. *et al.* Single cell kinase signaling assay using pinched flow coupled droplet microfluidics. *Biomicrofluidics* **8**, 034104 (2014).
- 263 Kemna, E. W. *et al.* High-yield cell ordering and deterministic cell-in-droplet encapsulation using Dean flow in a curved microchannel. *Lab on a Chip* **12**, 2881-2887 (2012).
- 264 Lin, J. M. *Cell Analysis on Microfluidics*. (Springer Singapore, 2017).
- 265 Mao, A. S. *et al.* Deterministic encapsulation of single cells in thin tunable microgels for niche modelling and therapeutic delivery. *Nature materials* **16**, 236-243 (2017).
- 266 Kamperman, T., Karperien, M., Le Gac, S. & Leijten, J. Single-cell microgels: technology, challenges, and applications. *Trends in biotechnology* **36**, 850-865 (2018).
- 267 Pekin, D. *et al.* Quantitative and sensitive detection of rare mutations using droplet-based microfluidics. *Lab on a Chip* **11**, 2156-2166 (2011).
- 268 Ding, Y., Choo, J. & DeMello, A. J. From single-molecule detection to next-generation sequencing: microfluidic droplets for high-throughput nucleic acid analysis. *Microfluidics and nanofluidics* **21**, 1-20 (2017).
- 269 Lin, L. & Lin, J.-M. Development of cell metabolite analysis on microfluidic platform. *Journal of pharmaceutical analysis* **5**, 337-347 (2015).
- 270 Sun, D. *et al.* Label-Free Detection of Multiplexed Metabolites at Single-Cell Level via a SERS-Microfluidic Droplet Platform. *Analytical Chemistry* **91**, 15484-15490 (2019).
- 271 Huebner, A. *et al.* Quantitative detection of protein expression in single cells using droplet microfluidics. *Chemical communications*, 1218-1220 (2007).

- 272 Joensson, H. N. & Andersson-Svahn, H. Droplet microfluidics—a tool for protein engineering and analysis. *Lab on a Chip* **11**, 4144-4147 (2011).
- 273 Barbulovic-Nad, I., Yang, H., Park, P. S. & Wheeler, A. R. Digital microfluidics for cell-based assays. *Lab on a Chip* **8**, 519-526 (2008).
- 274 Yang, F., Gao, C., Wang, P., Zhang, G.-J. & Chen, Z. Fish-on-a-chip: Microfluidics for zebrafish research. *Lab on a Chip* **16**, 1106-1125 (2016).
- 275 Chen, C. Y. & Cheng, C. M. Microfluidics expands the zebrafish potentials in pharmaceutically relevant screening. *Advanced healthcare materials* **3**, 940-945 (2014).
- 276 Aitken, R. J., De Iuliis, G. N. & McLachlan, R. I. Biological and clinical significance of DNA damage in the male germ line. *International journal of andrology* **32**, 46-56 (2009).
- 277 Suarez, S. S. & Pacey, A. Sperm transport in the female reproductive tract. *Human reproduction update* **12**, 23-37 (2006).
- 278 Nosrati, R., Driouchi, A., Yip, C. M. & Sinton, D. Two-dimensional slither swimming of sperm within a micrometre of a surface. *Nature communications* **6**, 1-9 (2015).
- 279 Suarez, S. S., Brockman, K. & Lefebvre, R. Distribution of mucus and sperm in bovine oviducts after artificial insemination: the physical environment of the oviductal sperm reservoir. *Biology of reproduction* **56**, 447-453 (1997).
- 280 Rakszewska, A., Tel, J., Chokkalingam, V. & Huck, W. T. One drop at a time: toward droplet microfluidics as a versatile tool for single-cell analysis. *NPG Asia Materials* **6**, e133 (2014).
- 281 Shestopalov, I., Tice, J. D. & Ismagilov, R. F. Multi-step synthesis of nanoparticles performed on millisecond time scale in a microfluidic droplet-based system. *Lab on a Chip* **4**, 316-321 (2004).
- 282 Li, J. & Barrow, D. A new droplet-forming fluidic junction for the generation of highly compartmentalised capsules. *Lab on a Chip* **17**, 2873-2881 (2017).
- 283 Janzen, W. P. in *Molecular Biomethods Handbook* 1097-1118 (Springer, 2008).
- 284 Chen, X., Glawdel, T., Cui, N. & Ren, C. L. Model of droplet generation in flow focusing generators operating in the squeezing regime. *Microfluidics and Nanofluidics* **18**, 1341-1353 (2015).
- 285 Tan, Y.-C., Cristini, V. & Lee, A. P. Monodispersed microfluidic droplet generation by shear focusing microfluidic device. *Sensors and Actuators B: Chemical* **114**, 350-356 (2006).

- 286 Piccin, E. *et al.* Generation of water-in-oil and oil-in-water microdroplets in polyester-toner microfluidic devices. *Sensors and Actuators B: Chemical* **196**, 525-531 (2014).
- 287 Jung, J. H. *et al.* In situ seriate droplet coalescence under an optical force. *Microfluidics and Nanofluidics* **18**, 1247-1254 (2015).
- 288 Chen, X., Brukson, A. & Ren, C. L. A simple droplet merger design for controlled reaction volumes. *Microfluidics and Nanofluidics* **21**, 34 (2017).
- 289 Park, J. *et al.* On-demand acoustic droplet splitting and steering in a disposable microfluidic chip. *Lab on a Chip* **18**, 422-432 (2018).
- 290 Kunstmann-Olsen, C., Hanczyc, M. M., Hoyland, J., Rasmussen, S. & Rubahn, H.-G. Uniform droplet splitting and detection using lab-on-chip flow cytometry on a microfluidic PDMS device. *Sensors and Actuators B: Chemical* **229**, 7-13 (2016).
- 291 Geng, H., Feng, J., Stabryla, L. M. & Cho, S. K. in *2017 IEEE 30th International Conference on Micro Electro Mechanical Systems (MEMS)*. 113-116.
- 292 Rogers, C. I. *et al.* Microfluidic valves made from polymerized polyethylene glycol diacrylate. *Sensors and Actuators B: Chemical* **191**, 438-444 (2014).
- 293 Bruus, H. *Theoretical microfluidics*. (Oxford university press Oxford, 2007).
- 294 Kirshner, J. M. *Design theory of fluidic components*. (Academic Press, 2012).
- 295 He, M. *et al.* Selective encapsulation of single cells and subcellular organelles into picoliter- and femtoliter-volume droplets. *Analytical chemistry* **77**, 1539-1544 (2005).
- 296 Zheng, B., Gerdts, C. J. & Ismagilov, R. F. Using nanoliter plugs in microfluidics to facilitate and understand protein crystallization. *Current opinion in structural biology* **15**, 548-555 (2005).
- 297 Shim, J.-u., Cristobal, G., Link, D. R., Thorsen, T. & Fraden, S. Using microfluidics to decouple nucleation and growth of protein crystals. *Crystal Growth and Design* **7**, 2192-2194 (2007).
- 298 Abou-Hassan, A., Sandre, O. & Cabuil, V. Microfluidics in inorganic chemistry. *Angewandte Chemie International Edition* **49**, 6268-6286 (2010).
- 299 Vyawahare, S., Griffiths, A. D. & Merten, C. A. Miniaturization and parallelization of biological and chemical assays in microfluidic devices. *Chemistry & biology* **17**, 1052-1065 (2010).
- 300 Theberge, A. B. *et al.* Microdroplets in microfluidics: an evolving platform for discoveries in chemistry and biology. *Angewandte Chemie International Edition* **49**, 5846-5868 (2010).

- 301 Crowley, T. A. & Pizziconi, V. Isolation of plasma from whole blood using planar microfilters for lab-on-a-chip applications. *Lab on a Chip* **5**, 922-929 (2005).
- 302 Han, K.-H. & Frazier, A. B. Paramagnetic capture mode magnetophoretic microseparator for high efficiency blood cell separations. *Lab on a Chip* **6**, 265-273 (2006).
- 303 Song, H. & Ismagilov, R. F. Millisecond kinetics on a microfluidic chip using nanoliters of reagents. *Journal of the American Chemical Society* **125**, 14613-14619 (2003).
- 304 Chokkalingam, V., Herminghaus, S. & Seemann, R. Self-synchronizing pairwise production of monodisperse droplets by microfluidic step emulsification. *Applied Physics Letters* **93**, 254101 (2008).
- 305 Hong, J., Choi, M., Edel, J. B. & Demello, A. J. Passive self-synchronized two-droplet generation. *Lab on a Chip* **10**, 2702-2709 (2010).
- 306 Huh, D. *et al.* Gravity-driven microfluidic particle sorting device with hydrodynamic separation amplification. *Analytical chemistry* **79**, 1369-1376 (2007).
- 307 Liu, Y. & Ismagilov, R. F. Dynamics of coalescence of plugs with a hydrophilic wetting layer induced by flow in a microfluidic chemistode. *Langmuir* **25**, 2854-2859 (2009).
- 308 Ahn, B., Lee, K., Panchapakesan, R. & Oh, K. W. On-demand electrostatic droplet charging and sorting. *Biomicrofluidics* **5**, 024113 (2011).
- 309 Lee, H., Xu, L., Ahn, B., Lee, K. & Oh, K. W. Continuous-flow in-droplet magnetic particle separation in a droplet-based microfluidic platform. *Microfluidics and nanofluidics* **13**, 613-623 (2012).
- 310 Oh, K. W., Lee, K., Ahn, B. & Furlani, E. P. Design of pressure-driven microfluidic networks using electric circuit analogy. *Lab on a Chip* **12**, 515-545 (2012).
- 311 Eisenbach, M. & Giojalas, L. C. Sperm guidance in mammals—an unpaved road to the egg. *Nature reviews Molecular cell biology* **7**, 276-285 (2006).
- 312 Nosrati, R. *et al.* Microfluidics for sperm analysis and selection. *Nature Reviews Urology* **14**, 707 (2017).
- 313 Gaffney, E. A., Gadêlha, H., Smith, D., Blake, J. & Kirkman-Brown, J. Mammalian sperm motility: observation and theory. *Annual Review of Fluid Mechanics* **43**, 501-528 (2011).
- 314 Tung, C.-k., Ardon, F., Fiore, A. G., Suarez, S. S. & Wu, M. Cooperative roles of biological flow and surface topography in guiding sperm migration revealed by a microfluidic model. *Lab on a chip* **14**, 1348-1356 (2014).

- 315 Nosrati, R., Driouchi, A., Yip, C. M. & Sinton, D. Two-dimensional slither swimming of sperm within a micrometre of a surface. *Nature communications* **6**, 8703 (2015).
- 316 Kervancioglu, M. E., Saridogan, E., Aitken, R. J. & Djahanbakhch, O. Importance of sperm-to-epithelial cell contact for the capacitation of human spermatozoa in fallopian tube epithelial cell cocultures. *Fertility and sterility* **74**, 780-784 (2000).
- 317 Timothy Smith, T. & Nothnick, W. B. Role of direct contact between spermatozoa and oviductal epithelial cells in maintaining rabbit sperm viability. *Biology of reproduction* **56**, 83-89 (1997).
- 318 Timothy Smith, T. & Yanagimachi, R. The viability of hamster spermatozoa stored in the isthmus of the oviduct: the importance of sperm-epithelium contact for sperm survival. *Biology of Reproduction* **42**, 450-457 (1990).
- 319 Suarez, S., Redfern, K., Raynor, P., Martin, F. & Phillips, D. Attachment of boar sperm to mucosal explants of oviduct in vitro: possible role in formation of a sperm reservoir. *Biology of reproduction* **44**, 998-1004 (1991).
- 320 Spassky, N. & Meunier, A. The development and functions of multiciliated epithelia. *Nature reviews Molecular cell biology* **18**, 423-436 (2017).
- 321 Dobrinski, I., Timothy Smith, T., Suarez, S. S. & Ball, B. A. Membrane contact with oviductal epithelium modulates the intracellular calcium concentration of equine spermatozoa in vitro. *Biology of reproduction* **56**, 861-869 (1997).
- 322 Thomas, P., Ignatz, G., Ball, B., Brinsko, S. & Currie, W. Effect of coculture with stallion spermatozoa on de novo protein synthesis and secretion by equine oviduct epithelial cells. *American journal of veterinary research* **56**, 1657-1662 (1995).
- 323 Barton, B. E. *et al.* Roles of steroid hormones in oviductal function. *Reproduction* **1** (2019).
- 324 Tung, C.-k. *et al.* Microgrooves and fluid flows provide preferential passageways for sperm over pathogen *Tritrichomonas foetus*. *Proceedings of the National Academy of Sciences* **112**, 5431-5436 (2015).
- 325 Kantsler, V., Dunkel, J., Blayney, M. & Goldstein, R. E. Rheotaxis facilitates upstream navigation of mammalian sperm cells. *Elife* **3**, e02403 (2014).
- 326 Nosrati, R., Graham, P. J., Liu, Q. & Sinton, D. Predominance of sperm motion in corners. *Scientific reports* **6**, 1-9 (2016).
- 327 Lauga, E. & Powers, T. R. The hydrodynamics of swimming microorganisms. *Reports on Progress in Physics* **72**, 096601 (2009).

- 328 Fauci, L. J. & McDonald, A. Sperm motility in the presence of boundaries. *Bulletin of mathematical biology* **57**, 679-699 (1995).
- 329 Li, G. *et al.* Accumulation of swimming bacteria near a solid surface. *Physical Review E* **84**, 041932 (2011).
- 330 Kantsler, V., Dunkel, J., Polin, M. & Goldstein, R. E. Ciliary contact interactions dominate surface scattering of swimming eukaryotes. *Proceedings of the National Academy of Sciences* **110**, 1187-1192 (2013).
- 331 Denissenko, P., Kantsler, V., Smith, D. J. & Kirkman-Brown, J. Human spermatozoa migration in microchannels reveals boundary-following navigation. *Proceedings of the National Academy of Sciences* **109**, 8007-8010 (2012).
- 332 Rothschild. Non-random distribution of bull spermatozoa in a drop of sperm suspension. *Nature* **198**, 1221-& (1963).
- 333 Jikeli, J. F. *et al.* Sperm navigation along helical paths in 3D chemoattractant landscapes. *Nature communications* **6**, 1-10 (2015).
- 334 Woolley, D. Motility of spermatozoa at surfaces. *REPRODUCTION-CAMBRIDGE-126*, 259-270 (2003).
- 335 Bukatin, A., Kukhtevich, I., Stoop, N., Dunkel, J. & Kantsler, V. Bimodal rheotactic behavior reflects flagellar beat asymmetry in human sperm cells. *Proceedings of the National Academy of Sciences* **112**, 15904-15909 (2015).
- 336 Berke, A. P., Turner, L., Berg, H. C. & Lauga, E. Hydrodynamic attraction of swimming microorganisms by surfaces. *Physical Review Letters* **101**, 038102 (2008).
- 337 Ishimoto, K., Gadêlha, H., Gaffney, E. A., Smith, D. J. & Kirkman-Brown, J. Coarse-graining the fluid flow around a human sperm. *Physical review letters* **118**, 124501 (2017).
- 338 Smith, D., Gaffney, E., Blake, J. & Kirkman-Brown, J. Human sperm accumulation near surfaces: a simulation study. *Journal of Fluid Mechanics* **621**, 289-320 (2009).
- 339 Knowlton, S. M., Sadasivam, M. & Tasoglu, S. Microfluidics for sperm research. *Trends in biotechnology* **33**, 221-229 (2015).
- 340 Rappa, K. L. *et al.* Sperm processing for advanced reproductive technologies: Where are we today? *Biotechnology advances* **34**, 578-587 (2016).
- 341 Zaferani, M., Palermo, G. D. & Abbaspourrad, A. Strictures of a microchannel impose fierce competition to select for highly motile sperm. *Science advances* **5**, eaav2111 (2019).

- 342 Su, T.-W., Xue, L. & Ozcan, A. High-throughput lensfree 3D tracking of human sperms reveals rare statistics of helical trajectories. *Proceedings of the National Academy of Sciences* **109**, 16018-16022 (2012).
- 343 Tasoglu, S. *et al.* Exhaustion of racing sperm in nature-mimicking microfluidic channels during sorting. *Small* **9**, 3374-3384 (2013).
- 344 Nosrati, R. *et al.* Rapid selection of sperm with high DNA integrity. *Lab on a Chip* **14**, 1142-1150 (2014).
- 345 Eamer, L. *et al.* Turning the corner in fertility: high DNA integrity of boundary-following sperm. *Lab on a Chip* **16**, 2418-2422 (2016).
- 346 Zaferani, M., Cheong, S. H. & Abbaspourrad, A. Rheotaxis-based separation of sperm with progressive motility using a microfluidic corral system. *Proceedings of the National Academy of Sciences* **115**, 8272-8277 (2018).
- 347 Kolahi, K. S. *et al.* Effect of substrate stiffness on early mouse embryo development. *PloS one* **7** (2012).
- 348 Chen, W. L. K. & Simmons, C. A. Lessons from (patho) physiological tissue stiffness and their implications for drug screening, drug delivery and regenerative medicine. *Advanced drug delivery reviews* **63**, 269-276 (2011).
- 349 Joanicot, M. & Ajdari, A. Droplet control for microfluidics. *Science* **309**, 887-888 (2005).
- 350 Mashaghi, S., Abbaspourrad, A., Weitz, D. A. & van Oijen, A. M. Droplet microfluidics: A tool for biology, chemistry and nanotechnology. *TrAC Trends in Analytical Chemistry* **82**, 118-125 (2016).
- 351 Drescher, K., Dunkel, J., Cisneros, L. H., Ganguly, S. & Goldstein, R. E. Fluid dynamics and noise in bacterial cell-cell and cell-surface scattering. *Proceedings of the National Academy of Sciences* **108**, 10940-10945 (2011).
- 352 Elgeti, J., Kaupp, U. B. & Gompper, G. Hydrodynamics of sperm cells near surfaces. *Biophysical journal* **99**, 1018-1026 (2010).
- 353 Smith, D. J., Gaffney, E., Gadélha, H., Kapur, N. & Kirkman-Brown, J. Bend propagation in the flagella of migrating human sperm, and its modulation by viscosity. *Cell motility and the cytoskeleton* **66**, 220-236 (2009).
- 354 Schulman, R., Backholm, M., Ryu, W. & Dalnoki-Veress, K. Undulatory microswimming near solid boundaries. *Physics of Fluids* **26**, 101902 (2014).
- 355 Shum, H. & Gaffney, E. A. Hydrodynamic analysis of flagellated bacteria swimming in corners of rectangular channels. *Physical Review E* **92**, 063016 (2015).

- 356 Rikmenspoel, R. The equation of motion for sperm flagella. *Biophysical journal* **23**, 177-206 (1978).
- 357 Rikmenspoel, R. Movements and active moments of bull sperm flagella as a function of temperature and viscosity. *Journal of experimental biology* **108**, 205-230 (1984).
- 358 Bahr, G. F. & Zeitler, E. Study of bull spermatozoa: Quantitative electron microscopy. *The Journal of cell biology* **21**, 175-189 (1964).
- 359 Lin, J., Okada, K., Raytchev, M., Smith, M. C. & Nicastro, D. Structural mechanism of the dynein power stroke. *Nature cell biology* **16**, 479-485 (2014).
- 360 Brokaw, C. J. Bend propagation along flagella. *Nature* **209**, 161-163 (1966).
- 361 Becker, L. E. & Shelley, M. J. Instability of elastic filaments in shear flow yields first-normal-stress differences. *Physical Review Letters* **87**, 198301 (2001).
- 362 Goldstein, R. E., Powers, T. R. & Wiggins, C. H. Viscous nonlinear dynamics of twist and writhe. *Physical Review Letters* **80**, 5232 (1998).
- 363 Gadêlha, H. & Gaffney, E. A. Flagellar ultrastructure suppresses buckling instabilities and enables mammalian sperm navigation in high-viscosity media. *Journal of The Royal Society Interface* **16**, 20180668 (2019).
- 364 King, S. M. Turning dyneins off bends cilia. *Cytoskeleton* **75**, 372-381 (2018).
- 365 Yagi, T. *et al.* An axonemal dynein particularly important for flagellar movement at high viscosity implications from a new chlamydomonas mutant deficient in the dynein heavy chain gene *dhc9*. *Journal of Biological Chemistry* **280**, 41412-41420 (2005).
- 366 Lin, J. & Nicastro, D. Asymmetric distribution and spatial switching of dynein activity generates ciliary motility. *Science* **360**, eaar1968 (2018).
- 367 Li, G. & Tang, J. X. Accumulation of microswimmers near a surface mediated by collision and rotational Brownian motion. *Physical review letters* **103**, 078101 (2009).
- 368 Collins, D. J., Neild, A., deMello, A., Liu, A.-Q. & Ai, Y. The Poisson distribution and beyond: methods for microfluidic droplet production and single cell encapsulation. *Lab on a Chip* **15**, 3439-3459 (2015).
- 369 Organization, W. H. WHO laboratory manual for the examination and processing of human semen. (2010).
- 370 Tenje, M., Fornell, A., Ohlin, M. & Nilsson, J. (ACS Publications, 2017).
- 371 Jayaprakash, K. & Sen, A. Droplet encapsulation of particles in different regimes and sorting of particle-encapsulating-droplets from empty droplets. *Biomicrofluidics* **13**, 034108 (2019).

- 372 Fornell, A., Ohlin, M., Garofalo, F., Nilsson, J. & Tenje, M. An intra-droplet particle switch for droplet microfluidics using bulk acoustic waves. *Biomicrofluidics* **11**, 031101 (2017).
- 373 Fornell, A., Cushing, K., Nilsson, J. & Tenje, M. Binary particle separation in droplet microfluidics using acoustophoresis. *Applied Physics Letters* **112**, 063701 (2018).
- 374 Park, K. *et al.* In-droplet microparticle separation using travelling surface acoustic wave. *Biomicrofluidics* **11**, 064112 (2017).
- 375 Qin, X., Wang, H. & Wei, X. Intra-droplet particle enrichment in a focused acoustic field. *RSC Advances* **10**, 11565-11572 (2020).
- 376 Fornell, A., Liu, Z. & Tenje, M. Optimisation of the droplet split design for high acoustic particle enrichment in droplet microfluidics. *Microelectronic Engineering*, 111303 (2020).
- 377 Hein, M., Moskopp, M. & Seemann, R. Flow field induced particle accumulation inside droplets in rectangular channels. *Lab on a Chip* **15**, 2879-2886 (2015).
- 378 Brouzes, E., Kruse, T., Kimmerling, R. & Strey, H. H. Rapid and continuous magnetic separation in droplet microfluidic devices. *Lab on a Chip* **15**, 908-919 (2015).
- 379 Han, S.-I., Kim, H. S. & Han, A. In-droplet cell concentration using dielectrophoresis. *Biosensors and Bioelectronics* **97**, 41-45 (2017).
- 380 Fornell, A., Garofalo, F., Nilsson, J., Bruus, H. & Tenje, M. Intra-droplet acoustic particle focusing: simulations and experimental observations. *Microfluidics and Nanofluidics* **22**, 75 (2018).
- 381 Liu, Z., Fornell, A., Barbe, L., Hjort, K. & Tenje, M. On-chip background dilution in droplets with high particle recovery using acoustophoresis. *Biomicrofluidics* **13**, 064123 (2019).
- 382 Doonan, S. R., Lin, M. & Bailey, R. C. Droplet CAR-Wash: continuous picoliter-scale immunocapture and washing. *Lab on a Chip* **19**, 1589-1598 (2019).
- 383 Park, J., Destgeer, G., Kim, H., Cho, Y. & Sung, H. J. In-droplet microparticle washing and enrichment using surface acoustic wave-driven acoustic radiation force. *Lab on a Chip* **18**, 2936-2945 (2018).

Appendix I

Droplet breakup at the Entrance to a Bypass Channel in a Microfluidic System

AI.1. Preface for Appendix I

This Appendix was published as a journal article in *Physical Review Applied* and reproduced with permission from ref. 34. Copyright (2019) by the American Physical Society⁴⁰. The candidate was the second author and Mr. Sagar N Agnihotri was the lead author for this work. The candidate played a primary role in designing the research, analysing the data, and writing the paper. Additional authors for the work include Dr. Rajneesh Bhardwaj, and Prof. Adrian Neild. Their contributions were central to the publication of this work and are gratefully acknowledged and appreciated.

In this chapter, we experimentally and numerically investigate breakup of a droplet at the entrance to a microfluidic bypass channel. The PDMS microchannels are manufactured using standard photolithography techniques, and we employ a high-speed camera to visualize the interfacial dynamics of the droplets. 3D numerical simulations are carried out for conditions causing both droplet breakup and non-breakup. The droplets are generated upstream of the bypass channel using a standard T-junction, the subsequent interaction with the entrance to the bypass channel is studied. In particular, the effects of capillary number (Ca) and the relative width of the bypass channel with respect to the main channel (β) are examined. The regimes of breakup and non-breakup are plotted on Ca - β plane, experimentally, with the volume of the daughter droplets formed and the finger length in the bypass channel are also plotted on this regime map. There exists a critical value of Ca at constant β and a critical value of β at constant Ca , at which droplet breakup occurs. Combining measurements with numerical simulations, we show that the droplet breakup occurs if the hydrodynamic pressure drops across the droplet and average shear stress overcomes the differential Laplace pressure. We also found out that droplet breakup at the entrance to the bypass channel can exhibit squeezing and dripping regimes which are equivalent to those occurring in droplet generation at a T-junction.

AI.2. Introduction

Droplet microfluidics is finding widespread use in applications as diverse as drug discovery, diagnostics, chemical synthesis, single cell encapsulation, on-chip chemistry, and the production of microstructures [1–5]. Droplets are produced when two immiscible liquids, one of which acting as the continuous phase and other as the discontinuous phase, interact with

each other within a microfluidic system [6]. The most common droplet production geometries are the simple T-junction [7, 8] at which two channels containing the immiscible liquids join with each other perpendicularly, flow focusing devices [9, 10] in which the discontinuous phase is introduced via a central channel and the continuous phase is introduced by two symmetrically aligned side channels and, co-flowing devices in which two co-axial cylindrical channels are employed to deliver the two fluids [11]. Using these geometries droplets can be produced in a broad range of volumes ranging from femtoliters to nanoliters [12]. The droplets produced are isolated from each other, and so in the paradigm of a lab-on-a-chip, they can be considered as analogous to test tubes at the laboratory scale. The presence of the continuous phase allows for easy transport of the droplets around the microfluidic system.

While droplet production is rapid and highly repeatable, there is a need to control and manipulate the droplets' passage, behavior within the microfluidic systems [4]. Techniques, to achieve this, are broadly classified as being either passive or active. Passive techniques require no external source of energy, rather they control droplet outcomes through the use of changes in channel geometry [13–16], gravity [17] and surface properties [18]. Active techniques require an external source of energy through various means like the use of electric forces [19], microvalves [20], dielectrophoresis [21, 22] magnetic forces [23] or surface acoustic waves [24–26]. Acoustic actuation can also be used to produce individual droplets on demand and volume of the droplet can be controlled via the applied power [27] or producing small (femtolitre) droplets [28]. Passive techniques cause the same outcome for each droplet, while the nature of active methods allows the possibility of bespoke interactions.

The physics of passive droplet generation at a T-junction displays three distinct regimes [29, 30], namely 'squeezing' 'dripping' and 'jetting.' In the squeezing regime, the discontinuous phase is broken into droplets in the stream of the continuous phase due to the buildup of pressure at the upstream interface between the two fluids. Typically the protrusion of the discontinuous phase into the stream of the continuous phase almost blocks the channel prior to breaking up. The range over which this occurs can be related to the capillary number, $Ca = \left(\frac{\mu v}{\gamma}\right)$ where μ , v and γ are the viscosity of a continuous phase, velocity of a continuous phase and interfacial tension between the two phases, respectively. The squeeze regime has been reported to exist for $Ca < 0.015$ when the width of the channels meeting at the T-junction are equal [29, 31, 32]. A simple model was proposed by Garstecki *et al.*[33] to predict the length

of the droplet : $\left(\frac{l}{w}\right) = \left(1 + \frac{\alpha Q_{in}}{Q_{out}}\right)$ where l, w, α, Q_{in} and Q_{out} are the length of the droplet, the width of the microchannel, a fitting parameter, the flow rate of continuous phase and the flow rate of discontinuous phase, respectively. In the dripping regime breakup occurs if shear forces, around the tip of the protruding discontinuous phase, become dominant over the surface tension forces [34]. The range of capillary number (Ca) reported for this regime is $Ca > 0.015$ [29]. Finally, a third regime exists, termed “jetting” in which the discontinuous phase extends downstream, and two phases move side-by-side in a laminar flow for a distance of at least a few channel widths [29].

As with droplet formation, there have also been studies into the conditions required for subsequent partition of the droplets at T-junctions. Link *et al.* [13] studied droplet breakup in a symmetric T-junction and demonstrated breakup into precisely controlled daughter droplets. Their analytical model yielded a critical capillary number, and a critical initial extension of the mother droplet into the branch of the T-junction which indicated when breakup would occur: $\varepsilon_0 = \frac{l_0}{(\pi w_0)}$ is the initial extension where l_0, w_0 are the length of the droplet and width of the channel, respectively. Menetrier-Deremble and Tabeling [14] experimentally investigated the droplet breakup at the junction between microfluidic channels which meet at various angles. They observed that if the droplet interacts with the asymmetric junction of arbitrary angles, three outcomes are possible, namely direct breakup, retarded breakup and no breakup. The authors proposed that a critical finger length exists to predict the breakup. Subsequently, Jullien *et al.* [35] identified two regimes of breakup for a droplet interacting symmetrically with a T-junction over a range of capillary numbers: $4 \times 10^{-4} < Ca < 2 \times 10^{-1}$. These two regimes were defined using the distance between the droplet and channel wall, in the first regime, there exists a gap between the droplet and the microchannel wall while in the second regime there is no gap between the droplet and microchannel wall, so the droplet completely obstructs the flow. Hoang *et al.* [36] studied the droplet breakup in symmetric T-junction using 3D full numerical simulations and “stop-flow” simulations, in which droplet breakup was studied by switching off the flow in the simulations, i.e., breakup occurs only by capillary effects. In doing so, they concluded that the droplet breakup occurs if the curvature of “neck” exceeds the value of curvature elsewhere on the interface. In all these works on the behavior of droplets at a T-junction, the outlet conditions of the two branches are controlled externally to the chip, either being at a specified pressure or extracted flow rate.

In this work, we examine breakup at the entrance to a bypass channel. By this, we mean a secondary channel which branches from and then rejoins the main channel. While the entrance to the bypass channel is a T-junction, the conditions which exist in each branch is dictated by conditions internal to the chip (the flow rate which occurs in each branch), the external control is limited to the outlet of the main channel once the bypass has recombined with it. Bithi *et al.* [37] used a bypass channel to examine the dynamics of the droplet coalescence in microfluidic parking network. While, Sesen *et al* [38] showed that by application of surface acoustic waves a transition could be made between breakup and non-breakup at the entrance to a bypass channel. However, while previous studies have offered significant clarity on behavior at a T-junction, the critical conditions for a bypass channel have not been explored previously. Here, we study breakup of a droplet during interaction with the entrance to a bypass channel and demonstrate the equivalence to the squeezing and dripping regimes displayed by droplet generation systems. We investigate the effect of the width of bypass channel and capillary number on the mechanism of droplet breakup experimentally and numerically.

AI.3. Methodology

AI.3.1. Experimental Methods

The microfluidic chips were fabricated from polydimethylsiloxane (PDMS) using standard photolithography techniques. First, we fabricate a mold for the microchannel on a 2-inch silicon wafer. The wafer was RCA cleaned, wet oxidized and a negative photoresist SU-8 (MicroChem, SU-8 2050) was spin coated on the wafer. The spin speed was adjusted based on the height of the microchannel needed. Further, the wafer was prebaked at 65 °C for 5 minutes and at 95 °C for 12 minutes. An iron oxide coated glass mask with a pattern of the microfluidic circuit (printed using Laser Writer, LW405, Microtech Inc) was aligned on the top of the spin-coated wafer using a mask aligner (Karl Suss, MJB4). The wafer was subjected to ultraviolet radiation with an intensity of 215 mJ/cm², later post-baked at 65 °C for 4 minutes, at 95 °C for 10 minutes and allowed to cool in ambient. Subsequently, it was developed by SU8 photo developer for 10 to 15 min and cleaned with isopropanol. The wafer was kept on a hot plate at 120 °C for 10 min for hard-baking and allowed to cool in ambient. We poured a PDMS 10:1 mixture (Dow Corning, Sylgard 184) over the prepared mold and a 6:1 mixture was used for manufacturing a PDMS base slab on a glass slide. Both mixtures in the mold as well as in the

base slab were baked in the furnace at $65\text{ }^{\circ}\text{C}$ for about 30-40 minutes until they became sufficiently hard. The PDMS replica of the microfluidic circuit was peeled from the mold and was appropriately punched to make inlets and an outlet to the fluid channels. The patterned PDMS replica and PDMS base slab were bonded in an oven at $95\text{ }^{\circ}\text{C}$ for 10-12 hours.

Figure AI.1 shows a schematic of the experimental setup along with the microchannel geometry. The width of the main channel (w_m), the width of inlet channel of the discontinuous phase (w_d) and channel height (h) are kept constant in all measurements at: $w_m = 130 \pm 5\ \mu\text{m}$, $w_d = 65 \pm 3\ \mu\text{m}$ and $h = 60 \pm 3\ \mu\text{m}$ (Figure AI.2a). We vary the width of bypass channel (w_b) over a range of six values: $60 \pm 3\ \mu\text{m}$, $70 \pm 3\ \mu\text{m}$, $80 \pm 3\ \mu\text{m}$, $90 \pm 3\ \mu\text{m}$, $105 \pm 5\ \mu\text{m}$ and $120 \pm 5\ \mu\text{m}$. As such the values of $\beta \left(\frac{w_b}{w_m}\right)$ are $\beta = 0.48, 0.54, 0.62, 0.77, 0.80$ and 0.91 , respectively. Deionized water was used for the dispersed phase, while for the continuous phase two types of oil were selected, these were silicone oil (50 cSt Sigma Aldrich Inc, $\rho = 960\ \text{kg/m}^3$, $\mu = 0.048\ \text{Pa}\cdot\text{s}$) and paraffin oil (30 cSt, Merck Inc, $\rho = 850\ \text{kg/m}^3$, $\mu = 0.022\ \text{Pa}\cdot\text{s}$). Both the water and oil flows were driven by a syringe pump (New Era pump systems Inc, USA). The range of flow rates for both silicone oil and water were 0.24 to $16.4\ \mu\text{L}/\text{min}$ when used together. When paraffin oil and water were used together this range of flow rates became 0.24 to $1.64\ \mu\text{L}/\text{min}$.

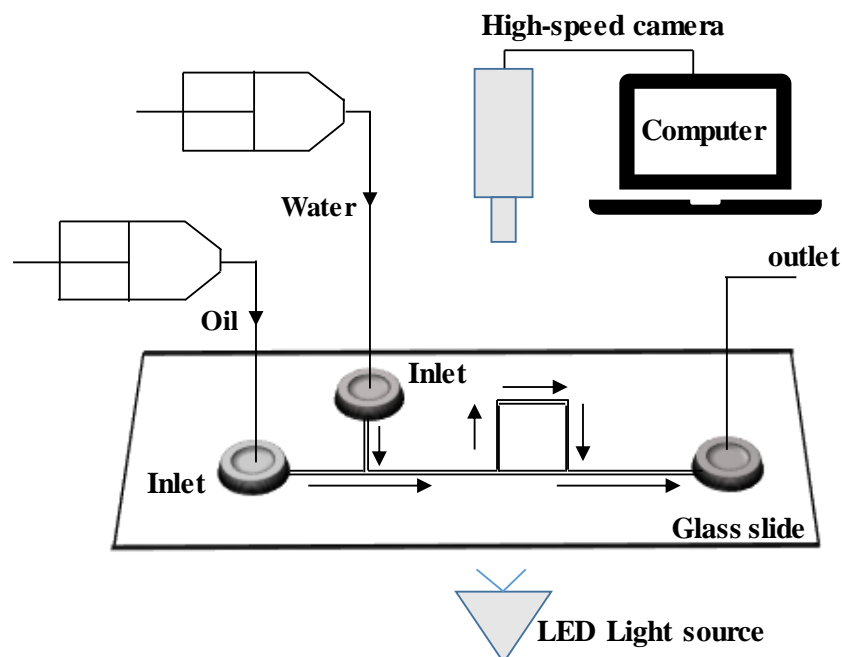


Figure AI.1. Schematic of the experimental setup used in the present work. Due to wetting properties of microfluidic chip de-ionized water is a discontinuous phase and oil is continuous phase.

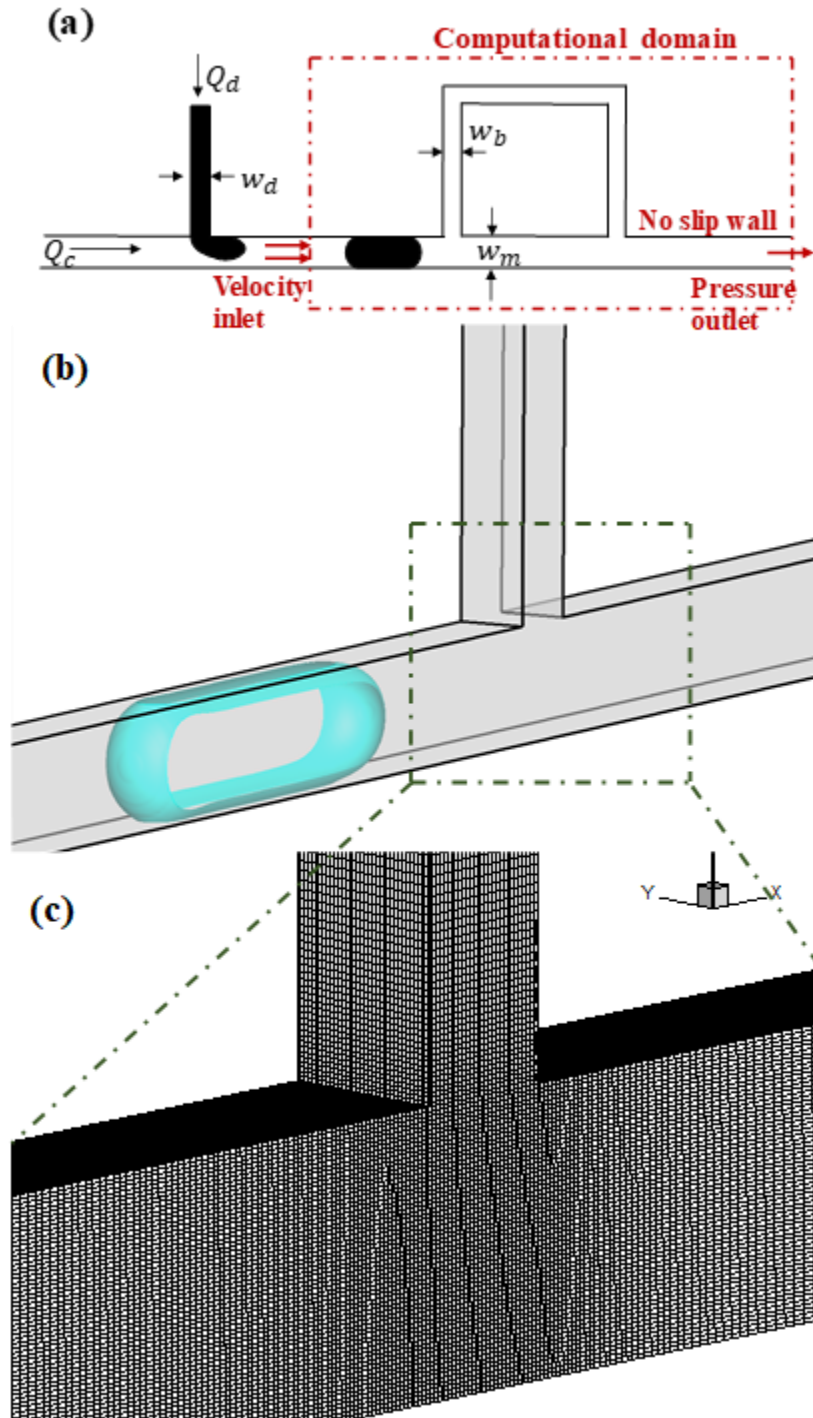


Figure A1.2. (a) Problem definition shown by a schematic. The computational domain is shown by a dotted box and boundary conditions are shown at the inlet, outlet and wall (b) Zoomed in view of the entrance to the bypass channel and droplet shape before interaction with it. (c) Mesh is plotted in the region close to the entrance to the bypass channel.

We utilized high-speed visualization to record the interfacial dynamics of the droplet interacting with the entrance to the bypass channel. A high-speed camera (Motion Pro Y3, IDT Inc, USA) with a long-distance working objective (Qioptiq Inc., Germany) was used to capture images at 300 frames per second resolution of 1280×1024 and a magnification such that the

image is $3\mu\text{m}$ per pixel. The velocity and size of droplets (generated at a T-junction upstream of the bypass channel) were measured using image processing, with the latter estimated assuming the plug consists of a cuboid section and spherical caps at either end. The maximum uncertainty in the volume measurement is around $\pm 2.8\%$, considering an error of ± 4 pixels during length measurement by our image processing method. The volume of the daughter droplet formed after breaking up at the entrance to the bypass channel was measured by taking the difference between the volumes of the mother droplet, before and after the breakup.

A spinning drop tensiometer (Dataphysics Inc, SVT20) was employed to measure the surface tension for the water-oil system, yielding values of 38 mN/m and 30 mN/m for water-silicon oil and water-paraffin oil, respectively. The corresponding range of the capillary number ($Ca = \frac{\mu v_c}{\gamma}$) in our measurements was 0.001 to 0.04, where μ , v_c and γ represent viscosity of the oil, velocity of the oil and surface tension for the oil-water system, respectively.

AI.3.2. Simulation Setup and Grid Size Independence Study

A commercial CFD software package (Fluent 15.0, ANSYS Inc, USA) was used to simulate the droplet behavior at the entrance to the bypass channel. Within the software, 3D Navier-Stokes equations were numerically solved using the finite volume method with the PISO (Pressure-Implicit with Splitting of Operators) scheme, and Volume-of-Fluid method was used for tracking the liquid-liquid interface. This was done using the computational domain shown in Figure AI.2a. We did not simulate the generation of the droplets at upstream T-junction and used a single droplet in the main channel. A 3D isometric view of the droplet just before the interaction with the entrance to the bypass channel is shown in Figure AI.2b. The volume and velocity of a droplet (v) generated at upstream T-junction were used as the input parameters for the simulation. At the inlet of the microchannel, a uniform velocity obtained from the experiments was imposed as a boundary condition. While, at the outlet of the microchannel the pressure was set to atmospheric. No slip conditions were applied to the walls of the microchannel.

A Cartesian structured mesh was generated using a commercial meshing software (ICEM, Ansys Inc). We used a uniform, structured Cartesian grid near the entrance to the bypass channel and a non-uniform grid with grid stretching is utilized away from the entrance to the

bypass channel (Figure AI.2c). A time step of $\Delta t = 10^{-5}$ s was used in all simulations. The following properties of silicone oil and water were used in the simulations: $\rho = 960$ kg/m³, $\mu = 0.048$ Pa-s; $\rho = 1000$ kg/m³ and $\mu = 0.00086$ Pa-s. The measured value of the contact angle of water-oil on PDMS from the recorded visualization of the droplet motion was around 140° , and we used this value in the simulation, assuming it as constant for a moving droplet.

Figure AI.3 shows a grid size independence study for $\beta = 0.62$ and $Ca = 0.007$ for the three refinements at the entrance to the bypass channel: $\Delta S = 2\mu m$, $3\mu m$, and $5\mu m$, where ΔS is the minimum grid size in x, y and z directions. The finger length (L_f , defined in left inset of Figure AI.3) and pressure drop (ΔP) between two fixed points (shown in the right inset of Figure AI.3) are plotted for the different grid refinements. The corresponding number of cells in these cases and the error with respect to the finest grid ($\Delta S = 2\mu m$) are shown in **Error! Reference source not found.**. As the error in case 2 is just 0.16 % and 2 % for ΔP and L_f , respectively, $\Delta S = 3\mu m$ was used in the simulations.

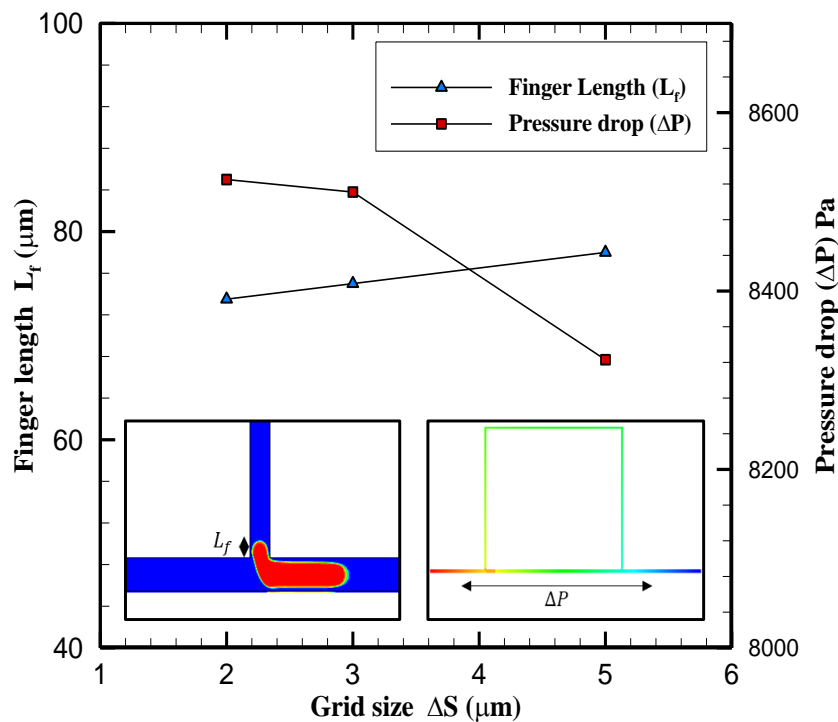


Figure AI.3. Grid size independence study: Finger length (L_f) on the left-hand side of the Y-axis for different grid sizes ($2\mu m$, $3\mu m$ and $5\mu m$) on the X-axis at constant $\beta = 0.62$. Pressure drop (ΔP) in a microchannel on the right-hand side of the Y-axis for different grid sizes ($2\mu m$, $3\mu m$, and $5\mu m$) on the X-axis when droplet interacts with the entrance of the bypass channel at constant $\beta = 0.62$.

Table AI.1. Grid independence study. Error in ΔP and L_f with respect to the finest grid ($2 \mu m$) used.

Cases	ΔS	Number of cells	Relative % error in ΔP with respect to case 3	Relative % error in L_f with respect to case 3
1	$5 \mu m$	0.3×10^6	2.2 %	3.8 %
2	$3 \mu m$	0.56×10^6	0.16 %	2 %
3	$2 \mu m$	1.12×10^6	-	-

AI.4. Results

We present results of droplet behavior at the entrance to the bypass channel, characterizing it as either a breakup or non-breakup event. The analysis of the bypass channel will start with a study of the effect of ratio of the width of the bypass to that of the main channel ($\beta = \frac{w_b}{w_m}$) in the range of 0.48 to 0.91, while keeping the capillary number constant ($Ca \approx 0.003$). Then, we vary the capillary number from 0.001 to 0.04, while $\beta \approx 0.48$. Finally, we will compare experimental and numerical results for interfacial dynamics and use this technique to explain the mechanisms of breakup. We combine the experimental data to present regime maps on Ca - β plane with contours of finger length and volume of the daughter droplet. We have examined the volume of the mother droplet generated at upstream T-junction and compared this with a previously reported model [33], this information is provided in supplemental information [39]. One of the effects of varying the inlet flow rates is that this volume will also change, however as we remain in the squeezing regime for droplet generation, this variation is relatively small. We have provided more information about mother droplet length in supplementary information.

AI.4.1. Effect of Channel Width Ratio (β)

To start the analysis of the droplet interaction with the entrance of the bypass channel we examine the effect of the ratio of width of the bypass channel to the main channel, β . A range of β from 0.48 to 0.91 was used, keeping the capillary number constant at 0.0028 ± 0.0002 . To classify the droplet interaction with bypass channel as droplet breakup, it must satisfy two conditions: i) the volume of the daughter droplet formed must be more than 2% of that of mother droplet volume and ii) the droplet breakup must be consistent. In Figure AI.4 image sequences are shown column-wise for three different values of β ($\beta = 0.48, 0.77, 0.91$). At β

$= 0.48$, when the droplet interacts with the bypass entrance, breakup does not occur (it does not satisfy the two conditions), the maximum finger length, L_f into the bypass channel was measured to be $71\mu\text{m}$. However, we observed tiny droplets inconsistently (the images have been chosen so that these droplets are observed). The percentage of the volume of these daughter droplets with respect to the volume of the original droplet (V_{ratio}) is less than 2%. At $\beta = 0.77$, the droplet breakup occurs consistently, with a finger length of $97\mu\text{m}$ prior to partition, and a volume ratio of 12%. When β was increased to 0.91 the finger length rises to $139\mu\text{m}$ and the volume ratio to 30%. From this data, a critical value of β exists at a given Ca , above which droplet production is consistent, and upon further increase of β the finger length and, hence the volume ratio will rise.

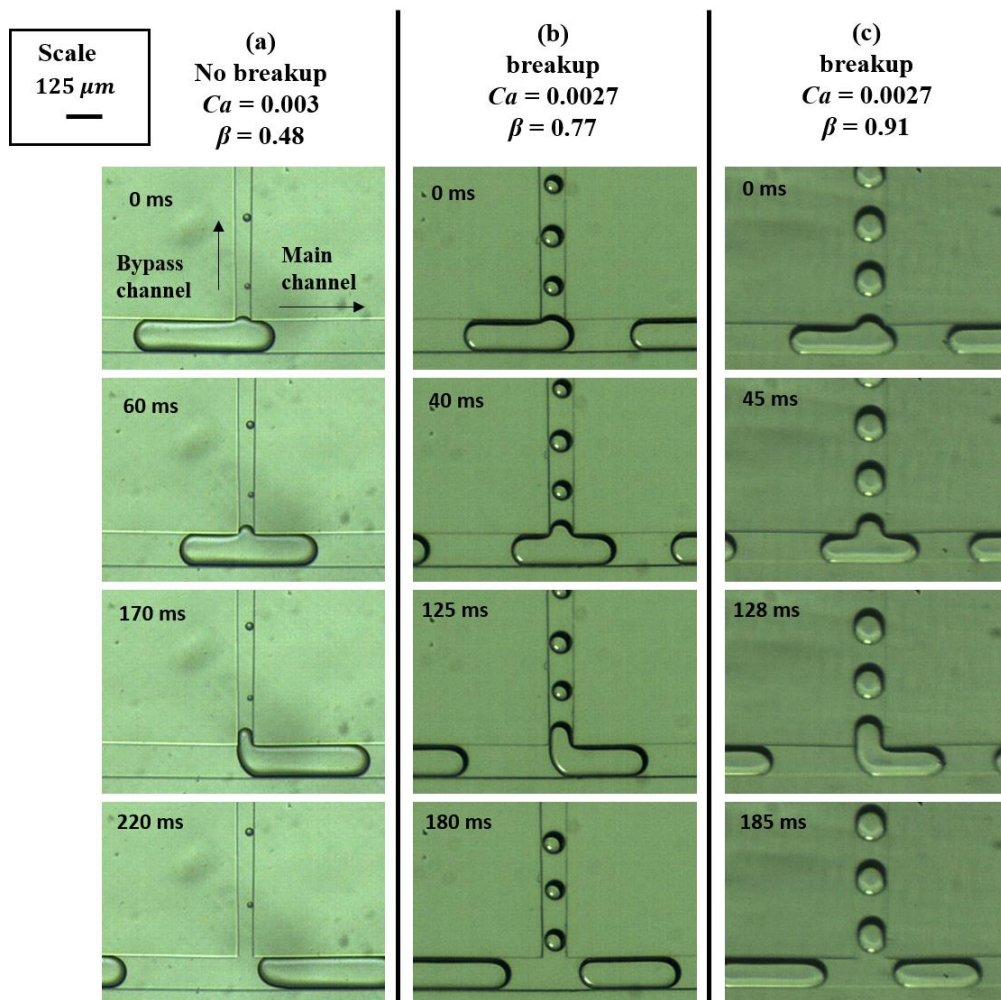


Figure AI.4. High-speed visualization of the droplet interaction with the entrance of the bypass channel showing the transition from no droplet breakup to droplet break up at different time intervals. Results are plotted for three cases of β . (a) $\beta = 0.48$ [39] (b) $\beta = 0.77$ [39] (c) $\beta = 0.91$ [39]. Capillary number is kept almost constant in all cases ($Ca = 0.0028 \pm 0.0002$).

AI.4.2. Effect of the Capillary Number (Ca)

We investigate the effect of Ca over the range of 0.001 to 0.04, while keeping β constant at 0.48. Figure AI.5 shows that at $Ca = 0.0022$, droplet breakup occurs at the bypass entrance with a finger length of $82\mu\text{m}$ and the volume ratio of 7%. However, with increased Ca , droplet breakup ceases. Instead at $Ca = 0.005$, we don't observe droplet breakup with a finger length of $71\mu\text{m}$. For further increase of Ca to 0.037 caused droplet breakup to cease completely and the finger length to drop further to $27\mu\text{m}$. Hence, a critical value of Ca exists to achieve breakup at a constant β . Also, L_f and V_{ratio} decrease with increased Ca .

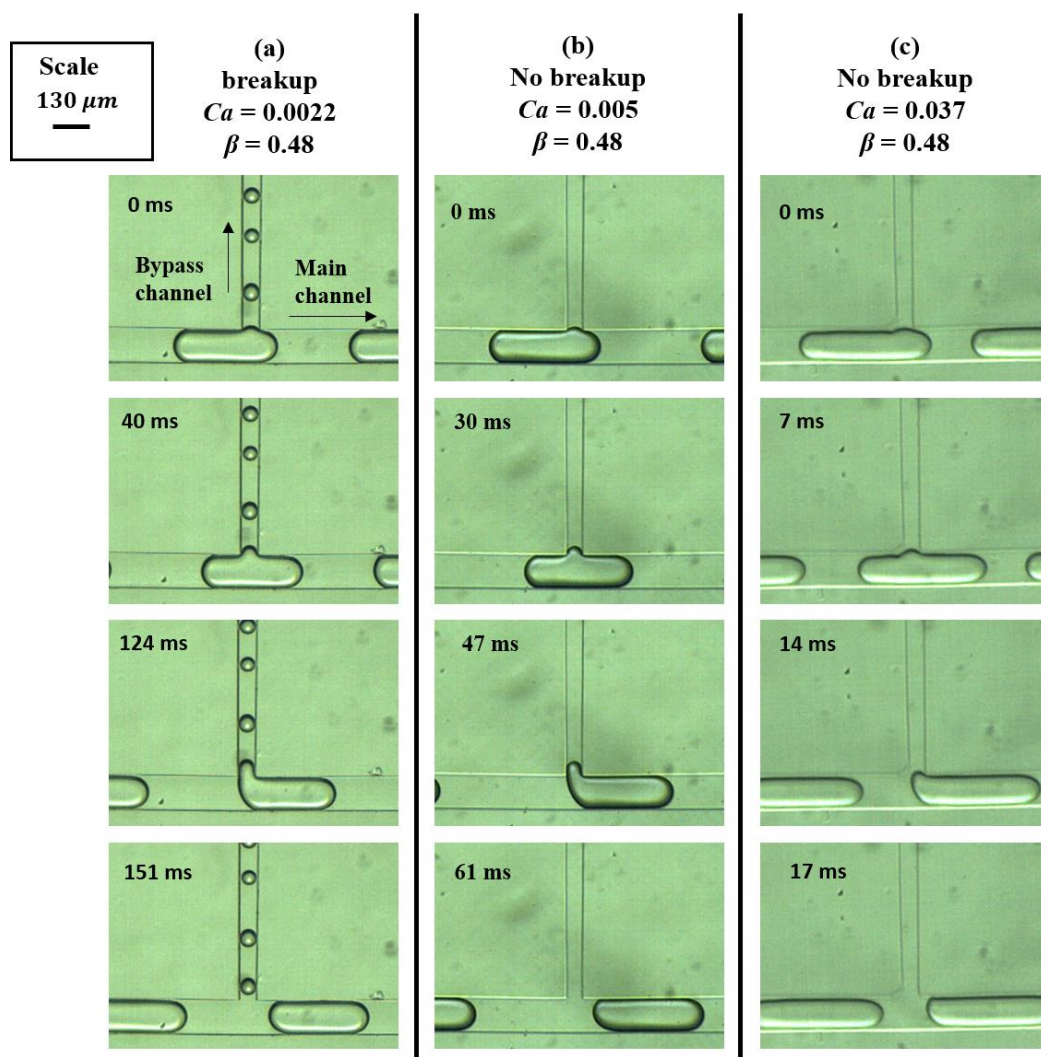


Figure AI.5. High-speed visualization of the droplet interaction with the entrance of a bypass channel showing the transition from no droplet breakup to droplet break up at different time intervals showing the effect of Ca (a) $Ca = 0.0022$ [39] (b) $Ca = 0.005$ [39] (c) $Ca = 0.037$ [39]. The ratio of channel width β is kept constant in all cases ($\beta = 0.48$).

AI.4.3. Comparison between Experimental and Computational Results

We compare computational results of the non-breakup case with the experimental results at $\beta = 0.48$ and $Ca = 0.005$ in Figure AI.6. The length of the mother droplet in the simulation was matched to that observed in the experimental work. The shape of the droplet interfaces obtained at different times is in very good agreement qualitatively with those recorded in the experiments. The experimentally measured maximum finger length (L_f) is $62\mu m$ while the numerical value is $53\mu m$. Similarly, Figure AI.7 compares measurements and computations for a case of droplet breakup ($\beta = 0.63$ and $Ca = 0.007$), again good agreement can be observed. The measured L_f is around $90\mu m$ as compared to a computed value of $78\mu m$. The percentage of daughter droplet as compared to original droplet (V_{ratio}) is measured to be 11.4% while in computational work it is around 7.2%. Overall, the computational results capture non-breakup and breakup with reasonable accuracy, this benchmarking allows the computer model to be used to examine the breakup mechanisms.

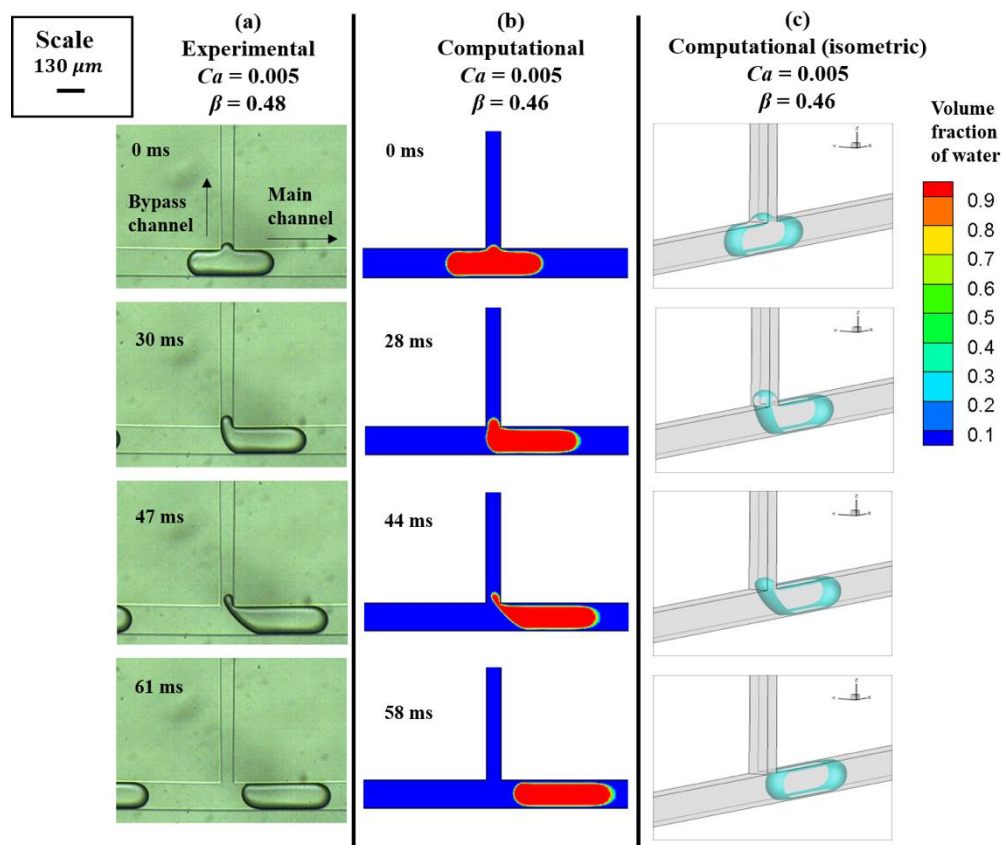


Figure AI.6. Comparison between experimental and computational work at $\beta = 0.48$ and $Ca = 0.005$. (a) High-speed visualization of the droplet interaction with the entrance of a bypass channel. (b) Computed contours of the volume fraction of water [39]. (c) Isometric view of the iso-surface of the volume fraction of water at 0.5.

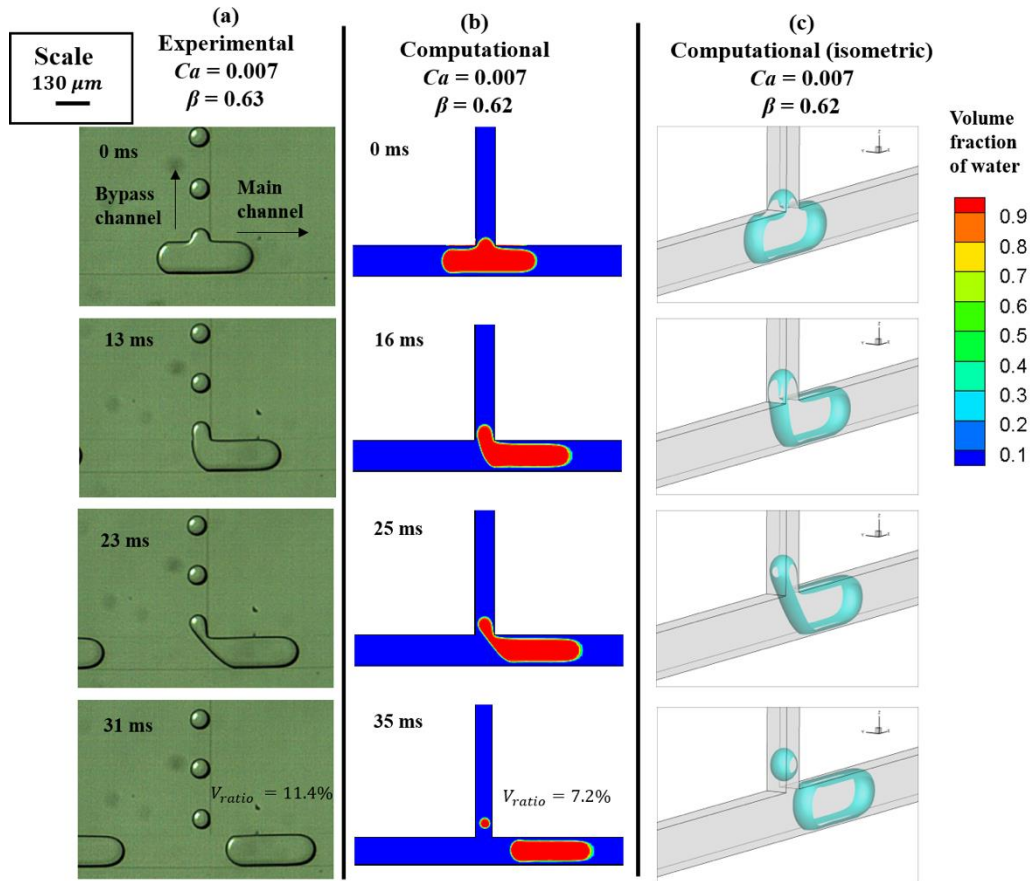


Figure AI.7. Comparison between experimental and computational work at $\beta = 0.63$ and $Ca = 0.007$. (a) High-speed visualization of the droplet interaction with the entrance of a bypass channel. (b) Computed contours of the volume fraction of water [39]. (c) Isometric view of the iso-surface of the volume fraction of water at 0.5.

AI.4.4. Regime Map

Figure AI.8 plots data of all the measurements performed in the present study on the $Ca - \beta$ plane and indicates the transition between the breakup and non-breakup regimes by way of the dashed line. We plot the corresponding finger length (L_f) obtained in five ranges, as shown by the legend of Figure AI.8a. Each range is represented using a different symbol and color. As mentioned earlier and shown by the regimes in Figure AI.8a, to achieve the breakup, a critical value of β exists at constant Ca , and a critical value of Ca exists at constant β . The finger length, $L_f = [125, 150] \mu m$, is found to be present at a smaller Ca and larger β . In the breakup region, L_f decreases with increase in Ca at constant β or with a decrease in β at constant Ca . $L_f = [25, 75] \mu m$ corresponds to non-breakup region. As pointed to in Ref. [14], we also observed the existence of a critical finger length ($75 \mu m$ in the present study) for achieving the droplet breakup.

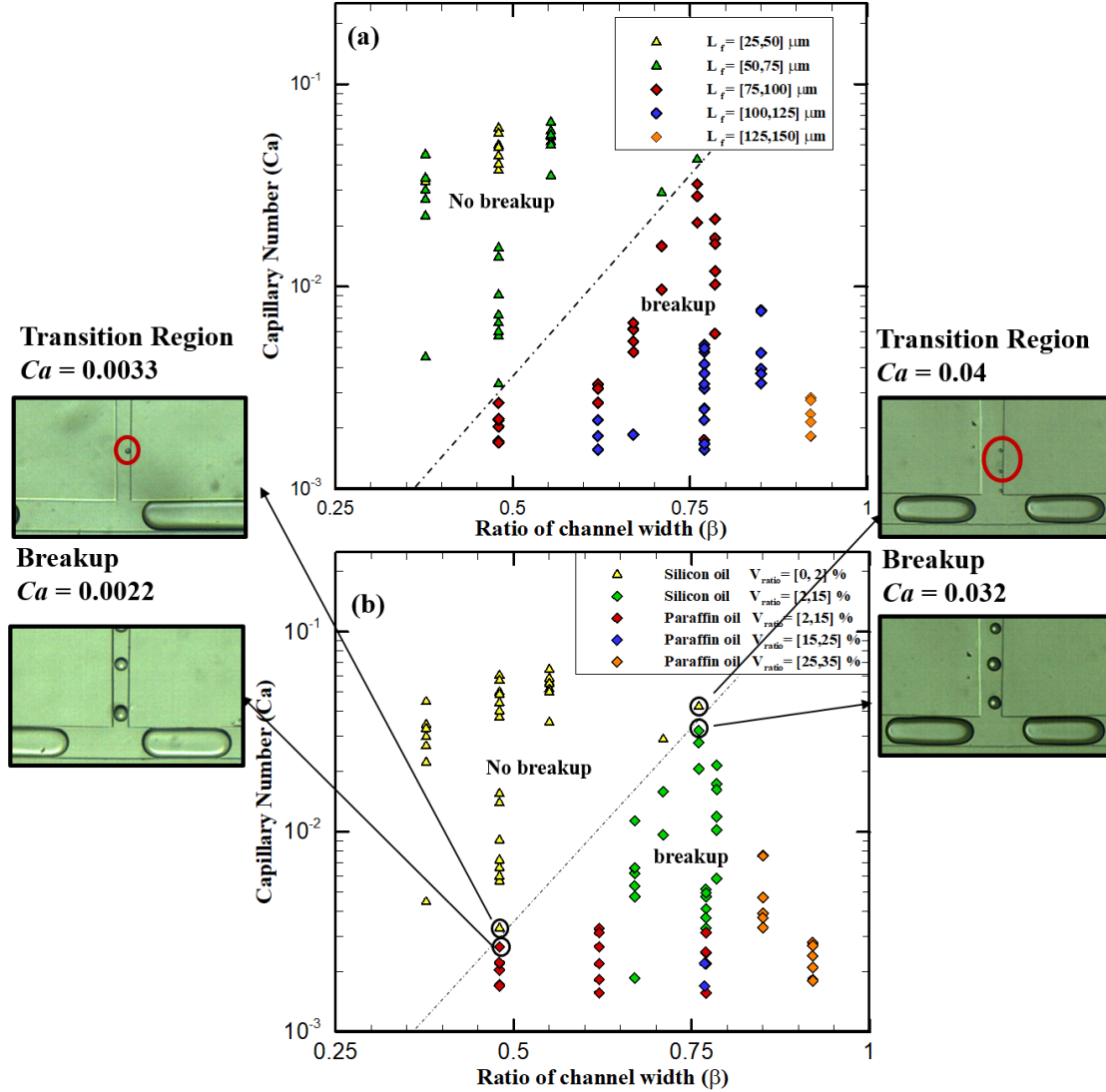


Figure AI.8. (a) Regime map is showing contours of finger length (L_f) on Ca - β plane. A dotted line is shown to demarcate regions of droplet breakup and no droplet breakup. (b) Regime map showing contours of V_{ratio} on Ca - β plane.

Figure AI.8b shows the regime map on the Ca - β plane, and we plot the percentage of daughter droplet volume with respect to original droplet volume (V_{ratio}) for the two regimes. The value of $V_{ratio} = [0, 2]$ % is assumed to be in the non-breakup region since droplet breakup in this region was very intermittent and inconsistent. In the droplet breakup region the maximum value of $V_{ratio} = [25, 35]$ % is measured when Ca is at the minimum of the range examined and β the maximum, as we go on increasing Ca or decreasing β , V_{ratio} starts decreasing from (25-35%) to (15-25%) to (2-15 %) and finally to (0 to 2%) which we classify as the non-breakup region due to its intermittency.

AI.4.5. Transition Region

When we increase Ca while keeping β constant, we observe a transition region where, tiny intermittent daughter droplets are produced. As volume of these droplets is less than 2% of mother droplet volume and these tiny droplets are produced once in four to five interactions we don't term this droplet breakup. Insets on the left-hand side of Figure AI.8 show the transition region at a constant β of 0.48. We observe that at $Ca = 0.0022$ when the mother droplet interacts with the bypass channel droplet breakup occurs. As Ca is increased to 0.0033, we observe tiny droplets being produced once in every few interactions. With further increase in Ca to 0.005, we observe no droplet breakup. Similarly, insets on right-hand side of Figure AI.8, shows transition region at constant β of 0.77. We observe that at $Ca = 0.032$ when mother droplet interacts with bypass channels, droplet breakup occurs. As Ca is increased to 0.04, we observe tiny droplets being produced in an irregular fashion. We observe that when the system is operating in transition region a slight change in flow condition, we are able to go from breakup to no breakup.

AI.5. Discussion

AI.5.1. Equivalence to Squeezing and Dripping Regimes

According to Garstecki *et al.* [33], surface tension acts as a stabilizing force while resistance to the flow of the continuous phase (F_R) and shear force (F_τ) have destabilizing effects in case of droplet generation at T-junction. If the gap between the droplet and main channel wall (ε) is smaller than the width of the main channel (w) i.e. $\varepsilon \ll w$, $F_R > F_\tau$ which means leading contribution for droplet breakup comes from F_R and this regime is generally referred as squeezing regime [29]. If $\varepsilon \sim w$, F_τ has a significant effect on droplet breakup along with F_R , and this regime is referred as dripping regime [29]. We now identify an equivalent squeezing and dripping regime in our measurements when generated droplet interacts with the entrance to the bypass channel.

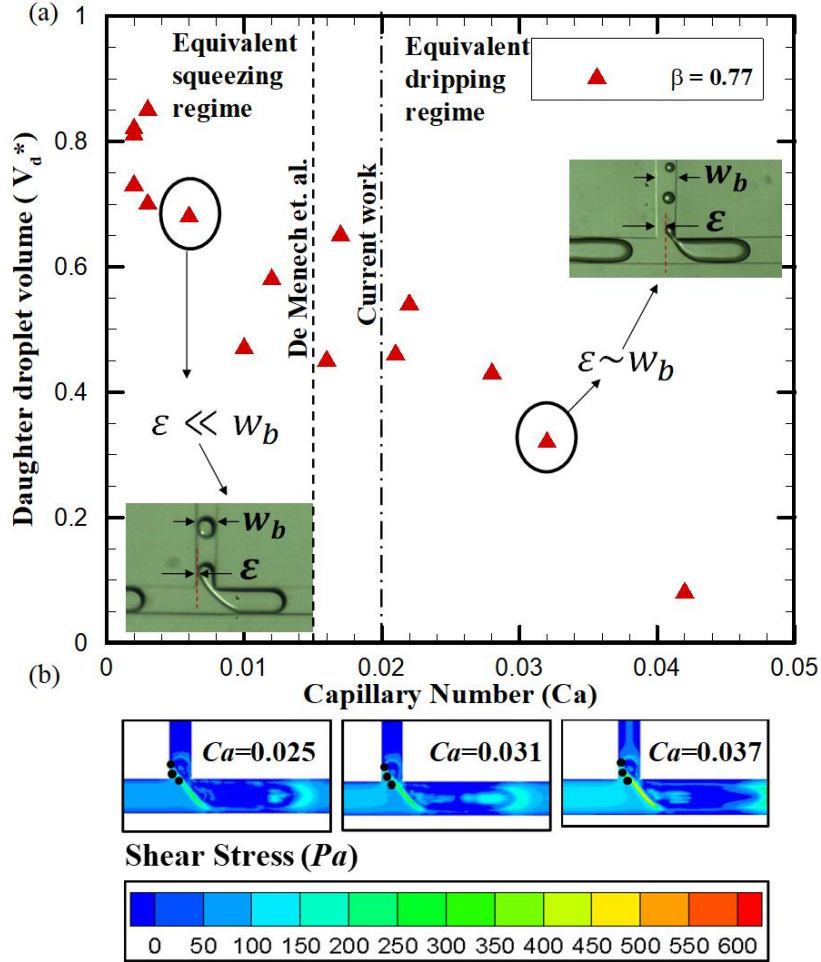


Figure AI.9. (a) Dimensionless daughter droplet volume as a function of the capillary number showing equivalent squeezing and dripping regime. The dotted line shows the squeezing regime given by Menech *et al.* and a dash-dot line showing current work. (b) Contours of shear stress at different Ca in the equivalent dripping regime.

For droplet generation, Menech *et al.* [29] plotted dimensionless droplet volume (V) as a function of Ca and found out that slope V versus Ca is constant in the squeezing regime (the droplet volume remains almost constant) and becomes steeper in the dripping regime (the droplet volume starts to decrease drastically). In Figure AI.9a, we plot the dimensionless daughter droplet volume (V_d^*) as a function of Ca when the droplet interacts with the entrance to a bypass channel for the case droplet breakup at $\beta = 0.77$, where $V_d^* = (\text{volume of daughter droplet}) / (w_m \times w_b \times h)$. We observed that for constant β , if we increase Ca , the size of the daughter droplet formed after breakup decreases, that is the slope of (V_d^*) as a function of Ca becomes steeper in the dripping regime. A similar trend to that observed by Menech *et al.* [29]. Insets of Figure AI.9a shows that as we increase Ca , ϵ also increases, where ϵ , in our case is the distance between the wall of the bypass channel and droplet interface when it is about to break. This means that the formation of the droplet takes place from a finger which is narrower than

the width of the bypass channel. In our case (droplet breakup), ε becomes comparable with w_b at $Ca \approx 0.02$, while Menech *et al.* [29] observed this at $Ca \approx 0.015$ (for droplet generation).

Thus far, we have defined our dripping regime by comparison of the value of ε with that occurring in the dripping regime of droplet generation. However, for this to be an accurate analogy, there should be more than a geometrical similarity, the physics should also be comparable. The key feature of the dripping regime is that the shear forces, occurring as the flow goes around the interface through the gap measured by ε , starts to play an important role in creating the droplet. We now examine if a rise in the prominence of shear is also evident in the case of droplet breakup in the dripping regime.

We plotted contours of the shear stress in three cases of breakup using numerical simulations for $Ca = 0.025$, 0.031 and 0.037 in Figure AI.9b. In these simulations, the mother droplet volume, the interfacial tension between continuous and discontinuous phase and the viscosity are kept constant, and the change in Ca is achieved through an increase in the droplet velocity. We have calculated the shear stress on the finger, due to the flow past the finger into the bypass channel. We have plotted component of shear stress, τ_{xz} , in the mid-XZ plane of the channel (see coordinate geometry in Figure AI.2b). τ_{xz} was averaged over the finger length (liquid-liquid interface), as shown in insets of Figure AI.9. Further information about the calculation of average shear stress is provided in the supplemental material [39].

We observe that in the dripping regime as Ca increases, the shear stress acting on the liquid-liquid interface also increases. To further investigate an equivalent squeezing and dripping regime, from our measurements, we plotted the evolution of the finger length and ε for $Ca = 0.003$ (squeezing regime) and $Ca = 0.030$ (dripping regime) with time in Figure AI.10. Both represent cases of droplet breakup and $\beta = 0.77$. Stage 1 represents the time before the droplet interacts with the entrance to the bypass channel and stage 6 represents the time just before the breakup. These stages of droplet interaction are also shown on top of the plot. We observe that as the droplet moves past the bypass entrance the finger length (L_f), as expected, keeps increasing, though the rate of change of the finger length for $Ca = 0.003$ is greater than that for $Ca = 0.030$. The maximum value of L_f observed for $Ca = 0.003$ is around $117\mu m$ while the maximum value of L_f observed for $Ca = 0.030$ is around $65\mu m$. The value of ε is plotted as constant, $3\mu m$ (a single pixel) for the case of $Ca = 0.003$, as there is no visible gap between the

droplet and channel wall. For the case of $Ca = 0.030$, the value of ε increases from $3\mu\text{m}$ to $35\mu\text{m}$ making $\varepsilon \sim w_b$ as the droplet advances further, which is consistent with the observation found in the dripping regime of droplet generation. As the value of ε becomes comparable with w_b shear stress should start to play an important role for this to be termed a dripping regime.

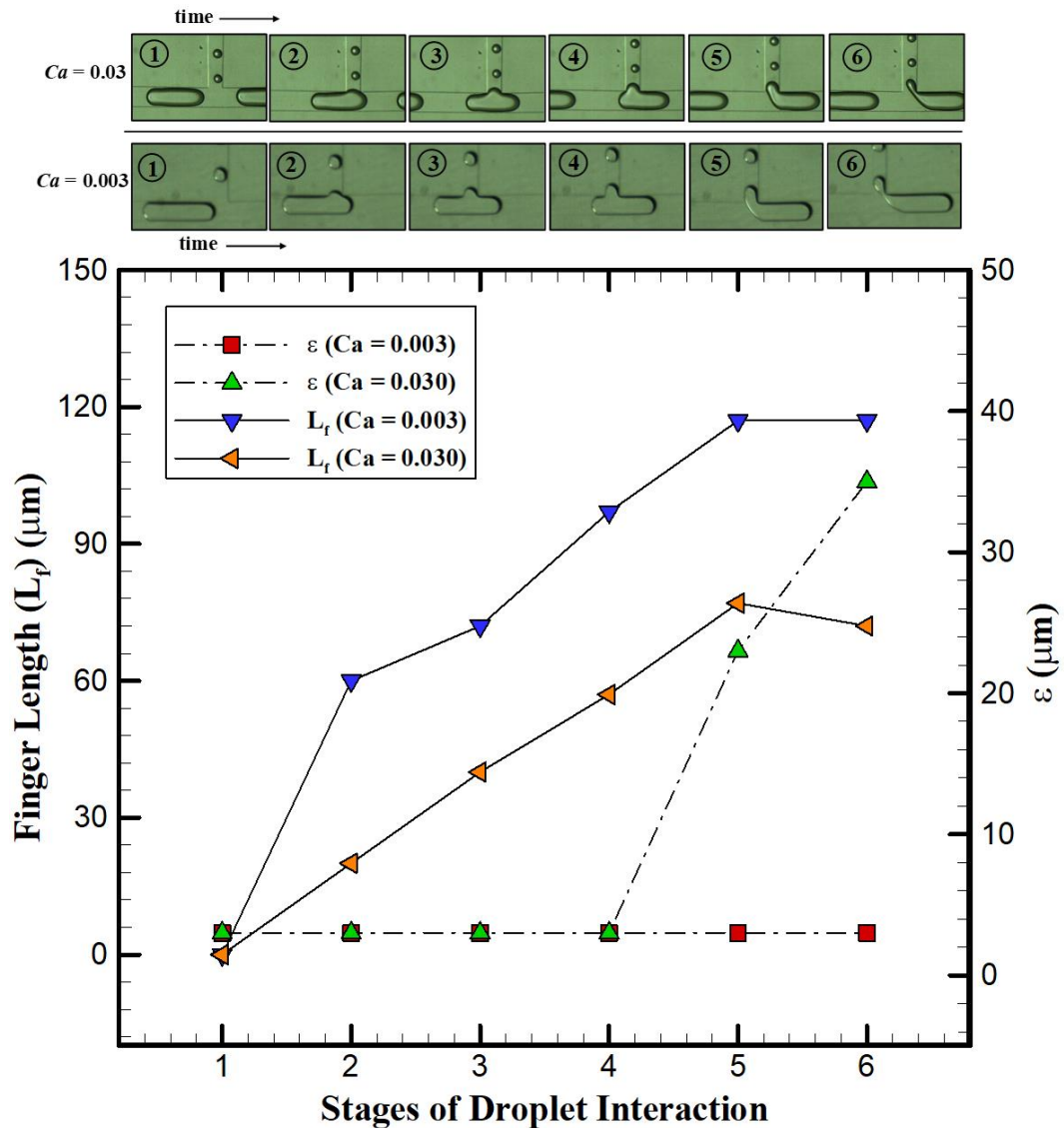


Figure AI.10. Evolution of finger length and ε with time. Finger Length (L_f) plotted on the left-hand of Y-axis and ε on the right-hand side of Y-axis Vs. stages of droplet interaction (evolution with time).

Figure AI.11 shows a zoomed-in view of the pressure inside and outside the droplet when it interacts with the entrance to the bypass channel, where P, P_h, P_t, P_1 and P_2 are upstream pressure in the main channel, pressure close to head of the droplet in main channel, pressure close to the tail of the droplet in the bypass channel, pressure inside the droplet near tail of the droplet and pressure inside the droplet close to head of the droplet. Figure AI.12 and Figure

AI.13 plots the average shear stress acting on the finger and the hydrodynamic pressure built up ($P - P_t$) against the stages of droplet interaction with the entrance to the bypass channel, obtained through numerical simulations. We calculate the shear stress for different values of Ca and show that the shear increases with rising Ca . We also plot the pressure build-up across the mother droplet for different values of Ca . In these simulations, the increase in Ca is achieved through an increase in the droplet velocity, while keeping the mother droplet volume, interfacial tension, geometry of microchannel and viscosity constant. All these simulations represent cases of droplet breakup. Insets in Figure AI.12 and Figure AI.13 shows the contours of shear stress, pressure and represent the corresponding stage of droplet interaction at which the current set of data is computed. We observe that as we increase the value of Ca there is a consistent increase in average shear stress acting on the finger while there is a consistent decrease in ($P - P_t$). In Figure AI.12, as the droplet advancement through the entrance to the bypass channel average shear stress goes on increasing, this can be linked to the increase in ε as the droplet progresses past the entrance as seen in Figure AI.10. As per Garstecki *et al.*[33], the shear stress in droplet generation $\tau = \left(\frac{\mu u_{gap}}{\varepsilon}\right)$, while $u_{gap} = \left(\frac{Q_{oil}}{h\varepsilon}\right)$, hence $\tau = \left(\frac{\mu Q_{oil}}{h\varepsilon^2}\right)$, where $\tau, \mu, u_{gap}, Q_{oil}$ and h are shear stress, viscosity of continuous phase, velocity in a gap between droplet interface and wall of microchannel and height of the microchannel respectively. In the case of droplet generation, as the discontinuous phase pushes further into the main channel, and blocks it more, the shear stress and build-up of pressure should increase, remembering that Q_{oil} is fixed. In the current study, the situation is more complex, as time advances the value of ε increases, however the flow through this gap is not fixed. As the gap grows this flow will increase (the droplet's progression in the main channel and bypass channel will slow accordingly), hence, Q_{oil} grows. The result is that the growth in ε caused a rise in shear stress as captured with the numerical simulations and shown in Figure AI.12. This means that even when the finger is narrower than the bypass channel, a droplet can be broken off. The finger length may retract slightly (as in Figure AI.10), but the rising shear can be enough to break the droplet.

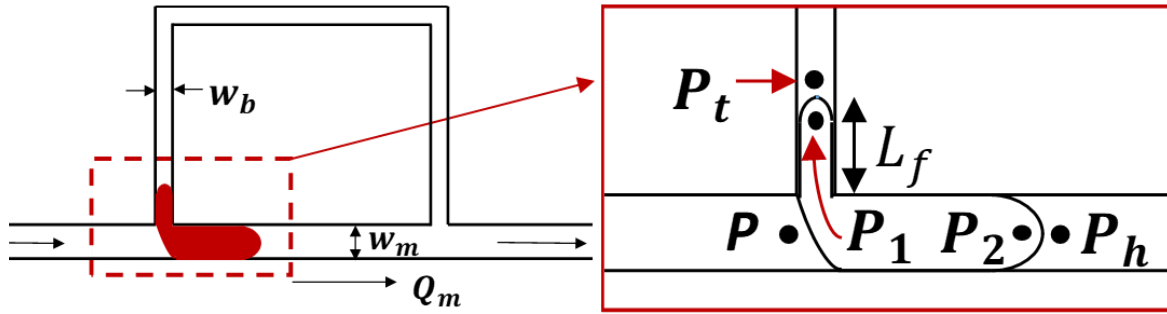


Figure AI.11. Schematic of the droplet interacting with the T-junction. Zoomed in view shows pressure notations inside and outside the droplet.

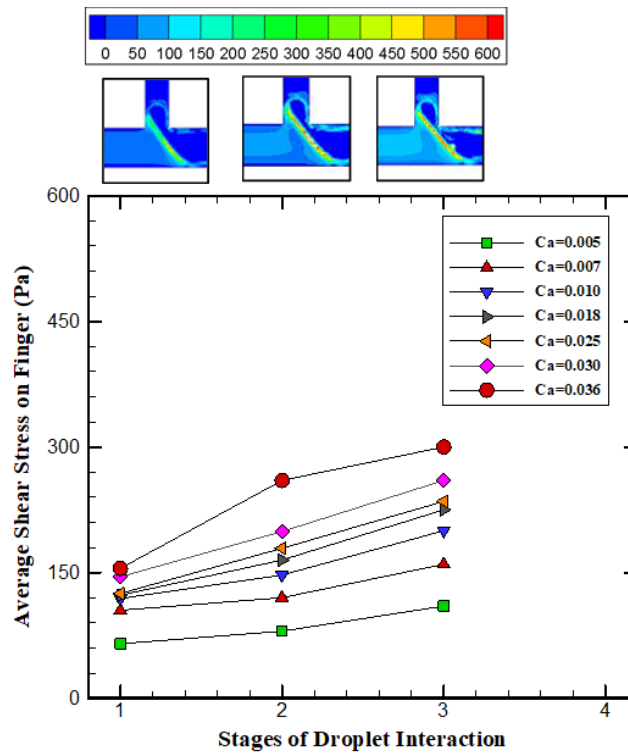


Figure AI.12. Evolution of average shear stress with time for Ca ranging from equivalent squeezing to the dripping regime. Contours at the top of the figure show average shear stress and corresponding stage of droplet interaction for given computed value.

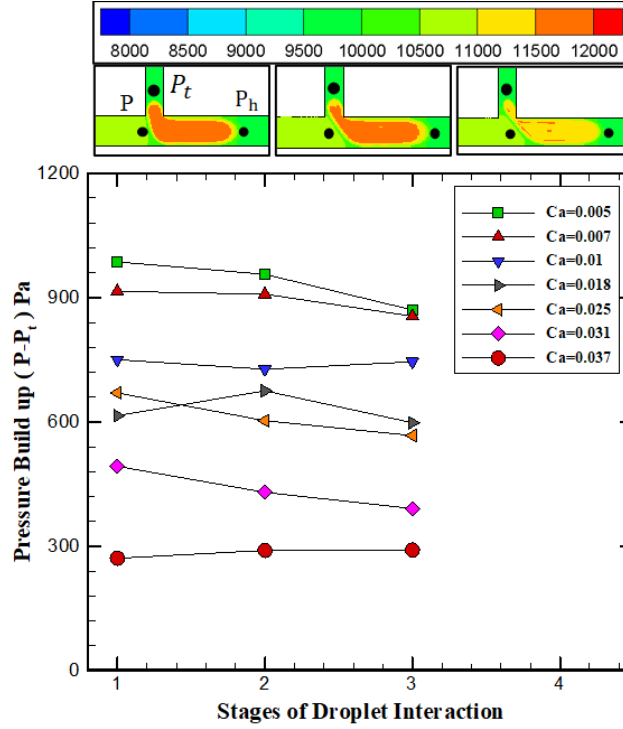


Figure AI.13. Evolution of pressure built up with time for Ca ranging from equivalent squeezing to the dripping regime. Contours at the top show pressure built up and corresponding stage of droplet interaction for given computed value.

In terms of the transition between regimes, we see from Figure AI.12 and Figure AI.13, that as Ca rises from 0.018 to 0.025 we move from a situation in which shear stress starts to play an important role. Hence, a movement from the squeezing regime to the dripping regime is observed. The transition aligns with that shown in Figure AI.9.

AI.5.2. Mechanism of Droplet Breakup

The flow of continuous fluid coming from upstream gets divided into the main channel and the bypass channel. Flow rate entering (thereby droplet entering) the main channel and bypass channel depends on the resistance of the channels. Because of the higher resistance of the bypass channel, only a small portion of the droplet enters the bypass channel compared to the main channel. Now when we assume droplet trapped in the T-junction, it is acting as a temporary blockage to the flow in the bypass channel which contributes to increasing the resistance to the flow of continuous phase. The corresponding force F_R is directly proportional to $(P - P_t)$ and is given by $F_R = (P - P_t)hw_b$. The shear force acting on the finger is given by, $F_\tau = shearstress \times hL_f$, where L_f is the finger length. Both F_R and F_τ helps in droplet breakup in the bypass channel.

Once the droplet enters into the bypass channel and as w_m is always more than w_b , surface tension will try to keep the droplet in the main channel. The surface tension force is directly proportional to the Laplace pressure jump across the interface. The Laplace pressure across the interface in bypass channel is $\Delta P_{LB} = \gamma \left(\left(\frac{2}{w_b} \right) + \left(\frac{2}{h} \right) \right)$ and oriented downstream in the main channel. Similarly, the Laplace pressure across the interface in the main channel is $\Delta P_{LM} = \gamma \left(\left(\frac{2}{w_m} \right) + \left(\frac{2}{h} \right) \right)$ and acting in opposite direction of the former one. The difference in the Laplace pressure is $\Delta P_d = \gamma \left(\left(\frac{2}{w_b} \right) - \left(\frac{2}{w_m} \right) \right)$ and acting in such a way that it opposes the droplet breakup in the bypass channel. The corresponding surface tension force (F_γ) is obtained by multiplying the ΔP_d by the cross-section area of the channel. Forces acting on the droplet trapped in the T-junction of the bypass channel is shown in Figure AI.14a.

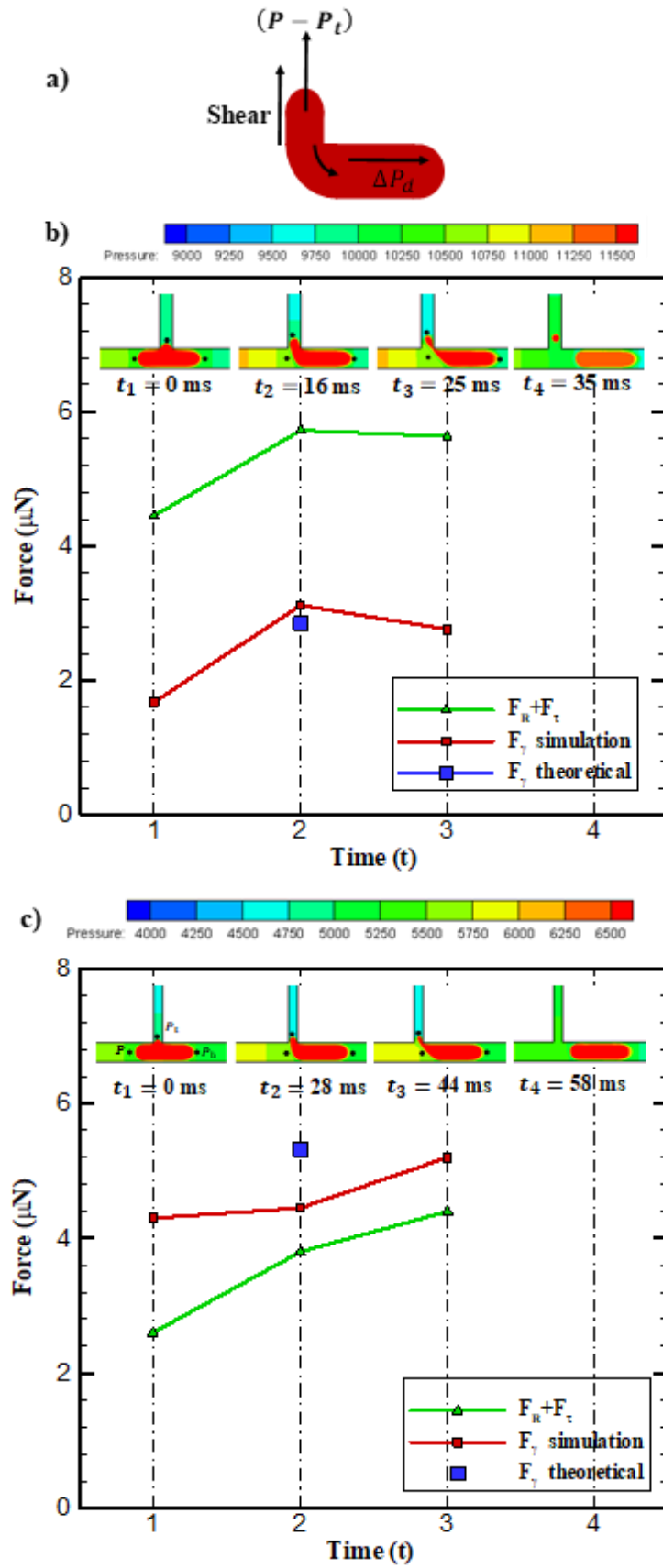


Figure AI.14. Evolution of $(F_R + F_\tau)$ and F_γ during various stages of the droplet interaction with the bypass channel. a) Forces acting on the trapped droplet (b) The case of droplet breakup (c) Case of no droplet breakup.

We compute $(P - P_t)$ and average shear stress at different instances during the interaction of the droplet with the T-junction for no droplet breakup and breakup from simulations and from this we compute corresponding F_R and F_t as shown in Figure AI.14b,c. We compute the value of ΔP_d thereby F_γ using both simulation and Laplace equation. These cases correspond to ones discussed in section 3.3. The insets show pressure contours representing the corresponding instance of the droplet interaction. In Figure AI.14b, $(F_R + F_t) > F_\gamma$ and break up occurs. By contrast, $(F_R + F_t) < F_\gamma$ is valid for all instances for no breakup in Figure AI.14c.

AI.6. Application of Present Work in Droplet-based Microfluidics

Drug research is conducted with the help of high throughput screening (HTS). In this method target cells are tested against the library of compounds. Selective combinations of samples and reagents required by HTS makes it difficult to bring it on a microfluidic chip, as continuous droplet production methods are still used. Large droplets of different samples are relatively easily introduced onto a chip. Each is individually isolated, hence in the lab on a chip analogy, can be considered as test tubes. If you can selectively break up these droplets, these test tubes become pipettes, and a technology is born which can react to different chemicals in multiple permutations. An active mechanism used for selectively breaking the droplet into mother droplet used by Sesen et al. [38], where authors allowed the mother droplet to interact with the bypass channel and with the help of surface acoustic waves achieved selective droplet breakup into the bypass channel. In such applications exactly knowing the transition between droplet breakup and no breakup will certainly help in optimizing the duration of surface acoustic pulse and voltage applied to the interdigital transducers (IDT) resulting in precise control of daughter droplet volume. This paper systematically examines the knife edge separating droplet breakup/no breakup (with the help of capillary number and geometry of the bypass channel), and forces at play so contribute significantly to the development of such technologies.

AI.7. Conclusion

We experimentally and computationally investigated the effect of the width of the bypass channel (β) and capillary number (Ca) on no droplet breakup to droplet breakup at the entrance of the bypass channel in a microfluidic circuit. The PDMS microchannel is fabricated using the standard photolithography techniques, and interfacial dynamics was visualized using a

high-speed camera. Silicon oil/paraffin oil and water were used as a continuous phase and a discontinuous phase, respectively. The range of β and Ca were 0.35 to 0.91 and 0.001 to 0.04, respectively. Measurements show that a critical value of β exists, keeping Ca constant, for achieving the droplet breakup. Similarly, a critical value of the Ca exists, keeping β as constant. We have proposed regime maps on Ca - β plane for demarcating regimes of no droplet breakup and droplet breakup. In regime maps, we have plotted contours of finger length (L_f) and percentage of the volume of daughter droplet to original droplet volume (V_{ratio}). The maximum volume of the daughter droplet corresponds to the lower Ca and larger β . 3D computational simulations were carried out using a commercial CFD software for the breakup and no-breakup cases and were compared with measurements. The simulated interfacial dynamics, L_f and V_{ratio} are found to be in good agreement with the experimental results. Comparison of simulations with measurements showed that if the hydrodynamic pressure drops across the droplet in the channel and average shear stress acting on the finger overcomes differential Laplace pressure of the droplet, breakup occurs otherwise not. Like breakup regimes for droplet generation at T-junction, we report regimes for droplet breakup at T-junction of a bypass channel and they exhibit equivalent squeezing and dripping regimes. In squeezing regime, the hydrodynamic pressure drop across the droplet is dominant while in equivalent dripping regime both shear stress and hydrodynamic pressure drop are dominant. The present results provide useful information regarding the knife edge separating droplet breakup and no breakup, thus significantly useful for the development of active technologies used for droplet breakup.

AI.8. Supplementary Information

AI.8.1. Droplet Generation

The droplets are generated at a T-junction using oil and de-ionized water as the continuous and discontinuous phases, respectively. Of the existing literature, the geometry we have used most closely matches with that of Garstecki *et al.* [33] ($w_d/w_m \approx 0.5$).

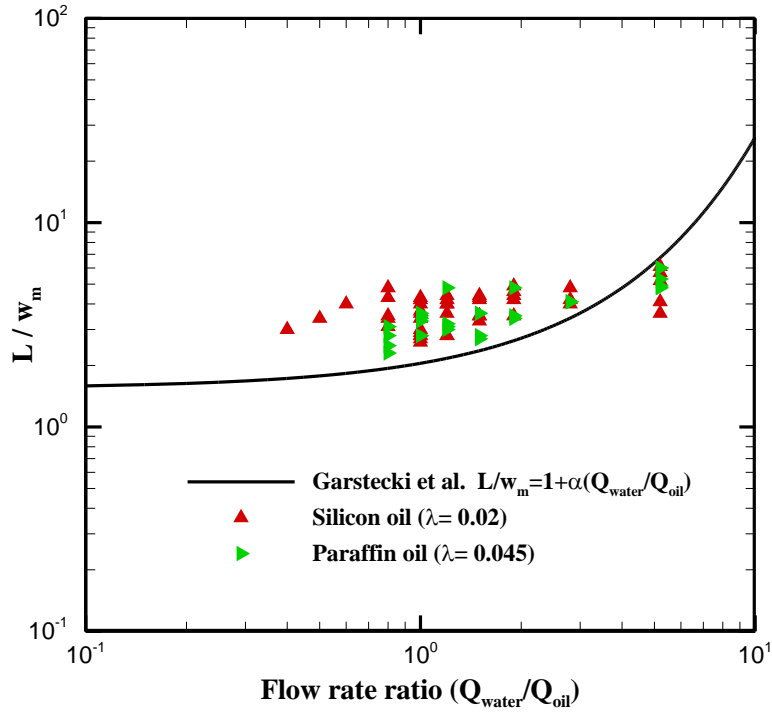


Figure AI.15. Comparison between dimensionless droplet length observed in experiments and model presented by Garstecki *et al.* [1]. The solid line is the curve showing predicted droplet size.

In most of our measurements the droplet production takes place in the squeezing regime ($Ca < 0.015$). We compare the measured length of the droplet formed at the T-junction with the predicted scaling model given by Garstecki *et al.* [1] as $L/w_m = 1 + \alpha(Q_{\text{water}}/Q_{\text{oil}})$, where L , w_m , α , Q_{water} and Q_{oil} are the length of droplet formed, the width of the main channel, a fitting parameter ($\alpha=1$), the flow rate of water and the flow rate of oil, respectively. Figure AI.15 plots the droplet length (L/w_m) as a function of flow rate ratio and we note that the measurements of droplet length (L/w_m) are clustered near the curve proposed by Garstecki *et al.* [33], and are slightly larger than the values predicted by the model. We observed that in our experiments, variation of mother droplet length is relatively small as it is mostly confined to squeezing regime.

AI.8.2. Mother Droplet Length

We have plotted mother droplet length distribution in Figure AI.16. Average length of mother droplet is $500 \mu\text{m}$ and we have maintained mother droplet length of $500 \pm 100 \mu\text{m}$ in 88 % of our experiments.

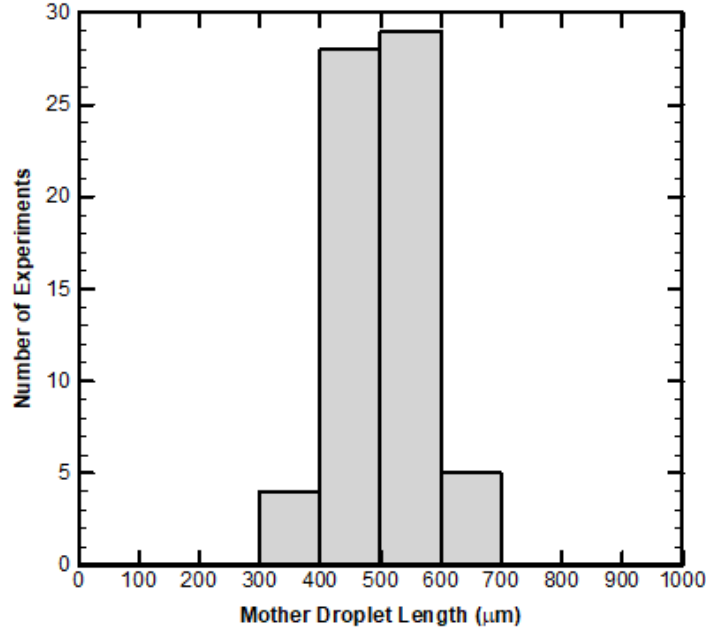


Figure AI.16. Mother droplet length Vs Number of experiments.

AI.8.3. Average Shear Stress Calculation

We have calculated the shear stress on finger in the gap between finger and bypass channel wall close to interface of the droplet. We have shown top view and locations where we have measured shear stress in Figure AI.17.

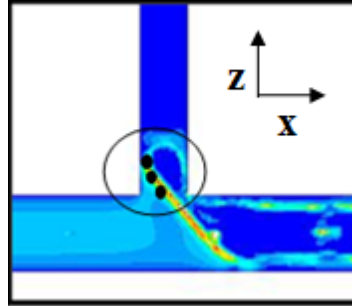


Figure AI.17. Contours of shear stress when droplet interacts with bypass channel. Black circle shows finger and bypass channel. Black dots in the gap are representative of locations where we computed shear stress.

Shear stress acting in xy , yz and zx plane is as follows

$$\tau_{xy} = \mu \left[\frac{\partial v}{\partial x} + \frac{\partial u}{\partial y} \right], \tau_{xz} = \mu \left[\frac{\partial u}{\partial z} + \frac{\partial w}{\partial x} \right], \tau_{zy} = \mu \left[\frac{\partial w}{\partial y} + \frac{\partial v}{\partial z} \right] \quad (\text{AI.1})$$

Where u , v and w are velocity in x , y and z direction respectively.

Total shear stress acting on small area dA is τ . As a finger consist of n number of small areas dA , and A is total area of finger exposed to the flow,

$$\tau_{average} = \frac{\int \tau dA}{A} \quad (\text{AI.2})$$

AI.9. References

- [1] A. Huebner, S. Sharma, M. Srisa-Art, F. Hollfelder, J. B. Edel, and A. J. deMello, Microdroplets: A sea of applications?, *Lab Chip* 8, 1244 (2008).
- [2] S. Y. Teh, R. Lin, L.-H. Hung, and A. P. Lee, Droplet microfluidics., *Lab Chip* 8, 198 (2008).
- [3] D. J. Collins, A. Neild, A. deMello, A.-Q. Liu, and Y. Ai, The Poisson distribution and beyond: methods for microfluidic droplet production and single cell encapsulation, *Lab Chip* 15, 3439 (2015).
- [4] M. Sesen, T. Alan, and A. Neild, Droplet control technologies for microfluidic high throughput screening (μ HTS), *Lab Chip* 17, 2372 (2017).
- [5] H. Zhang, E. Tumarkin, R. M. A. Sullan, G. C. Walker, and E. Kumacheva, Exploring microfluidic routes to microgels of biological polymers, *Macromol. Rapid Commun.* 28, 527 (2007).
- [6] C. N. Baroud, F. Gallaire, and R. Dangla, Dynamics of microfluidic droplets, *Lab Chip* 10, 2032 (2010).
- [7] J. D. Tice, H. Song, A. D. Lyon, and R. F. Ismagilov, Formation of Droplets and Mixing in Multiphase Microfluidics at Low Values of the Reynolds and the Capillary Numbers, *Langmuir* 19, 9127 (2003).
- [8] S. Okushima, T. Nisisako, T. Torii, and T. Higuchi, Controlled production of monodisperse double emulsions by two-step droplet breakup in microfluidic devices, *Langmuir* 20, 9905 (2004).
- [9] A. M. Gañán-Calvo and J. M. Gordillo, Perfectly Monodisperse Microbubbling by Capillary Flow Focusing, *Phys. Rev. Lett.* 87, 274501 (2001).
- [10] S. L. Anna, N. Bontoux, and H. A. Stone, Formation of dispersions using “flow focusing” in microchannels, *Appl. Phys. Lett.* 82, 364 (2003).
- [11] L. L. A. Adams, T. E. Kodger, S.-H. Kim, H. C. Shum, T. Franke, and D. A. Weitz, Single step emulsification for the generation of multi-component double emulsions, *Soft Matter* 8, 10719 (2012).
- [12] J. U. Shim, R. T. Ranasinghe, C. A. Smith, S. M. Ibrahim, F. Hollfelder, W. T. S. Huck, D. Klenerman, and C. Abell, Ultrarapid generation of femtoliter microfluidic droplets for single-molecule-counting immunoassays, *ACS Nano* 7, 5955 (2013).
- [13] D. R. Link, S. L. Anna, D. A. Weitz, and H. A. Stone, Geometrically Mediated Breakup of Drops in Microfluidic Devices, *Phys. Rev. Lett.* 92, 054503 (2004).

- [14] L. Ménétrier-Deremble and P. Tabeling, Droplet breakup in microfluidic junctions of arbitrary angles, *Phys. Rev. E* 74, 035303(R) (2006).
- [15] J. Hong, M. Choi, J. B. Edel, and A. J. deMello, Passive self-synchronized two-droplet generation, *Lab Chip* 10, 2702 (2010).
- [16] Y.-C. Tan, J. S. Fisher, A. I. Lee, V. Cristini, and A. P. Lee, Design of microfluidic channel geometries for the control of droplet volume, chemical concentration, and sorting., *Lab Chip* 4, 292 (2004).
- [17] D. Huh, J. H. Bahng, Y. Ling, H. H. Wei, O. D. Kripfhans, J. B. Fowlkes, J. B. Grotberg, and S. Takayama, Gravity-driven microfluidic particle sorting device with hydrodynamic separation amplification, *Anal. Chem.* 79, 1369 (2007).
- [18] L. M. Fidalgo, C. Abell, and W. T. S. Huck, Surface-induced droplet fusion in microfluidic devices, *Lab Chip* 7, 984 (2007).
- [19] B. Ahn, K. Lee, R. Panchapakesan, and K. W. Oh, On-demand electrostatic droplet charging and sorting, *Biomicrofluidics* 5, 024113 (2011).
- [20] A. R. Abate, J. J. Agresti, and D. A. Weitz, Microfluidic sorting with high-speed single-layer membrane valves, *Appl. Phys. Lett.* 96, 203509 (2010).
- [21] K. Ahn, C. Kerbage, T. P. Hunt, R. M. Westervelt, D. R. Link, and D. A. Weitz, Dielectrophoretic manipulation of drops for high-speed microfluidic sorting devices, *Appl. Phys. Lett.* 88, 024104 (2006).
- [22] J.-C. Baret, O. J. Miller, V. Taly, M. Ryckelynck, A. El-Harrak, L. Frenz, C. Rick, M. L. Samuels, J. B. Hutchison, J. J. Agresti, D. R. Link, D. A. Weitz, and A. D. Griffiths, Fluorescence-activated droplet sorting (FADS): efficient microfluidic cell sorting based on enzymatic activity., *Lab Chip* 9, 1850 (2009).
- [23] H. Lee, L. Xu, B. Ahn, K. Lee, and K. W. Oh, Continuous-flow in-droplet magnetic particle separation in a droplet-based microfluidic platform, *Microfluid. Nanofluidics* 13, 613 (2012).
- [24] M. Sesen, T. Alan, and A. Neild, Microfluidic on-demand droplet merging using surface acoustic waves, *Lab Chip* 14, 3325 (2014).
- [25] L. Schmid and T. Franke, SAW-controlled drop size for flow focusing, *Lab Chip* 13, 1691 (2013).
- [26] L. Schmid and T. Franke, Acoustic modulation of droplet size in a T-junction, *Appl. Phys. Lett.* 104, 133501 (2014).
- [27] D. J. Collins, T. Alan, K. Helmerson, and A. Neild, Surface acoustic waves for on-demand production of picoliter droplets and particle encapsulation., *Lab Chip* 13, 3225

- (2013).
- [28] J. C. Brenker, D. J. Collins, H. Van Phan, T. Alan, and A. Neild, On-chip droplet production regimes using surface acoustic waves, *Lab Chip* 16, 1675 (2016).
 - [29] M. De Menech, P. Garstecki, F. Jousse, and H.A.Stone, Transition from squeezing to dripping in a microfluidic T-shaped junction, *J. Fluid Mech.* 595, 141 (2008).
 - [30] Z. Nie, M. S. Seo, S. Xu, P. C. Lewis, M. Mok, E. Kumacheva, G. M. Whitesides, P. Garstecki, and H. A. Stone, Emulsification in a microfluidic flow-focusing device: Effect of the viscosities of the liquids, *Microfluid. Nanofluidics* 5, 585 (2008).
 - [31] H. Liu and Y. Zhang, Droplet formation in a T-shaped microfluidic junction, *J. Appl. Phys.* 106, 034906 (2009).
 - [32] G. F. Christopher, N. N. Noharuddin, J. A. Taylor, and S. L. Anna, Experimental observations of the squeezing-to-dripping transition in T-shaped microfluidic junctions, *Phys. Rev. E* 78, 036317 (2008).
 - [33] P. Garstecki, M. J. Fuerstman, H. A. Stone, and G. M. Whitesides, Formation of droplets and bubbles in a microfluidic T-junction - Scaling and mechanism of break-up, *Lab Chip* 6, 437 (2006).
 - [34] T. Thorsen, R. W. Roberts, F. H. Arnold, and S. R. Quake, Dynamic pattern formation in a vesicle-generating microfluidic device, *Phys. Rev. Lett.* 86, 4163 (2001).
 - [35] M. C. Jullien, M. J. Tsang Mui Ching, C. Cohen, L. Menetrier, and P. Tabeling, Droplet breakup in microfluidic T-junctions at small capillary numbers, *Phys. Fluids* 21, 072001 (2009).
 - [36] D. A. Hoang, L. M. Portela, C. R. Kleijn, M. T. Kreutzer, and V. van Steijn, Dynamics of droplet breakup in a T-junction, *J. Fluid Mech.* 717, R4 (2013).
 - [37] S. S. Bithi and S. A. Vanapalli, Collective dynamics of non-coalescing and coalescing droplets in microfluidic parking networks, *Soft Matter* 11, 5122 (2015).
 - [38] M. Sesen, C. Devendran, S. Malikides, T. Alan, and A. Neild, Surface acoustic wave enabled pipette on a chip, *Lab Chip* 17, 438 (2017).
 - [39] See Supplemental Material at [] for details on droplet generation, size of the mother droplet generated at T-junction, calculation of average shear stress and videos of droplet interaction with the T-junction of the bypass channel.

Appendix II

Microfluidic Valves for Selective On-chip Droplet Splitting at Multiple Sites

AII.1. Preface for Appendix II

This Appendix was published as a journal article in Langmuir and adapted with permission from ref. 35 Copyright (2020) American Chemical Society⁴¹. The candidate was the second author and Mr. Sagar N Agnihotri was the lead author for this work. The candidate played a primary role in designing the research, performing the experiments, analysing the data, and writing the paper. Additional authors for the work include Dr. Rajneesh Bhardwaj, and Prof. Adrian Neild. Their contributions were central to the publication of this work and are gratefully acknowledged and appreciated.

In this chapter, we describe a microfluidic system for control of droplet division at two locations using T-junction and expansion channel which are placed one after another. Droplets generated at standard T-junction are introduced into the droplet division section of the microchannel. In the first set of experiments, the Droplet division section consists of two consecutive identical T-junctions branching from the main channel. With this geometry, we were able to produce daughter droplets only at first junction while there was no droplet division at second junction. Resistive network analysis is used to redesign the microchannel geometry with expansion channel in place of second junction, to have the same quantity of flow entering in both the junctions. We observe five different regimes of droplet breakup namely 1) No droplet breakup in both junctions 2) Droplet breakup in first junction, 3) Droplet breakup in both junctions with higher daughter droplet volume in first junction 4) Daughter droplet volume higher in second junction 5) Intermittent droplet breakup in both the junctions. Under specific flow conditions, droplet interaction with both the junctions is similar. We then showed design requirements for location of microvalves, simulated by deformation of main channel wall and by experiments to selectively break the droplet.

AII.2. Introduction

Droplets in microfluidic systems have emerged as an excellent tool for conducting a wide range of biological and chemical processes [1]. Samples and reagents can be segmented allowing various screening or selection processes to be conducted. Compartmentalizing samples and reagents in nano to femtolitre sized volumes in a continuous immiscible phase enables the creation of thousands of reaction volumes. Droplets in a microfluidic system can also be used for analyzing small biological samples, even allowing single cells [2] to be encapsulated and

analyzed in isolation. Other notable applications of droplet microfluidics are microparticle synthesis [3, 4] immunoassays [5], reaction kinetics [6], protein crystallization [7, 8], clinical diagnosis [9, 10] and conducting high-throughput analysis [11, 12].

In the standard approach to high-throughput screening, target samples are exhaustively tested against a library of compounds in search of a positive reaction, a process currently performed using microtiter plates and robotic pipetting. However, miniaturisation limits have been reached due to the achievable accuracy of dispensing and evaporation issues. For further size reduction, minimising sample and reagent usage, droplet-based microfluidics provides a compelling alternative as very small samples can be handled in an evaporation-free environment. However, a key strength of droplet microfluidics, the rapid production of thousands of identical samples [13–18], does not lend itself well to achieve multiple reaction permutations between libraries of samples, which requires the merging of pairs of droplets of different types. As such, to conduct complex screening processes on a microfluidic device, one approach would be to input large droplets of different types and subdivide then at will. This allows for the correct sample to be dispensed at the right reaction site, an on-chip analogy to pipetting [19, 20]. Subsequently, the samples require merging and mixing.

Droplets can be divided into symmetric [21, 22] and asymmetric [23] daughter droplets using geometric features [24–26] and alteration of flow conditions [27]. However, these methods are passive, requiring no external energy input, which means that each droplet undergoes the same fate; they are all subdivided. To be able to divide droplets selectively active methods are required, here external interaction takes place which briefly controls the behaviour of a droplet at a certain location on the chip, the result is the division of a single droplet when and where required. The concept of how this can be used for high throughput screening is depicted in Figure AII.1. Various forms of interaction have been used in conjunction with droplets, including surface acoustic waves [20, 28–31], micro-valves [19], electric fields [32], microheaters [33] and use of a laser [34].

In order to develop a valve based approach to break-up of selected individual droplets, we first studied the behaviour of droplets as they pass a junction to a channel which later rejoins the main channel, we termed this a bypass channel. This study showed that there are flow conditions at which the droplet remains intact, but only just so [35]. With the physics behind this knife-edge condition better understood, we demonstrated that a transition from non-

breakup to breakup could be achieved by the partial closing of a valve at the entrance to the bypass channel [19]. However, in both cases, only one droplet breakup site was considered, to rapidly react multiple chemicals in various permutations, more will be needed. Here, we explore whether the knife-edge condition can be obtained at more than one location. Again, we use mother droplets (droplets generated upstream using standard T-junction) of the same sample, rather than introducing different chemicals for each droplet. We demonstrate the design considerations required for break up at the two T-junction using resistive network analysis. Subsequently, we demonstrated the capability for selective break-up at either junction by local reduction of the main channel width, which is akin to the operation of an on-chip microvalve. This demonstrates the potential for features performing pipette like-functions at multiple sites, so moving closer to the type of robotic dispensing utilised in microtitre plates being realised on a chip, and so at far smaller volumes and no evaporation.

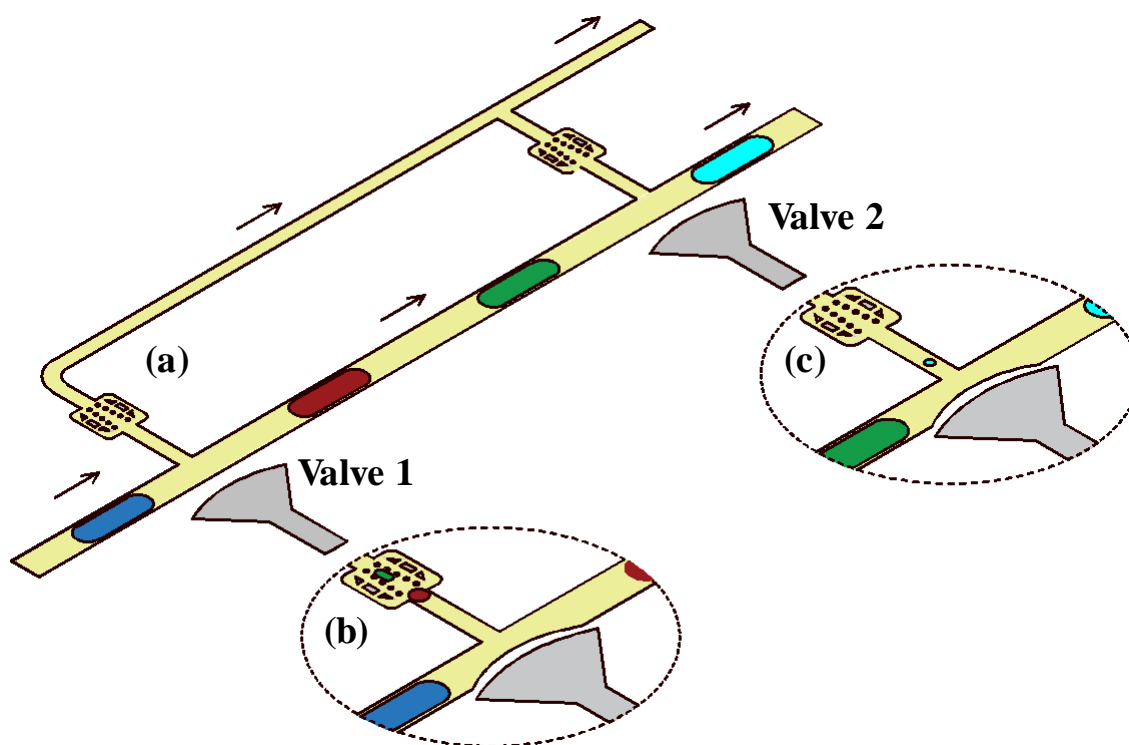


Figure AII.1. Conceptual depiction of selective droplet breakup using microvalves at two locations. (a) The “mother” droplets are generated at upstream T-junction (not shown) and, as they pass down the main channel, interacts with the first and second junctions positioned adjacent to valves 1 and 2. When the valves are off, operating conditions are chosen such that no droplet breakup occurs at these junctions. (b) When the first valve is pressurized and deforms, the selected droplet breaks up and a small droplet enters the side branch, here it is depicted that a sample of the green and red fluids are selected, subsequently these can be passively merged in the branch (c) Similarly, the second valve also allows selective break up such that different reactions can be initiated in its merging station. The result is a system in which a range of reaction permutations can occur between different reagents.

AII.3. Method and Material

AII.3.1. Experimental Methods

The microfluidic system consisted of a standard T-junction to form droplets, and, downstream from this, a pair of junctions which branched into a second outlet, it is at these junctions that the controllability of droplet breakup behavior will be observed. The chip was fabricated by bonding together two pieces of polydimethylsiloxane (PDMS), one of which was flat and acted as the substrate, the other patterned with the microfluidic features using standard soft lithography. Droplets of de-ionized water were formed in paraffin oil at a T-junction; this continuous stream of monodispersed droplets were used as a convenient substitute for mother droplets of different samples. The flows into the T-junction were driven by two syringe pumps (New Era pump systems Inc, USA). The interfacial tension between de-ionized water and paraffin oil was measured using a spinning drop tensiometer (Dataphysics Inc, SVT20) yielding a value of 30 mN/m , this value along with the oil viscosity ($0.022\text{ Pa}\cdot\text{s}$) and the flow speed was used to calculate the Capillary number of the continuous phase. Once formed, these mother droplets pass by the pair of splitting junctions; here the droplet interactions were recorded using a high-speed camera imaging at 300 frames per second (Motion Pro Y3, IDT Inc, USA) fitted with a long-distance working objective (Qioptiq Inc., Germany). The velocity, volume of the mother droplet generated at the upstream T-junction and daughter droplet (smaller droplet formed after breakup of mother droplet) generated after breaking up are calculated using image processing. The volume of the droplet is calculated assuming the plug consist of spherical caps at both the ends and cuboid section in the middle.

AII.3.2. Simulation Setup and Grid Independence Study

We have performed numerical simulations using commercial software Ansys Fluent, which uses the volume of fluid (VOF) method to capture the fluid-fluid interface. Rather than simulate the generation of the droplet at upstream T-junction, to save computational expense, we initialized the simulation with multiple cuboids of discontinuous phase along the length of the main channel. These had the same volume and separation as the droplets observed in the experiments. Surface tension causes these cuboids to form the shape of a droplet prior to the interactions with the junctions. At the start of the main channel, we imposed a uniform velocity boundary condition while at both outlets, a pressure outlet (atmospheric pressure) boundary

condition was used. At the wall of the microchannel, we imposed the no-slip boundary condition and used the equilibrium contact angle of 140° .

We used Cartesian structured mesh generated using commercial software ICEM (Ansys Inc.). A uniform structured grid with refinement was used near the entrances of the first and second junction, and adjacent to the microchannel wall, while at other locations a coarse grid was used. A variable time step is used in all the simulations; the time step being decided based on the Courant number, which is fixed at 0.5. Paraffin oil and de-ionized water are used as the continuous phase and discontinuous phase respectively in all the simulations.

Figure AII.2 shows the grid size independence test for the geometry we used in the regime with no droplet breakup in both the junctions. We used three different refinements of $\Delta S = 1 \mu\text{m}$, $2 \mu\text{m}$, $3 \mu\text{m}$ near the wall of the microchannel and the junction. The minimum grid size was kept the same in x, y and z directions. The finger length (L_f) when droplets interact with the first and second junction and details of grid size independence test are shown in Table AII.1 and Figure AII.2. As the error in case 2 is just 1.5% and 0% compared to the finest grid for L_f in first and second junction respectively, $\Delta S = 2 \mu\text{m}$ was used in the simulations. We found that for the refinement of $2 \mu\text{m}$, we got reasonable accuracy.

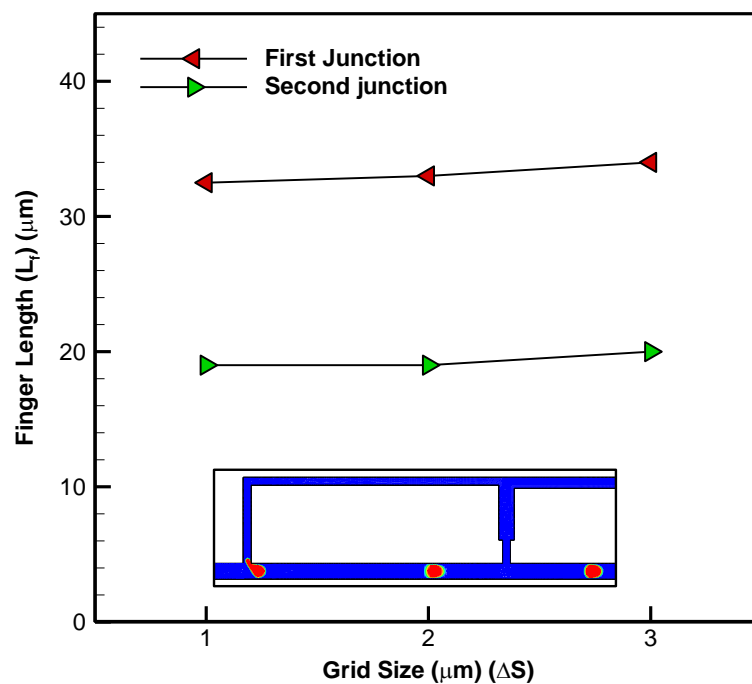


Figure AII.2. Grid size independence study showing finger length (L_f) vs minimum grid size (ΔS) for droplet interaction with the first and second junction.

Table AII.1. Grid size independence study showing error in finger length (L_f) with respect to the finest grid.

Cases	ΔS	Number of cells	% error in L_f with respect to case 3 in the first Junction	% error in L_f with respect to case 3 in the second junction
1	3 μm	0.6×10^6	4.6%	5%
2	2 μm	0.83×10^6	1.5%	0%
3	1 μm	1.2×10^6	-	-

AII.4. Results and Discussion

In all experiments, the ratio of the volumetric flow rates supplied into the droplet generation T-junction, $Q_{Continuous} / Q_{Discontinuous}$ is set at a value of 1. The range of flow rates used was 2 to 16 $\mu\text{l} / \text{min}$, resulting in droplets of between 0.6 and 1 nL (or 220 and 180 μm length). We start by analyzing the nature of these droplet interactions with the downstream T-junctions and then examine the potential for droplet breakup.

AII.4.1. Two Identical T-junctions

Firstly, we examine the interaction with two identical junctions, each connecting to the outlet channel by channels of the same width (50 μm), as shown in Figure AII.3. As the droplet interacts with the first junction, we observe daughter droplet generation for all the flow rates. When the remaining volume of the mother droplet interacts with the second junction, no breakup occurs, again across all flow rates tested. Figure AII.4a shows a series of images of the breakup which occurs at the first junction (Capillary number (Ca) is 0.01), as the mother droplet passes the junction a finger is formed into the branch channel, the length of which increases with time. It is this finger which ultimately breaks into a droplet. Figure AII.4b shows images from the second junction, here the finger can be seen to be shorter and to retract, the mother droplet remaining intact. Indeed, when the finger length is analyzed, Figure AII.4c for both junctions, consistently across all flow rates tested, this metric is larger for the first junction. There isn't a single critical finger length at which break-up occurs across all Ca. The reason for this is that there is a shear force acting on the finger, resulting from flow past it into the branch channel, this shear will be higher for larger flow rates; hence a smaller finger length is required for break up [35]. It can be seen in Figure AII.4d, in which the daughter droplet volume produced at the first junction is shown, despite the shorter finger created at higher flow

rates, the droplet does not decrease commensurately, this too is partly attributable to the shear acting on the finger which acts to prevent its retraction. In addition, there is simply less time for retraction to take place prior to the breakup. Finally, it is worth noting that the plotting is of percentage volume with respect to mother droplet volume, and that at higher flow rates smaller mother droplets are produced, which contributes to a shorter finger length.

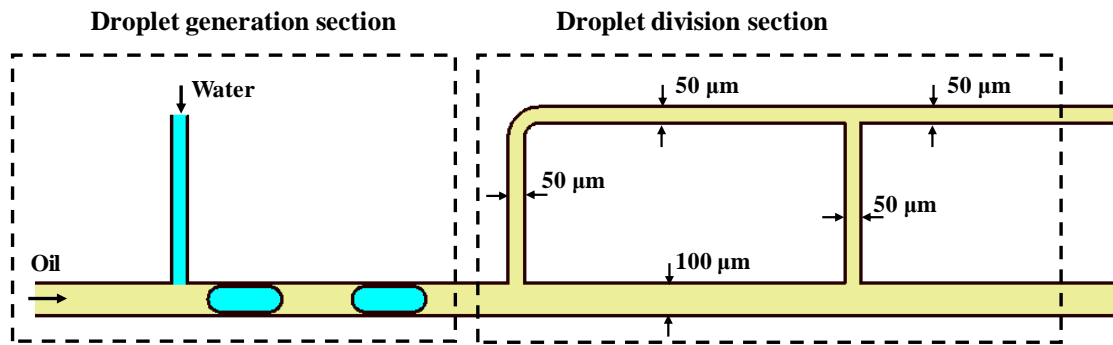


Figure AII.3. A schematic of microfluidic system design with upstream droplet generation section followed by two stage droplet division section. Mother droplets are produced upstream and are made to interact with identical droplet division junctions.

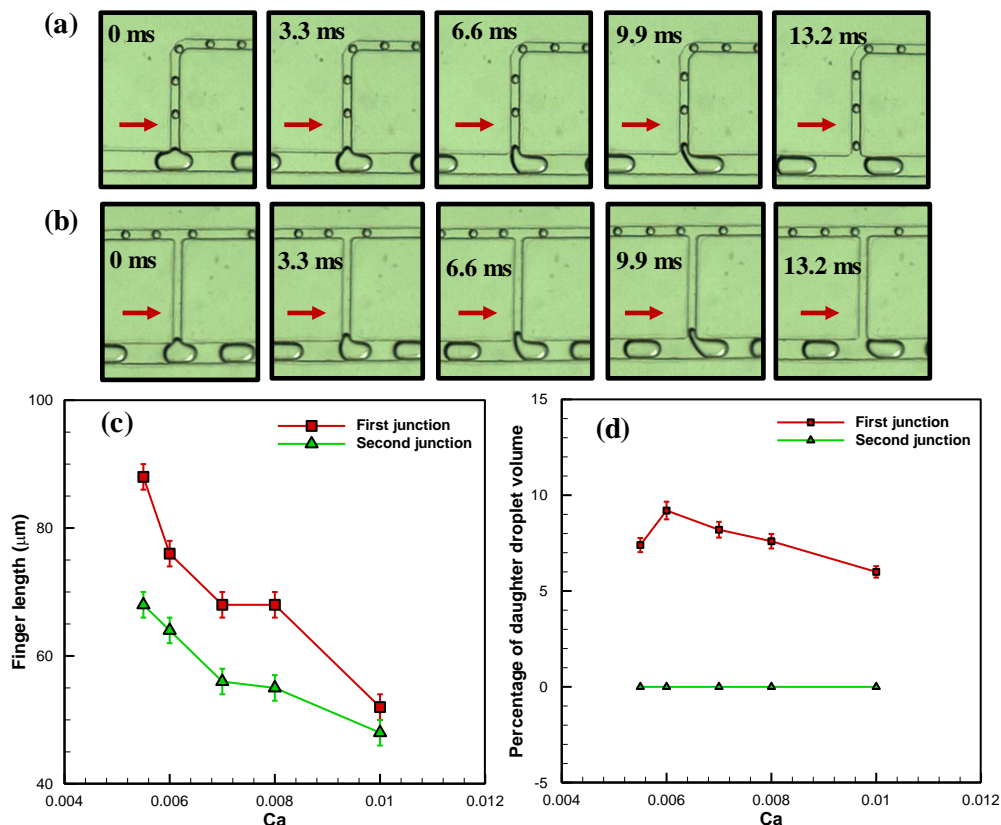


Figure AII.4. High-speed visualization, at a capillary number (Ca) of 0.01, of a mother droplet interacting with the (a) first and (b) second junctions. In which a finger is seen to develop in the branch and either break into a droplet or retract. The discrepancy, between the two junctions, of the maximum length of the finger length (c) and the (d) percentage of the volume of the mother droplet which breaks into a daughter droplet is seen across the Ca range tested.

As a result, we can conclude that the finger lengths grow with time; hence the size of the mother droplet will influence the finger length. The shear produced on the finger by the flow at higher flow rates lowers the length required for break up to occur. But most importantly, we also conclude that the behavior of the two junctions is very different; hence there can be no expectation that there is a flow condition which could provide a knife-edge condition (between the breakup and no breakup) at both junctions simultaneously. As such, this design would not lend itself well to selective droplet breakup at multiple locations.

AII.4.2. Channel Flow Rate Examination

We now analyze the system more fully, such that a system can be designed in which the droplet interaction behavior is similar at both junctions for given flow rates. To do this, we have conducted a theoretical examination of the flow distribution in the first and second junctions using an electric circuit analogy [36]. This will yield the relative flow rates around the chip, these in turn dictate the degree to which a finger is formed at the junctions, and hence they are very closely related to the condition for droplet breakup. To predict the flow rate distribution with least complexity, we analyzed only the continuous phase and did not consider the presence of droplets in the microfluidic system.

We considered the microfluidic system as a resistive network, where flow rate (Q) is equivalent to current, potential difference is equivalent to the pressure drop (ΔP) and resistance is equivalent to the hydrodynamic flow resistance of the microchannel. Figure AII.5 shows the microfluidic network with hydrodynamic resistance (R) in each branch. The height of microchannel was assumed to be constant at $60 \mu m$. The hydrodynamic resistance in each branch is calculated using the equation below [36],

$$R = \frac{12\mu l}{wh^3 \left[1 - 0.63 \left(\frac{h}{w} \right) \right]} \quad (\text{AII.1})$$

Where w , h , l , μ represent width, height, length of the channel and viscosity of continuous phase, respectively. Figure AII.5 shows the flow rate through each branch with the help of Kirchhoff's junction law which states that the net charge (equivalent to flow) coming towards the junction should be equal to that going away from the junction. To find out, the flow rate in each branch, we have used Kirchhoff's loop law which states that the algebraic sum of all the potential differences (equivalent to pressure drop) along a closed loop in a circuit is zero. We

are particularly interested in how the resistances R_3 and R_5 must be set such that the flows down these channels, Q_1 and Q_2 are similar.

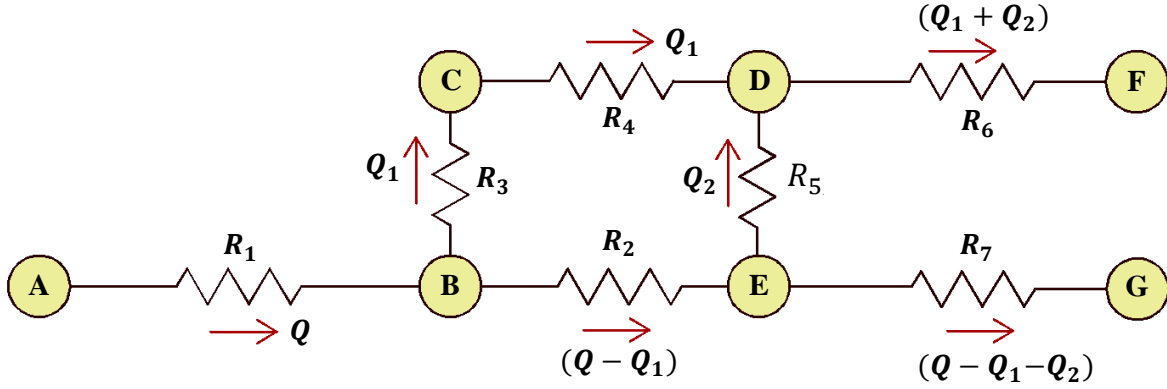


Figure AII.5. The Resistance network of the microfluidic system with the associated flow rate distribution of the continuous phase, without considering the resistance of the droplets.

Applying Kirchhoff's loop law for the 1st loop, we obtain:

$$R_5 = \left[\frac{(R_2 + R_3 + R_4)Q_1 - R_2Q}{Q_2} \right] \quad (\text{AII.2})$$

As both the outlets (points F and G) are subjected to atmospheric conditions, we can say $P_A = P_F = P_G$, this means that:

$$(P_E - P_G) = (P_E - P_D) + (P_D - P_F) \quad (\text{AII.3})$$

And so

$$R_5Q_2 = R_7(Q - Q_1 - Q_2) - R_6(Q_1 + Q_2) \quad (\text{AII.4})$$

We have fixed all the dimensions of the channel except the width of the second branch (w_{b_2}) which is channel with subscript 5, and the width of link 6. In the calculations the widths of these two channels are assumed to be the same. Now we have two equations (AII.2 and AII.4) and two unknowns (R_5 and Q_1 or Q_2). By solving equation AII.2 and AII.4 for flow rate condition of $Q_1 = Q_2$, we obtain a value of R_5 which would equate to a constant width of $w_{b_2} = 65 \mu m$. However, we are interested in the formation of droplets at these junctions, and we have already seen the importance of the finger formed prior to break up or retraction. Hence, the width of the opening of the channel, which is the location at which a finger forms, is significant. As such, instead of using the value of $65 \mu m$, we change the channel such that is

maintains the equivalent resistance. The channel geometry for link 5 is set such that it has the same opening ($50\ \mu\text{m}$) as link 2 for a distance larger than the longest finger we expect ($100\ \mu\text{m}$) and then expands such that the overall resistance is equal to that calculated. The resulting geometry is shown in Figure AII.6. By having this geometry, we can directly compare finger lengths in both the sections as the width of both the junctions is same and droplet trapped in both the junction will be subjected to same Laplace pressure [35].

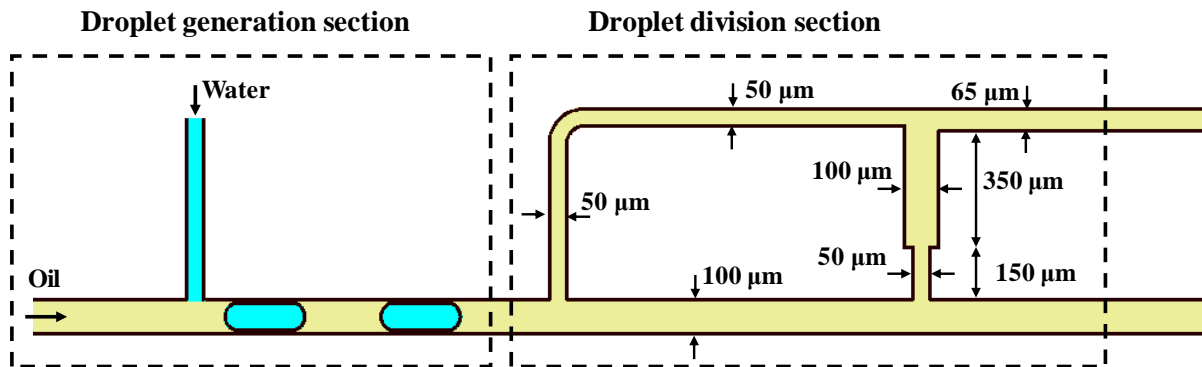


Figure AII.6. A schematic of a microfluidic system with upstream droplet generation section followed by droplet division section, designed such that the behavior at each splitting junction is balanced. To achieve this the second junction consists of a section of channel with the original width, followed by an expansion which drops the overall resistance of the branch.

AII.4.3. Expansion Channel for 2nd Junction

With the channel redesigned to match the flows in the two branches, albeit in the absence of droplets, we reassess the droplet interactions at the junctions to these branches. In contrast to the first design, we observe a range of behaviors. Figure AII.7 shows five different regimes, the finger lengths for each of which are shown in Figure AII.8:

- a) In the first regime, droplet develops a small finger which penetrates in the junction, recovers its original shape and moves into the main channel without breaking up in the first and second junction as shown in Figure AII.7a. We call this regime as “no breakup in both junctions.”
- b) In the second regime, we observe that droplet breaks up in the first junction while there is no droplet breakup in the second junction, as shown in Figure AII.7b. We call this regime as “breakup in the first junction.”
- c) In the third regime, we observe droplet breakup in both junctions, but the volume of daughter droplet formed in the second junction is much smaller than that of the first junction, as shown in Figure AII.7c. We call this regime as “breakup in first junction onset of breakup in the second junction.”

d) In the fourth regime, we observe droplet breakup in both the junctions, but the volume of daughter droplet formed in the second junction is more than that of the first junction, as shown in Figure AII.7d. We call this regime as “breakup in both junctions.”

e) In the fifth regime, we observe intermittent breakup in both junctions. By intermittent breakup, we mean we don’t observe daughter droplet continuously forming in both the junctions. Out of 10 droplets interacting with the first and second junction only 3 to 4 droplets break into the first and second junction, as shown in Figure AII.7e. We call this regime as “intermittent breakup.” The finger length for this regime is not shown in Figure AII.8 as it is not consistent across each droplet.

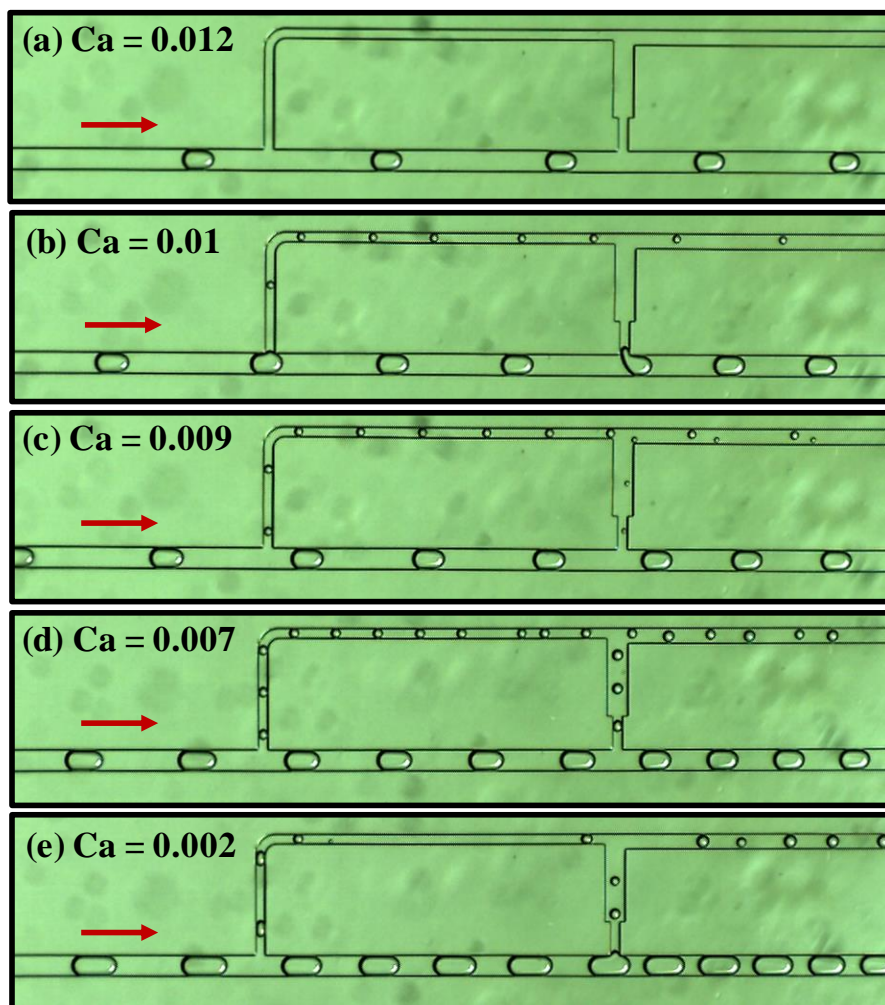


Figure AII.7. High-speed visualization of droplet interaction with straight channel branching from the first junction and the expansion channel stemming from the second junction. Five regimes are observed: (a) No droplet breakup in both junctions, (b) Breakup in the first junction, (c) Breakup in first junction onset of breakup in the second junction, (d) Breakup in both the junctions. (e) Intermittent breakup in both the junctions.

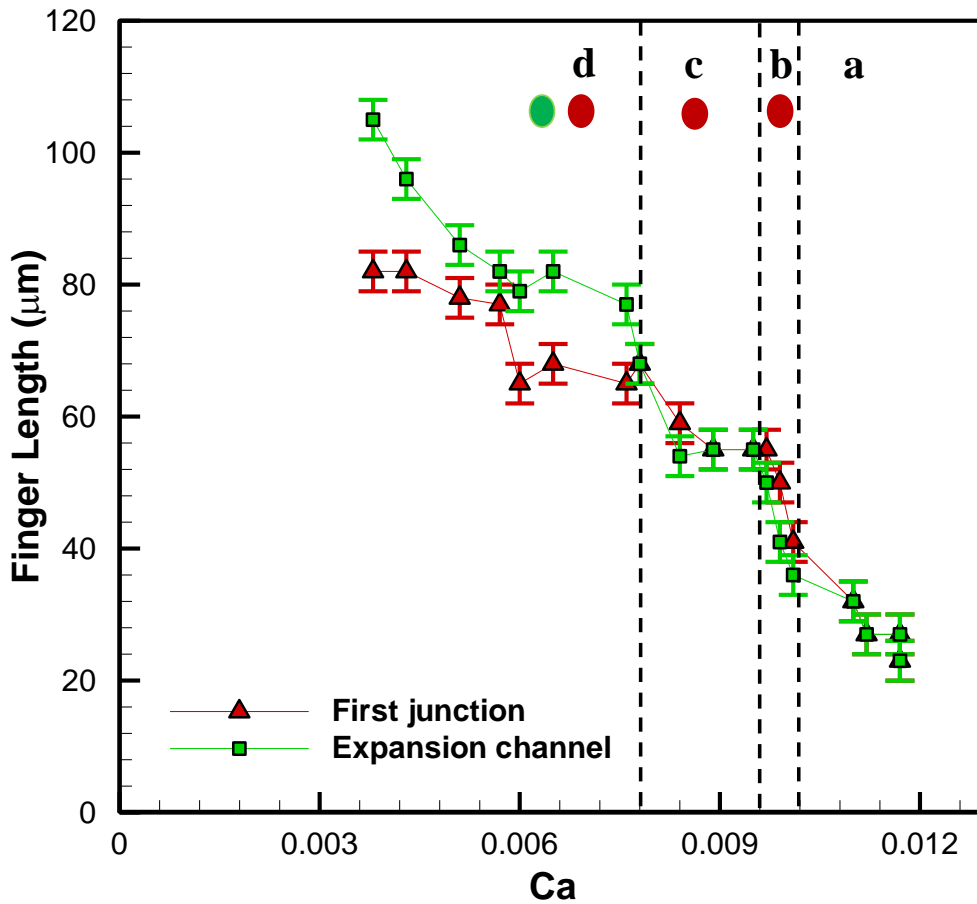


Figure AII.8. The finger length for four regimes of droplet interaction is plotted against Ca. The finger length from regime e (intermittent breakup regime) is not plotted as it is not consistent across each droplet. The dots below the regime letters indicates whether break up at the first (red) and second (green) junction occurs.

Clearly, by changing the chip design such that the branch flows are more similar, we have made the behavior of the droplets more similar under some conditions. In Figure AII.9, the finger length is shown as a function of time for each of the two designs. We see that the flow equalization in the branches in the second design makes for much more similar finger growth across the two channels, thus linking the role of branch flow with finger length.

We see that in this range, there will be a flow condition where we will get the same size of the daughter droplet volume in both junctions. With a slight change in flow conditions, we can either have regime (a) or regime (d). As the continuous phase flow rate is increased further (increase in Ca), we again start to get different daughter droplet volumes where the volume of daughter droplet formed in the second junction is higher than the first T-junction. Clearly, in this design, it is possible to obtain very similar behavior at each junction, either no droplet at each or droplets of the same size (Figure AII.10). Here, we move between these results by

altering the imposed flow; however, for the selective break-up, we will have a fixed flow rate and will seek to vary behavior by local alteration of geometry. By starting with the same behavior at each junction, we will now seek to alter that behavior in just one of the junctions by changing the local geometry.

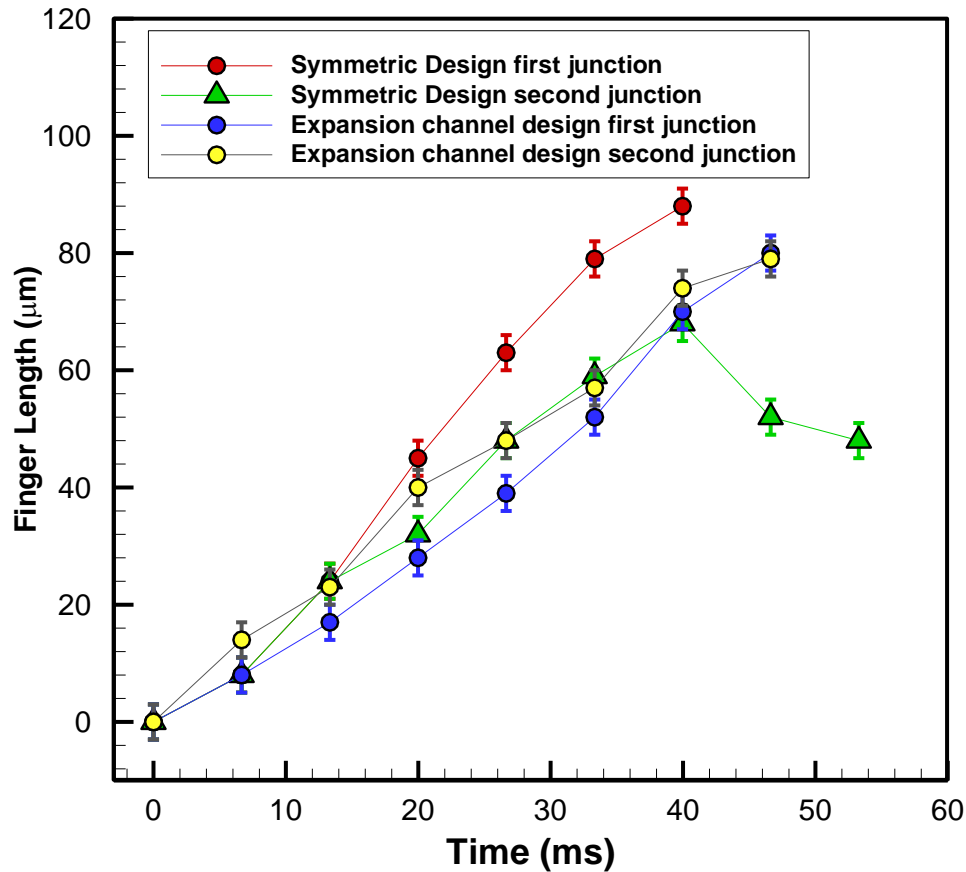


Figure AII.9. The evolution of finger length measured in the first and second junction for both the designs (symmetric and expansion channel) as a function of time under the same flow conditions ($Ca = 0.0055$). Case of symmetric design second junction yields no breakup while all other cases represent breakup.

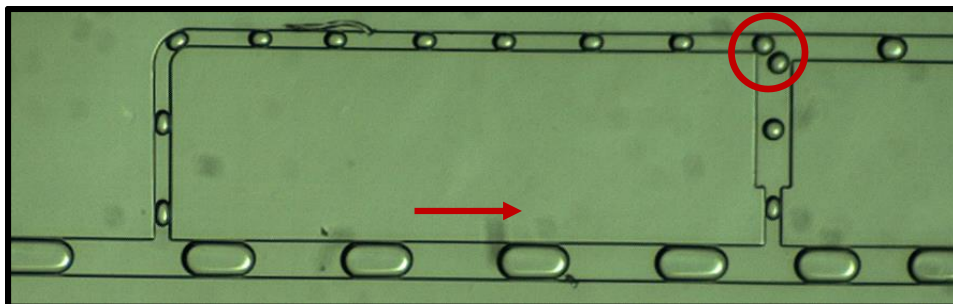


Figure AII.10. High-speed visualization of droplet interacting with the first T-junction and expansion channel, which yields the same volume of daughter droplets at both the junctions. This lies between regime 3 and 4.

AII.4.4. Selective Droplet Breakup at Two Locations (Two Valve System Using Simulations)

We compare results of numerical simulations at first and second junction in ‘regime a’ where there is no droplet breakup in both the junctions with the experimental results in the same regime specifically at $Ca = 0.011$. The separation distance between the droplets is kept similar to that measured in experiments. The length of the mother droplet in the simulation was matched to that observed in the experimental work. The shape of the droplet interfaces obtained at different times is in very good agreement with those recorded in the experiments (Shown in Figure AII.11). The experimentally measured maximum finger length is $27 \mu m$ while the numerical value is $33 \mu m$. Overall, the numerical results capture ‘regime a’ with reasonable accuracy, this benchmarking allows us to examine the deformation of channel wall similar to that of single-layer microvalve at two locations.

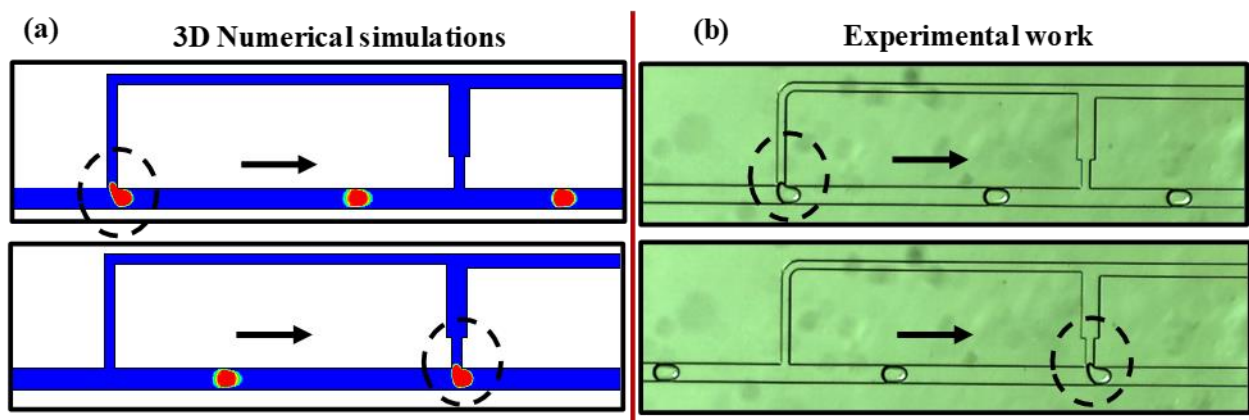


Figure AII.11. Comparison between experimental and 3D numerical simulations at $Ca = 0.011$. (a) Contours of the volume fraction of the continuous and discontinuous phase. (b) High-speed visualization of the droplet interaction with the first and second junction.

To be able to screen using permutations of reactions, we would like to have a selective breakup of droplets at different locations, in this way the mother droplet becomes the fluid in a pipette and the intervention becomes equivalent to depressing the pipette plunger. We have previously demonstrated selective breakup of mother droplet at a single location using a single layer microvalve [19], here, the change in local geometry moved results from a non-break up to a breakup regime. We turn to simulation to explore whether similar geometric changes can be used on this system with two junctions and balanced flows. We start by selecting the imposed flow condition, which places the system at the knife-edge between regime a and b. We

validated numerical simulations in the regime of “no droplet breakup at both junctions” with that of the experimental results (details in supplementary information). Subsequently, we change the wall shape such that there is an occlusion at the entrance to one of the junctions (as occurs when a single layer valve is partially closed). The wall deformation is assumed to be semi-elliptical with a major axis of the ellipse set as $500\mu m$, and the semi-minor axis is varied from $0\mu m$ to $60\mu m$. Dimensions of the deformation are similar to the dimensions used by Raveshi et al. [19] in their experiments.

In the first set of simulations, Figure AII.12, we introduced semi-elliptical deformation in the main channel at the entrance of the first branch. The semi-minor axis of deformation is varied from $0\mu m$ to $60\mu m$. Figure AII.12 shows the regularity of droplet breakup, for deformations above $30\mu m$ this is 100%. Insets of Figure AII.12 show droplet interaction with deformation of $0\mu m$ and $60\mu m$. It is worth noting that here we make a fixed geometrical change, when operating a valve, it is possible to switch the deformation rapidly, the requirement is that when this is done the next drop breaks up, hence 100% is required, but the valve would only be operated for the time that a single mother droplet passes the junction.

In the second set of simulations, we introduced semi-elliptical deformation in the main channel at the entrance of the second junction. The semi-minor axis of deformation is varied from $0\mu m$ to $60\mu m$. We observe that with these deformations we don't get droplet breakup in the second junction, but rather at first. The reason for this is that by introducing the deformation at the entrance of the second junction, it increases the hydrodynamic resistance of both R_2 and R_7 . This increase in hydrodynamic resistance of R_2 causes droplet to break in the first junction. To avoid this, we changed the location of deformation away from the entrance of the second junction, such that it only altered the resistance of channel 7. Figure AII.13 shows the efficiency of droplet breakup for different values of deformation and for two different designs; that of identical second junction and expansion channel. We observed in expansion channel design, for the deformation of $20\mu m$ and $30\mu m$ droplet breakup efficiency is found to be 0%, as deformation is increased to $40, 50, 60\mu m$ we start getting an efficiency of droplet breakup to 90%, 90% and 100% respectively. While in case of identical second junction even at the deformation of $60\mu m$ we don't observe droplet breakup.

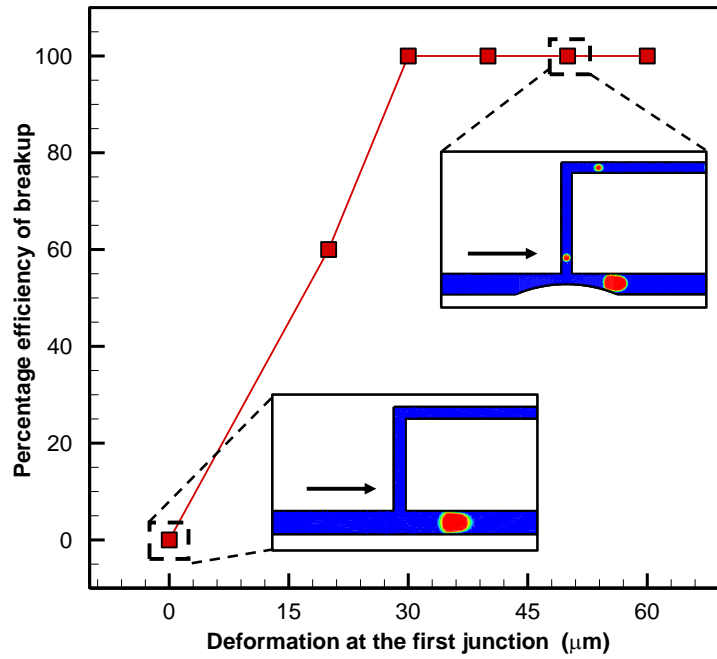


Figure AII.12. Percentage efficiency of droplet breakup in the first junction against deformation at the entrance of the first junction calculated using numerical simulations. Bottom inset shows a top view of the 3D numerical simulation without deformation at the entrance of first junction resulting in no breakup. The top inset shows a top view of the 3D numerical simulation with deformation of $50\mu\text{m}$ at the entrance of first junction resulting in a breakup.

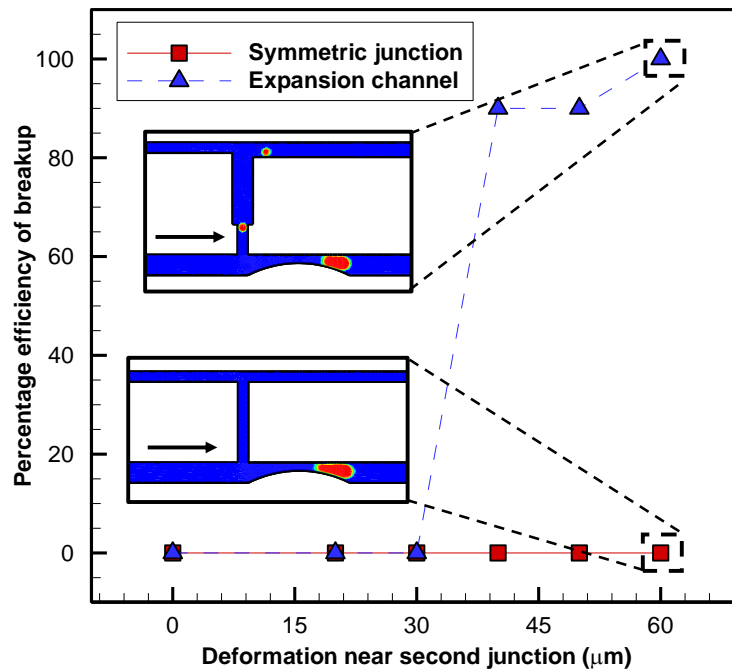


Figure AII.13. Percentage efficiency of droplet breakup in the second junction and expansion channel against deformation near the entrance of the second junction calculated using numerical simulations. Bottom inset shows a top view of the 3D numerical simulation with deformation of $60\mu\text{m}$ for symmetric second junction resulting in no breakup. The top inset shows a top view of the 3D numerical simulation with deformation of $60\mu\text{m}$ for expansion channel resulting in a breakup.

AII.4.5. Selective Droplet Breakup at Two Locations (Two Valve System Using Experiments)

To demonstrate the capability of selective droplet break-up at different locations, we fabricated a system with two single-layer microvalves. Each individual valve consists of a membrane of 30 μm separating a dead-end channel from the main channel, application of pressure in the former causes deformation of the membrane constricting the main channel. The location of the first valve is at the entrance of the first junction while we tried two different locations (at the entrance of the second junction and away from the second junction) for the second valve. Figure 1 shows that with the actuation of the valve, we can move from no breakup to breakup at each of the two locations. The microfluidic system is operated in the first regime (no breakup in both the junctions) when the valve is not activated. To examine the onset of selective droplet breakup in the first junction, the valve is pressurized systematically from 0 mbar to 1600 mbar.

Figure AII.14a shows the high-speed visualization for the conditions of no valve actuation, actuation at 1200 mbar and 1600 mbar pressure at first junction. We didn't observe droplet breakup below 1300 mbar, at 1400 mbar droplet breakup efficiency is just 5% and above 1500 mbar droplet breakup efficiency is observed to be 100% as shown in Figure AII.15a. Each of Figure AII.14b,c shows the high-speed visualization for three conditions, those of no valve actuation, actuation at 1200 mbar and 1600 mbar pressure, with the valve located (b) at the second junction and (c) downstream from it. We observe that the location of the valve slightly away from the second junction is far more efficient than at the entrance of the second junction, as to achieve 100 % droplet breakup efficiency the former location needs the valve pressure of 1000 mbar while the later position needs 1500 mbar as shown in Figure AII.15b.

While comparing simulation results with experiments for deformation at first junction, the trend is similar in both cases, but simulation gives the efficiency of 100% (full efficiency) at the deformation of 30 μm whereas experiments show that full efficiency is reached after the deformation of 56 μm . In the second junction, simulation gives the efficiency of over 90% at the deformation of 40 μm and experiments show that this efficiency is achieved after the deformation of 45 μm . The simulation results are in close agreement with the experimental results when we are not operating the valve. However, the simulation results under predicts the deformation required experimentally when we are operating the valve. This may be due to two reasons: firstly, the actual operation of the valve causes much more pressure variations in the

microchannel due to its dynamic nature compared to having a static deformation in the simulations. Secondly, it is quite difficult to get the exact shape of the deformed interface in the simulation.

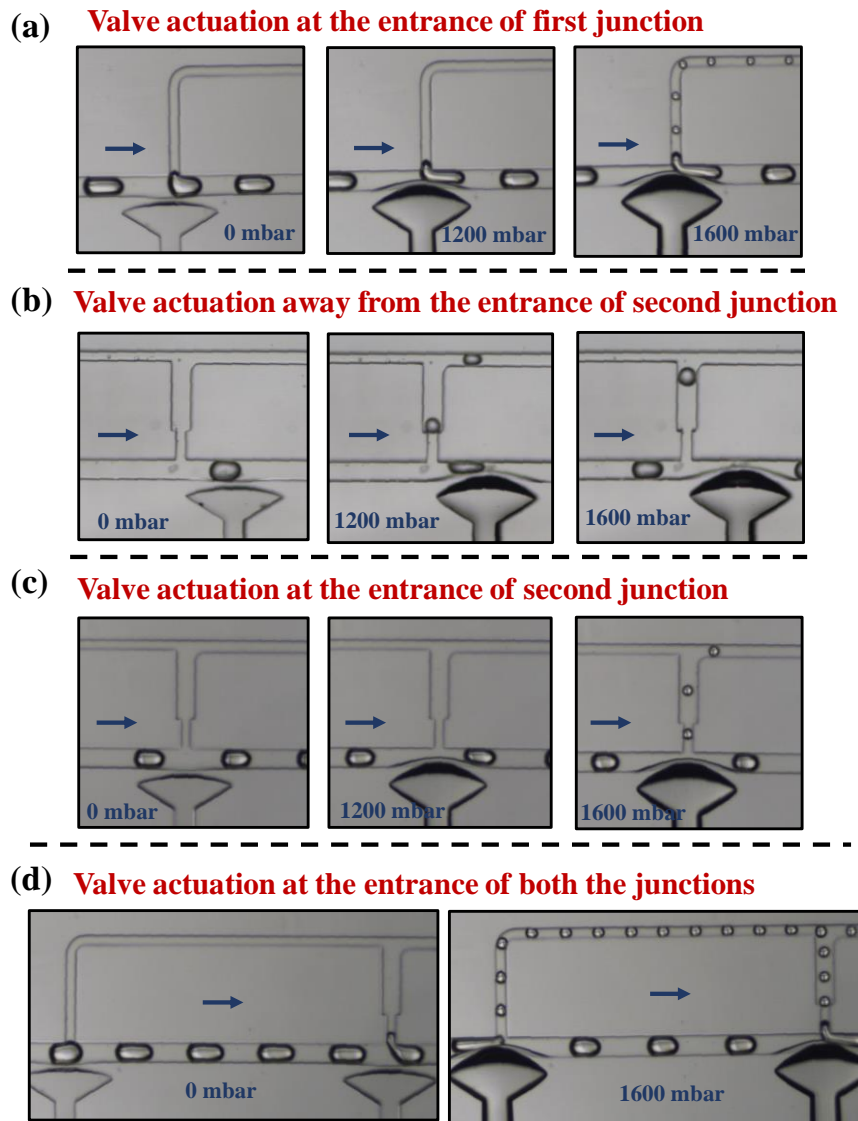


Figure AII.14. High-speed visualization showing the interaction of droplets with two junctions in the presence and absence of valve actuation. (a) Actuation of valve for the first junction (b) Actuation of the valve for the second junction with the valve away from the entrance of second junction (c) Actuation of the valve for the second junction with the valve at the entrance of second junction (d) Actuating both the valves simultaneously.

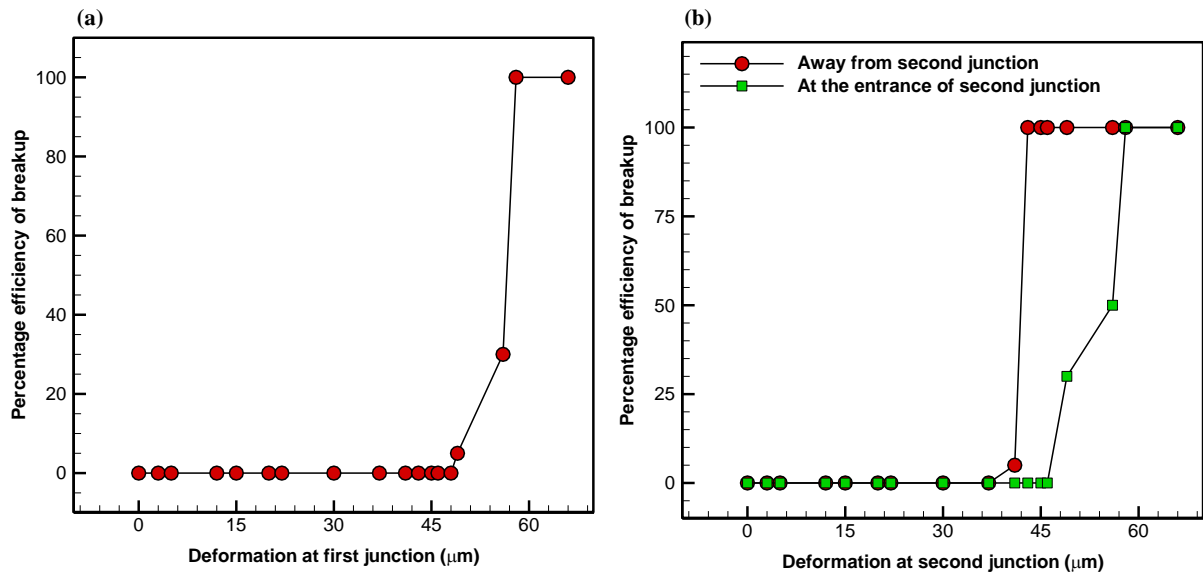


Figure AII.15. Percentage efficiency of droplet breakup vs valve deformation for (a) first junction (b) second junction with two valve locations.

AII.5. Conclusion

We analyze the droplet behaviors in a microfluidic system with two junctions, seeking to find the underlying requirements for selective droplet breakup in more than one location. We used resistive network analysis to design the microfluidic system, so that same flow rate of continuous phase enters both the junctions. With this achieved, we observed that under certain flow conditions, the droplet interaction with both junctions was similar, which allowed a critical operational condition to be selected at which break-up doesn't quite occur. We then showed the design requirements for the location of microvalves, simulated by deformations of the channel wall, such that we can alter the break-up condition at just one of the junctions. Taken as a whole, this work shows the design and experimental route to selective droplet breakup at multiple locations on a chip.

AII.6. Microfabrication

Standard photolithography was used to make the microchannel devices with the help of polydimethylsiloxane (PDMS). The 2-inch silicon wafer was RCA cleaned to make the mold of microchannel device using negative photoresist SU8-2050 (Microchem). The negative photoresist was spin coated on the silicon wafer at 500 rpm for 10 seconds and 2500 rpm for

next 30 seconds to achieve the height of 60 μm . The silicon wafer with photoresist was soft baked on a hot plate at 65°C and 95°C for 3 minutes and 9 minutes, respectively. The photomask having the pattern of the microfluidic device was prepared using a laser writer (LW405, Microtech Inc). The photomask and silicon wafer were aligned with each other using mask aligner (Karl Suss MJB4) and subjected to ultraviolet radiation with an intensity of 220 mJ/cm². The silicon wafer was then post-baked on a hot plate at 65°C and 95°C for 2 minutes and 7 minutes, respectively, developed using SU8 developer for 15-20 minutes and finally hard baked at 120°C for 10 minutes to get the desired mold. PDMS (Dow Corning, Sylgard 184) 10 parts was mixed with 1 part of curing agent and poured on the mold while 6 parts by weight of PDMS is mixed with 1 part of curing agent to prepare base slab on glass slide. The mold and the base slab were both kept in the oven at 60°C until they become sufficiently hard. The PDMS replica was peeled off from the mold, two inlets and two outlets were punched in the PDMS replica. The PDMS replica and base slab were bonded at 95°C in an oven for 10-12 hours.

AII.7. References

- [1] P. S. Dittrich, K. Tachikawa, and A. Manz, Micro Total Analysis Systems. Latest Advancements and Trends, *Anal. Chem.* 78, 3887 (2006).
- [2] M. He, J. S. Edgar, G. D. M. Jeffries, R. M. Lorenz, J. P. Shelby, and D. T. Chiu, Selective encapsulation of single cells and subcellular organelles into picoliter- and femtoliter-volume droplets, *Anal. Chem.* 77, 1539 (2005).
- [3] J. H. Kim, T. Y. Jeon, T. M. Choi, T. S. Shim, S. H. Kim, and S. M. Yang, Droplet microfluidics for producing functional microparticles, *Langmuir* 30, 1473 (2014).
- [4] E. Rondeau and J. J. Cooper-White, Biopolymer microparticle and nanoparticle formation within a microfluidic device, *Langmuir* 24, 6937 (2008).
- [5] R. Gao, Z. Cheng, A. J. Demello, and J. Choo, Wash-free magnetic immunoassay of the PSA cancer marker using SERS and droplet microfluidics, *Lab Chip* 16, 1022 (2016).
- [6] H. Song and R. F. Ismagilov, Millisecond Kinetics on a Microfluidic Chip Using Nanoliters of Reagents, *J. Am. Chem. Soc.* 125, 14613 (2003).
- [7] B. Zheng, L. S. Roach, and R. F. Ismagilov, Screening of protein crystallization conditions on a microfluidic chip using nanoliter-size droplets, *J. Am. Chem. Soc.* 125, 11170 (2003).
- [8] D. L. Chen, L. Li, S. Reyes, D. N. Adamson, and R. F. Ismagilov, Using three-phase flow of immiscible liquids to prevent coalescence of droplets in microfluidic channels:

- Criteria to identify the third liquid and validation with protein crystallization, *Langmuir* 23, 2255 (2007).
- [9] T. A. Crowley and V. Pizziconi, Isolation of plasma from whole blood using planar microfilters for lab-on-a-chip applications, *Lab Chip* 5, 922 (2005).
- [10] K. H. Han and A. B. Frazier, Paramagnetic capture mode magnetophoretic microseparator for high efficiency blood cell separations, *Lab Chip* 6, 265 (2006).
- [11] P. S. Dittrich and A. Manz, Lab-on-a-chip: Microfluidics in drug discovery, *Nat. Rev. Drug Discov.* 5, 210 (2006).
- [12] D. K. Kang, X. Gong, S. Cho, J. Y. Kim, J. B. Edel, S. I. Chang, J. Choo, and A. J. Demello, 3D Droplet Microfluidic Systems for High-Throughput Biological Experimentation, *Anal. Chem.* 87, 10770 (2015).
- [13] P. Garstecki, M. J. Fuerstman, H. A. Stone, and G. M. Whitesides, Formation of droplets and bubbles in a microfluidic T-junction - Scaling and mechanism of break-up, *Lab Chip* 6, 437 (2006).
- [14] T. Thorsen, R. W. Roberts, F. H. Arnold, and S. R. Quake, Dynamic pattern formation in a vesicle-generating microfluidic device, *Phys. Rev. Lett.* 86, 4163 (2001).
- [15] S. L. Anna, N. Bontoux, and H. A. Stone, Formation of dispersions using “flow focusing” in microchannels, *Appl. Phys. Lett.* 82, 364 (2003).
- [16] D. N. Josephides and S. Sajjadi, Increased drop formation frequency via reduction of surfactant interactions in flow-focusing microfluidic devices, *Langmuir* 31, 1218 (2015).
- [17] T. Glawdel, C. Elbuken, and C. L. Ren, Droplet formation in microfluidic T-junction generators operating in the transitional regime. I. Experimental observations, *Phys. Rev. E - Stat. Nonlinear, Soft Matter Phys.* 85, 1 (2012).
- [18] C. N. Baroud, F. Gallaire, and R. Dangla, Dynamics of microfluidic droplets, *Lab Chip* 10, 2032 (2010).
- [19] M. R. Raveshi, S. N. Agnihotri, M. Sesen, R. Bhardwaj, and A. Neild, Sensors and Actuators B: Chemical Selective droplet splitting using single layer micro fluidic valves, *Sensors Actuators B. Chem.* 292, 233 (2019).
- [20] M. Sesen, C. Devendran, S. Malikides, T. Alan, and A. Neild, Surface acoustic wave enabled pipette on a chip, *Lab Chip* 17, 438 (2017).
- [21] D. N. Adamson, D. Mustafi, J. X. J. Zhang, B. Zheng, and R. F. Ismagilov, Production of arrays of chemically distinct nanolitre plugs via repeated splitting in microfluidic devices, *Lab Chip* 6, 1178 (2006).

- [22] A. C. Hatch, J. S. Fisher, A. R. Tovar, A. T. Hsieh, R. Lin, S. L. Pentoney, D. L. Yang, and A. P. Lee, 1-Million droplet array with wide-field fluorescence imaging for digital PCR, *Lab Chip* 11, 3838 (2011).
- [23] Y.-C. Tan, J. S. Fisher, A. I. Lee, V. Cristini, and A. P. Lee, Design of microfluidic channel geometries for the control of droplet volume, chemical concentration, and sorting., *Lab Chip* 4, 292 (2004).
- [24] J. Clausell-Tormos, A. D. Griffiths, and C. A. Merten, An automated two-phase microfluidic system for kinetic analyses and the screening of compound libraries, *Lab Chip* 10, 1302 (2010).
- [25] E. Um, M. E. Rogers, and H. A. Stone, Combinatorial generation of droplets by controlled assembly and coalescence, *Lab Chip* 13, 4674 (2013).
- [26] K. Akamatsu, K. Minezaki, M. Yamada, M. Seki, and S. I. Nakao, Direct Observation of Splitting in Oil-In-Water-In-Oil Emulsion Droplets via a Microchannel Mimicking Membrane Pores, *Langmuir* 33, 14087 (2017).
- [27] D. R. Link, S. L. Anna, D. A. Weitz, and H. A. Stone, Geometrically Mediated Breakup of Drops in Microfluidic Devices, *Phys. Rev. Lett.* 92, 054503 (2004).
- [28] D. J. Collins, T. Alan, K. Helmerson, and A. Neild, Surface acoustic waves for on-demand production of picoliter droplets and particle encapsulation., *Lab Chip* 13, 3225 (2013).
- [29] M. Sesen, T. Alan, and A. Neild, Microfluidic on-demand droplet merging using surface acoustic waves, *Lab Chip* 14, 3325 (2014).
- [30] J. H. Jung, G. Destgeer, B. Ha, J. Park, and H. J. Sung, On-demand droplet splitting using surface acoustic waves, *Lab Chip* 16, 3235 (2016).
- [31] G. Destgeer and H. J. Sung, Recent advances in microfluidic actuation and micro-object manipulation via surface acoustic waves, *Lab Chip* 15, 2722 (2015).
- [32] S. R. Doonan and R. C. Bailey, K-Channel: A Multifunctional Architecture for Dynamically Reconfigurable Sample Processing in Droplet Microfluidics, (2017).
- [33] T. H. Ting, Y. F. Yap, N. T. Nguyen, T. N. Wong, J. C. K. Chai, and L. Yobas, Thermally mediated breakup of drops in microchannels, *Appl. Phys. Lett.* 89 (2006).
- [34] C. N. Baroud, M. Robert de Saint Vincent, and J.-P. Delville, An optical toolbox for total control of droplet microfluidics, *Lab Chip* 7, 1029 (2007).
- [35] S. N. Agnihotri, M. R. Raveshi, R. Bhardwaj, and A. Neild, Droplet Breakup at the Entrance to a Bypass Channel in a Microfluidic System, *Phys. Rev. Appl.* 10, 1 (2019).

- [36] K. Oh, K. Lee, and B. Ahn et al., Design of pressure-driven microfluidic networks using electric circuit analogy, *Lab Chip* 12, 515 (2012).